Development of MOFs as supports or host for organometallic complexes

Tristan Lescouet

N° d'ordre

Année 2012

THESE DE L'UNIVERSITE DE LYON

Délivrée par

L'UNIVERSITE CLAUDE BERNARD LYON 1

ECOLE DOCTORALE

DIPLOME DE DOCTORAT

(arrêté du 7 août 2006)

soutenue publiquement le 14 décembre 2012

par

M. LESCOUET Tristan

TITRE :

Conception et fonctionnalisation de MOFs pour le greffage et l'encapsulation de complexe organométallique

Directeur de thèse : David FARRUSSENG

JURY :

M. Mihail BARBOIU	DR, CNRS, Université de Montpellier 2
M. Dominique LUNEAU	Professeur, Université Claude Bernard Lyon 1
Mme. Caroline MELLOT-DRAZNIEKS	DR, Collège de France, Paris
M. Thomas DEVIC	Dr, Institut Lavoisier, Université de Versailles
M. Nicolas BATS	Dr, IFP Energies Nouvelles, Solaize
M. David FARRUSSENG	CR, CNRS, Université Lyon 1

UNIVERSITE CLAUDE BERNARD - LYON 1

Président de l'Université	**M. François-Noël GILLY**
Vice-président du Conseil d'Administration	M. le Professeur Hamda BEN HADID
Vice-président du Conseil des Etudes et de la Vie Universitaire	M. le Professeur Philippe LALLE
Vice-président du Conseil Scientifique	M. le Professeur Germain GILLET
Secrétaire Général	M. Alain HELLEU

COMPOSANTES SANTE

Faculté de Médecine Lyon Est – Claude Bernard	Directeur : M. le Professeur J. ETIENNE
Faculté de Médecine et de Maïeutique Lyon Sud – Charles Mérieux	Administrateur provisoire : M. le Professeur G. KIRKORIAN
UFR d'Odontologie	Directeur : M. le Professeur D. BOURGEOIS
Institut des Sciences Pharmaceutiques et Biologiques	Directeur : Mme la Professeure C. VINCIGUERRA.
Institut des Sciences et Techniques de la Réadaptation	Directeur : M. le Professeur Y. MATILLON
Département de formation et Centre de Recherche en Biologie Humaine	Directeur : M. le Professeur P. FARGE

COMPOSANTES ET DEPARTEMENTS DE SCIENCES ET TECHNOLOGIE

Faculté des Sciences et Technologies	Directeur : M. le Professeur F. De MARCHI
Département Biologie	Directeur : M. le Professeur F. FLEURY
Département Chimie Biochimie	Directeur : Mme le Professeur H. PARROT
Département GEP	Directeur : M. N. SIAUVE
Département Informatique	Directeur : M. le Professeur S. AKKOUCHE
Département Mathématiques	Directeur : M. le Professeur A. GOLDMAN
Département Mécanique	Directeur : M. le Professeur H. BEN HADID
Département Physique	Directeur : Mme S. FLECK
Département Sciences de la Terre	Directeur : Mme la Professeure I. DANIEL
UFR Sciences et Techniques des Activités Physiques et Sportives	Directeur : M. C. COLLIGNON
Observatoire de Lyon	Directeur : M. B. GUIDERDONI
Polytech Lyon	Directeur : M. P. FOURNIER
Ecole Supérieure de Chimie Physique Electronique	Directeur : M. G. PIGNAULT
Institut Universitaire de Technologie de Lyon 1	Directeur : M. C. VITON
Institut Universitaire de Formation des Maîtres	Directeur : M. R. BERNARD
Institut de Science Financière et d'Assurances	Directeur : Mme la Professeure V. MAUME-DESCHAMPS

Remerciements

Je tiens tout d'abord à remercier l'Union Européenne et plus particulièrement le projet FP7 NanoMOF pour avoir financé ma thèse et Michel Lacroix pour m'avoir permis d'effectuer mes travaux au sein de l'IRCELYON.

Je souhaite ensuite remercier mon encadrant, David Farrusseng, pour m'avoir donné l'opportunité de réaliser ces travaux de thèse. Ses qualités d'encadrement m'ont permis de jouir d'une réelle autonomie tout en profitant de ses conseils avisés.

Je remercie également M. Mihail Barboiu, M. Dominique Luneau, Mme. Caroline Mellot-Draznieks, M. Thomas Devic et M. Nicolas Bats pour avoir accepter de juger ce travail.

Je tiens à remercier tout particulièrement Marie Savonnet, Emanuel Kockrick et Jérôme Canivet pour m'avoir introduit dans le monde des matériaux et l'ambiance conviviale du laboratoire 131.

Je remercie les services scientifiques de l'IRCELYON, tout spécialement Françoise Bosselet pour les centaines de DRX et Noëlle Cristin et Pascale Mascunan pour mes isothermes et analyses élémentaires.

Merci aussi à tous les membres de l'équipe ingénierie pour avoir fait de ces trois années une expérience si agréable.

Enfin un grand merci à ma famille, à mes colocataires : Sid, Chamô et Lafouine, à mes amis : Diego, Lablatte, Rino, Zael, Chouki, Tomme, John, Gainsbourg, Petitfaon, Chat et LP pour ne citer qu'eux, et enfin, et surtout, à mon amie Carine-chan.

Table of Contents

Chapter 3: Synthesis and characterization of Amino functionalized Metal-organic frameworks; Starting host for Post synthetic functionalization and acid catalyst.

Chapter 4: Control of the amino site density in Metal-organic frameworks

Chapter 5: Alternative pathway for the synthesis of isocyanato and urea-functionalised metal-organic frameworks

Experimental

Abbreviations

aa	Amino Acid
abdc	2-aminobenzene-1,4-dicaboxylate
acac	acetylacetonate
AlPO	Alumino-Phosphate
Am_2Taz	3,5-diamino-1,2,4-triazole
APS	(3-aminopropyl)triethoxysilane
aq	aqueous
as	as-synthesized
bdc	benzene-1,4-dicaboxylate
BET	Brunauer, Emmet, Teller
BINOL	1,1'-bi-2-naphtol
btc	benzene-1,3,5-tricarboxylate
CAU	Chung-Ang University
CID	Coordination polymers with Interdigitated structures
cif	Crystallographic Information File
COSY	Correlation Spectroscopy
CPL	Coordination Pillared-Layer frameworks
CPO	Coordination Polymer of Oslo
CPS	(3-chloropropyl)trimethoxysilane
d	doublet or deuterium
DABCO	1,4-diAzabicyclo[2.2.2]octane
DCM	Dichloromethane
DDR	decadodecasil 3R
DEF	N,N-diethylformamide
DFT	Density Functional Theory
DMF	dimethylformamide
DMOF	DABCO Metal-Organic Framework
DMSO	Dimethyl sulfoxide
DRIFTS	Diffuse Reflectance Infra-Red Fourier Transformation Spectroscopy

DTA	Differential Thermal Analysis
EDS	Energy Dispersive Spectroscopy
ee	enantiomeric excess
ESI	Electrospray Ionization
EXAFS	Extended X-ray Absorption Fine Structure
FAU	Faujasite
FESEM	Field Emission Scanning Electron Microscopy
FID	Flame Ionization Detector
GC	Gas Chromatography
GGA	Generalised Gradient Approximation
HBEA	hydrogen beta
HKUST	Hong-Kong University of Science and Technology
HPA	heteropolyoxoanion
ht	high temperature
HY	hydrogen Y
Hz	Hertz
ICP	Inductively Coupled Plasma
IM	Institut Français du Pétrole/Mulhouse
IR	Infrared
IRCE	Institut de Recherche sur la Catalyse et l'Environnement
IRMOF	IsoReticular Metal-Organic Framework
IRMOP	Isoreticular Metal–Organic Polyhedra
ITQ	Instituto de Tecnologıa Quimica
IZA	International Zeolite Association
KIE	Kinetic Isotope Effect
LC	Large hexagonal Channel
lt	low temperature
LTA	Linde Type A
m	multiplet
MAS	Magic Angle Spinning
MCM	Mobil Composition Material
Me	Methyl
MFI	Mobil-five
MIL	Matériaux de l'Institut Lavoisier

MOF	Metal-Organic Framework
MOP	Metal-Organic Polyhedron
MOR	Mordenite
MPc	Metal Phthalocyanine complexes
MR	Member ring
MS	Mass spectrometry
MTBE	methyl tert-butyl ether
ndc	naphthalene dicarboxylate
NMR	Nuclear Magnetic Resonance
OES	Optical Emission Spectroscopy
OMS	Ordered Mesoporous Silicas
PAW	Projector Augmented Wave
POM	polyoxometalate
ppm	parts per million
PSM	postsynthetic modification
PXRD	Powder X-Ray Diffraction
Py	Pyridine
Pymo	hydropyrimidinolate
s	singlet
SAPO	alumino-silico-phosphate
SBA	Santa Barbara Amorphous
SBU	Secondary Building Unit
SDA	Structure Directing Agent
SEM	Scanning Electron Microscopy
t	triplet
TAZ	triazole
TC	Tight triangular Channel
teda	triethylenediamine
TEM	Transmission electron microscopy
TGA	thermogravimetry analysis
THF	tetrahydrofuran
TIPB	1,3,5-triisopropylbenzene
TMS	trimethylsilane
$TMSN_3$	Trimethylsilyl azide

TON	turnover number
UiO	University of Oslo
UMCM-1	University of Michigan Crystalline Material-1
USY	ultra stable Y
UV-vis	Ultraviolet-Visible
VASP	Vienna Ab-initio Simulation Package
VPI	Virginia Polytechnic Institute
XRD	X-ray diffractogram
ZIF	zeolitic imidazolate framework
ZMOF	zeolite-like Metal-Organic Framework

Introduction

Une part importante des procédés de la chimie utilise des matériaux poreux. Dès la fin des années 1950, les zéolithes furent utilisées pour la déshydratation, la séparation ou la purification de gaz. Quelques années plus tard les propriétés catalytiques de ces mêmes matériaux furent mises en avant lors de réactions de craquage ou d'isomérisation. A ce jour, les zéolites représentent environ un tiers du marché des catalyseurs. Malheureusement la taille réduite des pores des zéolithes (<10Å) limite leur application pour la transformation catalytique de larges molécules. Le début des années 1990 vit l'apparition des silices mésoporeuses organisées (OMS) dont les larges pores (50-300 Å) permirent des applications en imagerie médicale, en pharmaceutique et, bien sûr, en catalyse. Néanmoins la taille de ces pores est trop grande pour permettre d'observer un effet de confinement.

Dés lors la découverte de matériaux hybriques issus de l'assemblage de ligands organiques et de clusters métalliques à la fin des années 1990 fut perçue comme une avancée majeure dans le monde des solides poreux. Ces matériaux furent nommés Metal-Organic Framework (MOF) ou encore Porous Coordination Polymers (PCP). La multitude de métaux et de ligands permit la synthèse de centaines de matériaux poreux possédant un large panel de tailles de pores. De plus la nature organique des ligands permet une fonctionnalisation facile en vue de modifier les propriétés chimiques de ces matériaux.

Néanmoins, 10 ans après l'explosion de l'intérêt pour le domaine que révèle le nombre de publications sur les MOF, aucune application industrielle de MOF pour la catalyse n'est, à notre connaissance, mise en place.

En effet la faible stabilité thermique et chimique des MOFs est un réel frein pour une utilisation dans le domaine de la pétrochimie et du raffinage ; de nombreux clusters métalliques sont sensibles à l'humidité et les autres résistent rarement à des températures supérieures à 400°C. Enfin l'acidité ou la basicité modérée des MOF ainsi que le coût des réactifs empêchent la plupart de ces matériaux d'être compétitifs en comparaison de zéolithes et OMSs.

C'est pourquoi il convient de redéfinir les objectifs que peuvent atteindre ces matériaux.

Les propriétés catalytiques des enzymes sont une importante source d'inspiration ; le confinement du réactif dans une enzyme génère un champ électrostatique qui stabilise l'état de transition et permet une catalyse hautement sélective dans des conditions douces. La haute cristallinité des MOFs, leurs sites métalliques isolés, leur flexibilité, le contrôle de la taille des pores ainsi que la possibilité de greffer des groupements chimiques sur les murs organiques de la structure pourraient permettre la création d'enzymes artificielles possédant une stabilité accrue.

Néanmoins, parvenir à une interactivité entre le site actif et le réactif semblable à celle observée dans les enzymes nécessite plusieurs études : Une meilleur compréhension des phénomènes de reconnaissance entre la structure hybride des MOFs et les espèces adsorbées est essentielle. Il convient également de mettre au point une méthode pour créer des sites actifs parfaitement isolés les uns des autres. Enfin les méthodes actuelles de fonctionnalisation des MOFs ne sont efficaces qu'avec un nombre réduit de réactifs et peuvent altérer la cristallinité du matériau.

Les objectifs de cette thèse sont (i) le choix et la synthèse de MOFs aux structures stables à haute température ainsi qu'en solution, (ii) l'utilisation de différents ligands lors des synthèses pour contrôler la densité des potentiels sites actifs et la flexibilité du matériau (MIL-53) lors de l'adsorption de molécules et (iii) la mise au point de méthodes génériques pour encapsuler ou greffer des complexes organométalliques au sein des pores.

Le **chapitre 1** est une étude bibliographique montrant la difficulté des MOFs à être compétitifs par rapport aux matériaux poreux classiques de la catalyse hétérogène. Dans un second temps la possibilité de créer des matériaux hybrides agissant comme des enzymes est mise en avant grâce aux nombreuses similarités entre les sites actives des protéines et les MOFs. La post-fonctionnalisation de la structure des MOFs est un moyen d'obtenir des environnements analogues aux enzymes et de potentiellement mimer leurs propriétés catalytiques. Les différentes réactions de greffage post-synthétiques appliquées à ce jour sont présentées.

Le **chapitre 2** présente nos travaux sur l'encapsulation d'analogues aux porphyrines, les phthalocyanines, dans les cavités du MOF MIL-101. L'encapsulation d'espèces biomimétiques dans des pores calibrés est une manière de se rapprocher de l'environnement enzymatique. Le catalyseur hétérogène ainsi obtenu est évalué dans l'oxydation sélective de la tétraline.

Le **chapitre 3** décrit les différentes structures des MOFs pré-fonctionnalisés utilisés dans la suite de l'étude et leur caractérisation complètes. Ces MOFs présentent tous une fonction amine sur leur partie organique, disponible pour le greffage de groupements fonctionnels. L'influence de ce groupement NH_2 sur les propriétés acide/base du MOF MIL-68(In) est

également étudiée par modélisation et par la transformation catalytique de l'oxyde de styrène en carbonate sous pression de dioxyde de carbone.

Le **chapitre 4** présente la synthèse de « mixed linker » MOF par dilution du ligand aminé avec son analogue non fonctionnalisé. L'analyse des différents matériaux par diffraction de rayons-X en température ainsi que la mesure de l'absorption (dioxyde de carbone et azote) permet une meilleure compréhension de l'influence du substituant sur la flexibilité et la stabilité de ce solide. L'organisation des groupes substituant au niveau microscopique a également pu être mieux comprise.

Le **chapitre 5** se concentre sur la post-fonctionnalisation des matériaux décrits dans le chapitre 3 et 4. Afin d'améliorer la réactivité du substituant, le groupe amino est transformé en deux étapes en isocyanate. Cette méthode générique permet le greffage d'une grande diversité d'amines au sein des pores de MOF. La nécessité de sites potentiels isolés est ici mise en avant pas le suivi *in situ* des transformations.

Cette thèse a été financée par le projet européen FP7-NanoMOF et a été réalisée au sein de l'Institut de Recherche sur la Catalyse et l'Environnement (IRCELYON).

Chapter 1

Bibliography: MOF – From zeolite analogue to enzyme biomimetism.

Introduction

When Metal organic frameworks (MOFs) were discovered in the late 1990s, it took very short time for scientists to see the potential of these materials for catalytic applications. This chapter aims to compare MOFs to other catalytic systems in order to define appropriate domains of applications and improvements needed to design viable MOF catalysts. MOFs are first compared to inorganic porous catalysts. Then similarities of their structure with that of the enzyme active sites are highlighted. Finally the state of the art of MOF post-functionalization, which is a way to design MOF with enzyme-like environment, is presented.

I. State of art of porous materials

Industries intensively use Zeolites and Ordered Mesoporous Silicas (OMS) which possess micro or mesoporous inorganic frameworks. Unfortunately the inorganic nature of the framework does not allow the total control of the pore size which is essential for a high selectivity in catalysis. This also strongly limits the grafting of catalytically active species. MOFs frameworks, thanks to their organic linkers, allow a high tunability of the physical (pore size, dimensionality) and chemical properties (Lewis and Bronsted acidity and basicity). Nevertheless the weakness of the some metal coordination bonds has for consequence some stability issues. Hereafter we describe the pros and cons of these three family of materials for catalysis purpose.

I.1. Zeolites

With 201 unique frameworks identified, Zeolites form one of the main familiy of crystalline porous materials. They are widely used in gas separation[1, 2,3] catalysis (petrochemicals cracking) and in ion exchange beds (water purification) [4]. Zeolites are tridimensional crystalline aluminosilicates constituted by Si and Al tetrahedra linked through bridging oxygen atoms giving rise to the so-called secondary building units (SBUs)[5], constituted by rings and prisms of various sizes[6, 7].

Furthermore, by using a wide variety of organic molecules based on quaternary ammonium cations as Structure Directing Agents (SDAs), a large number of new zeolitic materials are discovered every year.

Three main features determine the structural properties of zeolites: the size of their pore apertures defined by rings formed by oxygen atoms, the dimensionality of their pore systems and the Si/Al ratio.

Pore size

Zeolites can be broadly classified as narrow-pore (3.5-4.5 Å), constituted by 8-member rings (8-MR), medium-pore (4.5-6.0 Å), constituted by 10-MR, large-pore (6.0-9.0 Å), formed by 12-MR or super-large pore (>9.0 Å).

The pores and their apertures have a regular nature with dimensions in the same order than molecular sizes. This property gives zeolites their value as selective adsorbents for separating substances. Depending on the type of zeolite and its pore system, the molecules can penetrate into the cavity system or can be excluded from it.

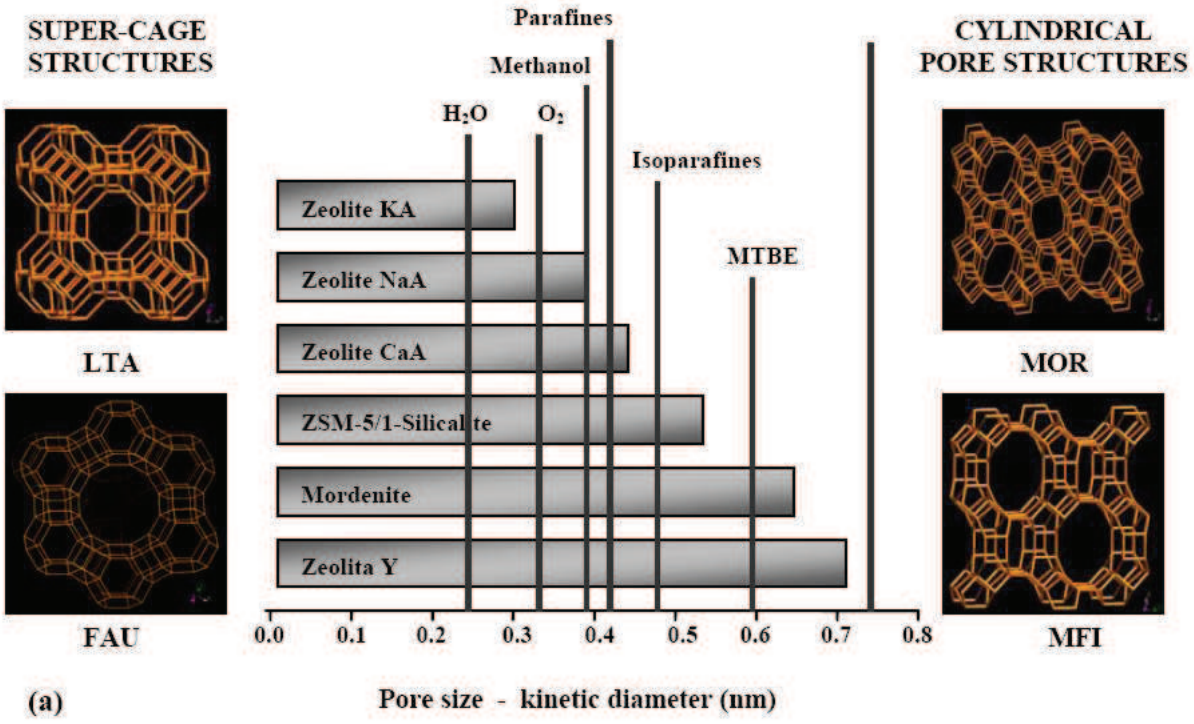

Figure 1. Framework structures of zeolites (Images adapted from International Zeolite Association (IZA) website) and comparison of pore size with adsorbent kinetic diameters.

Their reduced pore size limited to 10 Å is usually underlined as a key limitation to perform catalytic transformations of large molecules. Nevertheless few examples of zeolite (aluminophosphate and silicogermanate) such as VPI-5[8], IM-12[9], ITQ-33[10] and ITQ-37[11]

possess pore with 14 or 18-MR (up to 12 Å). However the introduction of germanium as a co-structure directing agent strongly decreases the hydrothermal stability of the zeolites.

Dimensionality of pore system

Zeolitic frameworks differ by the dimensionality of their pore systems. For instance, LTA and FAU zeolites are based on a 3D array of super-cages, while MOR zeolites are constituted by 1D elliptical-structured pores (Figure 1). As they avoid diffusion issues, 3D zeolites are more appropriate for adsorption and catalysis.

Si/Al ratio

Most of chemical and physical properties of zeolites are essentially determined by their Si/Al or SiO_2/Al_2O_3 ratio. A distinction can be made between the low-silica (Si/Al<2), the intermediate-silica (2<Si/Al <10) and the high-silica (10<Si/Al<100) zeolites.

An high silica content leads to a strong hydrophobic character. Among the most hydrophobic zeolites are Silicalite-1 (MFI) and all-silica zeolite (DDR), having no Al in their structure. The transition from hydrophilic to hydrophobic behaviour occurs at a Si/Al ratio around 10.

In the case of AlPO (alumino-phosphate) and SAPO (alumino-silico-phosphate) zeolites, in addition to Al, the structure also contains trivalent phosphorus.

I.2. Ordered mesoporous silicas (OMS)

In the early nineties, Beck *et al*[12] and Kresge *et al*[13] at Mobil Oil Research and Development discovered a new family of mesoporous molecular sieves (M41S). This family of materials, commonly termed MCM (MCM = “Mobil Composition Material”) includes a whole class of ordered structures, made of amorphous silicate wall, with uniform and tunable pore size distributions (Figure 2).

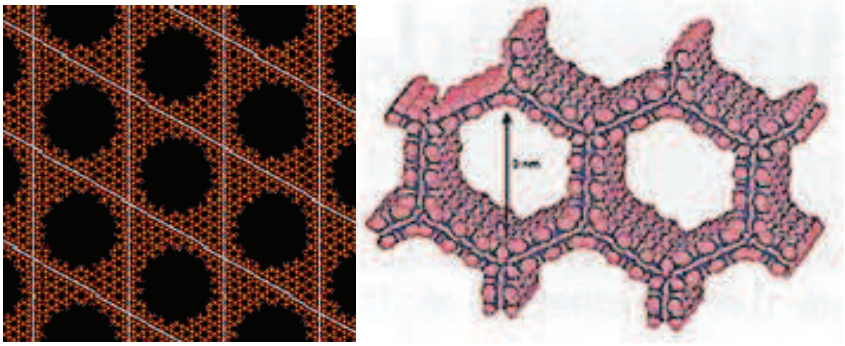

Figure 2. MCM-type silica.

Ordered mesostructured materials are prepared by what was originally described as a liquid crystal templating mechanism. The structure is defined by the organisation of surfactant molecules (most often cationic or non-ionic) into liquid crystals which serve as templates form the formation of the M41S materials (figure 3). Unlike conventional mesoporous silicas showing intercrystalline and irregular mesoporosity, the porosity induced by the structure-directing effect of the template in mesostructured silicas is essentially internal and regular. As a result, despite the amorphous nature of pore walls, mesostructured materials show long-range crystalline arrangements translating into XRD patterns showing defined peaks at low angles (<10°).

Pore size

The pore sizes of these silica based-MCM can be tailored on the basis of the synthesis method used and can range from about 20 to 500 Å. In addition to silica based-MCM materials, synthesized using cationic surfactants, other ordered mesostructured silicates, aluminosilicates and metal oxide materials (e.g. SBA-15) with larger pore sizes (50-300 Å), such as block copolymers, have been reported using non-ionic surfactants [14-16].

Dimensionality of pore system

Depending upon the surfactant concentration and synthesis conditions, the final silica structures exhibit different pore dimensionality[17, 18] (Figure 3). The three most important members of the M41S family are the hexagonal MCM-41 with a one-dimensional pore system, the cubic MCM-48 with a three-dimensional pore system, and the lamellar MCM-50.

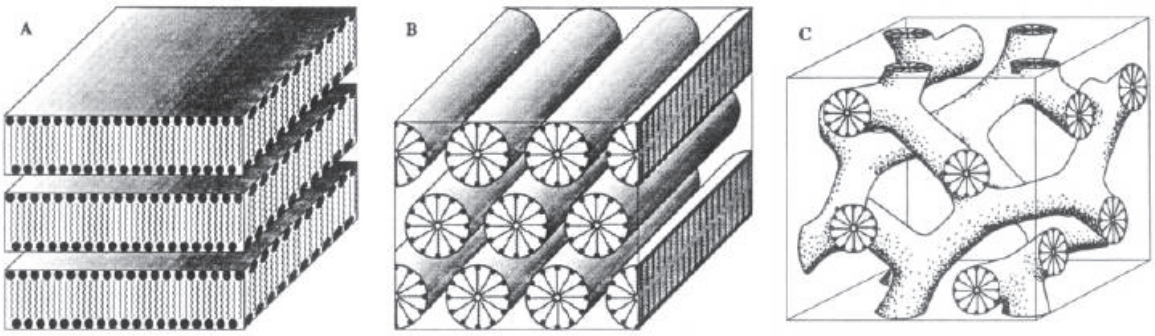

Figure 3. A schematic presentation of three inorganic-surfactant mesostructures: (A) the lamellar phase. (B) the hexagonal phase, and (C) the "bicontinuous" cubic phase. Note that only the surfactant parts of the structures are presented for clarity. In real materials, all the empty spaces in the figures between the surfactant assemblies (rods, layers. etc.) are filled with extended inorganic frameworks. [17, 18]

I.3. Post synthetic modification of inorganic porous materials for catalytic applications

Different post synthetic methods (PSM) have been set up to modify the adsorption and acid properties of zeolite and related zeolitic materials (aluminophosphates). Dealumination and desilylation processes have been carried out by hydrothermal treatments to create mesopores and remedied to diffusional limitations. To modify the catalytic properties, ionic exchange of the organic-cation components of the materials could be performed. Acid sites can be introduced by ion exchange for NH_4^+ followed by thermal decomposition.

However PSM by grafting organic species have been less abundant presumably due to the relatively small pores size and lack of accessible chemical functionalities. Nevertheless, the grafting of various organic moieties onto zeolites has been reported[19]. Cauvel and co-workers studied the influence of the Al sites and pore size on the grafting of (3-chloropropyl)trimethoxysilane (CPS) and (3-aminopropyl)triethoxysilane (APS) on zeolite Y with various Si/Al ratios (calcined and dealuminated). The PSM of the amino functionalized zeolites was then performed by the addition of 4-anisoyl chloride and 2,3-butanedione.

In addition, in the nineties, Corma and coworkers described both rhodium and nickel complexes anchored to USY-zeolite through a silane bond for C=C hydrogenation reactions leading to enhanced catalytic activities compared to that found with the homogeneous catalyst itself.[20, 21] This was attributed to a cooperative effect of the zeolite which was supposed to increase the reactants concentration inside the pores. Similarly, the immobilization of L-

proline rhodium complex still on the USY-zeolite led to an improved enantioselectivity for the asymmetric hydrogenation of dehydrophenylalanine derivatives. [22, 23]

In contrast to zeolites, PSM of mesoporous silicas, which possess much larger pores that are lined with reactive silanol (SiOH) groups, have been more extensively investigated [24]. Grafting of organic functionality to meoporous silica is commonly realized by reacting organosilanes, chlorosilanes or silazanes with the free silanol groups at the pore surfaces[25].

Brunel *et al* introduced amine species into MCM-41 type silicas by grafting and used the solids as basic catalysts for the Knoevenagel condensation of benzaldehyde and ethyl cyanoacetate [26, 27].

Ordered mesoporous silicas have also been treated by multi step post functionalization to allow the covalent grafting of elaborated group such as organometallic complex. Sutra *et al* reported in 1997 the grafting of Mn(salen) in the nanopores of mesoporous materials[28] (figure 4) and Li *et al*, ten years later, systemically investigated the asymmetric epoxidation on similar Mn(salen) catalysts immobilized in MCM-41[29].

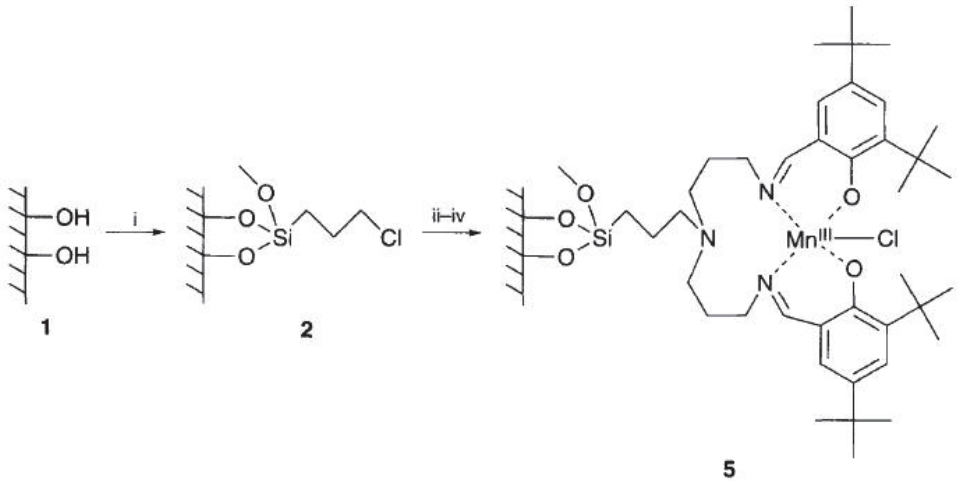

Figure 4. Grafting of manganese(III) shiff-base in 4 steps on the MCM-41 wall[28].

More recently, Thomas *et al.* have reported a confinement effect with a rhodium catalyst anchored on silica using a non convalent approach (Figure 5). The chiral catalyst within the nanopores has shown improved catalytic performance compared to its homogeneous analogue. Furthermore it has been notice that the pore diameter has a strong influence on the enantioselectivity of the reaction. The cavity size determines the face differentiation of the substrate during the asymmetric hydrogenation of the methyl

benzoylformate: smaller is cage, higher are the constraints and better is the enantioselectivity. [30]

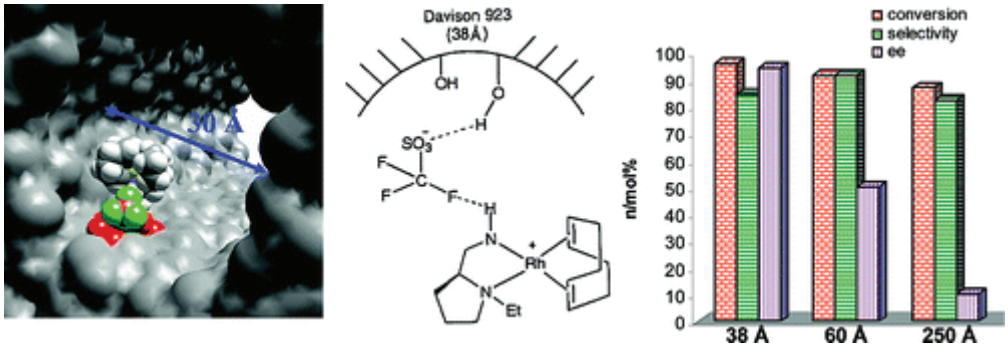

Figure 5. Confinement of immobilized, single-site chiral catalyst enhances enantioselectivity.

I.4 Limitations

Despite their efficiency in these pioneering examples, porous materials such as zeolite and OMS however present some general limitations for their use as catalysts support. These purely inorganic materials can be hardly functionalized with organic grafts due to the difficulties to create well defined and isolated anchoring sites. The pores of usual zeolites are too small to accommodate both relatively large organometallic complexes and catalysis substrates, and also too rigid to accommodate substrate on a specific manner (selectivity).

On the other hand, ordered Mesoporous Silica such as MCMs usually exhibit too large pores to impose confinement effects and leaching can easily take place, posing a problem for the retention of guest species. Furthermore the amorphous nature of Ordered Mesoporous Silica can be a drawback for single-site control in order to avoid mutual deactivation of too close catalytic species.

Thereafter we will show that MOFs offer new opportunities as support for catalytic species with the additional advantages of a possible discrete variation of the pore size as well as well-defined single-sites allowing a complete characterization of the catalytic species.

I.5 Metal organic frameworks

I.5.1. Self assembled material

The conceptual approach for MOF engineering is based on the self-assembly of organic and inorganic species and can be described by the organisation of secondary buildings units (SBU) or blocks. Metallic clusters, acting as nodes, are connected by organic linkers, acting as spacers to form a net[31-42]. As an analogy to zeolite frameworks, this SBU approach for MOF construction allows the design of specific nanometer-scale framework geometries with particular pore structures. In contrast to zeolites, for which a relatively limited number of structures exists, MOFs provide diverse combinations of coordination chemistry, polytopic linkers and terminated ligands (F-, OH- and H_2O, among others), which make it possible to design an almost infinite variety of MOF structures. Polytopic organic ligands are generally nitrogen-, and oxygen-donor rigid molecules such as bipyridine or polycarboxylic acids. The diversity in terms of ligand is almost infinite. The most simple and frequently used is the terephtahlic acid (1,4-benzyldicarboxylic acid). The most frequently observed SBUs are binuclear clusters called $M_2(CO_2)_4$ "paddle-wheel" such as found in MOP-1 [43], $Cu_3(btc)_2$ (HKUST-1)[44] and μ_4-oxo $M_4O(CO_2)_6$ [45, 46] such as those found in IRMOF series (Figure 6).

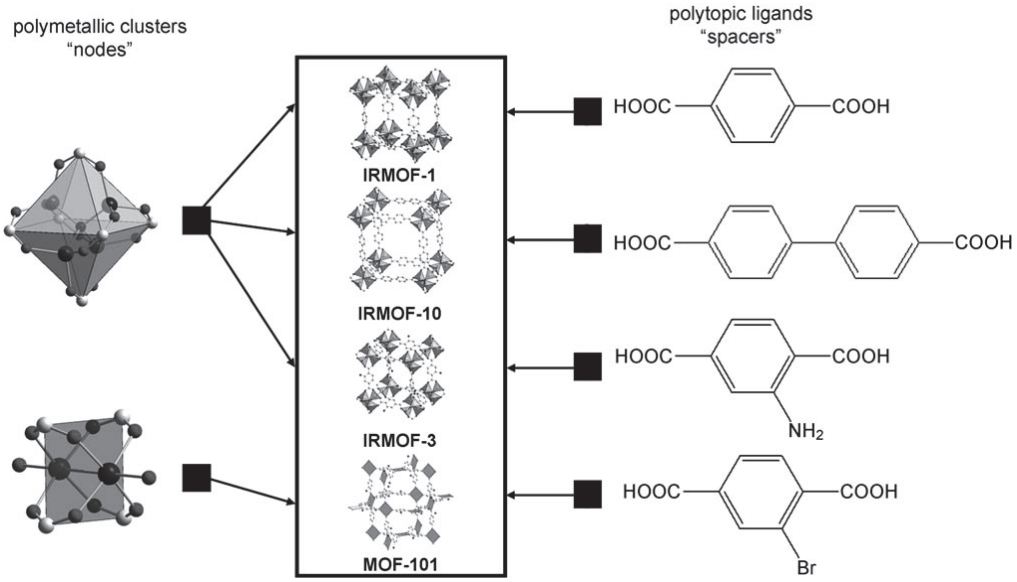

Figure 6. Self-assembly of polymetallic clusters [μ_4-oxo $M_4O(CO_2)_6$, $M_2(CO_2)_4$ paddlewheel] and organic linkers yielding Metal-Organic Frameworks[46]

MOFs can be classified into different families according to the dimensionality of the inorganic framework (Figure7)[33] : 0D "inorganic" clusters or isolated metal ions connected by bridging organic polytopic ligands such as MOF-5 and HKUST-1; 1D inorganic chains such as MIL-53; 2D inorganic layers that are separated by organic pillars such as MIL-71; or 3D structures such as MIL-73 with three dimensional porous channels. This classification is not only conceptual. For example in 0D structures, polycationic nodes can act as semiconductor quantum dots and can be activated upon photostimuli with the linkers serving as photon antennae which make them potential candidate for photocatalysis applications.

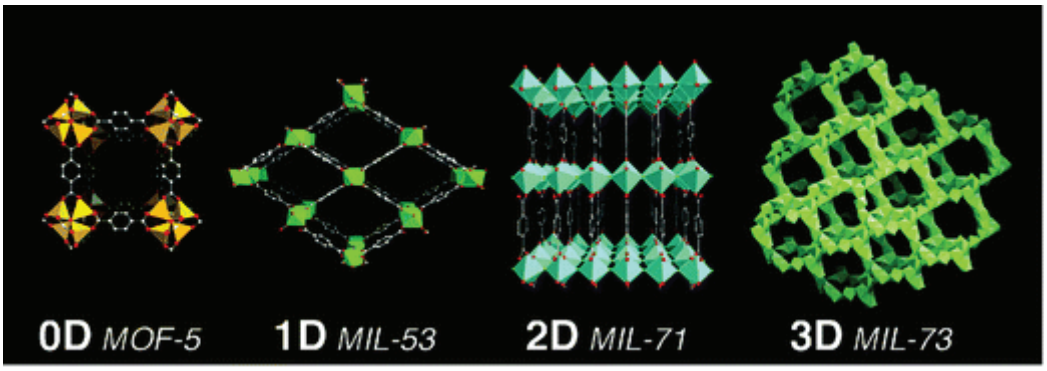

Figure 7. Examples of MOFs[47] with various dimensionalities: MOF-5,[151] MIL-53,[152] MIL-71,[153] MIL-73.[154]

As for the others porous materials, MOF materials can also be characterized by the pore topologies (Figure 8): ZIF-8, MOF-5, HKUST-1, MIL-101, etc present 3D porous channel. On the other hand CPO-27, MIL-53, MIL-68, etc possess 1D porous channel: They have systems of one dimensional channel (yellow balls of the MIL-53 - figure 8) that do not intersect, which leads to diffusion limitations.

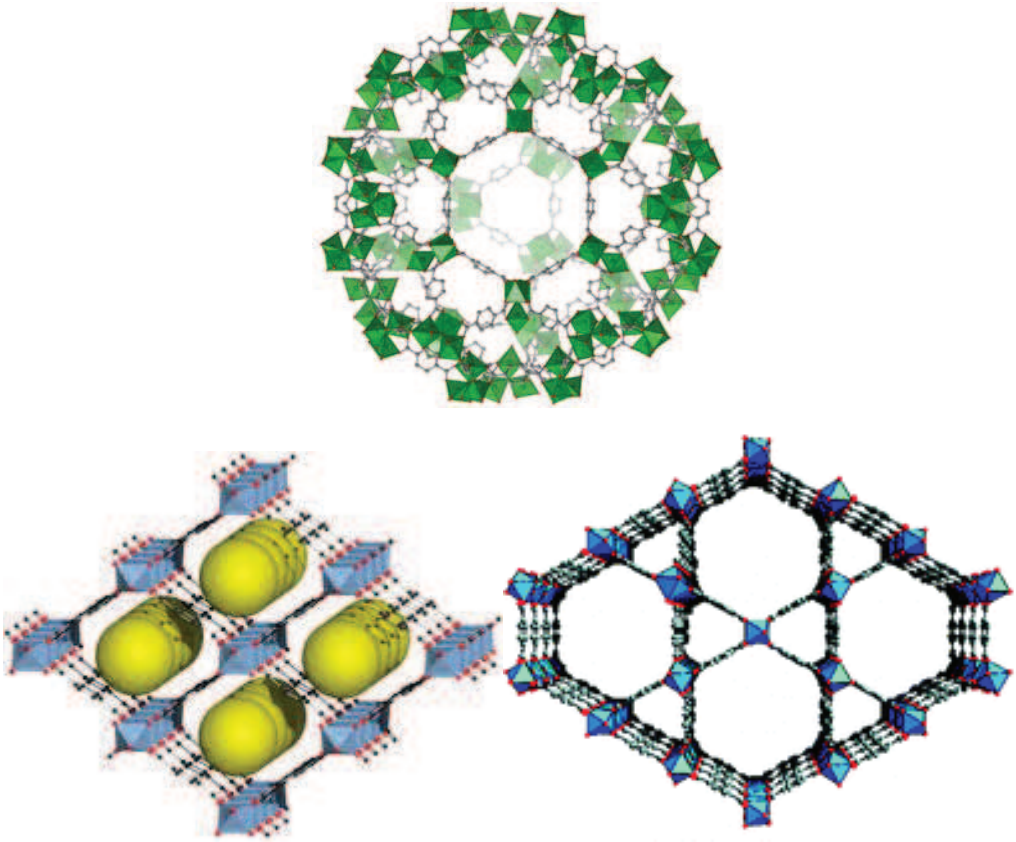

Figure 8. Examples of MOF with different pore topologies: 3D MIL-101 (top), 1D MIL-53 (bottom left) and 1D MIL-68 (bottom right)

I.5.2. Bridging the pore size between Zeolite and Ordered mesoporous materials.

The reduced pore size of zeolites is usually underlined as a key limitation to perform the catalytic transformation of large molecules such as polyaromatics, carbohydrates and glycerides. Intensive efforts have been devoted to the discovery of aluminophosphates and silicogermanate zeolites with very large pores (VPI-5[8], IM-12[9], ITQ-33[10], ITQ-37[11]). On the other hand, mesoporous silicate materials such as MCM-41 have pores too large to impose confinement effects for enantioselective catalysis, for example. MOF materials actually bridge the gap between these two porous material types, since ultramicroporous to mesoporous MOFs have been reported, as shown in the arbitrary selection in Figure 9. The size of selected potential guests is also shown in the top axis (MTBE = methyl tert-butyl ether; TIPB = 1,3,5-triisopropylbenzene). The abundant choice of structure associated with pore size tunability is a great opportunity for designing MOFs with pore openings appropriate for generating shape selectivity.

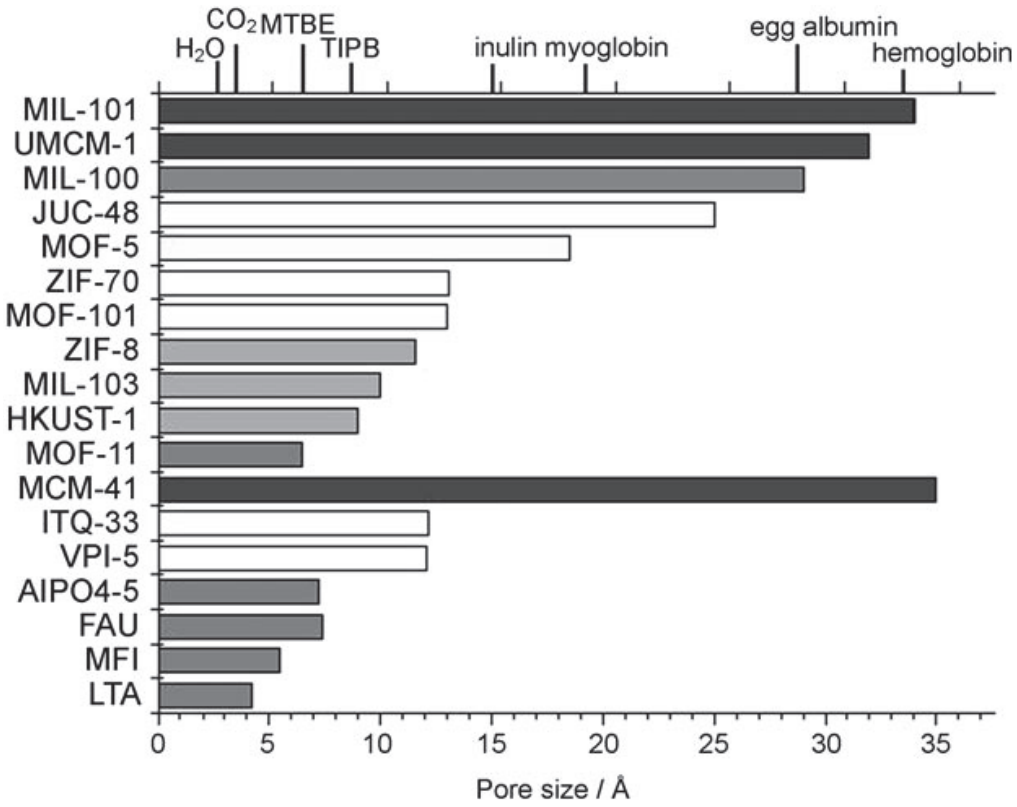

Figure 9. Cavity size and window aperture of porous MOFs (Å) compared with standard aluminosilicates and aluminophosphates. (Aluminosilicate = MCM-41, ITQ-33, VPI-5, FAU, MFI, LTA, aluminophospate = AlPO4-5)[48].

The interest of the ‘‘node and spacer’’ approach is that it offers a route to functional networks with tuneable pore size [38, 46]. The strategy for increasing the pore size and volume involves the expansion of known structure types through the use of elongated but geometrically equivalent organic bridging ligands forming isoreticular compounds. For the IRMOF series based on MOF-5 structure, the pore size can vary from 3.8 Å to 28.8 Å by selecting linkers of various sizes [46] (Figure 10).

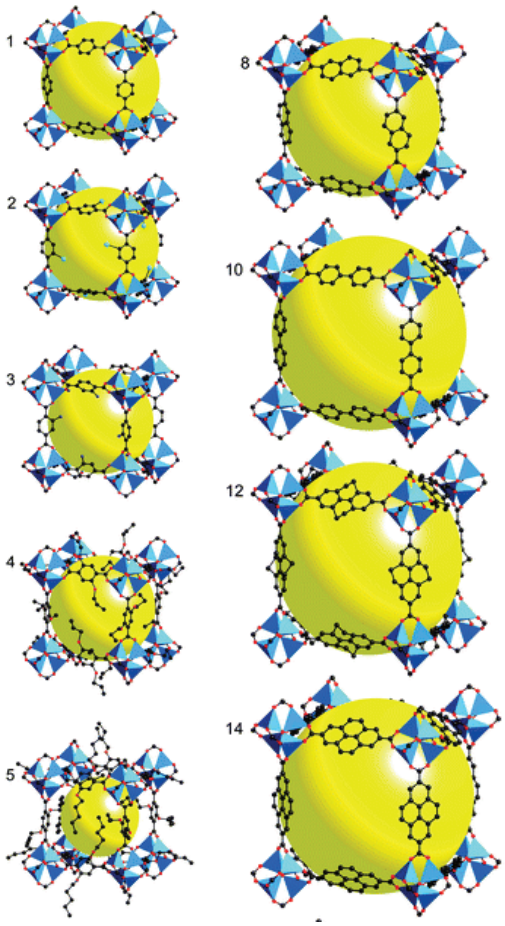

Figure 10. Example of 3D isoreticular compounds (IRMOFs)

Other examples are [Cu(OOC-R-COO)(teda)] (teda = triethylenediamine) for which the pore size can be monitor between 7 and 11 Å [49], the IRMOP series [50], the MIL-53 series [51], the MIL-88 series [52], the MOF-69 series [53] and UiO-66 to -68 [54]. This method allows the design of MOF with control pore size where the target molecule perfectly fit as found in enzyme (Figure 11).

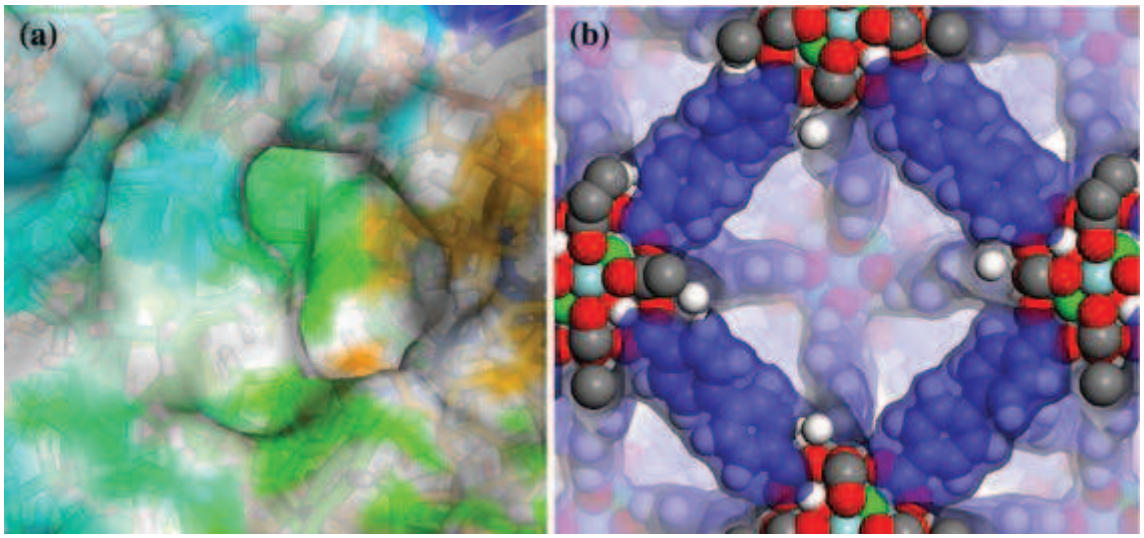

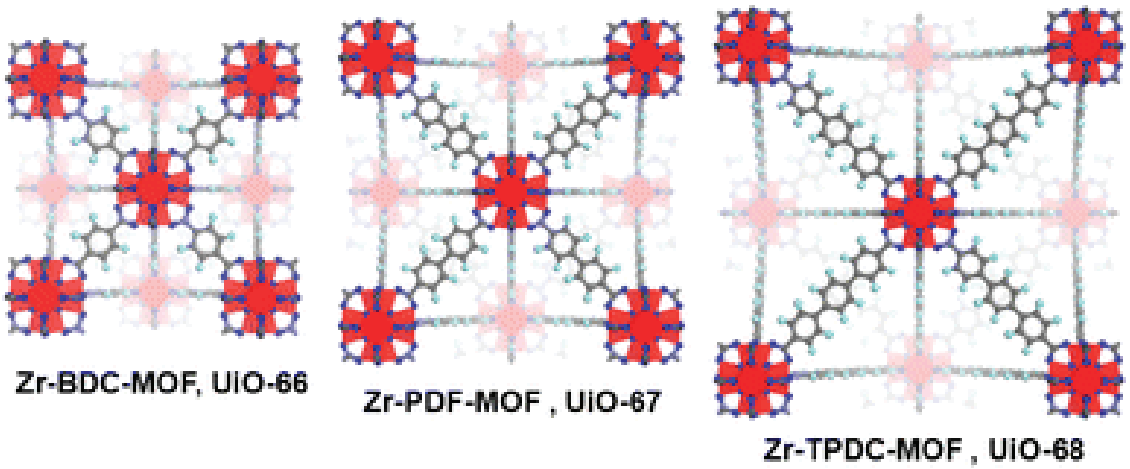

Figure 11. (top left) The cavity around the active site in the anhydrase enzyme. (top right) The surface in the octahedral cage of the UiO-67 MOF structure[55].(bottom) isoreticular UiO series.

I.5.3. MOF as solid porous catalyst

The catalytic properties of MOF can have different origins. The organometallic properties of the unsaturated metal node, the acidity of the hydroxyl group or basic group supported by the organic linkers have showed activity in catalysis.

I.5.3.1. High transition metal site density

MOF contains metal ions at every framework node which can be potential actives site if their coordination spheres possess lacunary position. In addition large diversity of metal centers can be used. In zeolite, metal can be incorporated into the framework by replacing a silicon atom. The need of similar radii and properties strongly limit the isomorphic replacement. Furthermore the lower stability of the incorporate species makes them migrate outside the framework upon thermal treatment. Transition metal can also be supported as charge balancing cation but in this case metal can undergo hydrolysis even under mild heating.

In contrast, several transition-metal MOFs have show high stability under liquid phase reactions conditions[56, 57]. Xamena *et al* described a Palladium containing MOF with the molecular formula $[Pd(2\text{-pymo})_2]_n$ (2-pymo = 2-hydroxypyrimidinolate) (Figure 12). The

material exhibits the typical behaviour of heterogeneous palladium catalysts, promoting C-C cross coupling, aerobic oxidation, and hydrogenation reactions.

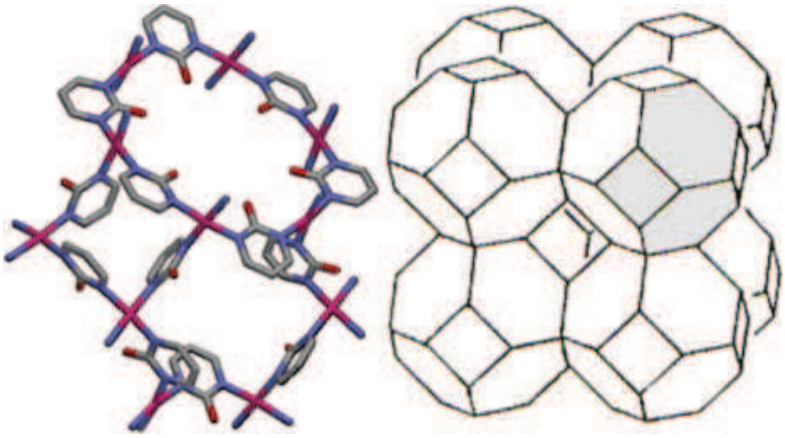

Figure 12. (left) Detail of Pd-MOF, showing the 4-membered and the two 6-membered rings. Atom colors: C = gray, N = blue, O = red and Pd = pink. (right) 3D arrangement in sodalite-type frameworks[57].

I.5.3.2. Lewis acid properties

Lewis acid catalysis has been of great interest in organic synthesis[58]. While many different types of lewis acid-promoted reaction have been developed, and many have been applied at industrial scale, there is still a considerable interest in developing new heterogeneous Lewis acid catalysts. The high metal density and the open metal sites of MOFs are convenient to use them as Lewis acid catalysts. As the evaluation of acidity by the use of basic probe molecule (ammonia) can not be performed due to their chemical sensitivity, their activity is generally evaluated in test reaction.

HKUST-1, which has accessible copper clusters, is an outstanding demonstration of the concept of Lewis acid MOFs.[59, 60] The $[Cu_3(btc)_2(H_2O)]$ structure includes a binuclear Cu_2 paddlewheel.[44] The Cu^{2+} ions are connected through a weak bond and the second axial coordination site is filled by a weakly bonded water molecule pointing towards the interior of the cavity. Coordinated water can therefore be easily removed by heat treatment at 383 K, making the Cu Lewis acid center directly accessible to a reactant diffusing within the porous network. Various model reactions for characterizing Lewis acidity were tested: benzaldehyde cyanosilylation,[60] isomerization of alpha-pinene oxide, citronellal cyclization, and

rearrangement of ethylene acetal of 2-bromopropiophenone.[59] HKUST-1 was shown to be quite selective, which is typical of hard Lewis acid centers.

I.5.3.3. Brønsted acidity

Horcajada and co-workers have reported the catalytic activity of two different MIL-100 (Fe, Cr) for Friedel–Crafts benzylation[61]. Despite their identical structures $[M_3OF_{0.85}(OH)_{0.15}(H_2O)_2(btc)_2]$, the iron based catalyst shows much higher catalytic activity than the chromium based catalyst and even surpasses HBEA and HY zeolites. However CO chemisorption at low temperature have demonstrated that MIL-100(Cr^{3+}) possess Cr-OH Brønsted sites of medium acidity and several types of Lewis centers[62, 63].

Ravon *et al*. have tested pure Brønsted MOF materials with structurally well identified hydroxyl centres, namely Ga(OH)(bdc) and $Zn_3(OH)_2(bdc)$, also known as MIL-53 and MOF-69C[64], respectively. It has been anticipated that bridging OH groups would generate a Brønsted-type acidity such as that found in the H form of zeolites[65]. Gallium based MIL-53 shows full conversion for toluene terbutylation at 50°C temperature (TON = $220h^{-1}$ at 100°C)[66], while MOF-69C is 100% shape selective for the alkylation of large polycyclic aromatics such as biphenylene[67].

I.5.3.4. Brønsted basicity

The Knoevenagel reaction has been widely used to assess the strength of solid bases having sites of weak to medium basicity. Zeolite and mesoporous silicas can be covalently functionalized to introduce pendant amino group. Thus, amino-grafted Cs-exchanged NaX zeolite[68] and amine-modified pore expanded MCM-41[69] exhibit moderate to high yields of 70 and 99%, respectively, with 100% selectivity for the condensation of ethyl cyanoacetate and benzaldehyde.

Amino-functionalized MOFs have been obtained by direct self-assembly. Solvothermal syntheses using amino-derived ligands, such as 2-aminoterephthalic acid and 3,5-diamino-1,2,4-triazole (Am_2Taz), with zinc yield IRMOF-3, and [ZnF(Am_2Taz)], respectively. IRMOF-3 shows conversion for the Knoevenagel reaction,[70] while IRMOF-3 and [ZnF(Am_2Taz)] are active for Aza-Michael condensations (TON of $1.4\,h^{-1}$ and $0.15\,h^{-1}$,

respectively at 25 °C) and fatty methyl ester transesterification (TON=3.3 h^{-1} and 0.3 h^{-1} at 130 °C).[71]

There are only few examples of MOF materials containing free Lewis bases that are accessible for catalytic applications. This might be due to experimental difficulties associate with the synthesis of free-nitrogen-donating MOF materials. Indeed, when nitrogen-containing aromatic moieties in carboxylic-based ligands (such as pyridine/imidazole dicarboxylates[72]) are used, the nitrogen lone pair usually strongly coordinates to the metal ion and is therefore not available for substrate activation.

I.5.4. Limitations

The principal weakness of MOFs my lied in their lower thermal, hydrothermal, and chemical stability compared to that of oxides (zeolites). Unfortunately, stability data are usually lacking in the literature. Moreover, when reported, these data are often obtained under different conditions (air or neutral atmosphere, different temperature) and by different means (thermogravimetric analysis (TGA) or thermodiffraction), which makes them impossible to compare. Usually, according to TGA, the best thermal stability of carboxylate- and imidazolte-based MOFs is limited to 300–400°C under air. On the other hand, the chemical stability depends essentially on the cation coordination. It is now well established that IRMOF compounds based on Zn_4O clusters are very moisture sensitive and are readily transformed to MOF-69 type, with an accompanying drastic decrease in surface area. On the other hand, (Al)MIL-53, UiO-66 and ZIF-8 are very stable under hydrothermal treatment. As the majority of MOFs dissolved in aqueous acid solution, the domains of MOF applications are limited. Horcajada et al[73] use this weakness toward solution to design drug filled MOFs which are slowly degraded in phosphate buffer solution (isotonic to human body fluid) and liberated active species over a week.

However heterogeneous catalysts are often deactivated over the course of the reaction and reactivation is needed to regenerate materials; the limited thermal and chemical stability of MOFs precludes the usual procedures to reactivate porous catalysts such as combustion, pyrolysis or thermal treatment. In order to recycle MOF catalysts, poison must be extracted under mild temperature and reduced pressure.

MOFs are usually made by reaction of a metal ions source and a linker in solvent. Most of the linker syntheses are multi-steps syntheses or/and production is still at small scale. DMF is

a solvent used in many MOFs synthesis. This polar compound is expensive, toxic and has a very high boiling point (153°C). Furthermore even if some of the most common MOFs are synthesized with relatively cheap metal (aluminium, iron, zinc, etc) some are copper, zirconium or chromium based. These metals are expensive and/or present toxicity issue (chromium) limiting their development as industrial catalysts. To summarize, only few MOF can be synthesized at large scale with acceptable price and hold concurrence with other inorganic porous material.

Zeolites and ordered mesoporous silicas are fully inorganic and thus lack synthetic flexibility and structural diversity/tailorability. However pore-size tunable MOFs opened new perspective in catalysis. The thermal and chemical stability is a key point to select appropriate MOF candidats for catalytic test at high temperature or in acidic condition. Carboxylate based MOF as MIL-101, MIL-53 or MIL-68 have a high stability and will be used as starting materials in the following works.

As far as catalysis is concerned, MOFs will likely compete with zeolites or resins acting as acid catalysts. In a similar way, for heterogeneous oxido-reduction processes, MOFs will hardly compete with metal oxides or metal/carbon catalyst because of their lower stability and higher cost. A window that remains opened is their application in the preparation of compounds with high value added such as chiral synthons for pharmaceutical, fragance, food, etc ...

In this sense we can envisage MOFs as artificial metalloenzymes able to operate stereoselective transformations and/or separations.

II. Transcending the inorganic matter – toward enzyme-like materials

II.1. The enzymatic model

In a society were sustainability becomes increasingly important, enzymes which operate under mild conditions (room temperature, atmospheric pressure) with high selectivity are a source of inspiration for everyone who works within the field of catalysis.

Fisher rationalized the enzyme specificity thanks to a "lock and key" model in 1894. This purely geometrical point of view evolved to a model which explains the stabilization of the transition state thanks to the electrostatic field inside the cavity where the reaction takes place. The binding of a substrate by an enzyme is an interactive process.[74] Thanks to the flexibility of the structure, the shape of the enzyme's active site is modified upon binding the substrate, in a process of dynamic recognition between enzyme and substrate aptly called induced fit.

Essential step to understand specific enzyme mechanism is solving its crystal structure. In 1965, Blake *et al* published the first resolution of the crystal structure of an enzyme (Triclinic lysozyme)[75].

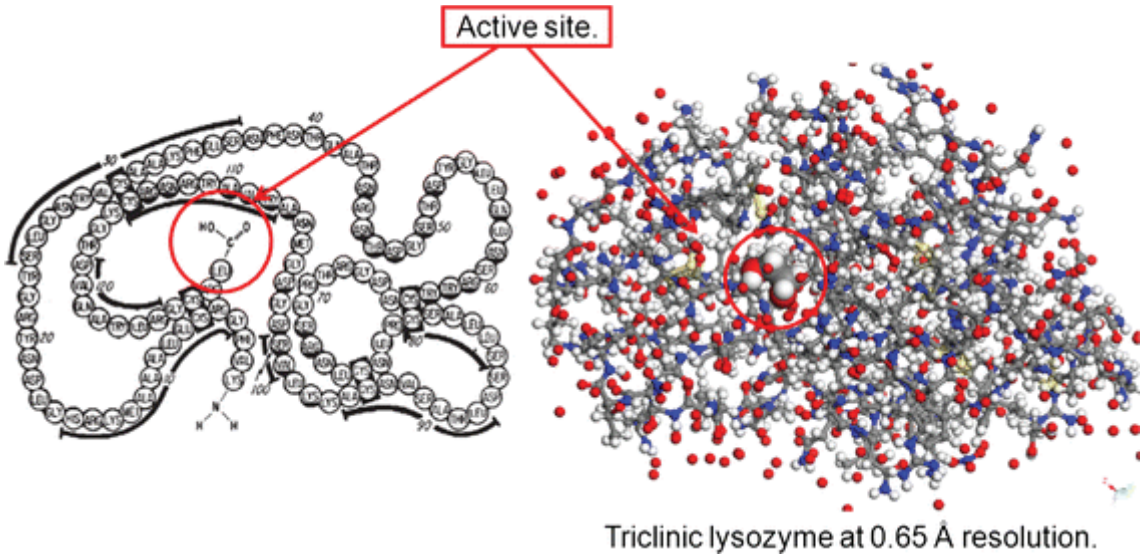

Figure 13. Blake illustration and resolved structure of the Triclinic lysozyme

From then, unravelling the catalytic site of enzymes was possible. Nowadays, protein crystallography allows solving structures with high resolution thanks to the development of synchrotrons giving brighter X-ray sources, the technique of freezing the crystals in liquid nitrogen and the amelioration of softwares and calculations capacity of computer (Figure 13).

Nevertheless obtaining crystal of protein remains challenging and active sites of many interesting enzymes are still unknown.

The nature of the internal cavities of zeolite or related oxide based microporous materials is too different from what we see in enzymes to allow a transfer of knowledge from enzymatic catalysis to these materials. Few examples of zeolite, such as Mordenite in the carbonylation of Methanol[76], present selectivity as found with enzymes but most of them have been discovered by pure serendipity.

II.2. Isolated polynuclear sites

Cooperative catalysis involving two metal ions is a common feature in enzymatic systems. The resulting cooperative activation of both reaction partners leads to enhanced reactivity and more specific control, thus making enzymes very powerful catalysts. Some well-known examples of dinuclear and higher nuclearity metal sites in biological systems include: the diiron soluble methane monooxygenase, dicopper of cytochrome C oxidase and tricopper oxidases[77].

The tyrosinase is another exemple of enzyme which carried out the oxidation of phenols such as tyrosine and dopamine using dioxygen. The active site is a coupled dicopper site coordinated with three histidine residues. The proposed mechanism[78] involved dioxygen binding to Cu_2 sites to generate a Cu_2-O_2 adduct that undergoes an O-O bond scission either prior to or concomitant with attack on the substrate (Figure 14).

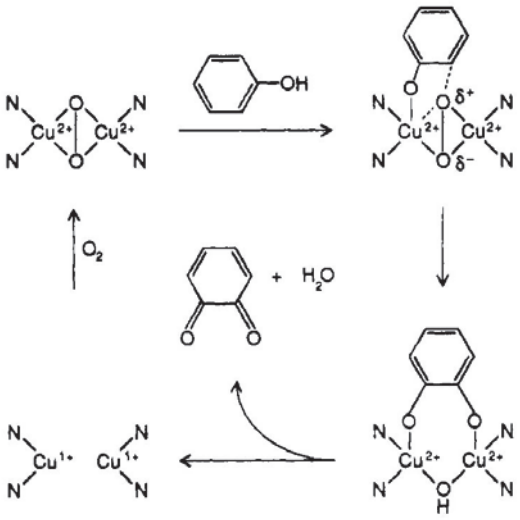

Figure 14. Proposed mechanism by Solomon[78] for oxygen activation in tyrosinase.

Due to the unusual geometry and electronic structure induced at the active site by the protein ligand, the copper enzyme present outstanding activity in metabolic conditions.
Inspired by this biological example, Ratnasamy *et al*[79] encapsulated copper acetate dimers in zeolites which present a paddle wheel configuration analogue to the tyrosinase active site in order to perform selective phenol oxidation reactions under environmentally friendly conditions (Figure 15).

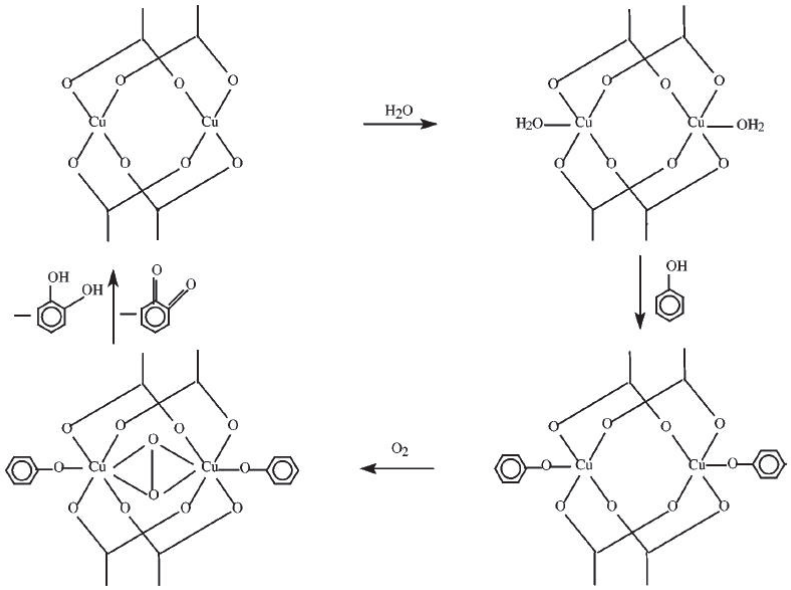

Figure 15. Proposed mechanism by Ratnasamy[79] for oxygen activation by copper acetate dimers.

Investigation probes the effect of encapsulation on the molecular structure. The Cu-Cu antiferromagnetic exchange interaction increases upon encapsulation. Geometric constrains imposed by the cavities of the zeolite, probably cause this structural change in the copper dimer. Due to the greater Cu-Cu bonding, the strength and the lability of the Cu-phenolate and Cu-dioxygen bonds are modified by a trans axial ligand effect leading to enhanced reactivity of the encapsulated complex.

In MOFs, polynuclear architectures are found in the 0D coordination polymers such as binuclear copper clusters called $M_2(CO_2)_4$ paddle-wheel in MOP-1[43] and $Cu_3(btc)_2$ (HKUST-1)[44] (Figure 16) or trinuclear units $Fe_3O(CO_2)_6$ MIL-88 [52], IRMOP-51 [50]. Thus, clearly 0D MOFs possesse accessible potentially bio-mimetic catalytic centres.

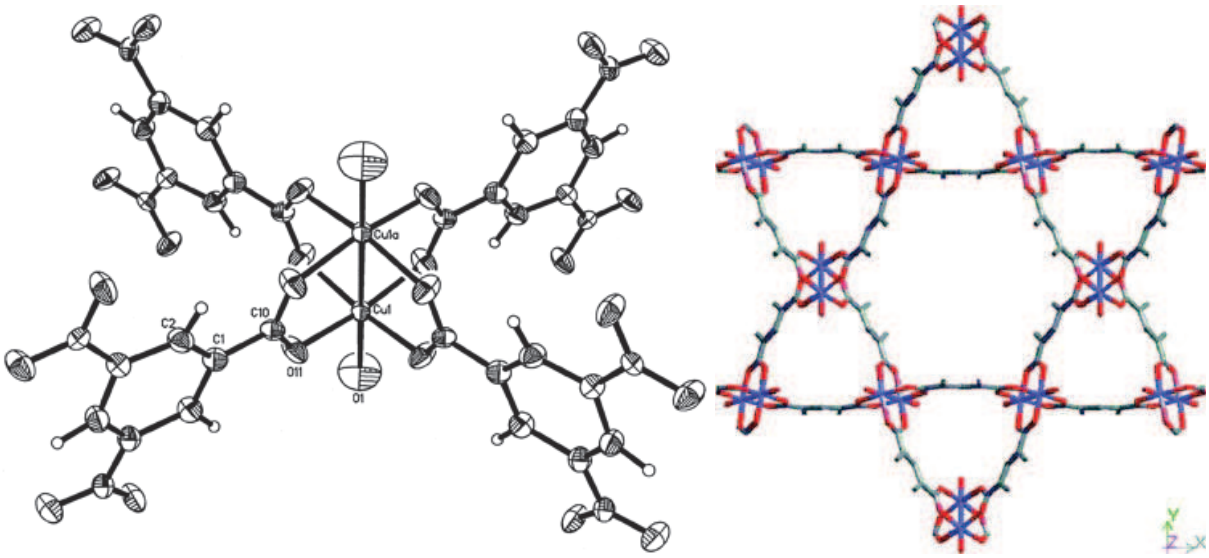

Figure 16. (left) Dicopper(II) tetracarboxylate building block for HKUST-1. (right) $[Cu_3(TMA)_2(H_2O)_3]_n$ viewed along the cell body diagonal [111][44], showing a hexagonal-shaped 18 Å window at the intersection of the nanopores.

The active sites could be the undercoordinated metal centers of the framework. This strategy have prove its value in the past. Nevertheless, the functionalization of the organic linker by metal coordination in a controlled environnement seems more appealing in order to generate flexibility as well as chirality to mimic enzyme catalytic site.
At this point, we can envisage MOFs as artificial metalloenzymes able to operate stereoselective transformations and/or separations.

II.3 Hydrophobicity-hydrophilicity balance

In enzyme, the hydrophilic/hydrophobic balance of the environment around the active site play a crucial role in the catalytic process. For example the active site in the carbonic anhydrase is a Zinc complex coordinated to a water molecule. The activation of water is an important step in the proposed catalytic cycle. The active site is situated at the bottom of a cleft lined with hydrophobic groups in the protein molecule. This local hydrophobic environment modifies the pKa of the coordinated water and makes possible the reaction. By choosing the right linker and metal precursor, the hydrophobicity within the MOF pore can be control to selectively adsorb of reagents, intermediates and products, and thus drive catalytic selectivity. The hydrophobic-hydrophilic properties of a few MOF have been investigated by water adsorption measurements [80].

HKUST-1 is highly hydrophilic, MIL-101 and MIL-100(Fe) moderately hydrophilic, whereas ZIF-8 is highly hydrophobic. Furthermore, unlike zeolites, different pore systems with different levels of polarity can coexist within the same structure [81].

II.4 Flexibility induced by organic spacers

Enzyme specificity is the result of the synergy between the active site itself and the shaping of the environment around this site; protein units have a high affinity for specific substrates. The beneficial effect of the confinement of chiral species into porous solids has been demonstrated by Corma in the case of zeolites[21] and Thomas for MCM-41[30, 82, 83]. This confinement of a chiral organometallic catalyst in the mesopores led to an enhanced enantioselectivity. They also showed that the size of the cavity determines the face differentiation of the substrate during asymmetric hydrogenation. However, limitations of classical inorganic supports remain problematic:

-Pores of usual zeolites are too small and too rigid to accommodate chiral graft and substrates, and they can be hardly functionalised due to a lack of well defined anchoring sites.[84]

-Ordered Mesoporous Silica (such as MCMs) exhibit amorphous structure which is a drawback for single-site control

The organic nature of the MOFs walls, their dynamic features and guest-shape responses make MOFs more suitable to mimic enzyme behaviour.

II.4.1 Ligand rotation and size

In MOFs, the degree of freedom of single bond and the void of the pore allow ligand molecules such as 1,4-dicarboxylates to undergo a partial motion such as rotation [85, 86] as found in $[Zn_2(1,4\text{-ndc})_2(dabco)]_n$. ^2H solid state NMR show that the aromatic rings are allowed to spin until an adsorbed guest (benzene) hinders the rotation[87, 88]; the guest is then "locked-in" providing, a specific orientation (Figure 17). Because the rotation of the ligand is associated with the dynamic pore size and pore shape, it should affect the adsorption/desorption properties of MOF.

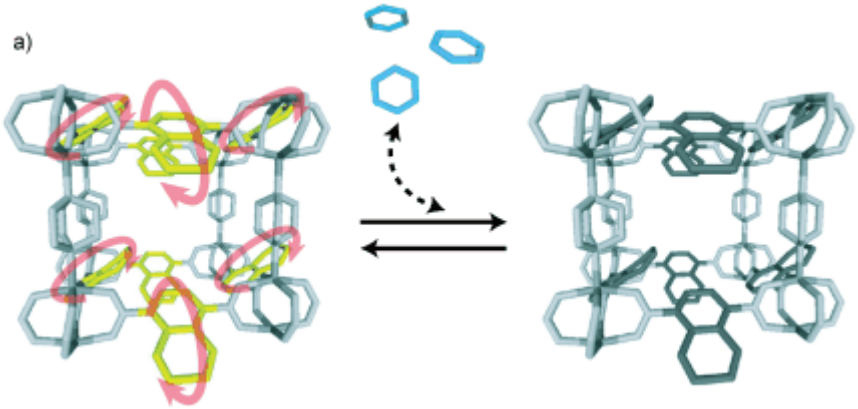

Figure 17. Rotation of naphthalenate linkers upon input of thermal energy in $[Zn_2(1,4\text{-}ndc)_2(dabco)]_n$.

II.4.3. Shape-responsive fitting

Some MOFs, exhibits structural flexibility upon external stimuli such as temperature or pressure changes[47, 89-91]. Gas adsorption on these materials is characterized by a prominent step (S-shaped isotherm) associated with a structural change promoted by guest-host accommodation. This inflection is usually accompanied by a marked hysteresis loop between the adsorption and desorption branches. This peculiar adsorption/desorption behaviour, usually termed "breathing" or "gate opening," arises from an intrinsic flexibility of the porous network[92] (Figure 18).

In the case of MIL-53 the hydroxyl groups of the metal coordination sphere make symmetrical hydrogen bonds with the guest and trigger the transition. The narrow pore-large pore transition is fully reversible when water is involved but structure shows a very high selectivity toward other adsorbable species[92]. For example, whereas MIL-53-large pore is strictly inactive for the readsorption of acetone and ethanol, it immediately adsorbs DMF in a reversible way. The reversible structure changes prove the adaptability of the breathing network to the shape of the chemical stimulus.

Recent efforts have focused on engineering these breathing properties MIL-53(Al, Cr, Fe, Ga)[93-98]. On a fundamental side, the predictive simulation of the breathing properties of Al(OH)(bdc) has made it possible to identify the pressure and temperature ranges over which the phase transformation occurs[99-103]. The effect of cation substitution (Al, Fe, Ga, Cr) on the breathing properties has been investigated[104]. Whereas the MIL-53(Al) framework transforms into the lp phase at low temperature (T=50 °C), the analogous MIL-53(Ga) framework still shows the np phase at T=220 °C. Recently,

Kitagawa showed that the flexibility of CID-5/6 MOFs can be modulated by tuning the composition of two different linkers[105]. By varying their relative ratio, the pressure at which the network begins expansion (the gate opening pressure) can be finely controlled. "Mixed linkers" MIL-53(Al) in which the terephthalate linker (bdc) is partially substituted by 2-aminobenzene-1,4-dicarboxylate (abdc) has been also synthesized[106] but consequence on breathing behaviour was not studied.

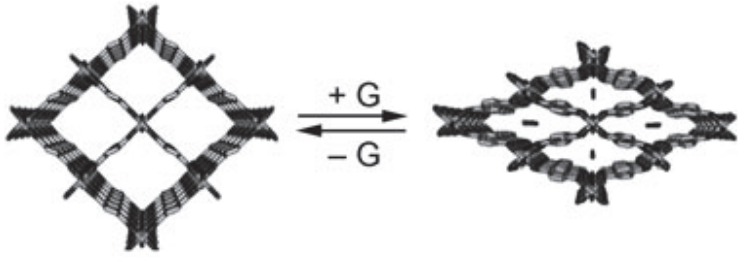

Figure 18. Pore shape response upon guest (G) adsorption-desorption

In order to use MOFs for drug storage and delivery, larger molecule as Ibuprofen have been adsorb in MIL-53 (Fe and Cr)[107]. IR spectroscopy indicates the formation of a strong hydrogen bond between the hydroxyl group of the framework inorganic chains and the ibuprofen carboxylic group. This analogy to enzyme where active site shape is modified upon binding the substrate comforts the idea of MOF a manmade enzyme.

II.4.4. Molecular recognition with homochiral MOF

Homochiral MOFs are able to create an environment generating chiral induction and allowing molecular recognition from weak host-guest interactions. Lin[108] reported the synthesis of a homochiral MOFs built from chiral organic linkers ((*R*)-6,6'-dichloro-2,2'-diethoxy-1,1'-binaphthyl-4,4'-bipyridine) and cadmium precursors. The MOF adopted an an unprecedented 4-connected network topology as a result of the cis-configuration of the [Cd(Py)4(H_2O)$_2$] nodes (Figure 19). Chiral sorption studies showed a preferential adsorbion of the (*R*)-enantiomer of 1-phenylethanol with a modest enantio-enrichment of 6%.

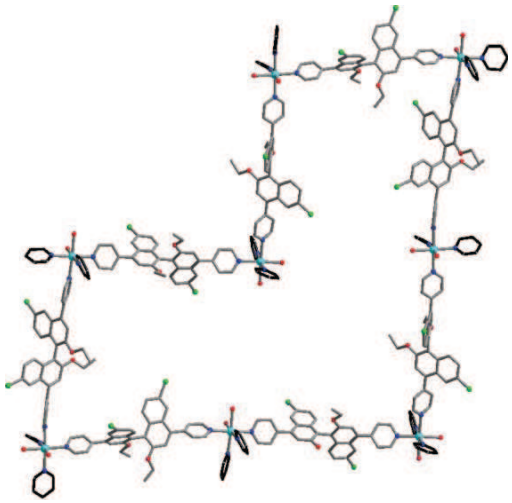

Figure 19. formation of octagons from linking the cis-[Cd(Py)4(H2O)2] nodes. The Py rings shown in black link the octagon to other polygons[108].

Biological molecules are often chiral. Using them as linker is an interesting way to synthesized homochiral and biocompatible materials. Several MOFs were synthesized from biomolecules as amino acid[109-111], peptide (Metal Peptide Framework)[112, 113] and nucleotide base (BioMOF)[114, 115].

Wang *et al* Synthetized a chiral MOF starting with serine modified with a pyridyl group as linker and copper precursors[109]. The solid was use to catalyse the reaction of Grignard reagent with α,β-unsaturated ketone. Enantiomeric excess (ee) up to 99% was obtained. Rosseinsky *et al*[111] published the discovery of a aspartic acid based MOF and reported enantiomeric excess (ee) values up to 54% using hindered substituted diols and he attributed the selectivites observed to bonding between hydrogen of the diol groups and oxygen atoms in aspartate walls (Figure 20). However, the ee values usually range from 1.5 to 15 %.

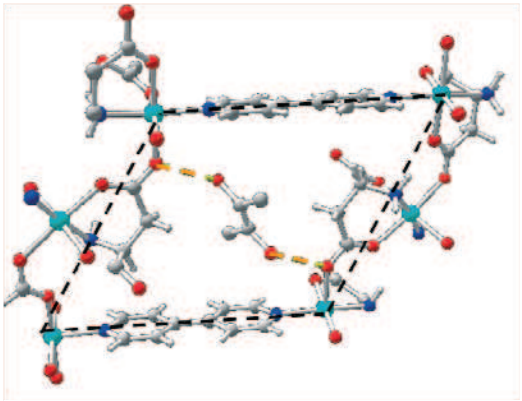

Figure 20. Location of 1,2-propanediol within the channels of aspartate-based MOF[111]

Homochiral MOF have also been applied for the combined selective oxidation of prochiral thioethers and separation of chiral sulfoxides in semipreparative scale chromatography.[116] Fedin and coworkers successfully obtained ee values reaching 60 % using a zinc-lactate-based MOF when standard values are around 15-30 %.

Thanks to their enzyme like biological architectures, BioMOF can also perform molecular recognition. Rabone *et al* synthetized MOF from dipeptide linker (glycylalanine)[113]. The flexibility of the linker allows the change of the pore conformation in response of methanol or CO_2 adsorption. Unfortunately the synthesis of MOF from biomolecules which possess few potential coordination center is complicated. Our several attend to synthesized porous MOF from histidine amino acid or carboxylate functionalized porphyrin failed.

In order to obtain the tools to build enzyme-like MOFs, scientists have investigated both the flexibility and the potential catalytic centers in MOFs.
The organic linkers can take a specific orientation upon the adsorption of guest in the structure which can lead to the enantiomeric separation of a racemic mixture. Furthermore the pores can selectively adsorb molecules and modify the structure upon this chemical stimulus. Engineering this molecular recognition behaviour is a key to mimic the enzyme environment. The "mixed linkers" strategy which consists in introducing different linkers during the self-assembly of the material have show an influence on the flexible of MOF[117]. Indeed modification or dilution of the linker substituents strongly modify the guest-host interactions.

MOFs possess isolated polynuclear clusters which present important similarity with the metal sites found in several biological systems. Nevertheless using these clusters as catalytic centers present limitations. The accessibility of the metal by the reactant can be limited by the steric bulk of the coordination sphere. Furthermore the reaction on the metal can change the cluster coordination and lead to structure degradation.
An alternative is the functionalization of the organic framework by direct self assembly or post synthetic modification. It brings organic or organometallic active species on linker within the pore and design environment similar to the enzyme active site. The synthesis of homochiral MOF with biomolecules as linkers has proved efficiency in the separation or selective catalysis of racemic mixture enantiomers. Unfortunately the

biomolecules have many coordination possibilities and crystalline and porous MOF are often found by serendipity. At this point, PSM appears to be the most efficient way to easily graft organic group in MOF.

III. Post synthetic Modification of MOFs

The post-synthetic modification of MOFs, either at the organic linkers or at the inorganic clusters,[118-122] is the best tool to open new possibilities to design efficient confined catalytic systems having defined single active site and flexibility to accommodate substrates in a specific orientation: in one word, the fine tuning of MOFs allows enzyme mimicking.

III.1. Post-functionalization of MOFs by covalent bond

The interactions involved in encapsulation process are generally weaker than those existing in covalent bonds among main group elements. The creation of covalent bonds though synthetic organic chemistry is a powerful and almost unlimited tool. The application of classical organic chemistry to MOFs, having on their walls reactive groups such as amino in the cases of IRMOF-3,[46] DMOF-1(-NH_2),[123] UMCM-1(-NH_2),[124] MOF-LIC-1,[125] MIL-53-(NH_2)[126], MIL-68-(NH_2)[127, 128], MIL-88-(NH_2) and MIL-101-(NH_2)[129] or formyl in ZIF-90,[130] has been envisaged by many research teams. They succeeded in creating covalent bonds into MOFs following different approaches based on the reactivity of amino- or formyl-containing MOFs to form amides or imines, some examples even reported sophisticated "click chemistry" applied to MOFs when other, rather than the modification of the organic linkers, dealt with the reactivity of bridging hydroxyl groups.

III.1.1. Chemical Modification by Amide Coupling

Among simple organic reactions involving an amino substituent, the formation of an amide by reaction with a carboxylic acid or an anhydride can be one of the first envisaged. However, applying a homogeneous chemical mechanism in a heterogeneous system is not trivial. Cohen and coworkers initiated a systematic investigation on the reactivity of porous MOFs based on 2-amino-terepththalate (NH_2-BDC) towards a variety of symmetric anhydride

(Figure 21).[123, 131-134] The IRMOF-3, which is the amino-susbtituted equivalent of IRMOF-1, was first chosen to perform that study due to its high porosity, crystallinity and the presence of the reactive amino groups on the NH_2-BDC linker. The target reaction was the acetylation of the amino group with acetic anhydride solution in chloroform.[131] ^{1}H NMR analyses of the MOF after digestion, i.e. dissolution in an acidic solution, showed that acetylation occurred quantitatively under optimized conditions, giving the IRMOF-3-AM1 product. Powder X-ray diffraction and thermal gravimetric analyses revealed that the integrity of the IRMOF-3 crystalline structure remained after reaction, without loss of thermal stability. Moreover, single-crystal X-ray analysis of the functionnalized MOF provided unambiguous evidence of the presence of the amide group.

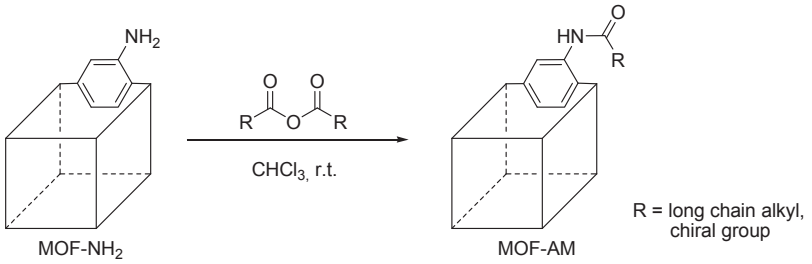

Figure 21. Post-modification of NH_2-BDC-based MOF through amide coupling to give the amido-functionalized MOF-AM.

This strategy was subsequently expanded to other anhydrides. A series of ten straight-chain symmetric alkyl anhydride having a general formula of $O[CO(CH_2)_nCH_3]_2$ (n = 1 to 18) was used as acetylating agents.[133] The reactions yielded to IRMOF-3-AM(n+1) solids with a degree of modification essentially ranged from quantitative for short to medium chain length ($n \leq 5$) to less than 10 % for the longest ($n \geq 18$). Cohen also showed that the surface area of the functionalized MOF correlated inversely with number of atoms added per unit volume (combining yield and chain length) and that the reactivity trend could be rationalized by a sterically controlled heterogeneous mechanism where the size of the reagents is critical.

Following a similar approach, Cohen used cyclic anhydride to form IRMOF-3 derivatives decorated with free carboxylic groups and a chiral anhydride to convert an achiral MOF to a chiral material.[135] Our group successfully applied solid phase peptide synthesis to the post-functionalization of the MIL-68(In)-NH_2 in order to anchor D-alanine and L-proline inside the MOF cavities (Figure 22).[136]

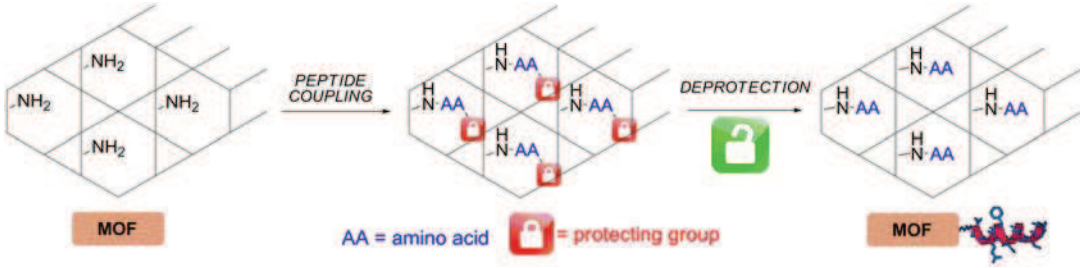

Figure 22. MOF-anchored amino acids through post-synthetic modification.

III.1.2. Chemical Modification by Click Chemistry

The "Click Chemistry" was introduced by Sharpless in 2001 and consists on the azide alkyne Huisgen cycloaddition, i.e. the reaction of an alkyne with azido-functionalized compound catalyzed by copper(I) species to form a triazole heterocycle.[137, 138] It proceeds efficiently even at micromolar concentrations of reactants with high yields and high specificity in the presence of various functional groups. Such key features prompt its application for the modification of well-defined MOFs.

Hupp reported the synthesis of a functionalized MOF composed by dimeric Zn(II) secondary building units, 2,6-naphthalenedicarboxylate, and bipyridyl ligand, namely the 3-[(trimethylsilyl) ethynyl]-4-[2-(4-pyridinyl)ethenyl]pyridine. The bipyridyl ligand presents an acetylene moiety protected by a terminal trimethylsilane (TMS) which provides a suitable platform for post-synthetic modification (Figure 23).[139]

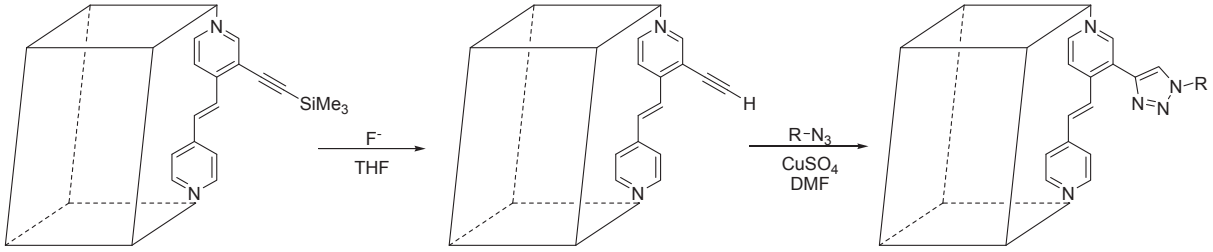

Figure 23. From TMS-protected alkyne containing MOF to triazole-anchored structure via Huisgen cycloaddition.

The MOF was initially treated with tetrabutylammonium fluoride in order to desilylate the surface. Ethidium bromide monoazide was chosen as the azide to perform the copper sulphate catalyzed cycloaddition with the terminal alkynes because its fluorescence can be used for direct visualization of the modification. By comparing the UV-vis absorption spectra

of the azide solution before and after the "click" reaction, they determined that < 0.8% of the dipyridyl ligands had been "clicked" while the crystallinity and the porosity of the MOF remain. Microscopy imaging confirmed that the modification only occurred at the surface of the material.

In a reverse methodology, Sada and coworkers prepared the N3-MOF-16, derived from its parent IRMOF-16, using a bis(azidomethyl) functionnalized *p*-terphenyl-4,4″-dicarboxylate derivative as ligand combined with zinc nitrate in *N*,*N*-diethylformamide (DEF).[140] The N3-MOF-16 was allowed to react with terminal alkynes under copper catalysis to form the corresponding MOF decorated with triazole moieties (Figure 24).

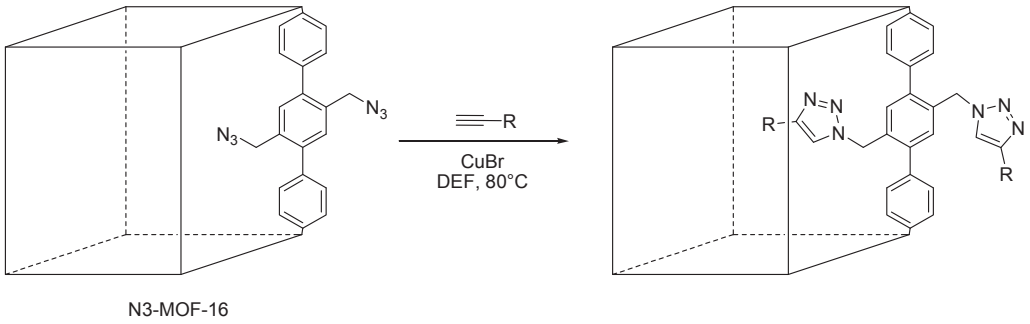

Figure 24. Reactivity of the "clickable" azido-functionalized N3-MOF-16 towards terminal alkynes under copper (I) catalysis.

Following a similar strategy, we used in our group the known DMOF-1(-NH_2) as starting platform for the "click" functionalization. In a first step, the amino group was transformed into an azide (Figure 25).[141] The usual route for preparing azide compounds from the corresponding amines via their diazonium salts being not applicable here because DMOF-1(-NH_2) dissolves under acidic conditions, we investigated another pathway that uses milder conditions and involves stable, non explosive compounds.

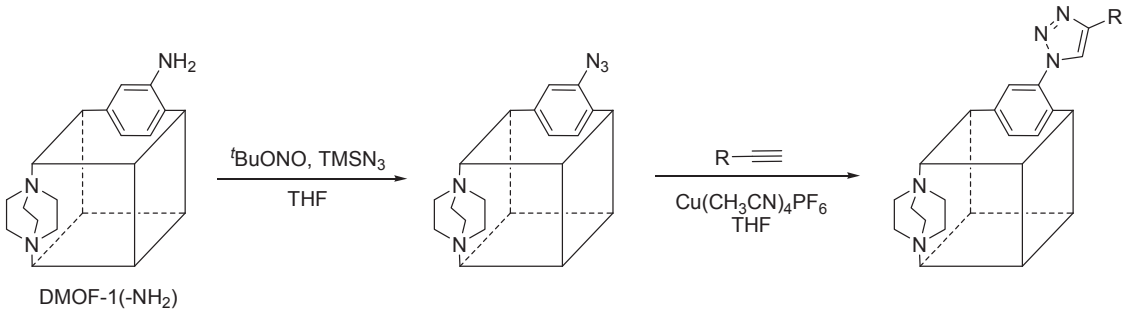

Figure 25. The two-steps triazoyl-anchored MOF formation from the amino-functionalized DMOF-1(-NH_2).

The azido-functionalized MOF obtained then reacted with phenylacetylene in the copper-catalyzed Huisgen cycloaddition to form the corresponding triazole-fucntionalized framework. We also successfully applied their approach to the MIL-68(In)-NH_2.[142] Evidences of the azide formation and the subsequent (3 + 2) cycloaddition were obtained by IR spectroscopy supported by the ^1H NMR analyses of the different materials after digestion in an acidic deuterated solution. Finally, our group generalized this functionalization methodology to four different MOFs, having different 2D or 3D morphologies, using a broad scope of applicable terminal alkynes (Figure 26)[127].

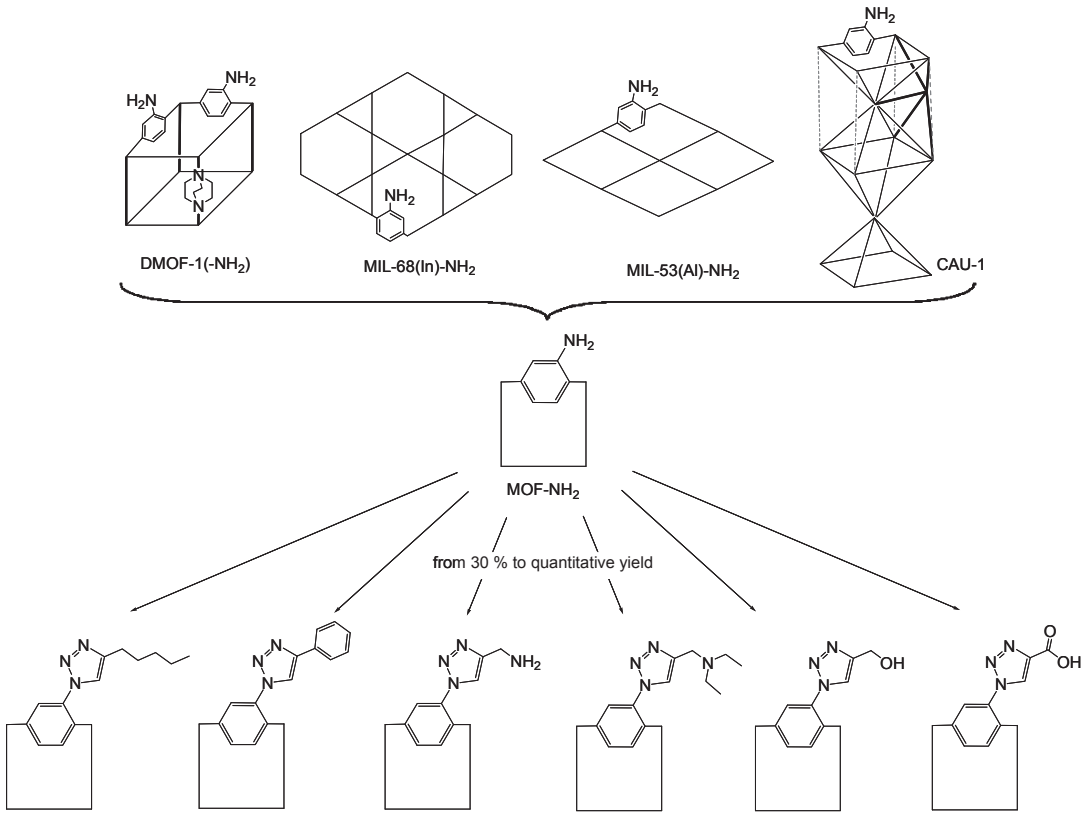

Figure 26. Generic post-functionalization route from amino-derived MOFs by "click chemistry".

As starting platform, in addition to the DMOF-1(-NH_2) and MIL-68(In)-NH_2, they used the MIL-53(Al)-NH_2 [143] and the CAU-1,[144] all of them having the 2-aminoterephthalate as spacer. After the azido-MOF formation, they apply a range of six different terminal alkynes presenting functional groups such as primary or tertiary amine, hydroxyl or carboxylic acid with yields ranging from 30% to quantitative.

III.2. Post-functionalization of MOFs based on coordination chemistry

Metal-ligand interactions can be involved in two different approaches for the post-synthetic modification of MOFs. The first approach targets the unsaturated metal sites, whereas the second exploits the coordination chemistry of the organic linkers, both showing high versatility in incorporating a variety of functionalities into MOFs.

III.2.1. Coordination to Unsaturated Metal Centers

At the end of the nineties, Williams *et al*. described a highly porous 3D MOF known as the HKUST-1, also named CuBTC, formed by Cu(II) secondary building units and 1,3,5-benzenetricarboxylate as ligand.[44] They studied the lability of the axial aqua ligands on the metal clusters and their replacement by other molecules. The dehydratation of the HKUST-1 and its treatment with pyridine led to a framework with new axial ligands but without change of the 3D lattice, the pyridine-decorated MOF being not directly obtained by addition of pyridine to the reaction mixture.

Other investigations were made by the Férey laboratory on the chromium based 3D MOFs MIL-100 [145] and MIL-101.[146] These materials both present potential open metal sites at the $Cr^{(III)}$ clusters which are occupied by water molecule in their as-synthesized form. The preparation of alcohol decorated MIL-100 by reaction of the dehydrated MOF with methanol at room temperature was supported by infrared studies, showing the stability of the post-functionalized material even after being evacuated overnight at 373 K.[63]

III.2.2. Coordination to the Organic Linkers

In coordination chemistry, the organic linkers of the MOF structure can be envisaged as ligands thanks to the presence functional groups. As mentioned above, ligands with potential coordinative sites could interfere during the synthesis of the desired MOF. Nevertheless, some reports already deal with the direct coordination of a metal to the organic ligands of a MOF structure. This approach can be related to the well known “surface organometallic chemistry”, pioneered by Basset *et al*.[147-150] It relies in the bonding of organometallic species onto oxides/hydroxides used as supports in order to achieve single-site

heterogeneous catalyst. The role of the support is assimilated to that of a rigid ligand in the corresponding molecular analogous complex. A key advantage of this "heterogenized" catalyst over molecular species is to access novel chemistry which has no precedent in solution or surface science such as dinitrogen splitting on an isolated silica-grafted tantalum atom.[151]

In a similar manner, Lin and coworkers designed a 3D homochiral MOF based on cadmium and on the BINOL derivative (BINOL = 1,1'-bi-2-naphtol) which present an axial chirality.[152] The BINOL ligand presents both pyridyl and orthogonal hydroxyl groups, the OH being not involved in the coordination of the $Cd^{(III)}$ atoms are available for further chemical modifications. The obtained MOF was treated with $Ti(O^iPr)_4$, a coordination complex known to form Lewis-acid catalyst by coordination to BINOL derivatives (Figure 27). Even if the resulting Ti@MOF material was not fully characterized, it showed interesting catalytic activities for the addition of $ZnEt_2$ to a variety of aromatic aldehydes, the enantiomeric excess found being high but however in the range of those found for the equivalent homogeneous catalyst. It showed also remarkable size selectivity, the substrate conversion decreasing as the size of the aldehyde increased.

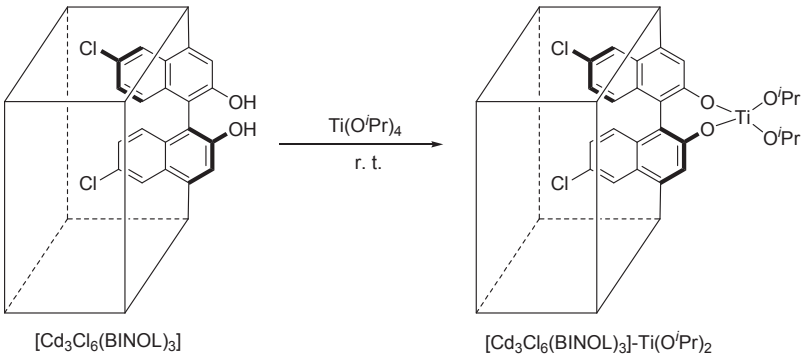

Figure 27. MOF-supported chiral titanium(BINOL) complex by coordination to the walls functional groups.

III.3. Two-steps post-modification for the grafting of organometallic catalysts

Concerning MOF applications, mainly gas storage/separation and catalysis promoted by the MOFs *as synthesized* are reported. The tandem post-synthetic modification methodologies could give an access to sophisticated catalytic species, especially MOFs-

containing organometallics. It consists on the combination of a covalent modification, in order to introduce coordination sites, and coordination chemistry to finally obtain organometallic complexes immobilized in the MOF cavities.

Rosseinsky and coworkers already reported the post-modification of IRMOF-3 with salycilaldehyde by imine condensation leading to the formation of the MOF-supported Schiff base with 13% yield. They used the obtained salicylidene-functionalized IRMOF-3 as N-O ligand for a vanadium oxide complex, characterized by liquid state NMR and PXRD analysis.[153] The obtained MOF-supported catalyst was found to be active for the cyclohexene oxidation with tBuOOH, although both conversion and turnover frequency were relatively low, with a possible problem involving framework collapse. Starting from the same approach, Corma *et al.* reported later a dichloro gold (III) complex supported in IRMOF-3 through coordination to the salycilidene group (Figure 28).[154] The state of the gold species as well as its stability was confirmed by UV-Vis analysis, PXRD and TEM, excluding the formation of metallic gold particles. The Au@IRMOF-3 material catalyzed domino coupling and cyclization reactions in liquid phase with higher activities than the homogeneous and gold supported catalysts reported earlier. Moreover, the Au(III) species remain after reaction and the catalyst is fully recyclable.

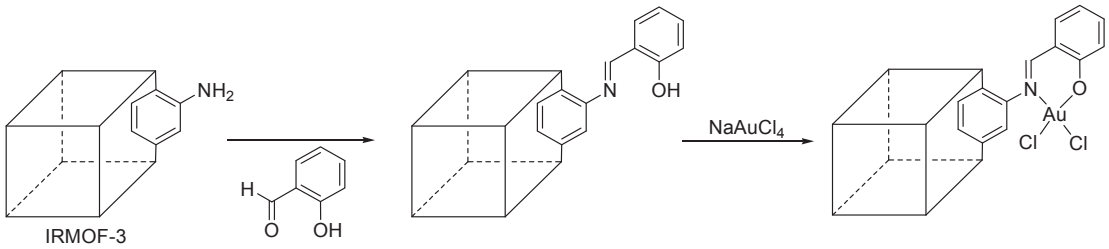

Figure 28. IRMOF-3 containing Au(III) Schiff base complex by tandem post-functionalization[154].

Cohen applied the post-synthetic modification principle to the synthesis of MOF-supported Cu/Fe catalysts.[155] As shown in the figure 29, by reacting the amino functionalized UMCM-1-NH_2 with two different anhydrides under mild conditions, the corresponding amides were obtained with moderate yields (35 to 50%) while the structural integrity of the framework is maintained. Then, addition of iron (III) or copper (II) salt led to the formation of the supported complexes, UMCM-1-AMFesal and UMCM-1-AMCupz respectively. Thereby they showed new evidence of the great versatility of the post-functionalization technique by achieving two different MOF-supported metal species, containing different ligands and

metals, starting from the same MOF carrier. Following the described method, 50% of the potential chelator sites are occupied by a metal. It is noteworthy that the metallated MOFs remain almost as porous as the stating material, with a specific surface of around 3600 $m^2.g^{-1}$. The resulting material was also characterized by PXRD and TGA analysis. The diffuse reflectance electronic spectroscopy supported the formation of Cu^{2+} pyrazine carboxylate and Fe^{3+} salycilate compounds. The latter were tested in the Mukaiyama-aldol reaction which is an extensively studied C-C bond formation involving Lewis-type catalyst. The UMCM-1-AMFesal was found to catalyze the reaction at room temperature with moderate activity but being robust, retaining full activity over 3 catalytic cycles and remaining crystalline.

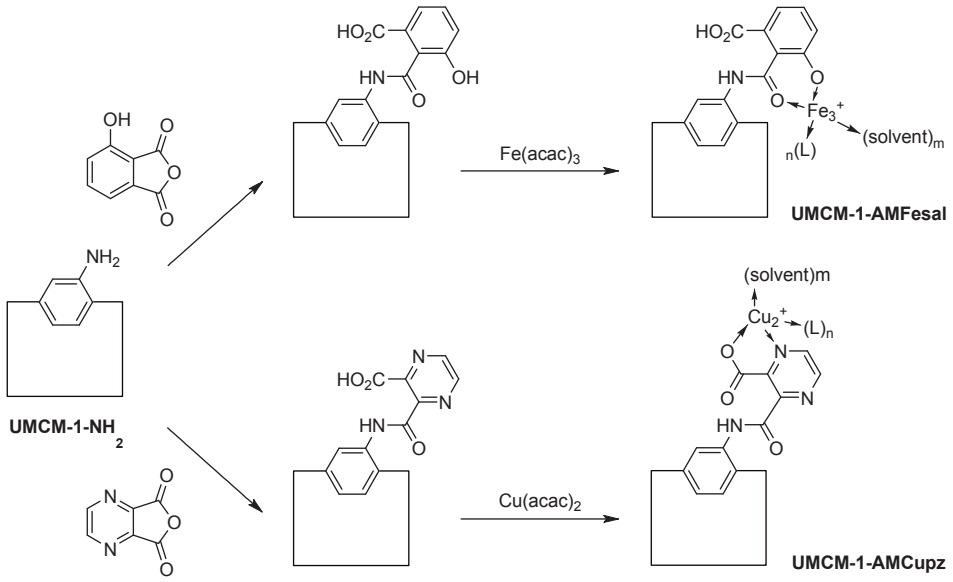

Figure 29. Synthesis of UMCM-1-supported Fe(III) and Cu(II) complexes[155].

MOFs constructed from 2-aminoterephthalate [127, 128] are the most common starting platforms for post-synthesis because they can be easily obtained as long as their unfunctionalized counterpart exist. Anhydride, acid chloride or isocyanate[119, 156-158] were condensated on amino MOF to form amide and urea functionalized MOF. These grafted materials are an efficient platform to coordinated metal and design enzyme-like catalyst. Nevertheless, amino MOF shows a major drawback for their post functionalization. The $–NH_2$ substituent on the aromatic ring has a relatively weak nucleophilicity and only strong electrophilic molecules shall be used to carry out chemical reactions. Unfortunately only a few of these molecules are commercially available. However, for condensation with acid chloride, the liberation of HCl damages strongly the structure of

most of MOFs. An alternative strategy is to convert the amino functionalities into a more reactive functionality. Our group previously converted amino group into azido to enable click chemistry reactions[127, 128]. We present in this thesis a new generic method to synthesize isocyanate and urea functionalized MOF.

Conclusions

The discovery of MOF opened new perspectives in the domain of porous crystalline materials. The hybrid nature of this material allows a better customization of the chemical (acid/base) and physic (flexibility, dimensionality and size of the pores) properties than the fully inorganic zeolites and ordered mesoporous silicas. For exemple, the tunability of the MOF's pore-size makes possible selective conversion in catalysis. Unfortunately their lower stability and higher cost limit the application of MOF as industrial catalyst.

The flexibility, the organic nature of the wall and single metal sites of the MOF are few of the characteristics that MOF have in commun with enzyme catalyst. In this sense we can envisage MOFs as artificial metalloenzymes able to operate stereoselective transformations and/or separations.

In order to obtain the tools to build enzyme-like MOFs, scientists have investigated their molecular recognition behaviour and flexibility upon external stimuli. The "mixed linkers" strategy which consists in introducing different linkers during the auto assembly of the material have show strong influence on the breathing behaviour of flexible MOF[117]. The full study of the Al-MIL-53 breathing upon functionalization with amino group will be presented in this manuscript.

MOF isolated polynuclear clusters present similarity with enzyme active sites but the accessibility of the metal by the reactant and it stability in the catalytic cycle limited their use. In the other hand functionalization of the organic framework by direct self assembly or post synthetic Modification are efficient ways to bring organic or organometallic active species on linker within the pore and design environment similar to the enzyme active site.

The synthesis of homochiral MOF with biomolecules as linkers has proved efficiency in the separation or selective catalysis of racemic mixture enantiomers but the synthesis of biomolecules based MOF are not easily controlled. After failing at the self-assembly of MOF

from metal and sophisticated linker, post functionalization and encapsulation strategies have been choose.

Amino moieties is both a convenient starting group to grafted elaborated organic group and also a source of amino group to created a potentially chelating environment for metal. Unfortunately the mild reactivity of the amino group limits the use of a large library of reactants. Hereafter works to increase the reactivity of the linker and grafted different groups within MOF pores will be described.

References

[1] M. W. Ackley, S. U. Rege and H. Saxena, *Microporous Mesoporous Mater.*, **2003**, **61**, 25-42.
[2] J. Janák, M. Krejčí and E. E. Dubský, *Ann. N. Y. Acad. Sci.*, **1959**, **72**, 731-738.
[3] A. Corma, *Chem. Rev.*, **1997**, **97**, 2373-2420.
[4] M. Pansini, C. Colella and M. De Gennaro, *Desalination*, **1991**, **83**, 145-157.
[5] W. M. Meier, *Molecular Sieves*, Society of Chemical Industry Ed, 1968.
[6] R. M. Barrer, *Zeolites and clay materials as sorbents and molecular sieves*, Academic Press, London, 1978.
[7] D. W. Breck, *Zeolite Molecular Sieves: Structure, Chemistry and Use*, Wiley, New York, 1974.
[8] M. E. Davis, C. Saldarriaga, C. Montes, J. Garces and C. Crowder, *Zeolites*, **1988**, **8**, 362-366.
[9] J.-L. Paillaud, B. Harbuzaru, J. I. Patarin and N. Bats, *Science*, **2004**, 990-992.
[10] A. Corma, M. J. Diaz-Cabanas, J. L. Jorda, C. Martinez and M. Moliner, *Nature*, **2006**, 842-845.
[11] J. L. Sun, C. Bonneau, A. Cantin, A. Corma, M. J. Diaz-Cabanas, M. Moliner, D. L. Zhang, M. R. Li and X. D. Zou, *Nature*, **2009**, **458**, 1154-U1190.
[12] J. S. Beck, J. C. Vartuli, W. J. Roth, M. E. Leonowicz, C. T. Kresge, K. D. Schmitt, C. T. W. Chu, D. H. Olson and E. W. Sheppard, *J. Am. Chem. Soc.*, **1992**, **114**, 10834-10843.
[13] C. T. Kresge, M. E. Leonowicz, W. J. Roth, J. C. Vartuli and J. S. Beck, *Nature*, **1992**, 710-712.
[14] D. M. Antonelli and J. Y. Ying, *Current Opinion in Colloid & Interface Science*, **1996**, **1**, 523-529.
[15] P. Behrens, *Angewandte Chemie International Edition in English*, **1996**, **35**, 515-518.
[16] D. Zhao, Q. Huo, J. Feng, B. F. Chmelka and G. D. Stucky, *J. Am. Chem. Soc.*, **1998**, **120**, 6024-6036.
[17] Q. S. Huo, D. I. Margolese and G. D. Stucky, *Chem. Mater.*, **1996**, **8**, 1147-1160.
[18] C. A. Fyfe and G. Fu, *J. Am. Chem. Soc.*, **1995**, **117**, 9709-9714.
[19] A. Cauvel, D. Brunel, F. DiRenzo and P. Fajula, in *Catalysis by Microporous Materials*, eds. H. K. Beyer, H. G. Karge, I. Kiricsi and J. B. Nagy, Elevier Science Publ B V, Amsterdam, 1995, pp. 286-293.
[20] A. Corma, M. I. de Dios, M. Iglesias and F. Sanchez, *Heterogeneous Catalysis And Fine Chemicals Iv*, **1997**, **108**, 501-507.
[21] A. Corma, M. Iglesias and F. Sanchez, *Catal. Lett.*, **1995**, **32**, 313-318.

[22] A. Carmona, A. Corma, M. Iglesias, A. Sanjose and F. Sanchez, *J. Organomet. Chem.*, **1995**, **492**, 11-21.
[23] A. Corma, M. Iglesias, C. Delpino and F. Sanchez, *J. Organomet. Chem.*, **1992**, **431**, 233-246.
[24] A. P. Wight and M. E. Davis, *Chem. Rev.*, **2002**, **102**, 3589-3614.
[25] F. Hoffmann, M. Cornelius, J. Morell and M. Fröba, *Angewandte Chemie International Edition*, **2006**, **45**, 3216-3251.
[26] D. Brunel, *Microporous Mesoporous Mater.*, **1999**, **27**, 329-344.
[27] D. Brunel, A. C. Blanc, A. Galarneau and F. o. Fajula, *Catal. Today*, **2002**, **73**, 139-152.
[28] P. Sutra and D. Brunel, *Chem. Comm.*, **1996**, 2485-2486.
[29] C. Li, H. Zhang, D. Jiang and Q. Yang, *Chem. Comm.*, **2007**, 547-558.
[30] J. M. Thomas and R. Raja, *Acc. Chem. Res.*, **2008**, **41**, 708-720.
[31] M. Eddaoudi, D. B. Moler, H. Li, B. Chen, T. M. Reineke, M. O'Keeffe and O. M. Yaghi, *Acc. Chem. Res.*, **2001**, **34**, 319-330.
[32] G. Férey, *J. Solid State Chem.*, **2000**, **152**, 37-48.
[33] G. Férey, *Chem. Mater.*, **2001**, **13**, 3084-3098.
[34] M. W. Hosseini, *Acc. Chem. Res.*, **2005**, **38**, 313-323.
[35] S. Kaskel, *Porous Metal-Organic Frameworks*, Wiley-VCH Verlag GmbH, 2008.
[36] J. Kim, B. Chen, T. M. Reineke, H. Li, M. Eddaoudi, D. B. Moler, M. O'Keeffe and O. M. Yaghi, *J. Am. Chem. Soc.*, **2001**, **123**, 8239-8247.
[37] M. O'Keeffe, M. Eddaoudi, H. Li, T. Reineke and O. M. Yaghi, *J. Solid State Chem.*, **2000**, **152**, 3-20.
[38] N. L. Rosi, M. Eddaoudi, J. Kim, M. O'Keeffe and O. M. Yaghi, *CrystEngComm*, **2002**, **4**, 401-404.
[39] M. J. Rosseinsky, *Microporous Mesoporous Mater.*, **2004**, **73**, 15-30.
[40] B. Wang, A. Côté, H. Furukawa, M. O'Keeffe and O. Yaghi, *Nature*, **2008**, **453**, 207-211.
[41] O. M. Yaghi, H. Li, C. Davis, D. Richardson and T. L. Groy, *Acc. Chem. Res.*, **1998**, **31**, 474-484.
[42] J.-P. Zhang and X.-M. Chen, *J. Am. Chem. Soc.*, **2008**, **130**, 6010-6017.
[43] M. Eddaoudi, J. Kim, J. B. Wachter, H. K. Chae, M. O'Keeffe and O. M. Yaghi, *J. Am. Chem. Soc.*, **2001**, **123**, 4368-4369.
[44] S. S. Y. Chui, S. M. F. Lo, J. P. H. Charmant, A. G. Orpen and I. D. Williams, *Science*, **1999**, **283**, 1148-1150.
[45] M. Eddaoudi, J. Kim, M. O'Keeffe and O. M. Yaghi, *J. Am. Chem. Soc.*, **2001**, **124**, 376-377.
[46] M. Eddaoudi, J. Kim, N. Rosi, D. Vodak, J. Wachter, M. O'Keeffe and O. M. Yaghi, *Science*, **2002**, **295**, 469-472.
[47] G. Ferey, *Chem. Soc. Rev.*, **2008**, **37**, 191-214.
[48] D. Farrusseng, S. Aguado and C. Pinel, *Angew. Chem., Int. Ed.*, **2009**, **48**, 7502-7513.
[49] K. Seki and W. Mori, *J. Phys. Chem. B*, **2002**, **106**, 1380-1385.
[50] A. C. Sudik, A. R. Millward, N. W. Ockwig, A. P. CÃ´tÃ©, J. Kim and O. M. Yaghi, *J. Am. Chem. Soc.*, **2005**, **127**, 7110-7118.
[51] T. Loiseau, C. Mellot-Draznieks, H. Muguerra, G. Férey, M. Haouas and F. Taulelle, *Comptes Rendus Chimie*, **2005**, **8**, 765-772.
[52] S. Surble, C. Serre, C. Mellot-Draznieks, F. Millange and G. Ferey, *Chem. Comm.*, **2006**, 284-286.
[53] N. L. Rosi, J. Kim, M. Eddaoudi, B. Chen, M. O'Keeffe and O. M. Yaghi, *J. Am. Chem. Soc.*, **2005**, **127**, 1504-1518.

[54] J. H. Cavka, S. r. Jakobsen, U. Olsbye, N. Guillou, C. Lamberti, S. Bordiga and K. P. Lillerud, *J. Am. Chem. Soc.*, **2008**, **130**, 13850-13851.
[55] K. Lillerud, U. Olsbye and M. Tilset, *Top. Catal.*, **2007**, **53**, 859-868.
[56] V. Guillerm, S. Gross, C. Serre, T. Devic, M. Bauer and G. Ferey, *Chem. Comm.*, **2000**, **46**, 767-769.
[57] F. X. Llabrés i Xamena, A. Abad, A. Corma and H. Garcia, *J. Catal.*, **2007**, **250**, 294-298.
[58] A. Corma and H. Garcia, *Chem. Rev.*, **2003**, **103**, 4307-4366.
[59] L. Alaerts, E. Séguin, H. Poelman, F. Thibault-Starzyk, P. A. Jacobs and D. E. De Vos, *Chemistry – A European Journal*, **2006**, **12**, 7353-7363.
[60] K. Schlichte, T. Kratzke and S. Kaskel, *Microporous Mesoporous Mater.*, **2004**, **73**, 81-88.
[61] P. Horcajada, S. Surble, C. Serre, D.-Y. Hong, Y.-K. Seo, J.-S. Chang, J.-M. Greneche, I. Margiolaki and G. Ferey, *Chem. Comm.*, **2007**, 2820-2822.
[62] T. Krahl, A. Vimont, G. Eltanany, M. Daturi and E. Kemnitz, *The Journal of Physical Chemistry C*, **2007**, **111**, 18317-18325.
[63] A. Vimont, J. M. Goupil, J. C. Lavalley, M. Daturi, S. Surble, C. Serre, F. Millange, G. Ferey and N. Audebrand, *J. Am. Chem. Soc.*, **2006**, **128**, 3218-3227.
[64] N. L. Rosi, M. Eddaoudi, J. Kim, M. O'Keeffe and O. M. Yaghi, *Angew. Chem., Int. Ed.*, **2001**, **41**, 284-+.
[65] A. Corma, *J. Catal.*, **2003**, **216**, 298-312.
[66] U. Ravon, G. Chaplais, C. Chizallet, B. Seyyedi, F. Bonino, S. Bordiga, N. Bats and D. Farrusseng, *Chemcatchem*, **2010**, **2**, 1235-1238.
[67] U. Ravon, M. Savonnet, S. Aguado, M. E. Domine, E. Janneau and D. Farrusseng, *Microporous Mesoporous Mater.*, **2010**, **129**, 319-329.
[68] X. Zhang, E. S. Man Lai, R. Martin-Aranda and K. L. Yeung, *Applied Catalysis A: General*, **2004**, **261**, 109-118.
[69] D. D. Das, P. J. E. Harlick and A. Sayari, *Catal. Commun.*, **2007**, **8**, 829-833.
[70] J. Gascon, U. Aktay, M. D. Hernandez-Alonso, G. P. M. van Klink and F. Kapteijn, *J. Catal.*, **2009**, **261**, 75-87.
[71] M. Savonnet, S. Aguado, U. Ravon, D. Bazer-Bachi, V. Lecocq, N. Bats, C. Pinel and D. Farrusseng, *Green Chemistry*, **2009**, **11**, 1729-1732.
[72] H. Hayashi, A. P. Côté, F. Hiroyasu, M. O'Keeffe and O. M. Yaghi, *Nature Materials*, **2007**, **7**, 501-506.
[73] P. Horcajada, T. Chalati, C. Serre, B. Gillet, C. Sebrie, T. Baati, J. F. Eubank, D. Heurtaux, P. Clayette, C. Kreuz, J.-S. Chang, Y. K. Hwang, V. Marsaud, P.-N. Bories, L. Cynober, S. Gil, G. Ferey, P. Couvreur and R. Gref, *Nat Mater*, **2010**, **9**, 172-178.
[74] D. E. Koshland, *Proc. Natl. Acad. Sci. U. S. A.*, **1958**, **44**, 98-104.
[75] K. D. Blake CC, Mair GA, North AC, Phillips DC, Sarma VR, *Nature*, **1965**, **206**, 757.
[76] M. Boronat, C. Martiì□nez-Saì□nchez, D. Law and A. Corma, *J. Am. Chem. Soc.*, **2008**, **130**, 16316-16323.
[77] E. I. Solomon, A. J. Augustine and J. Yoon, *Dalton Transactions*, **2008**, 3921-3932.
[78] E. I. Solomon, F. Tuczek, D. E. Root and C. A. Brown, *Chem. Rev.*, **1994**, **94**, 827-856.
[79] S. Chavan, D. Srinivas and P. Ratnasamy, *Top. Catal.*, **2000**, **11-12**, 359-367.
[80] P. Küsgens, M. Rose, I. Senkovska, H. Fröde, A. Henschel, S. Siegle and S. Kaskel, *Microporous Mesoporous Mater.*, **2009**, **120**, 325-330.
[81] M. Kawano, T. Kawamichi, T. Haneda, T. Kojima and M. Fujita, *J. Am. Chem. Soc.*, **2007**, **129**, 15418-15419.

[82] J. M. Thomas, T. Maschmeyer, B. F. G. Johnson and D. S. Shephard, *Journal of Molecular Catalysis a-Chemical*, **1999**, **141**, 139-144.
[83] S. J. M. Thomas, *Chemcatchem*, **2010**, **2**, 127-132.
[84] T. F. Degnan, *J. Catal.*, **2003**, **216**, 32-46.
[85] A. Kuc, A. Enyashin and G. Seifert, *J. Phys. Chem. B*, **2007**, **111**, 8179-8186.
[86] E. Y. Lee, S. Y. Jang and M. P. Suh, *J. Am. Chem. Soc.*, **2005**, **127**, 6374-6381.
[87] S. Bureekaew, S. Shimomura and S. Kitagawa, *Sci. Technol. Adv. Mater.*, **2008**, **9**.
[88] S. Horike, R. Matsuda, D. Tanaka, S. Matsubara, M. Mizuno, K. Endo and S. Kitagawa, *Angew. Chem., Int. Ed.*, **2006**, **45**, 7226-7230.
[89] S. Kitagawa and K. Uemura, *Chem. Soc. Rev.*, **2005**, **34**, 109-119.
[90] J. A. R. Navarro, E. Barea, A. Rodriguez-Diéguez, J. M. Salas, C. O. Ania, J. B. Parra, N. Masciocchi, S. Galli and A. Sironi, *J. Am. Chem. Soc.*, **2008**, **130**, 3978-3984.
[91] S. Horike, S. Shimomura and S. Kitagawa, *Nat Chem*, **2009**, **1**, 695-704.
[92] G. Ferey and C. Serre, *Chem. Soc. Rev.*, **2009**, **38**, 1380-1399.
[93] P. L. Llewellyn, P. Horcajada, G. Maurin, T. Devic, N. Rosenbach, S. Bourrelly, C. Serre, D. Vincent, S. Loera-Serna, Y. Filinchuk and G. Férey, *J. Am. Chem. Soc.*, **2009**, **131**, 13002-13008.
[94] S. Bourrelly, P. L. Llewellyn, C. Serre, F. Millange, T. Loiseau and G. Férey, *J. Am. Chem. Soc.*, **2005**, **127**, 13519-13521.
[95] C. Serre, S. Bourrelly, A. Vimont, N. A. Ramsahye, G. Maurin, P. L. Llewellyn, M. Daturi, Y. Filinchuk, O. Leynaud, P. Barnes and G. Férey, *Adv. Mater.*, **2007**, **19**, 2246-2251.
[96] P. L. Llewellyn, S. Bourrelly, C. Serre, Y. Filinchuk and G. Férey, *Angew. Chem.*, **2006**, **118**, 7915-7918.
[97] N. A. Ramsahye, G. Maurin, S. Bourrelly, P. L. Llewellyn, C. Serre, T. Loiseau, T. Devic and G. Ferey, *J. Phys. Chem. C*, **2007**, **112**, 514-520.
[98] C. Serre, F. Millange, C. Thouvenot, M. NoguÃ¨s, G. r. Marsolier, D. Louër and G. Férey, *J. Am. Chem. Soc.*, **2002**, **124**, 13519-13526.
[99] F. o.-X. Coudert, M. Jeffroy, A. H. Fuchs, A. Boutin and C. Mellot-Draznieks, *J. Am. Chem. Soc.*, **2008**, **130**, 14294-14302.
[100] A. M. Walker, B. Civalleri, B. Slater, C. Mellot-Draznieks, F. Cora, C. M. Zicovich-Wilson, G. Roman-Perez, J. M. Soler and J. D. Gale, *Angew. Chem., Int. Ed.*, **2010**, **49**, 7501-7503.
[101] A. Torrisi, R. G. Bell and C. Mellot-Draznieks, *Cryst. Growth Des.*, **2010**, **10**, 2839-2841.
[102] A. Torrisi, C. Mellot-Draznieks and R. G. Bell, *J. Chem. Phys.*, **2010**, **132**.
[103] A. Boutin, F. o.-X. Coudert, M.-A. Springuel-Huet, A. V. Neimark, G. Férey and A. H. Fuchs, *J. Phys. Chem. C*, **2010**, **114**, 22237-22244.
[104] C. Volkringer, T. Loiseau, N. Guillou, G. Ferey, E. Elkaim and A. Vimont, *Dalton Trans.*, **2009**, 2241-2249.
[105] T. Fukushima, S. Horike, Y. Inubushi, K. Nakagawa, Y. Kubota, M. Takata and S. Kitagawa, *Angew. Chem., Int. Ed.*, **2010**, **49**, 4820-4824.
[106] S. Marx, W. Kleist, J. Huang, M. Maciejewski and A. Baiker, *Dalton Trans.*, **2010**, **39**, 3795-3798.
[107] P. Horcajada, C. Serre, G. Maurin, N. A. Ramsahye, F. Balas, M. Vallet-Rega, M. Sebban, F. Taulelle and G. Férey, *J. Am. Chem. Soc.*, **2008**, **130**, 6774-6780.
[108] C. D. Wu and W. B. Lin, *Chem. Commun.*, **2005**, 3673-3675.
[109] M. Wang, M.-H. Xie, C.-D. Wu and Y.-G. Wang, *Chem. Comm.*, **2009**, 2396-2398.
[110] C.-D. Wu, L. Li and L.-X. Shi, *Dalton Transactions*, **2009**, 6790-6794.

[111] R. Vaidhyanathan, D. Bradshaw, J.-N. Rebilly, J. P. Barrio, J. A. Gould, N. G. Berry and M. J. Rosseinsky, *Angew. Chem., Int. Ed.*, **2006**, **45**, 6495-6499.
[112] A. Mantion, L. MassÃ¼ger, P. Rabu, C. Palivan, L. B. McCusker and A. Taubert, *J. Am. Chem. Soc.*, **2008**, **130**, 2517-2526.
[113] J. Rabone, Y.-F. Yue, S. Y. Chong, K. C. Stylianou, J. Bacsa, D. Bradshaw, G. R. Darling, N. G. Berry, Y. Z. Khimyak, A. Y. Ganin, P. Wiper, J. B. Claridge and M. J. Rosseinsky, *Science*, **2010**, **329**, 1053-1057.
[114] J. An, S. J. Geib and N. L. Rosi, *J. Am. Chem. Soc.*, **2009**, **131**, 8376-8377.
[115] Y. Chen and J. Jiang, *ChemSusChem*, **2010**, **3**, 982-988.
[116] A. L. Nuzhdin, D. N. Dybtsev, K. P. Bryliakov, E. P. Talsi and V. P. Fedin, *J. Am. Chem. Soc.*, **2007**, **129**, 12958-12959.
[117] T. Fukushima, S. Horike, Y. Inubushi, K. Nakagawa, Y. Kubota, M. Takata and S. Kitagawa, *Angew. Chem., Int. Ed.*, **2010**, **49**, 4820-4824.
[118] D. Farrusseng, J. Canivet and A. Quadrelli, in *Metal-Organic Frameworks*, Wiley-VCH Verlag GmbH & Co. KGaA, 2011, pp. 23-48.
[119] Z. Q. Wang and S. M. Cohen, *Chem. Soc. Rev.*, **2009**, **38**, 1315-1329.
[120] S. M. Cohen, *Chem. Sci.*, **2010**, **1**, 32-36.
[121] K. K. Tanabe and S. M. Cohen, *Chem. Soc. Rev.*, **2011**, **40**, 498-519.
[122] S. M. Cohen, *Chem. Rev.*, **2012**, **112**, 970-1000.
[123] Z. Q. Wang, K. K. Tanabe and S. M. Cohen, *Inorg. Chem.*, **2009**, **48**, 296-306.
[124] K. Koh, A. G. Wong-Foy and A. J. Matzger, *Angew. Chem.-Int. Edit.*, **2008**, **47**, 677-680.
[125] J. S. Costa, P. Gamez, C. A. Black, O. Roubeau, S. J. Teat and J. Reedijk, *Eur. J. Inorg. Chem.*, **2008**, 1551-1554.
[126] T. Ahnfeldt, D. Gunzelmann, T. Loiseau, D. Hirsemann, J. r. Senker, G. Férey and N. Stock, *Inorganic Chemistry*, **2009**, **48**, 3057-3064.
[127] M. Savonnet, D. Bazer-Bachi, N. Bats, J. Perez-Pellitero, E. Jeanneau, V. Lecocq, C. Pinel and D. Farrusseng, *Journal of the American Chemical Society*, **2010**, **132**, 4518-4519.
[128] M. Savonnet, E. Kockrick, A. Camarata, D. Bazer-Bachi, N. Bats, V. Lecocq, C. Pinel and D. Farrusseng, *New J. Chem.*, **2011**, **35**, 1892-1897.
[129] S. Bauer, C. Serre, T. Devic, P. Horcajada, J. Marrot, G. Ferey and N. Stock, *Inorg. Chem.*, **2008**, **47**, 7568-7576.
[130] W. Morris, C. J. Doonan, H. Furukawa, R. Banerjee and O. M. Yaghi, *J. Am. Chem. Soc.*, **2008**, **130**, 12626-+.
[131] Z. Q. Wang and S. M. Cohen, *J. Am. Chem. Soc.*, **2007**, **129**, 12368-+.
[132] E. Dugan, Z. Q. Wang, M. Okamura, A. Medina and S. M. Cohen, *Chem. Commun.*, **2008**, 3366-3368.
[133] K. K. Tanabe, Z. Q. Wang and S. M. Cohen, *J. Am. Chem. Soc.*, **2008**, **130**, 8508-8517.
[134] Z. Q. Wang and S. M. Cohen, *Angew. Chem.-Int. Edit.*, **2008**, **47**, 4699-4702.
[135] S. J. Garibay, Z. Q. Wang, K. K. Tanabe and S. M. Cohen, *Inorg. Chem.*, **2009**, **48**, 7341-7349.
[136] J. Canivet, S. Aguado, G. Bergeret and D. Farrusseng, *Chem. Commun.*, **2011**, **47**, 11650-11652.
[137] W. D. Sharpless, P. Wu, T. V. Hansen and J. G. Lindberg, *J. Chem. Educ.*, **2005**, **82**, 1833-1836.
[138] M. G. Finn, H. C. Kolb, V. V. Fokin and K. B. Sharpless, *Prog. Chem.*, **2008**, **20**, 1-4.
[139] T. Gadzikwa, G. Lu, C. L. Stern, S. R. Wilson, J. T. Hupp and S. T. Nguyen, *Chem. Commun.*, **2008**, 5493-5495.

[140] Y. Goto, H. Sato, S. Shinkai and K. Sada, *J. Am. Chem. Soc.*, **2008**, **130**, 14354-+.
[141] M. Savonnet, D. Bazer-Bachi, N. Bats, J. Perez-Pellitero, E. Jeanneau, V. Lecocq, C. Pinel and D. Farrusseng, *J. Am. Chem. Soc.*, **2010**, **132**, 4518-+.
[142] M. Savonnet and D. Farrusseng, 2009.
[143] T. Ahnfeldt, D. Gunzelmann, T. Loiseau, D. Hirsemann, J. Senker, G. Ferey and N. Stock, *Inorg. Chem.*, **2009**, **48**, 3057-3064.
[144] T. Ahnfeldt, N. Guillou, D. Gunzelmann, I. Margiolaki, T. Loiseau, G. Ferey, J. Senker and N. Stock, *Angew. Chem.-Int. Edit.*, **2009**, **48**, 5163-5166.
[145] G. Ferey, C. Serre, C. Mellot-Draznieks, F. Millange, S. Surble, J. Dutour and I. Margiolaki, *Angew. Chem.-Int. Edit.*, **2004**, **43**, 6296-6301.
[146] G. Ferey, C. Mellot-Draznieks, C. Serre, F. Millange, J. Dutour, S. Surble and I. Margiolaki, *Science*, **2005**, **309**, 2040-2042.
[147] J. M. Basset, *Journal Of Molecular Catalysis*, **1994**, **86**, 1-4.
[148] C. Coperet, M. Chabanas, R. P. Saint-Arroman and J. M. Basset, *Angew. Chem.-Int. Edit.*, **2003**, **42**, 156-181.
[149] C. Nedez, A. Choplin, J. Corker, J. M. Basset, J. F. Joly and E. Benazzi, *Journal Of Molecular Catalysis*, **1994**, **92**, L239-L244.
[150] V. Vidal, A. Theolier, J. ThivolleCazat and J. M. Basset, *Science*, **1997**, **276**, 99-102.
[151] P. Avenier, M. Taoufik, A. Lesage, X. Solans-Monfort, A. Baudouin, A. de Mallmann, L. Veyre, J. M. Basset, O. Eisenstein, L. Emsley and E. A. Quadrelli, *Science*, **2007**, **317**, 1056-1060.
[152] C. D. Wu, A. Hu, L. Zhang and W. B. Lin, *J. Am. Chem. Soc.*, **2005**, **127**, 8940-8941.
[153] M. J. Ingleson, J. P. Barrio, J. B. Guilbaud, Y. Z. Khimyak and M. J. Rosseinsky, *Chem. Commun.*, **2008**, 2680-2682.
[154] X. Zhang, F. Llabres and A. Corma, *J. Catal.*, **2009**, **265**, 155-160.
[155] K. K. Tanabe and S. M. Cohen, *Angew. Chem., Int. Ed.*, **2009**, **48**, 7424-7427.
[156] S. M. Cohen, *Chemical Reviews*, **2012**, **112**, 970-1000.
[157] S. J. Garibay, Z. Wang, K. K. Tanabe and S. M. Cohen, *Inorganic Chemistry*, **2009**, **48**, 7341-7349.
[158] M. Savonnet, S. Aguado, U. Ravon, D. Bazer-Bachi, V. Lecocq, N. Bats, C. Pinel and D. Farrusseng, *Green Chemistry*, **2009**, **11**, 1729-1732.

Chapter 2

Encapsulation of molecular catalyst

I. Introduction

MOFs exhibit high and permanent porosity but also have calibrated pore size which is very promising for the design of catalyst. We first gave effort to synthesize MOF with bioactive or bio inspired molecules for linker (histidine and phthalocyanine). Unfortunately all our attempts produced amorphous materials. We report two examples of synthesis that have been tried.

Histidine is a chiral amino acid substituted with an imidazole group. This imidazole group was widely used as linker to create a sub class of MOF called Zeolite Imadazole Framework (ZIF). Furthermore zinc histidine complex is found in several enzymatic catalysis. Differant synthetic method (solvothermal and precipitation), solvent system (water, Methanol, THF, DMF) and temperature were tried. A partially crystalline was obtained by adding ammoniac into an equimolar mixture of L-histidine and zinc nitrate in DMF. ^{1}H NMR of the digested MOF clearly showed the signals of the histidine. Unfortunately the solid was not porous.

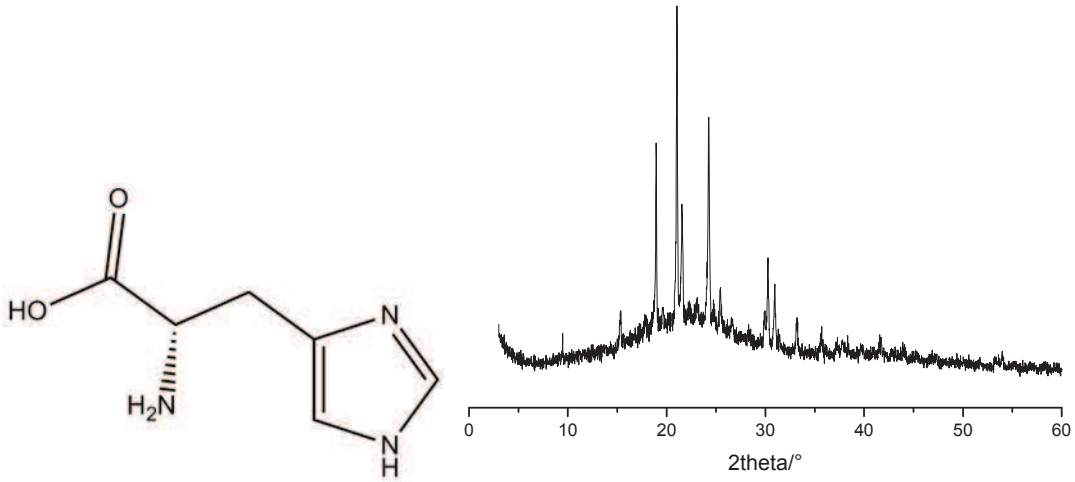

Figure 1. L-histidine (left) and XRD pattern of an histidine based solid (right)

We also investigated the synthesis of a MOF with carboxylate substituted phthalocyanine as linker. No crystalline structure was obtained. We believe that the random distribution of carboxylate groups on the benzene ring do not allow the self assembly of the solid.

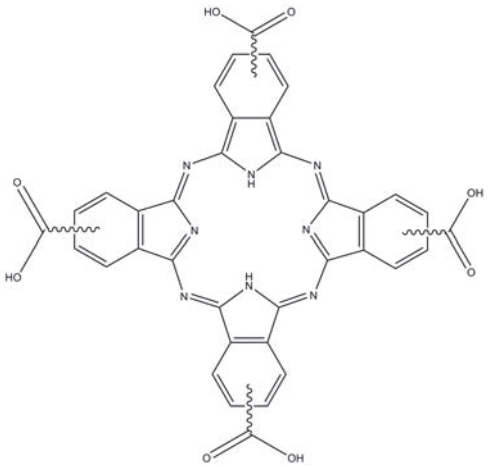

Figure 2. Phthalocyanine

Our second idea was to develop supported metal complexes as "ship-in-a-bottle" catalysts. Such an approach has recently been undertaken to encapsulate inorganic clusters such as polyoxometalates,[1-4] metallic nanoparticles[5-7] and molecular catalysts[8-10] in MOF.

The ability of MOF to offer cavities where fit one catalyst molecule may have different advantage: avoiding aggregation of catalyst (better molecular accessibility and/or avoiding deactivation) and increasing the selectivity of the reaction by steric effect. Furthermore interactions with the framework can modify the chemical properties of the encapsulated species. In the following work, we encapsulated four phthalocyanines in the highly stable Cr-MIL-101 to design an heterogeneous catalyst for the oxidation of organic molecules under oxygen.

II. State of the Art of encapsulation in MOFs

II.1 Encapsulation of metallic particles

Nanosized metallic particles dispersed in sharply microporous metal-organic frameworks are of a great interest in the field of catalysis. The position of the metallic clusters within the MOF and their size distribution can readily be investigated by electron microscopy leading to a good knowledge of the potential active sites.

Chemical vapour infiltration of organometallic precursors was shown to be an appropriate method for very high loading of nanoparticles based on Pt, Au, Pd [6, 11] and Ru [12] into the porosity of MOF-5 and MOF-177.[13] The Pd-based catalyst was found to be active for the CO oxidation and olefin hydrogenation.

More recently, chemical-based methods have been developed using wetness impregnation. Kaskel reported composite of Pd-supported MOF-5 prepared by impregnation

showing a catalytic activity superior to that found for Pd/C for the hydrogenation of various alkenes and esters in three-phase reactions.[7] Haruta described nanosized Au hosted in various support, such as CPL-1 & -2, HKUST-1, MIL-53 and MOF-5, by deposition of the $Me_2Au(acac)$ precursor followed by mild reduction under mild hydrogen flow at 120°C.[14] All the Au supported catalysts were active for the aerobic oxidation of benzyl alcohol in methanol with a cooperative effect of the MOF support allowing the activation of the alcohol in the absence of a base. MOF-supported palladium nanoparticles were very recently reported by Jiang (Figure 3).[15] The composite was prepared by impregnation of the large 3D MOF MIL-101 with $Pd(NO_3)_2$ then reduced under an hydrogen stream, resulting on a palladium loading of 1wt% without loss of crystallinity.

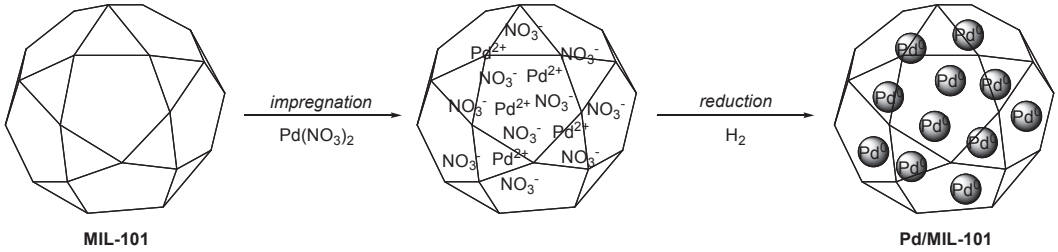

Figure 3. MIL-101-supported palladium nanoparticles made by impregnation/reduction.

The Pd/MIL-101 was found to catalyze the water mediated Suzuki-Miyaura and Ullmann couplings of aryl chlorides. The MOF-supported palladium nanoparticles were stable under several catalytic cycles with negligible metal leaching, demonstrating that MOFs as catalyst supports could bring new opportunities to heterogeneous catalysis.

II.2 Encapsulation of polyoxometalates

Another source of active site are heteropoly acids. Main of the work realised in this domain was focusing on the incorporation of Keggin polyoxometalates (POM), a strong brønsted acid catalyst[16], in MOFs. Keggin heteropolyanion is thermally stable solid which exhibit fast reversible multi-electron redox transformations under mild conditions. Furthermore acid-base and redox properties could be tune by modifying the chemical composition. Unfortunately the catalytic activity of the POMs supported on activated carbon is much lower that in homogeneous phase. It is explained by the too strong interactions of the POM with the support. In the other hand too weak interactions lead to dramatic leaching. MOFs as CuBTC and Cr-MIL-101 possess large spherical pores (≥12 Å) suitable for the

accommodation of POM molecule with Keggin structure ($XM_{12}O_{40}$, X central atom)[17]. Polyoxotungstate Keggin in situ encapsulated in CuBTC show better activity in ester hydrolysis than most inorganic solid acid[18]. Impregnation of polyoxotungstate in Cr-MIL-101 gives a material with activity comparable of the homogeneous POM in the selective oxidation of alkenes with aqueous hydrogen peroxide[4]. Moreover, confinement of POM within MIL-101 nanocages slightly increases the epoxide selectivity. In situ encapsulation of polyoxotungstate have also been carried out by Juan-Alcaniz et al[3]. A partial substitution of POM tungsten by Cr^{3+} is observed. The lacunary structure formed is highly active and show outstanding results in Knovenagel condensation.

II.3 encapsulation of molecular catalyst

Adsorptions of organic species have been widely studied in MOF. Benzene or linear alkane could be adsorbed but the process is often reversible. Several papers report irreversible encapsulation of molecular species or organometallics in MOF materials. The adsorbed species form interaction with the host matrice avoiding leaching phenomenon. Yaghi and Fisher groups reported adsorption of dye[19, 20] and C_{60} fullerene[19] in MOFs. Several washings with solvent do not decrease the quantity of species trapped inside the solids. Interaction of fullerene with the host is proved by the shift between the free and encapsulated species in Raman spectroscopy. Kim *et al* reposted an other case[21] where included ferrocene was forming well-ordered array in the pores of the host framework without strong interaction with it.

An other method is the *in situ* synthesis: species are encapsulated during the synthesis and the hindrance of pore does not allow them to leave the structure. Under these conditions Eddaoudi synthesized one of the only MOF-encapsulated organometallics used for catalysis[8]. Highly active manganese porphyrin is encapsulated in the cage of a zeolite imidazole framework (Figure 4) during the synthesis. The loaded material shows activity in the oxidation of cyclohexane in presence of *tert*-butyl hydroperoxide.

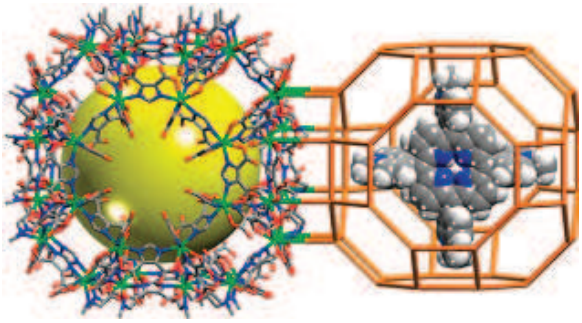

Figure 4. Porphyrin encapsulated in ZMOF[8]

III. Synergistic effects of encapsulated phthalocyanine complexes in MIL-101 for the selective aerobic oxidation of tetralin

(*Chem. Commun*., **2011**, 47, 1562-1564)

III.1 Objective

Metal phthalocyanine complexes (MPc) (Figure 5) exhibit outstanding performance as oxidation catalysts.[22, 23] Recently, our group showed that a bulky N-bridged diiron phthalocyanine complex, $(FePc^{t}Bu_4)_2N$, allows the selective oxidation of methane, benzene and alkylaromatics.[24-26] The EXAFS structural determination indicates a linear $Fe^{+3.5}(\mu\text{-}N)Fe^{+3.5}$ unit with equivalent Fe–N distances (1.65 Å) and a 3.33 Å distance between parallel Pc planes.[27] Unfortunately, MPc usually self-assemble to oligomer structures in solution through π-π stacking, which strongly limits their catalytic applications in homogeneous processes.[28] To overcome this issue, silica- and zeolite-supported MPc have therefore been developed.[29-33]

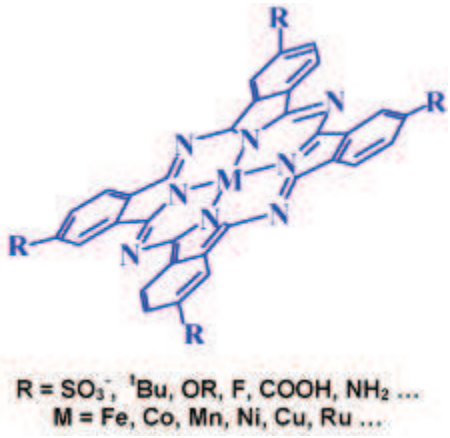

Figure 5. Metal phthalocyanine complexes

The MIL-101, which exhibits a 3D pore system with calibrated cavities of 2.9 nm and 3.4 nm is a perfect candidate as host for the MPc.

The objective of our work was to encapsulate large MPc in the cavities of MIL-101 for the selective oxidation of tetralin into 1-tetralone, a diesel fuel additive and an intermediate for the synthesis of agricultural chemicals.[34] To the best of our knowledge, this is the first report on the synergistic effect of the confinement of molecular catalysts in porous MOFs.

III.2 Synthesis

III.2.1 MIL-101

Mesoporous MIL-101 was prepared and purified by a modified synthesis introduced by *Ferey et al.*[2] A solution containing 2.4 g chromium nitrate nonahydrate ($Cr(NO_3)_3 \cdot 9 \cdot H_2O$) (Sigma-Aldrich), 1.50 g 1,4-benzenedicarboxylic acid (bdc) (Sigma-Aldrich), 0.30 ml of hydrofluoric acid (40 % in water) (Sigma-Aldrich) and 30 ml deionised H_2O was introduced in a 48 ml Teflon-liner autoclave and was heated to 493 K for 9 h (heating ramp 25K/h). After a cooling period of 8 h, the reaction mixture was filtered through a large pore fritted glass filter to eliminate excess of recrystallised terephthalic acid. The product was separated from water by centrifugation at 4000 rpm for 20 min. In order to remove incorporated 1,4-benzenedicarboxylic acid, the as-synthesized product was first treated in 100 ml of ammonium fluoride solution in water/ethanol 1:1 v/v (3.7 g NH_4F) for 24 h at 70 °C. Afterwards the halide salt excess was washed by an aqueous soxhlet-extraction for 20 h. Finally, the solid was dried at 423 K for 9 h under reduced pressure to obtain activated, fine powdered MIL-101.

III.2.2 Synthesis of pthhalocyanine complexes

The preparation of metal phthalocyanine complexes was performed according to published procedures: $FePc(COOH)_4$[35], $FePc^tBu_4$ [36], $(FePc^tBu_4)_2N$ [26], $FePc(SO_3H)_4$ [37], $FePcF_{16}$ [38], $RuPcF_{16}$ [29], $CoPc(COOH)_8$[39].

III.2.3 Encapsulation of phthalocyanine complexes inside MIL-101

The MPc–MOF composite materials were prepared by wet infiltration of the deep blue-colored MPc solutions into Cr–MIL-101. 25 mg of $MPcF_{16}$ (M=Fe, Ru) or $(FePc^tBu_4)_2N$ complexes were dissolved in 25 ml of acetone or dichloromethane, respectively. 250 mg of activated MIL-101 were added to the intense blue coloured solution and continuously stirred for 72 h. After complete solvent evaporation the composite materials were washed with solvent (acetone or DCM), stirred for 2 h and centrifuged at 4000 rpm for 20 min several times until the solutions remain colourless. Finally, solids were dried under air for 4 h at 423 K followed by drying under reduced pressure overnight at the same temperature to obtain activated catalyst systems.

III.3 Characterizations

III.3.1 Elementary analysis

Elemental analysis was measured by Inductively Coupled Plasma Optical Emission Spectroscopy (ICP-OES). The samples were dissolved in a boiling sulphuric and nitric acid mixture under reflux conditions and metal contents were analyzed using ICP-OES Activa spectrometer (Jobin-Yvon).

The actual complex loading for the perfluorinated complexes inside the MIL-101 was determined by ICP-OES measurements to be 2.1 wt% and 3.6 wt% for $FePcF_{16}$ and $RuPcF_{16}$, corresponding to approximately 0.8 and 1.2 complexes per large pore respectively. Considering also the access to the smaller pores, the total pore filling would correspond to an average of app. 0.3 ($FePcF_{16}$) and 0.4 ($RuPcF_{16}$). A higher loading of 5.2 wt% is obtained for the $(FePc^{t}Bu_4)_2N$ dimeric complex.

III.3.2 Diffuse reflectance UV-VIS spectroscopy

This last result was also confirmed by diffuse reflectance UV-VIS spectra of pristine and complex loaded MOFs (Figure 6). UV-VIS experiments were carried in transmission (solutions) and diffuse reflectance mode (MPcX@MIL-101) using a Perkin-Elmer Lambda 35.

In agreement with the literature, two adsorption maxima at 446 nm and 600 nm can be identified for the non-loaded MIL-101.[40] For the loaded materials, a shift of the peak maximum to around 615 nm was observed due to the presence of the Pc complexes.[29]

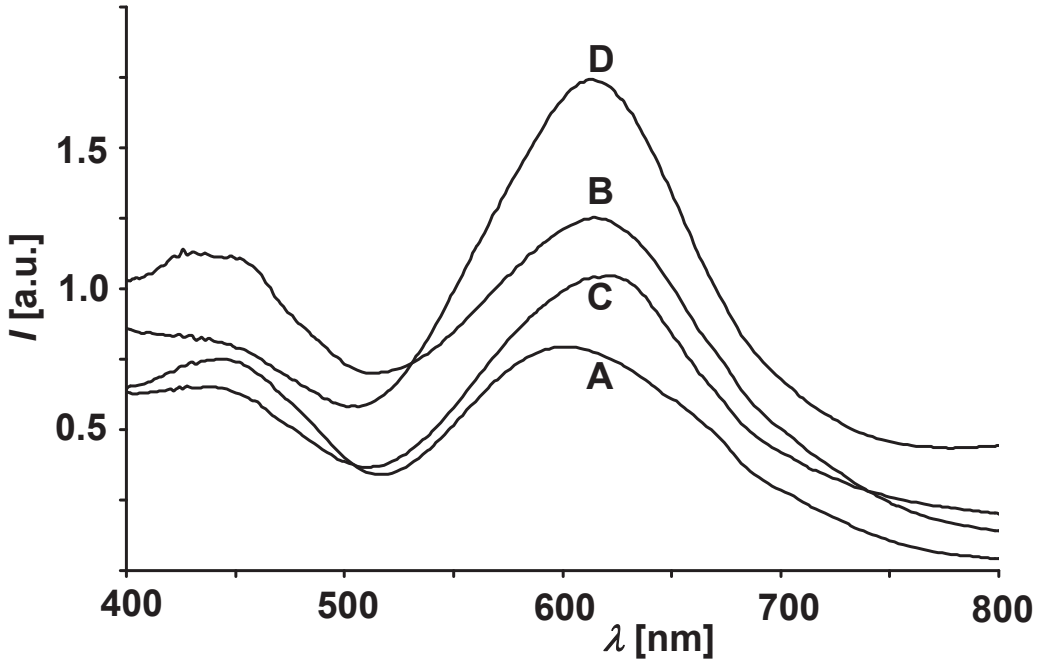

Figure 6. Diffuse reflectance UV-VIS spectra of non-loaded MIL-101 (A), $(FePc^{t}Bu_4)_2N$)@MIL-101 (B), $FePcF_{16}$@MIL-101 (C) and $RuPcF_{16}$ @MIL-101(D).

III.3.3 Powder X-ray diffraction.

Powder X-ray diffraction patterns were recorded using a Bruker D-5005 diffractometer (Bragg–Brentano geometry, graphite monochromator, Cu Kα radiation). Powder XRD patterns are identical to the simulated one. Furthermore no structural change is observed upon encapsulation.

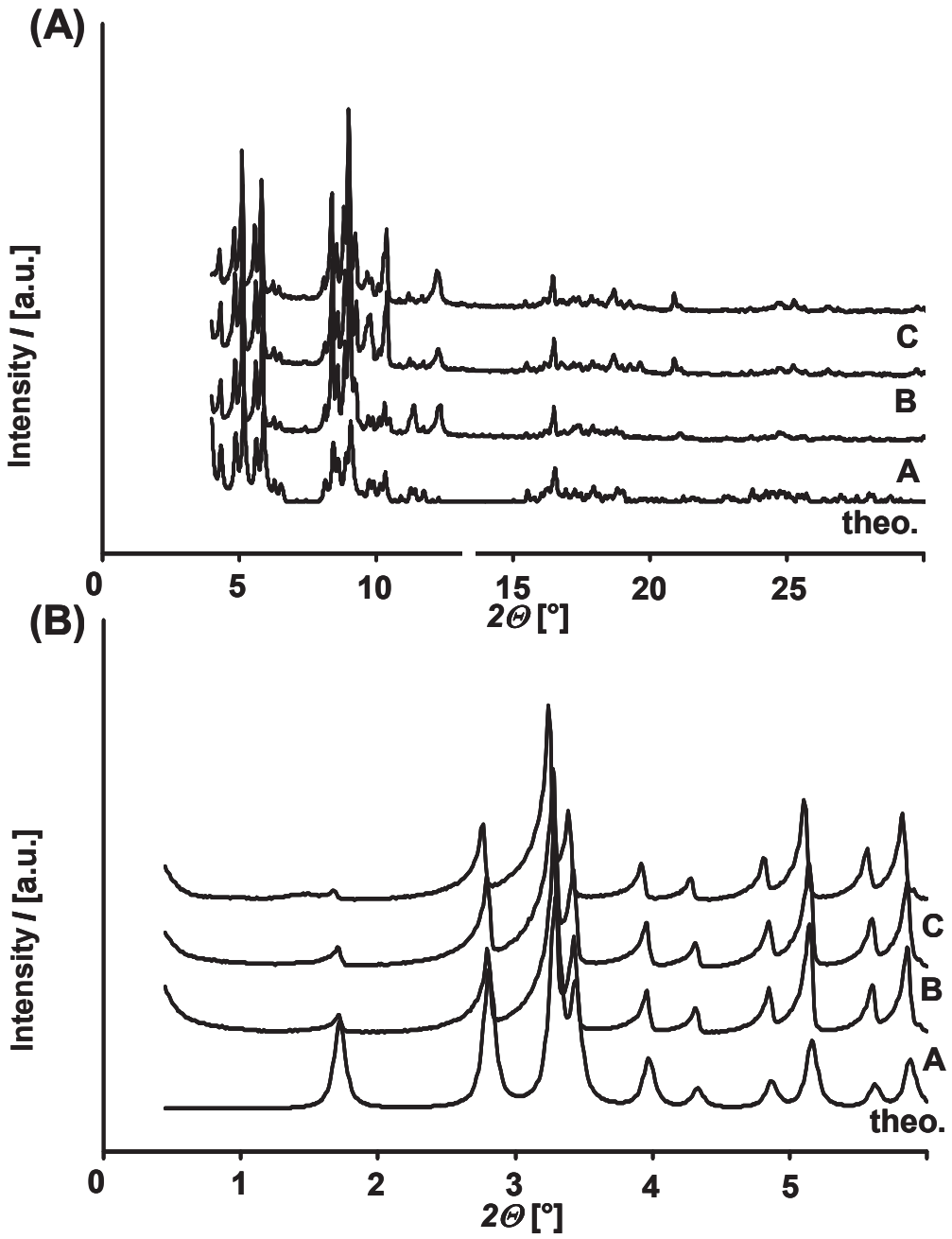

Figure 7. X-ray powder diffraction patterns of non-loaded MIL-101 (A), $FePcF_{16}$@MIL-101 (B) and $RuPcF_{16}$@MIL-101 (C).

III.3.4 Physisorption measurements

Nitrogen and hydrogen physisorption isotherms were measured at –196 °C using a Micromeretics 2020 apparatus. Prior to the measurement, the samples were activated in primary vacuum at 150°C for 24 hours. Specific surface areas were calculated using the BET equation (p/p_o = 0.05-0.2).

X-Ray powder diffraction and N_2 physisorption measurements demonstrate the stability of MIL-101 host materials after the encapsulation process, since similar diffraction patterns and isotherm shapes were obtained (Figure 7 and 8). As expected, the specific surface area and pore volume decrease for complex-containing MOF systems (Table 1).

Pc@MIL-101	MIL-101	N(FePc^{t}Bu$_4$)$_2$@MIL-101	FePcF$_{16}$@MIL-101	RuPcF$_{16}$@MIL-101
S_{BET} [m^2 g^{-1}] [a]	2500	2450	2220	2120
V_P [cm^3 g^{-1}] [b]	1.22	1.16	1.08	1.03
X [%] [c]	0/—	4/—	17/33	34/48
S_{one} [%] [d]	—/—	79/—	80/80	62/74
TON [e]	0/—	5100/—	24 200/48 200	30 900/46 300
Size [nm × nm]	1.47 × 1.6 [f]	≈2.0 × 2.0 [g]	≈1.3 × 1.3 [g]	≈1.3 × 1.3 [g]

Table 1. N_2 physisorption results and catalytic performance of incorporated MPc@MIL-101 after 6 h and 24 h. [a] S_{BET} at p/p_0 = 0.05–0.2. [b] Total volume at p/p_0 = 0.95. [c] Conversion of tetralin. [d] Selectivity toward 1-tetralone. [e] Turnover number after 6 h/24 h. [f] Hexagonal pore window of MIL-101. [g] Sizes of Pc complexes.

For RuPcF$_{16}$@MIL-101, the total pore volume decreases by 16 % with respect to pure MIL-101, which is more than the weight loading of 3.6 wt%. This clearly shows that the complexes are incorporated into the porous structure and thus reduce the pore volume by preventing the N_2 from entering the cavities.

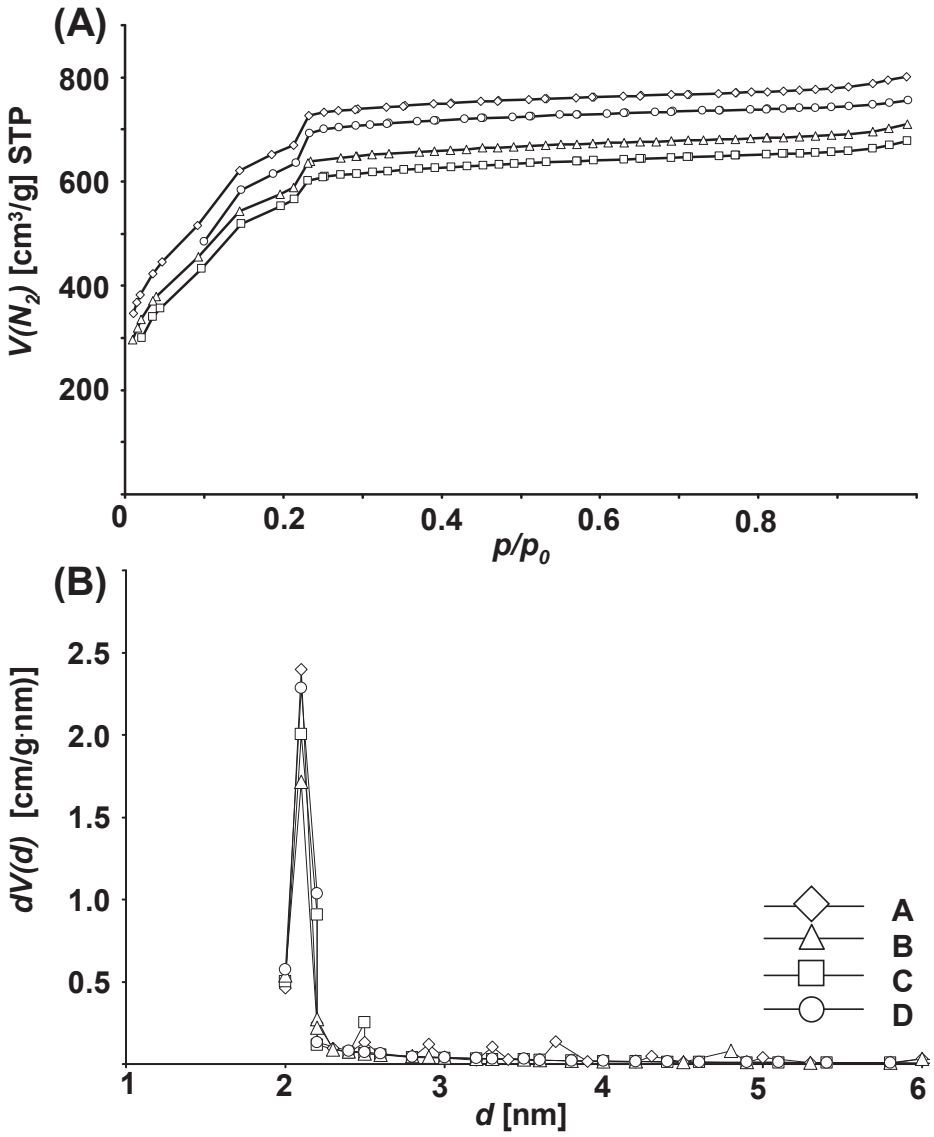

Figure 8. Nitrogen physisorption isotherms patterns of non-loaded MIL-101 (A), $FePcF_{16}$@MIL-101 (B), $RuPcF_{16}$@MIL-101 (C) and $(FePc^tBu_4)_2N$@MIL-101 (D).

Similar decreases in specific surface area and pore volume were also reported for nanoparticle and polyoxometalate functionalized MIL-101 materials.[3, 5] For the bulky $(FePc^tBu_4)_2N$@MIL-101, the total pore volume decreases by only 5%, which corresponds to the weight gain of 5.2 wt% after loading. This indicates that the voluminous $(FePc^tBu_4)_2N$ complex is not incorporated into the mesoporous structure of the MIL-101. Indeed, the dimer (~2.0 × 2.0 nm) is too large to enter the hexagonal pore windows of the MIL-101 (1.47 × 1.6 nm).[2] It would appear that $(FePc^tBu_4)_2N$ complexes are strongly adsorbed at the outer surfaces of the crystallites and/or in macroporous cavities formed by MOF particle agglomeration.

III.3.5 Field Emission Scanning Electron Microscopy

FESEM (Field Emission Scanning Electron Microscopy) and EDS-analysis (Energy Dispersive Spectrometer) on complex containing MIL-101 catalysts were carried out with a Stereoscan 260 SEM with EDX analysis system using SE (Secondary Electrons) and BSE (Backscattered Electrons) detectors, respectively. Elemental analyses using EDX were obtained as a mean value of five measurements in a magnification of 3000.

The homogeneous distribution of different iron and ruthenium complexes inside the MIL-101 support was verified by EDS analysis (Figure 9).

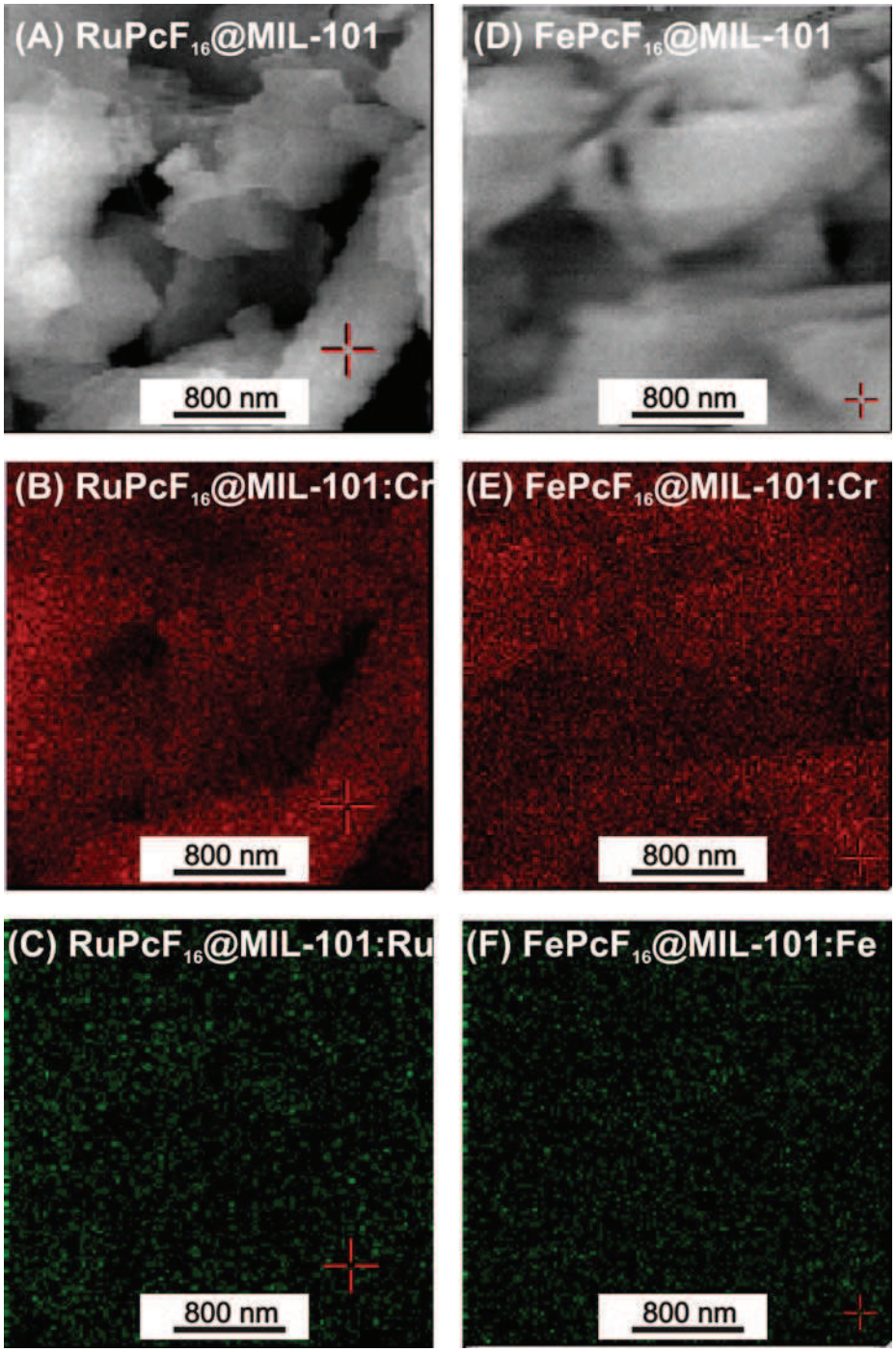

Figure 9. EDS analysis of iron and ruthenium perfluorophthalocyanines containing Cr-MIL-101

III.4 Catalytic results

III.4.1 Catalytic tetralin oxidation

Catalytic tetralin oxidation under static pressure was carried out in parallel reactors with eight pressure stable micro-reaction-vessels (3 ml) inside a temperature-controlled steel vessel. In a typical reaction a mixture of 2.5 ml of tetralin and 1 mg of the pure complexes or

5 mg of the MIL-101 supported complex systems was placed into the batch reactor and heated under continuously stirring at 900 rpm to the desired temperature (50-130 °C) under static oxygen or synthetic air pressure up to 6-10 bar for 1 to 24 h. After cooling down to room temperature, the reaction mixtures were depressurized and centrifuged. The conversion and selectivity of the oxidation reactions were subsequently analyzed by gas chromatography (GC) using a HP-5 capillary column and a flame ionization detector (FID).

A catalytic screening of different unsupported metal phthalocyanine catalysts in aerobic tetralin oxidation (Table 2) has enabled the identification of two different perfluorinated complexes ($MPcF_{16}$, M = Fe, Ru) and the bulky dimer $(FePc^tBu_4)_2N$ which were selected for encapsulation. The activities and selectivities are presented in Table 1. This reaction was performed in parallel batch reactors at 8 bar of O_2 at 90 °C with a substrate-to-MPc molar ratio of 36 000 : 1. The products were analyzed by GC and GC-MS. The TONs of the molecular catalysts follow the order $(FePc^tBu_4)_2N$ > $RuPcF_{16}$ > $FePcF_{16}$. Interestingly, similar selectivities toward 1-tetralone were obtained for the three molecular complexes.

Complex	FePc $(COOH)_4$	FePc $^tBu_4$	$(FePc(^tBu)_4)_2N$	FePc $(SO_3H)_4$	FePc F_{16}	RuPc F_{16}	CoPc $(COOH)_8$
X [%][a]	0	27	25	0	21	38	0
S_{one} [%][b]	-	68	69	-	68	70	-
TON [c]	0	3800	7400	0	3400	5200	0

Table 2. Catalytic activity, selectivity, turnover number after 6 h and sizes of applied phthalocyanine complexes as homogeneous catalysts in tetralin oxidation.[a] Conversion of tetralin, [b] selectivity toward 1-tetralone, [c] turnover number for the tetralin oxidation into 1-tetralol and 1-tetralone after 6 h.

The encapsulated perfluorinated complexes were tested under similar conditions with a tetralin-to-complex molar ratio of 147 000 : 1 for $FePcF_{16}$@MIL-101 and 92 000 : 1 for $RuPcF_{16}$@MIL-101, respectively. It is noteworthy that pure MIL-101 shows no catalytic activity (Table 1). $FePcF_{16}$@MIL-101 and $RuPcF_{16}$@MIL-101 catalysts show very high TONs. The turnover number of $FePcF_{16}$@MIL-101 was 48 200 after 24 h, almost eight times higher than for the homogeneous $FePcF_{16}$ catalyst (TON = 6300).

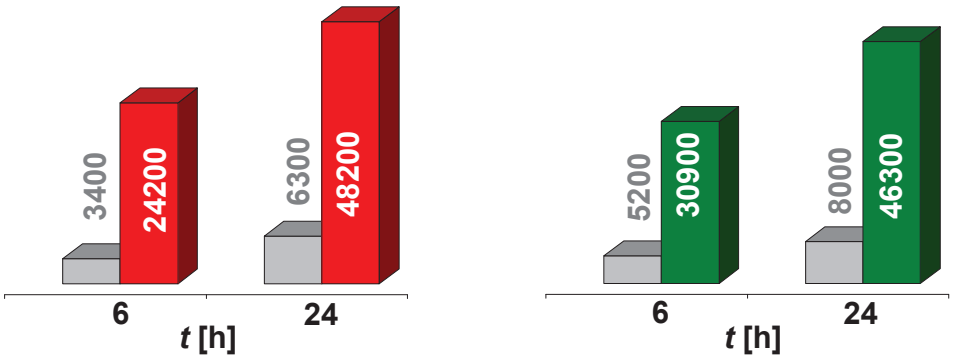

Figure 10. Turnover number (TON) of $FePcF_{16}$@MIL-101 (red) and $RuPcF_{16}$@MIL-101 (green) compared to homogeneous catalyst (grey).

Significantly, the $FePcF_{16}$@MIL-101 catalyst provided a higher selectivity (up to 80 %) toward the desired 1-tetralone compared to the homogeneous $FePcF_{16}$ (68 %) under similar conversion. An analogous rise and change in selectivity was already reported for the hydroperoxide-mediated cyclohexane oxidation of zeolite-supported Ru complexes.[29]

The higher activity for encapsulated complexes has previously been explained by the preclusion of the dimerization process by π-π stacking that is typically observed for homogeneous catalysts.[29] Previously published activities of up to 3000 TON d^{-1} are, however, significantly lower than those determined in the present study. To the best of our knowledge, this is the highest catalytic activity ever reported for homo- and heterogeneous tetralin oxidations. Note that the terminology of TON may be generally misused for metal-initiated free-radical oxidations. It expresses the activity in terms of the product (mol)/catalyst (mol) ratio, which is the indicator commonly used by the community.

In contrast, a limited conversion of up to 4 % was obtained for the $(FePc^tBu_4)_2N$@MIL-101 catalyst. In this case, the synergistic effects arising from the confinement in the pore do not take place. This is consistent with the hypothesis that $(FePc^tBu_4)_2N$ is not encapsulated within the mesoporous structure of the MIL-101. The observed residual conversion (4 %) may arise from the $(FePc^tBu_4)_2N$ complexes that are on or close to the external surface of the MIL crystallites and that are easily accessible for the tetralin.[2, 41] This hypothesis is confirmed by similar TONs obtained for $(FePc^tBu_4)_2N$ (7400) and $(FePc^tBu_4)_2N$@MIL-101 (5100).

Compared to the homogeneous perfluorinated catalysts, an induction period of up to three hours was observed for the encapsulated systems (Fig. 11). A similar phenomenon was

also obtained for Co–MOF catalyzed aerobic cyclohexene (MFU-1) and tetralin oxidations (Co-ZIF-9), respectively.[34, 42]

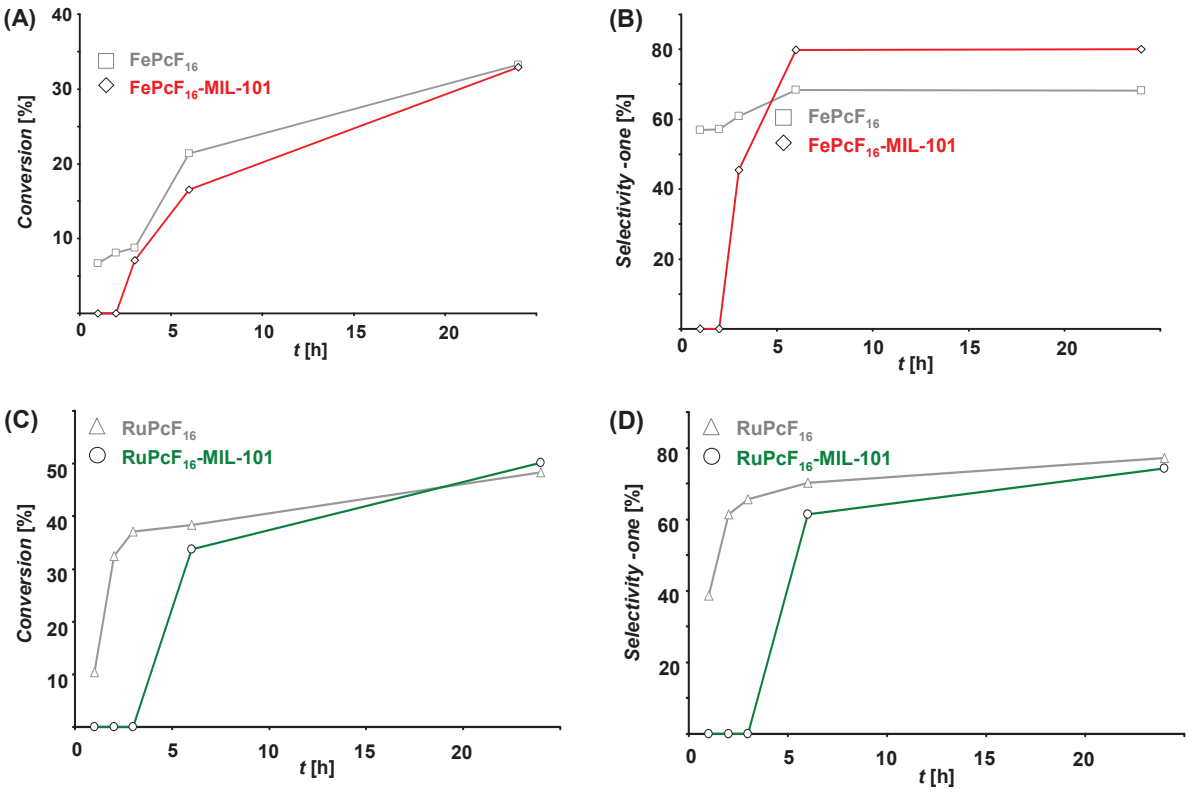

Figure 11. Tetralin conversion (A and C) and selectivity toward 1-tetralone (B and D) of homogeneous $FePcF_{16}$ and $RuPcF_{16}$ complexes (grey) and $FePcF_{16}$@MIL-101 (red) and $RuPcF_{16}$@MIL-101 (green) with significantly lower catalyst contents ($n_{tetralin}$: n_{MPcF16} = 147 000 : 1 (Fe) and 92 000 : 1 (Ru)) compared to the non-incorporated complexes (36 000 : 1) explaining the clear difference in turnover numbers (TONs) after 6 h and 24 h (inset), respectively.

A release of the complexes by progressive degradation of the host structure in the reaction medium could have led to an induction period, as found for drug delivery mechanisms.[43]

No leaching of the complexes was detected by UV-VIS as the reaction proceeded, even is pure phthalocyanine structures are soluble in the reaction medium. This further demonstrates the robustness of the host matrix and the strong adsorption of the complexes into the MOF porous structure.

III.4.2 Oxidation of adamantane-1,3-d_2

In order to gain insight into the mechanism of this oxidation, we studied the kinetic isotope effect (KIE) on the oxidation of adamantane-1,3-d_2 (Figure 12). This substrate is a

useful probe to determine an *intra*-molecular KIE since it contains two equal tertiary C–H and two C–D bonds in the same molecule.[39] It should be noted that the reactivity of adamantane was much lower compared to tetralin. The analysis of the isotopic composition of the adamantanol-1 product directly provides an intrinsic KIE:

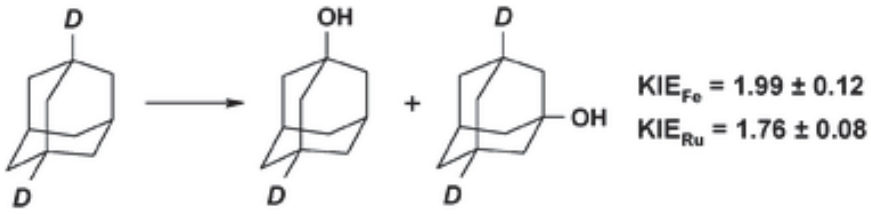

Figure 12. The oxidation of adamantane-1,3-d_2

Adamantane-1,3-d_2 (Ad-d_2) was prepared as previously described[44]. Ad-d_2 (3.4 mg) was dissolved in 2.5 mL of acetonitrile and 5 mg of the $FePcF_{16}$–MIL-101 or $RuPcF_{16}$–MIL-101 materials were added. The resulting mixture was stirred at 90 °C at 8 bars of dioxygen for 6 h in the parallel batch reactors applied for tetralin oxidation. The reaction products were analyzed by GC-MS method (Hewlett Packard 5973/6890 system ; electron impact ionization at 70 eV, He carrier gas, 30 m x 0.25 mm cross-linked 5 % PHME (0.25 µm coating) capillary column, HP-5MS). The exact isotopic composition of 1-adamantanol was calculated by integration of all scans of the 1-adamantanol peak since AdOH-d_1 and AdOH-d_2 were partially separated on the GC column. KIEs were obtained from the intensities of molecular peak at *m/z*=154 (for AdOH-d_2) and m/z=153 (for AdOH-d_1) after correction on natural ^{13}C abundance (1.08 % x 10 carbon atoms = 10.8 %).

The KIE values were determined to be 1.99 ± 0.12 and 1.76 ± 0.08 for $FePcF_{16}$@MIL-101 and $RuPcF_{16}$@MIL-101, respectively. The KIE measured using $FePcF_{16}$ and $RuPcF_{16}$ in homogeneous solutions are similar: 1.94 ± 0.10 and 1.68 ± 0.11, respectively, suggesting that the same mechanism should be operating in homogeneous and heterogeneous systems. These low KIE values indicate the involvement of a radical mechanism in this reaction. The occurrence of an induction period and the detection of a small concentration of tetralin hydroperoxide by GC-MS over the course of tetralin oxidation are also consistent with a free radical mechanism of oxidation, as previously suggested elsewhere.[34]

IV. Conclusions

In summary, this study demonstrates that the encapsulation of MPc in MIL-101 allows an activity enhancement by approximately one order of magnitude. This increase in activity may arise from the dispersion of the molecular complexes as isolated monomers in the nanopore cavities and/or from the confinement effects provided by the host porous structure. In contrast, the $(FePc^tBu_4)_2N$ dimer, which is too large to penetrate into the porous structure, does not show this synergistic effect. Unfortunately the ex-situ impregnation and the non-covalent interaction of the catalyst with the MOF host do not allow the controlled design of enzyme-like environment. The following chapters will focus on the synthesis of stable amino MOF, the isolation of their potentially active site and their post-functionalization to reach this goal.

V. References

[1] S. R. Bajpe, C. E. A. Kirschhock, A. Aerts, E. Breynaert, G. Absillis, T. N. Parac-Vogt, L. Giebeler and J. A. Martens, *Chem.-Eur. J.*, **2010**, **16**, 3926-3932.

[2] G. Ferey, C. Mellot-Draznieks, C. Serre, F. Millange, J. Dutour, S. Surble and I. Margiolaki, *Science*, **2005**, **309**, 2040-2042.

[3] J. Juan-Alcaniz, E. V. Ramos-Fernandez, U. Lafont, J. Gascon and F. Kapteijn, *Journal of Catalysis*, **2010**, **269**, 229-241.

[4] N. V. Maksimchuk, K. A. Kovalenko, S. S. Arzumanov, Y. A. Chesalov, M. S. Melgunov, A. G. Stepanov, V. P. Fedin and O. A. Kholdeeva, *Inorg. Chem.*, **2010**, **49**, 2920-2930.

[5] A. Henschel, K. Gedrich, R. Kraehnert and S. Kaskel, *Chem.Commun.*, **2008**, 4192-4194.

[6] S. Hermes, M. K. Schroter, R. Schmid, L. Khodeir, M. Muhler, A. Tissler, R. W. Fischer and R. A. Fischer, *Angew. Chem.-Int. Edit.*, **2005**, **44**, 6237-6241.

[7] M. Sabo, A. Henschel, H. Froede, E. Klemm and S. Kaskel, *J. Mater. Chem.*, **2007**, **17**, 3827-3832.

[8] M. H. Alkordi, Y. L. Liu, R. W. Larsen, J. F. Eubank and M. Eddaoudi, *J. Am. Chem. Soc.*, **2008**, **130**, 12639-+.

[9] S. Horike, S. Shimomura and S. Kitagawa, *Nat Chem*, **2009**, **1**, 695-704.

[10] R. Makiura, S. Motoyama, Y. Umemura, H. Yamanaka, O. Sakata and H. Kitagawa, *Nat. Mater.*, **2010**, **9**, 565-571.

[11] S. Hermes, F. Schroder, S. Amirjalayer, R. Schmid and R. A. Fischer, *J. Mater. Chem.*, **2006**, **16**, 2464-2472.

[12] F. Schroeder, D. Esken, M. Cokoja, M. W. E. van den Berg, O. I. Lebedev, G. van Tendeloo, B. Walaszek, G. Buntkowsky, H. H. Limbach, B. Chaudret and R. A. Fischer, *J. Am. Chem. Soc.*, **2008**, **130**, 6119-6130.

[13] M. Muller, O. I. Lebedev and R. A. Fischer, *J. Mater. Chem.*, **2008**, **18**, 5274-5281.

[14] T. Ishida, M. Nagaoka, T. Akita and M. Haruta, *Chem.-Eur. J.*, **2008**, **14**, 8456-8460.

[15] B. Yuan, Y. Pan, Y. Li, B. Yin and H. Jiang, *Angewandte Chemie International Edition*, **2010**, **49**, 4054-4058.

[16] I. V. Kozhevnikov, *Chemical Reviews*, **1998**, **98**, 171-198.

[17] L. Yang, H. Naruke and T. Yamase, *Inorganic Chemistry Communications*, **2003**, **6**, 1020-1024.
[18] C. Y. Sun, S. X. Liu, D. D. Liang, K. Z. Shao, Y. H. Ren and Z. M. Su, *J. Am. Chem. Soc.*, **2009**, **131**, 1883-1888.
[19] H. K. S.-p. r. D. Y. K. J. Y. M. A. J. O. k. M. O. M. Chae, *Nature*, **2004**, **427**, 523-527.
[20] M. Muller, A. Devaux, C.-H. Yang, L. De Cola and R. A. Fischer, *Photochemical & Photobiological Sciences*, **2010**, **9**.
[21] H. Kim, H. Chun, G.-H. Kim, H.-S. Lee and K. Kim, *Chemical Communications*, **2006**.
[22] I. M. Geraskin, M. W. Luedtke, H. M. Neu, V. N. Nemykin and V. V. Zhdankin, *Tetrahedron Lett.*, **2008**, **49**, 7410-7412.
[23] A. B. Sorokin and E. V. Kudrik, *Catal. Today*, **2010**, doi:10.1016/j.cattod.2010.1006.1020.
[24] U. Isci, P. Afanasiev, J. M. M. Millet, E. V. Kudrik, V. Ahsen and A. B. Sorokin, *Dalton Trans.*, **2009**, 7410-7420.
[25] E. V. Kudrik and A. B. Sorokin, *Chem.-Eur. J.*, **2008**, **14**, 7123-7126.
[26] A. B. Sorokin, E. V. Kudrik and D. Bouchu, *Chem. Commun.*, **2008**, 2562-2564.
[27] P. Afanasiev, D. Bouchu, E. V. Kudrik, J.-M. M. Millet and A. B. Sorokin, *Dalton Trans.*, **2009**.
[28] P. E. Ellis and J. E. Lyons, *J. Chem. Soc.-Chem. Commun.*, **1989**, 1315-1316.
[29] K. J. Balkus, M. Eissa and R. Levado, *J. Am. Chem. Soc.*, **1995**, **117**, 10753-10754.
[30] K. J. Balkus, Jr., A. G. Gabrielov, S. L. Bell, F. Bedioui, L. Roue and J. Devynck, *Inorg. Chem.*, **1994**, **33**, 67-72.
[31] A. B. Sorokin, S. Mangematin and C. Pergrale, *J. Mol. Catal. A: Chem.*, **2002**, **182-183**, 267-281.
[32] A. B. Sorokin and A. Tuel, *Catal. Today*, **2000**, **57**, 45-59.
[33] J. M. Thomas, R. Raja, G. Sankar and R. G. Bell, *Nature*, **1999**, **398**, 227-230.
[34] F. X. Llabres i Xamena, O. Casanova, R. Galiasso Tailleur, H. Garcia and A. Corma, *J. Catal.*, **2008**, **255**, 220-227.
[35] A. Sorokin, A. Robert and B. Meunier, *J. Am. Chem. Soc.*, **1993**, **115**, 7293-7299.
[36] J. Metz, O. Schneider and M. Hanack, *Inorg. Chem.*, **1984**, **23**, 1065-1071.
[37] J. H. Weber and D. H. Busch, *Inorg. Chem.*, **1965**, **4**, 469-&.
[38] J. G. Jones and M. V. Twigg, *Inorg. Chem.*, **1969**, **8**, 2018-&.
[39] S. A. Mikhalenko, L. I. Solov'eva and E. A. Luk'yanets, *Russ. J. Gen. Chem.*, **2004**, **74**, 451-459.
[40] J. Kim, S. Bhattacharjee, K. E. Jeong, S. Y. Jeong and W. S. Ahn, *Chem. Commun.*, **2009**, 3904-3906.
[41] S. B. Lei, C. Wang, S. X. Yin, H. N. Wang, F. Xi, H. W. Liu, B. Xu, L. J. Wan and C. L. Bai, *J. Phys. Chem. B*, **2001**, **105**, 10838-10841.
[42] M. Tonigold, Y. Lu, B. Bredenkotter, B. Rieger, S. Bahnmuller, J. Hitzbleck, G. Langstein and D. Volkmer, *Angew. Chem. Int. Ed.*, **2009**, **48**, 7546-7550.
[43] P. Horcajada, C. Serre, G. Maurin, N. A. Ramsahye, F. Balas, M. Vallet-Regi, M. Sebban, F. Taulelle and G. Ferey, *J. Am. Chem. Soc.*, **2008**, **130**, 6774-6780.
[44] J. G. Jones and M. V. Twigg, *Inorg. Chem.*, **1969**, **8**, 2018-&.

Chapter 3

Synthesis and characterization of Amino functionalized Metal-organic frameworks; Starting host for Post synthetic functionalization and acid catalyst.

I. Introduction

MOF with amino group on their linkers are very convenient starting material for post-synthetic treatment. Once synthesized a MOF without functional groups, the corresponding amino-modified one could generally be simply obtain by replacing the precursor of the linker by its equivalent bearing the amino functionality and using the same conditions of synthesis. Furthermore a wide library of reactions can be apply on amino groups such as condensation of acyl chloride, anhydric acid, isocyanate, transformation into azide, etc. In this work we focused on the two structures discovered by the Lavoisier Institute in Versailles, the MIL-53 and MIL-68. This Chapter reports the synthesis, the structure and the characterization (PXRD analyses, BET measurements, liquid state NMR of digested solids, TGA and SEM) of four different amino-MOFs: MIL-53(Al)-NH_2 and MIL-68(In)-NH_2 which will be used in the following study as "starting materials" and MIL-53(Ga)-NH_2 and MIL-68(Ga)-NH_2, the amino substituted analogue of the MIL-53(Ga)[1, 2] and MIL-68(Ga)[3]. In matter to understand the influence of the amino group on the acid/base properties of the MOFs, MIL(In)-68 and MIL(In)-68-NH_2 have been test in the synthesis of styrene carbonate from styrene oxide and carbon dioxide and Density Functional Theory (DFT) calculations have been performed.

II. MIL-53(Al)-NH_2

II.1. Synthesis

MIL-53(Al)-NH_2 was prepared and purified using a modified synthesis protocol based on Stock et al[4]. Briefly, solutions containing 1.931 g (8 mmol) of aluminum chloride hexahydrate (Sigma-Aldrich), 8 mmol of 2-aminobenzene-1,4-dicarboxylate (abdc) (Sigma-Aldrich) and 30 mL deionized H_2O were introduced into a 48- mL Teflon-lined autoclave and subjected to solvothermal synthesis at 150°C for 9 h. After the synthesis, product was separated from water by centrifugation at 4000 rpm for 5 min. To remove any excess linker trapped within the porous network, the as-synthesized product was placed in an autoclave with 30 mL anhydrous N,N-dimethylformamide (DMF) and heated at 150°C for 24 h.[5] The solvent was then substituted by fresh DMF and the solvothermal treatment was repeated twice. Afterwards, the DMF-containing solid was submitted to dichloromethane (DCM) Soxhlet-extraction for 20 h to remove DMF. Finally, the solids were dried at 100°C for 9 h under reduced pressure to obtain MIL-53(Al)-NH_2 as a yellow powder.

II.2. Structure description

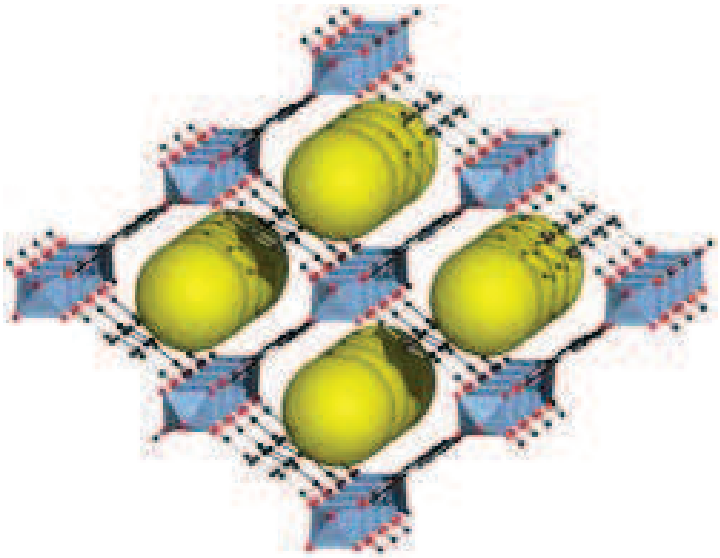

Figure 1. MIL-53 structure (Carbon atom: black, oxygen: red, metal coordination sphere: blue, 1D channels are represented by a queue of yellow balls)

The MIL-53(Al)-NH_2 framework is built up from chains of corner-sharing Al(III) octahedral connected by μ_2-OH and carboxylate groups. These chains are connected by 2-aminoterephthalate ions to form a 1D rhombohedral-shape channel system (Figure 1). The combination of these chains allows the formation of three different 3D frameworks. In parent MIL-53 as synthesized (as) structure, the channels (7.3 Å x 7.7 Å) are occupied by disordered benzene-1,4-dicarboxylate (bdc) template molecules. The total removal of the template upon heating at 275°C generates the MIL-53 high temperature form (ht) showing empty pores of 8.5 Å x 8.5 Å. The reversible adsorption of water at room temperature gives rise to MIL-53low temperature (lt) with channel dimensions of 2.6 Å x 13.6 Å. Here, the MIL-53(Al)-NH_2 framework having the lt form is obtained after synthesis and purification.

II.3. Characterization MIL-53(Al)-NH_2

II.3.1. Powder X-ray Diffraction (PXRD)

The MIL-53(Al)-NH_2 sample was studied by PXRD at room temperature in order to confirm its structure.

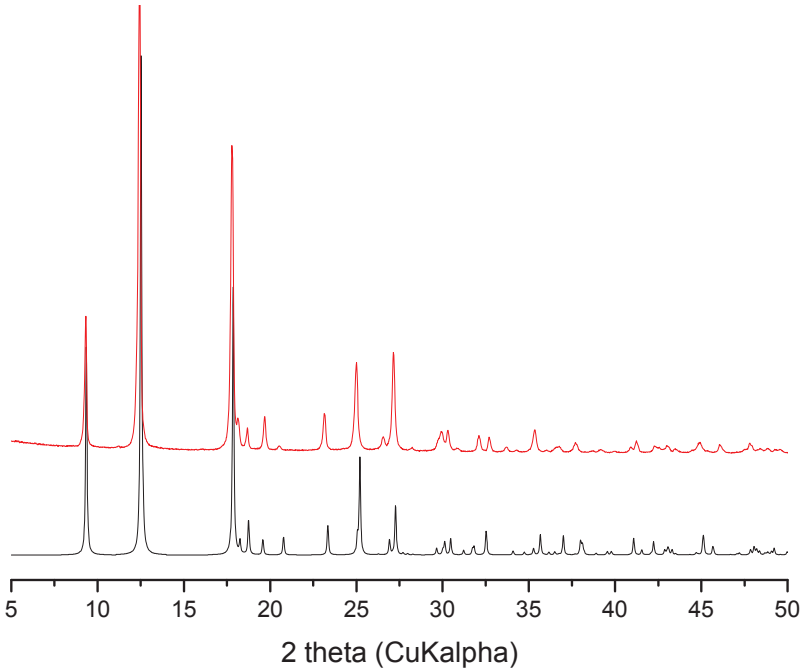

Figure 2. Powder X-ray diffraction patterns of simulated MIL-53(lt) (black-bottom) and experimental MIL-53(Al)-NH_2 (red, top)

Experimental PXRD patterns match with the simulated pattern obtained from Crystallographic Information File (CIF)[6, 7] (Figure 2 and Table 1).

Table 1. Cell parameters of MIL-53(Al)

Sample	*a*/Å	*b*/Å	*c*/Å	*β*/°	*V*/Å^3
MIL-53(as)[7]	17.129(2)	6.628(1)	12.182(1)		1383.0(2)
MIL-53(lt)[7]	19.513(2)	7.612(1)	6.576(1)	104.24(1)	946.5(2)
MIL-53-NH_2(as)[4]	16.898(20)	12.539(18)	6.647(8)	-	1408.4(4)
MIL-53-NH_2(DMF)[4]	17.578(17)	11.483(9)	6.630(6)	-	1338.9(25)
MIL-53-NH_2(lt)[4]	19.722(7)	7.692(3)	6.578(4)	105.1(3)	961.5(10)

II.3.2. Nitrogen physisorption

The porosity of MIL-53(Al) and MIL-53(Al)-NH_2 sample have been studied by N_2 adsorption at 77K.

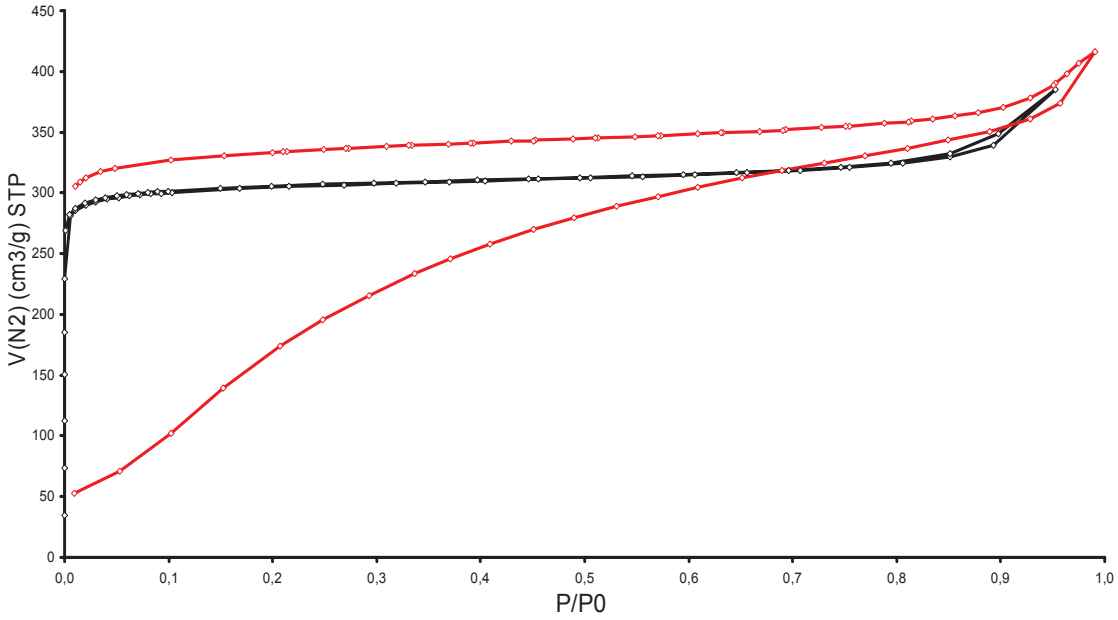

Figure 3. Nitrogen isotherms of MIL-53(Al) (black line) and MIL-53(Al)-NH_2 (red line)

MIL-53(Al) isotherm presents a typical isotherm of type I with identical adsorption and desorption branch. In the other hand, MIL-53(Al)-NH_2 isotherm shows an important hysteresis. The same isotherm shape was obtained in a previous work by Stock et al[4]. This behaviour reflects the flexibility of the framework (transition narrow pore-large pore) which happens at higher pressure for the MIL-53(Al)-NH_2. The measured BET surface area and the microporous volume (calculated from the desorption branch) are 940m2/g and 0.37cm3/g, respectively. These values are comparable to the one obtain on MIL-53(Al)

II.3.3. Thermogravimetric Analysis (TGA)

The thermal stability of MIL-53(Al)-NH_2 sample has been determined by TGA under synthetic air.

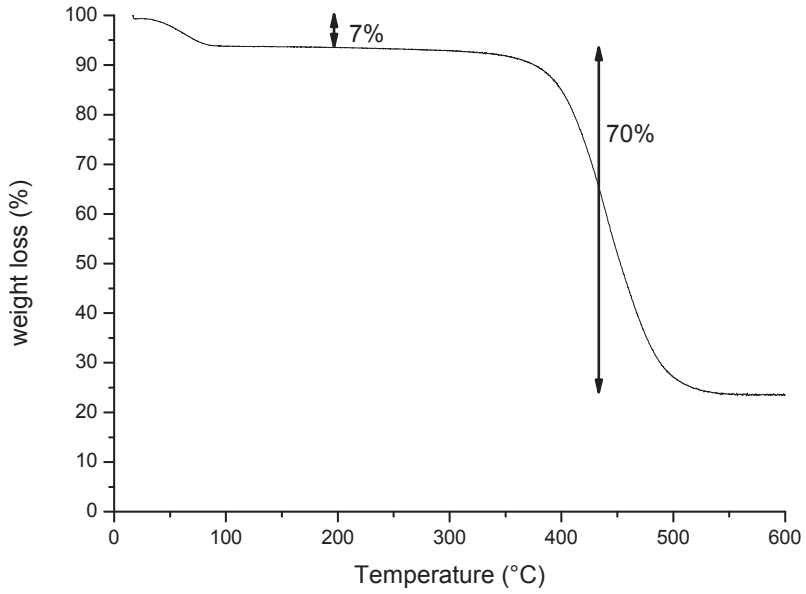

Figure 4. TGA of the MIL-53(Al)-NH_2

Two-step weight loss is observed. The first step (7% weight loss at 50°C) corresponds to the release of the water from the pore. The second weight loss (70% weight loss at 400°C) is due to the decomposition of the 2-amino terephthalic acid and the formation of alumina. The calculated formula is Al(OH)(abdc).1,1H_2O

II.3.4. ^{1}H liquid Nuclear Magnetic Resonance (^{1}H NMR)

^{1}H-NMR spectra were recorded using an automated procedure for routine analysis. The spectra were calibrated using the deuterium signals of DMSO. Amino-MOF samples are commonly digested and dissolved in HF/DMSO-d_6 solution. Although ^{1}H liquid NMR doesn't provide any structural data (spatial arrangement, function distribution, interactions...), this method can give useful chemical information (detection of some impurities or remaining solvents). Thus, all ^{1}H NMR spectra of the MOFs based on 2-amino-terepththalate present almost the same resonance signals corresponding to the aromatic protons of free 2-aminoterephathalic acid in NMR tube solution. The non aromatic part of the spectrum show a wide signal around 3-5.5ppm corresponding of the water of the HF solution and the sharp peak of the DMSO at 2.5ppm. In order to focus on the relevant information, spectrum will mainly be set on the aromatic part (9.2-6.8ppm).

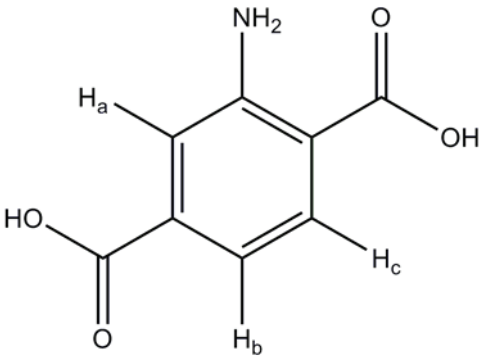

Figure 5. Scheme. Aromatic protons of abdc

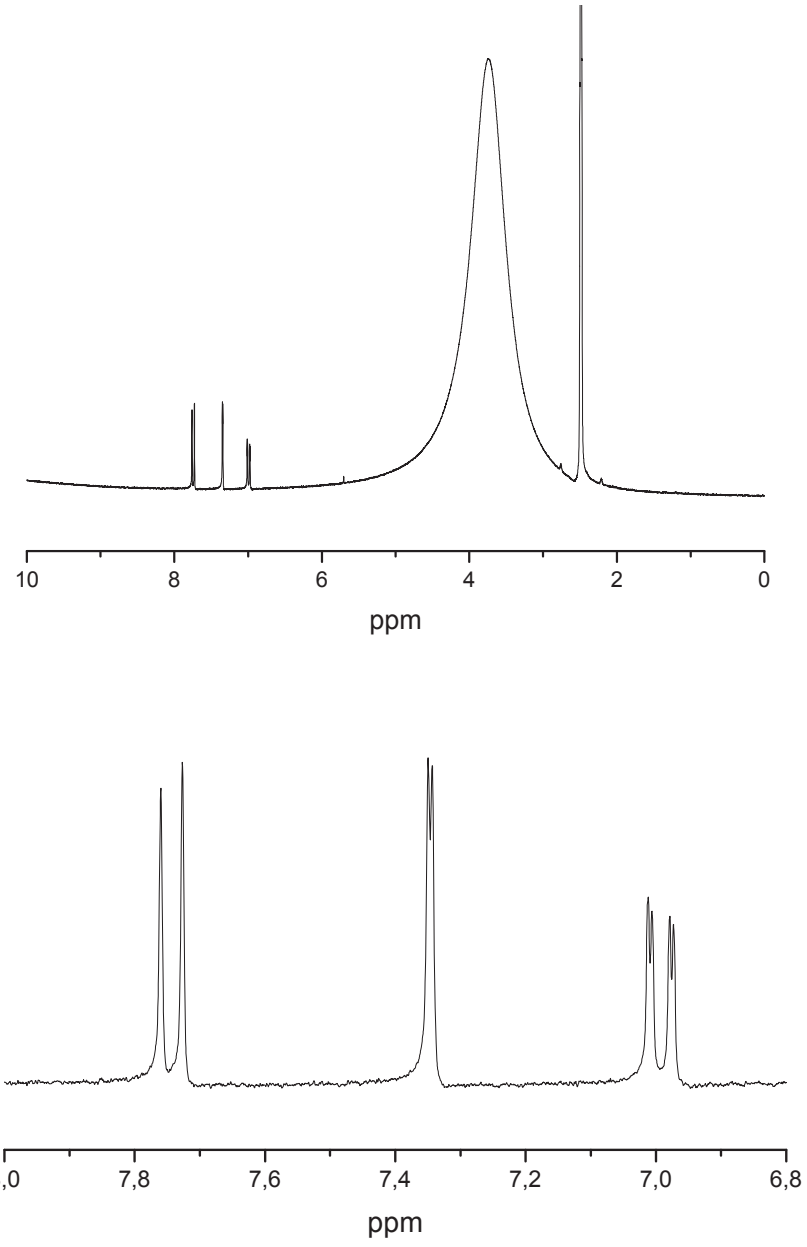

Figure 6. ^{1}H NMR spectrum of MIL-53(Al)-NH_2 after digestion (full and magnify on the aromatic domain)

^{1}H NMR spectra of MIL-53(Al)-NH_2 presents two doublets (7ppm-Hb and 7.75ppm-Hc) and a singlet (7.35ppm-Ha) which correspond to the three aromatic protons of 2-amino terephthalic acid.

II.3.5. Solid state ^{13}C NMR spectroscopy

In order to keep the structure intact, MIL-53(Al)-NH_2 sample has been studied by solid state NMR spectroscopy

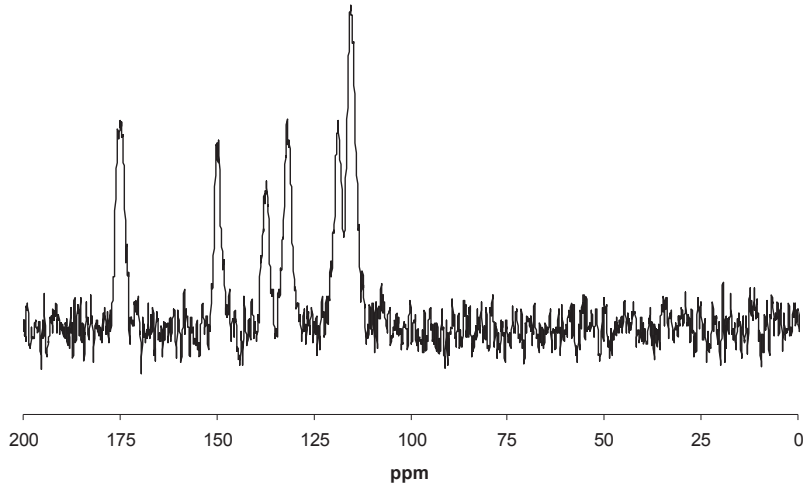

Figure 7. ^{13}C MAS NMR spectrum of MIL-53(Al)-NH_2

The ^{13}C spectrum of the MIL-53(Al)-NH_2 exhibits five broad signals between 149,5 and 115,4 ppm due to the C atoms of the phenyl ring and one signal at 174,9 ppm which match with the carboxylate groups. No signals attribuable to DMF molecules are observed and the whole spectrum is consistent with the MIL-53(Al)-NH_2 lt one described in the literature[4].

II.3.6. Diffuse reflectance infrared fourier transform (DRIFT) spectroscopy

DRIFT spectroscopy is an efficient method to check if no free linker remained in the activated MIL-53(Al)-NH_2. Furthermore it is a powerful method to follow the transformation of the amino group by post-functionalization (cf. Chapter 5). Indeed the bands at 3500 and 3390 cm^{-1} correspond to the symmetric and asymmetric stretching of the primary amine. The doublet at 3660 and 3700 cm^{-1} is due to the bridging OH in the chains of trans corner-sharing $AlO_4(OH)_2$

octahedra[8]. The broad signals between 3100 and 2500cm^{-1} are due to the hydroxyl group in the presence of NH_2 group. Large signals between 1600 and 1300cm^{-1} are carboxylic acid function. The C=O band of free acid and DMF are not observed[4].

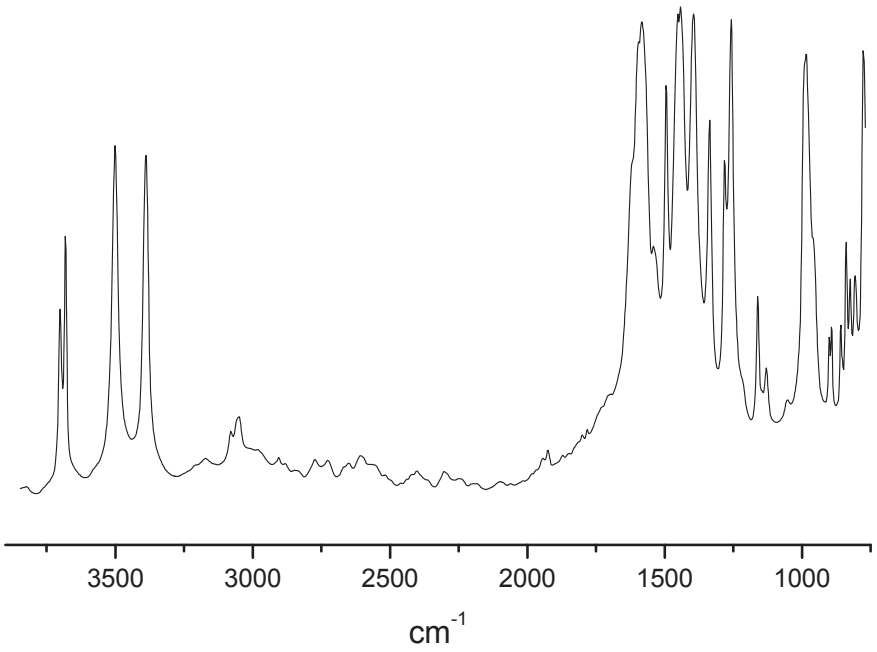

Figure 8. DRIFT spectra of MIL-53(Al)-NH_2

II.3.7. Scanning Electron Microscopy (SEM)

In order to determine the crystallites shape and size, SEM was performed on MIL-53(Al)-NH_2 sample.

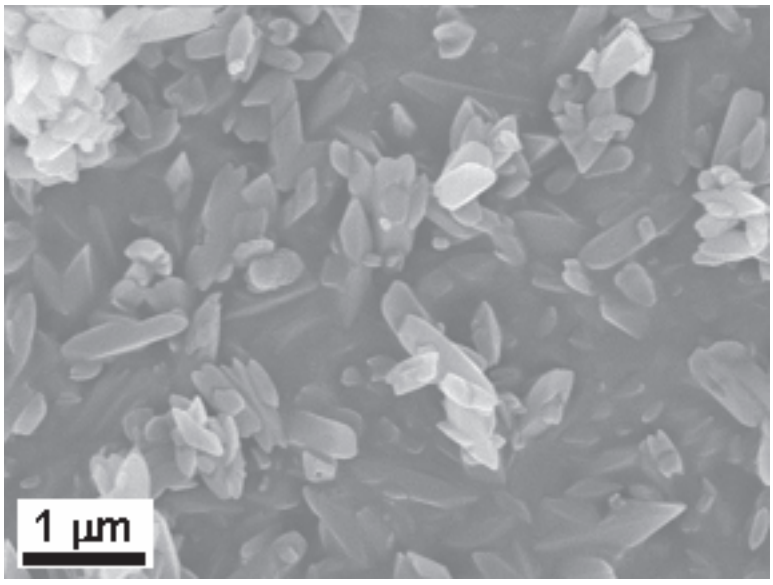

Figure 9. SEM image of the MIL-53(Al)-NH_2

As shown on the SEM picture, MIL-53(Al)-NH_2 powder is constituted of elongated crystal with size between 0.55 and 1.23µm.

III. MIL-53(Ga)-NH_2

III.1. Synthesis

MIL-53(Ga)-NH_2 could be obtained by a solvothermal method analogous to the one described by Stock et al[4] or by a precipitation method. Solutions containing 2.046 g (8 mmol) of Gallium nitrate hydrate (Sigma-Aldrich), 8 mmol of 2-aminobenzene-1,4-dicarboxylate (Sigma-Aldrich) and 30 mL deionized H_2O were introduced into a 48- mL Teflon-lined autoclave and subjected to solvothermal synthesis at 110°C for 48h. In the precipitation procedure, Gallium nitrate and 2-aminoterephthalic acid were solvated in water. The reaction mixtures were stirred for 5 minutes, and then a solution of triethylamine (Et_3N, 2 equivalents, Sigma-Aldrich) in water was added. After stirring for 120 minutes at room temperature, the resulting precipitates were filtered, washed intensively with water and dried. Products of the both two methods were purified by three DMF extractions and a DCM soxhlet.

III.2. Characterization MIL-53(Ga)-NH_2

III.2.1. PXRD

PXRD analysis show that the activated MIL-53(Ga)-NH_2 has high crystallinity and presents at room temperature the MIL-53(lt) configuration.

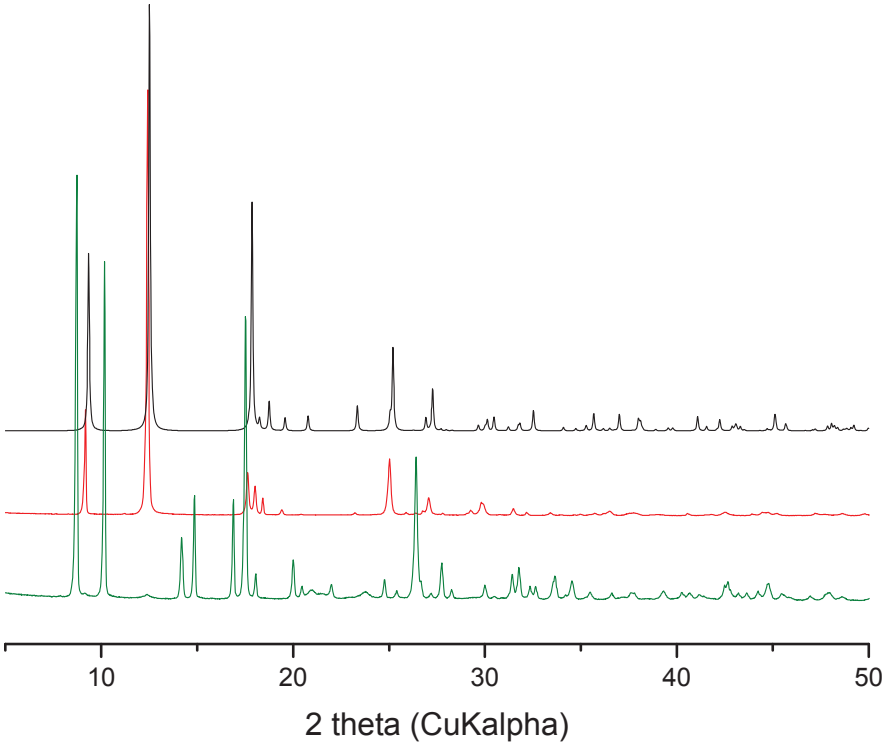

Figure 10. Powder X-ray diffraction patterns of MIL-53(Ga)-NH_2 as synthesized (as) (green-bottom), simulated MIL-53(lt) (red-middle) and activated MIL-53(Ga)-NH_2 (black, top)

Rietveld refinement was performed by using as starting model the MIL-53(Ga) lt described by Volkringer *et al* [2].

Table 2. Cell parameters of MIL-53(Ga)-NH_2

Sample	*a*/Å	*b*/Å	*c*/Å	*β*/°	*V*/Å^3	Rwp
MIL-53(Ga)-NH_2	19.983	7.332	6.708	105.11	949	19.9

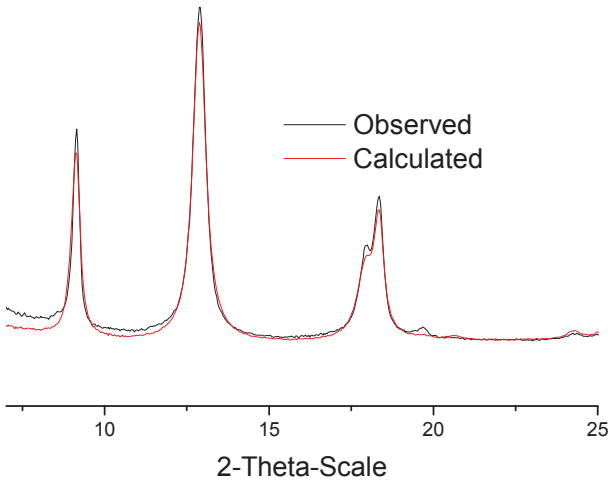

Figure 11. Rietveld refinement (Indexation in a monoclinic lattrice (C2/c space group) at 373K)

III.2.2. Nitrogen physisorption

The porosity of MIL-53(Ga)-NH_2 sample have been studied by N_2 (77K) and CO_2 (303K).

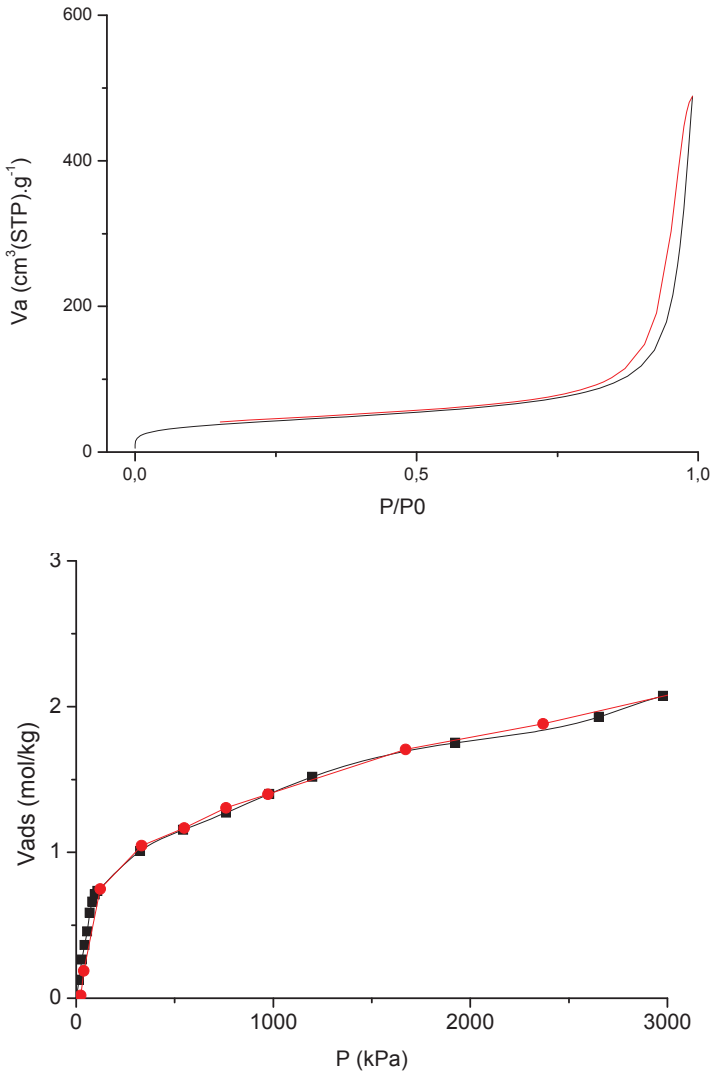

Figure 12. Adsorption of nitrogen at 77K (top) and CO_2 at 303K (bottom).

Isotherms do not present the hysteresis observed in MIL-53(Al)-NH_2 isotherm. This behaviour reflects the rigidity of the structure which stay in it narrow pore configuration. Furthermore the adsorption capacities are very low compare to it aluminium analogue.

III.2.3. TGA

For the as synthesis MOF, three-step weight loss is observed. The first step (300°C) corresponds to the release of the free abdc from the pore (16% weight loss). The second weight loss (380°C) is due to the collapsing of the framework and the formation of Gallium oxide

(Ga_2O_3). It may remain carbon with the oxide because a third weight loss happened at 650°C. At this point the solid is completely oxidized and only Gallium oxide remained (58% weight loss between 380 and 800°C).

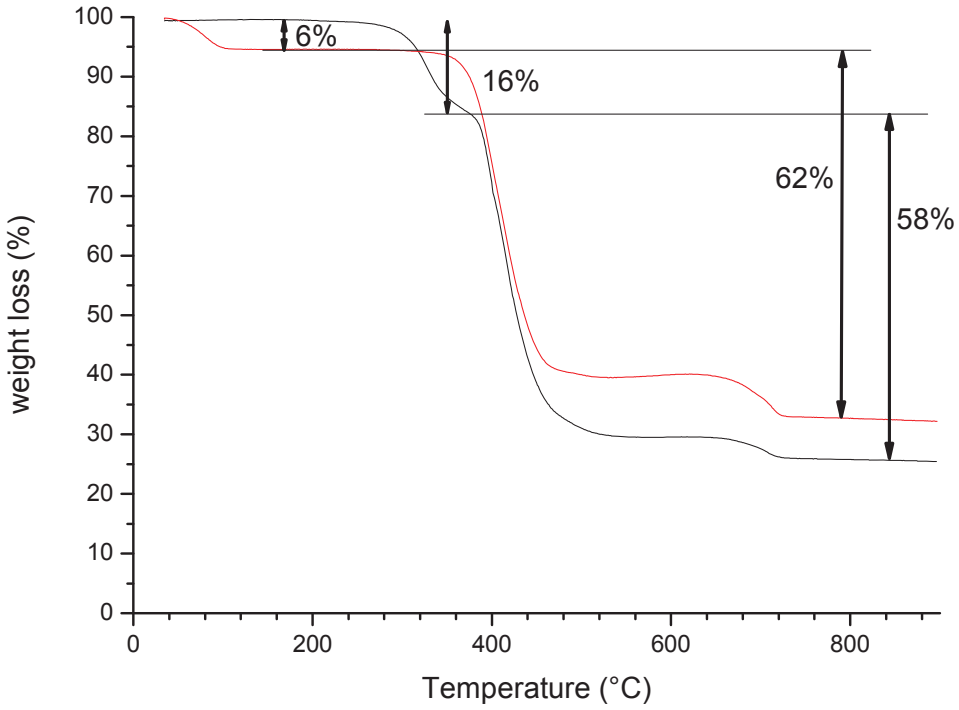

Figure 13. TGA of the MIL-53(Ga)-NH_2 as (black line) and MIL-53(Ga)-NH_2 (red line)

The activated MIL-53(Ga)-NH_2 has been emptied of unreacted abdc and have adsorbed atmospheric water. Water molecules leave the structure at (6% weight loss at 50°C). Second and third weight loss are similar to the MIL-53(Ga)-NH_2 as (62%).

The calculated formula obtained are $Ga(OH)(abdc)_{0.97}$-0.24abdc for the MIL-53(Ga)-NH_2 as and $Ga(OH)(abdc)_{0.70}$-0.78H_2O for MIL-53(Ga)-NH_2.

III.2.4. ^{1}H liquid NMR

^{1}H NMR spectra of the digested sample only show the aromatic protons of the abdc.

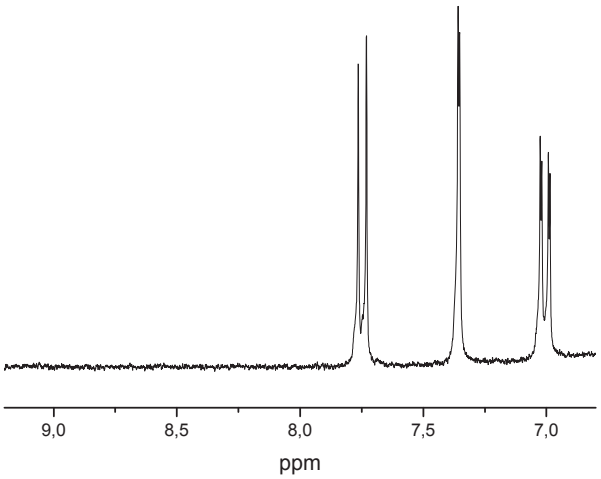

Figure 14. ^{1}H NMR spectra of MIL-53(Ga)-NH_2

III.2.5. DRIFT spectroscopy

DRIFT spectroscopy of MIL-53(Ga)-NH_2 shows the same primary amine (symmetric and asymmetric stretching at 3500 and 3380cm^{-1}), bridging hydroxyl (3660 with shoulder at 3640 cm^{-1}) and carboxylic signals than MIL-53(Al)-NH_2.

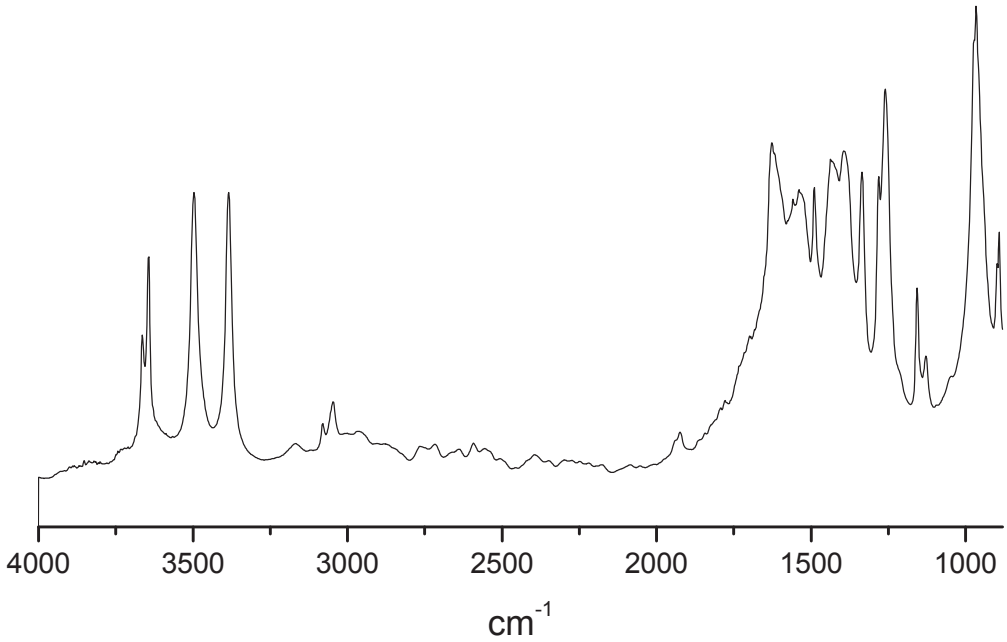

Figure 15. DRIFT spectra of MIL-53(Ga)-NH_2

III.2.6 SEM

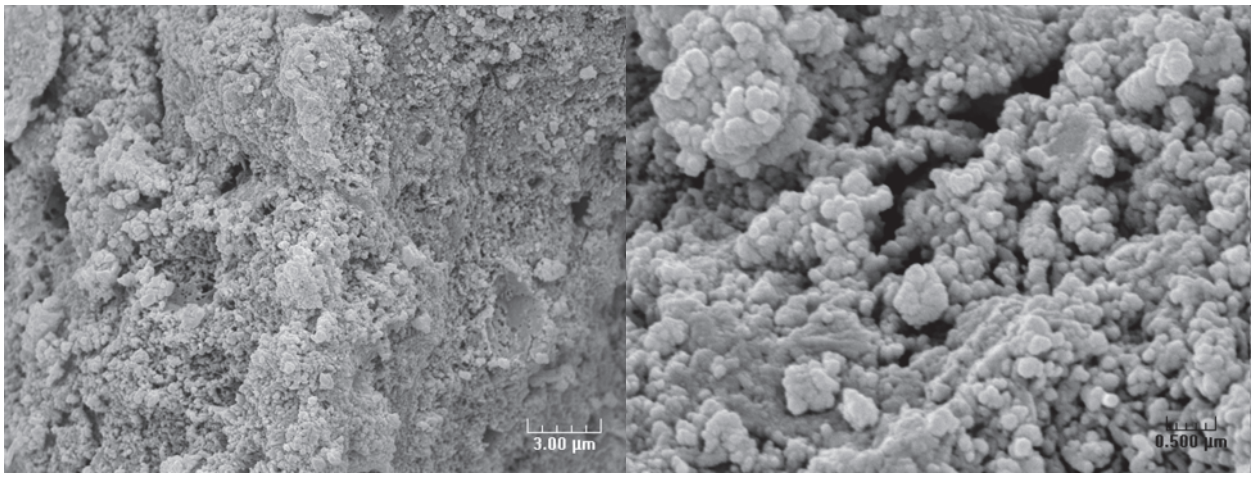

Figure 16. SEM image of the MIL-53(Ga)-NH_2

As shown on the SEM picture, MIL-53(Ga)-NH_2 powder is constituted of aggregate of particle with size below 0.25µm.

IV. MIL-68(In)-NH_2

IV.1. Synthesis

MIL-68(In)-NH_2 was obtained by precipitation[9] in a Pyrex beaker (capacity 100 mL) starting from a mixture of 4.82 mL (4.14 mmol) of 0.86 M indium nitrate in anhydrous N,N-dimethylformamide (DMF) and 10.06 mL (3.32 mmol) of 0.33 M 2-aminoterephthalic acid in DMF. The reaction mixture was stirred for 5 minutes, then 4.83 mL (6.67 mmol) of 1.38 M 4-diazabicyclo[2.2.2] octane (DABCO) in DMF were added. The reaction mixtures were stirred for 120 minutes at room temperature. The precipitates obtained were washed with DMF at 160°C followed by a dichloromethane Soxhlet extraction for 24 h in order to remove remaining free acid. The resulting mass of dried MIL-68(In)-NH_2 was 880 mg.

IV.2 Structure description

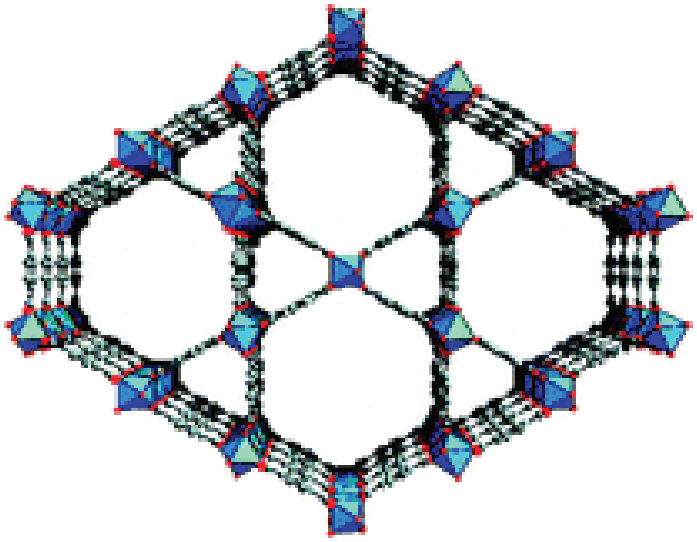

Figure 17. Structure of the MIL-68

MIL-68(In) and MIL-68(In)-NH_2 frameworks (orthorhombic system) are built up from infinite straight chains of metal-centered $InO_4(OH)_2$ octahedra connected to each other through the bdc/abdc ligands, generating 1D channels. The octahedral units are linked together via two hydroxyl groups located in *trans* positions, two adjacent octahedra also being connected via the carboxylate functions. These corner-sharing octahedral species MO_6 form a network of three- and six-membered windows, generating two types of channels with diameter openings of 6 and 17 Å, for the triangular and hexagonal rings[3], respectively.

IV.3. Characterization MIL-68(In)-NH_2

IV.3.1. PXRD

The X-ray diffraction patterns of MIL-68(In)-NH_2 correspond to a structure discovered by Ferey *et al*[3] (figure 18).

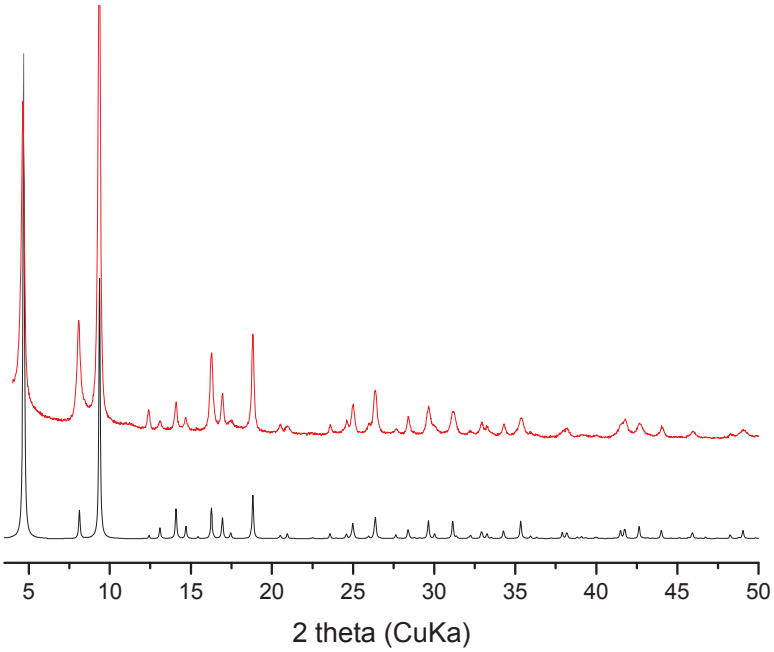

Figure 18. Powder X-ray diffraction patterns of simulated MIL-68(In) (black-bottom), and experimental MIL-68(In)-NH_2 (red, top)

IV.3.2. Nitrogen physisorption

Nitrogen isotherm of MIL-68(In)-NH_2 shows a type II trend. Brunauer-Emmett-Teller (BET) surface area of MIL-68(In)-NH_2 is 1120 $m^2.g^{-1}$. It is higher than the value report by Volkringer et al[3]. It should be notice that equilibrium time was extended compare to routine method to realized theses measurements.

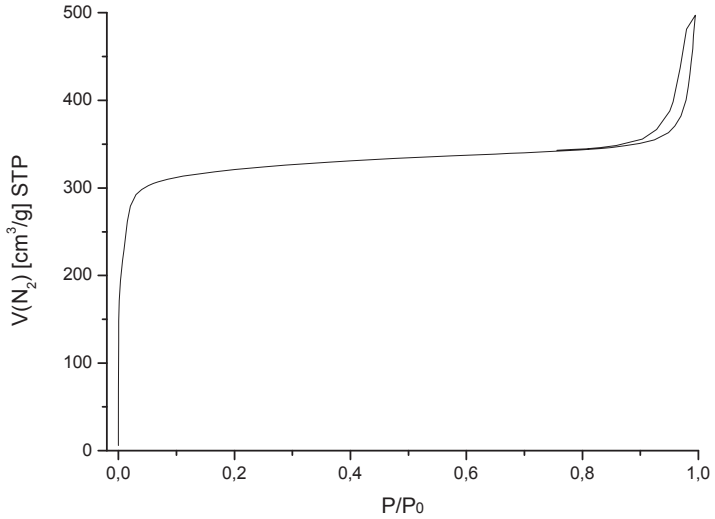

Figure 19. N_2 isotherm at 77K of MIL-68(In)-NH_2

IV.3.3. TGA

The first loss in the range of 50-100°C is due to the liberation of the guest molecules of water. Second weight loss after 350°C is the decomposition of the frameworks and the formation of the Indium oxide. This analyse matches with the TGA data of the MIL-68[3]. The calculated formula is $In(OH)(abdc)_{0,96}.\ 1.16H_2O$

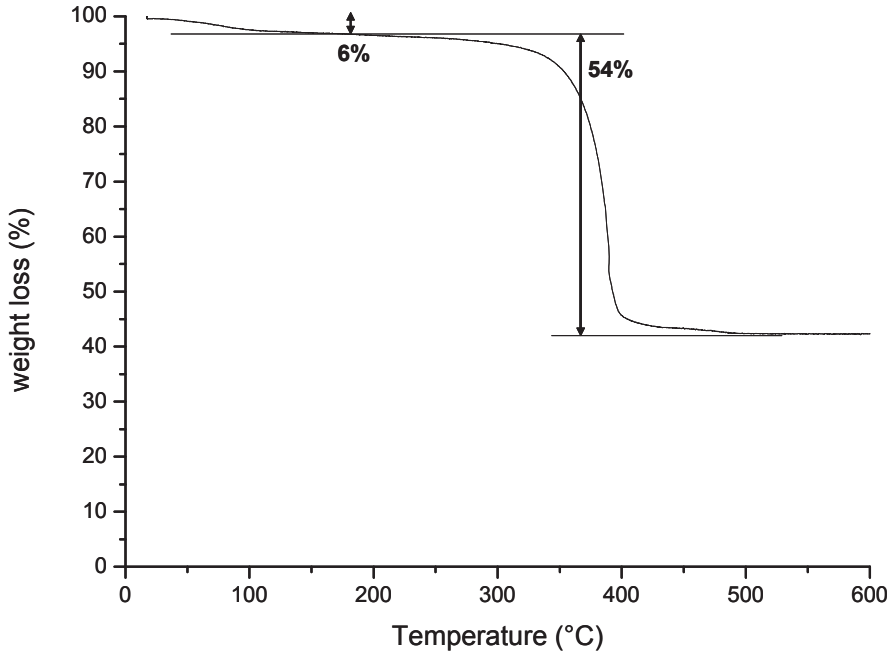

Figure 20. TGA of MIL-68(In)-NH_2

IV.3.4. ^{1}H liquid NMR

^{1}H NMR of the digested materials was performed. Results are identical to those previously published [3, 9] and confirmed that the MOFs are empty of any organic solvant or remaining reactants (figure 21).

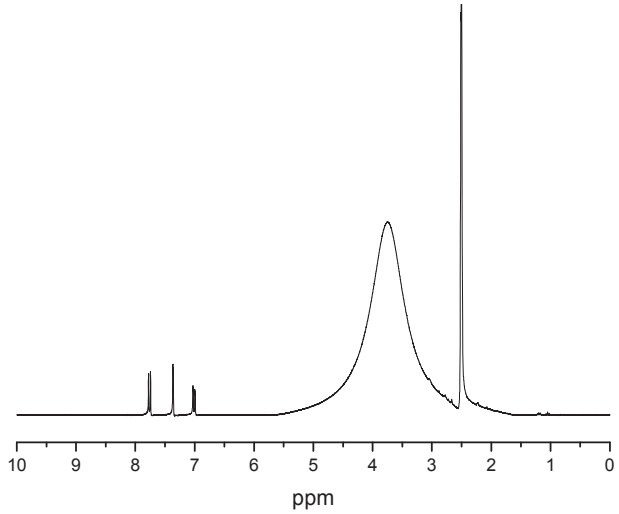

Figure 21. Liquid ^{1}H NMR spectra of MIL-68(In)-NH_2.

IV.3.5. DRIFT spectroscopy

DRIFT spectroscopy of the materials was performed. Results are identical to those previously published [3, 9] (figure 22).

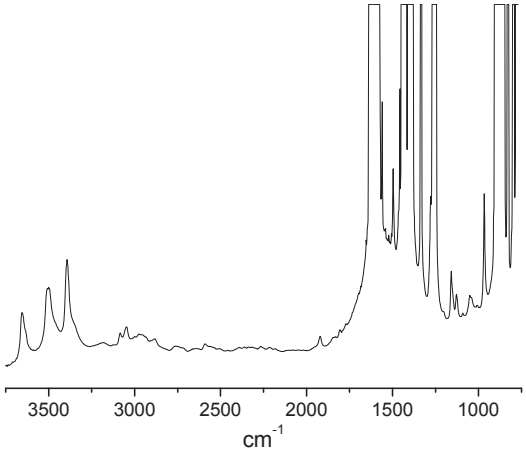

Figure 22. DRIFT spectra of MIL-68(In)-NH_2.

The band at 3660 cm^{-1} is attributed to the bridging OH in the chains of trans corner-sharing $InO_4(OH)_2$ octahedra. DFT calculations predict anharmonic frequencies of 3630-3656 cm^{-1} for these groups, in good agreement with the experiments.

IV.3.6 SEM

SEM was performed on MIL-68(In)-NH_2 sample. Picture shows aggregation of particles with a size below one micron.

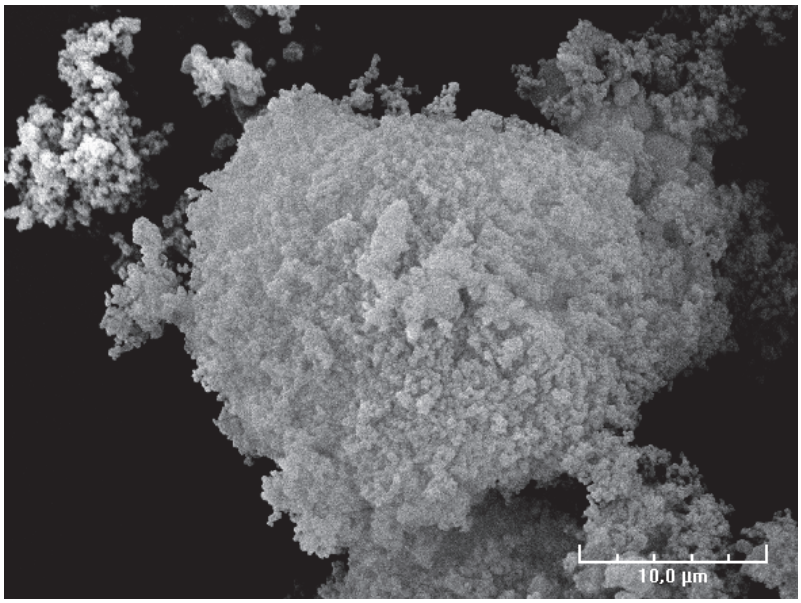

Figure 23. SEM image of the MIL-68(In)-NH_2

V. MIL-68(Ga)-NH_2

V.1. Synthesis

As for MIL-53(Ga)-NH_2, MIL-68(Ga)-NH_2 can be obtained by solvothermal or precipitation synthesis. Solutions containing 2.046 g (8 mmol) of Gallium nitrate hydrate , 8 mmol of 2-aminobenzene-1,4-dicarboxylate and 30 mL anhydrous DMF (THF gives identical result) were introduced into a 48- mL Teflon-lined autoclave and subjected to solvothermal synthesis at 110°C for 48 h. In the precipitation procedure, Gallium nitrate and 2-aminoterephthalic acid were solvated in DMF. The reaction mixtures were stirred for 5 minutes, and then a solution of triethylamine (Et_3N) in DMF was added. After stirring for 120 minutes at room temperature, the resulting precipitates were filtered and dried. Products of both methods were purified by three DMF extractions at 150°C and a DCM soxhlet. The activated solid was dried under vaccum to give 860mg of an off-white powder.

V.2. Characterization MIL-68(Ga)-NH_2

V.2.1. PXRD

The X-ray diffraction patterns of MIL-68(Ga)-NH_2 mainly fit with the structure discovered by Ferey *et al*[3] (figure 24). An extra peak is observed at 12° which can be MIL-53(Ga)-NH_2 side produced.

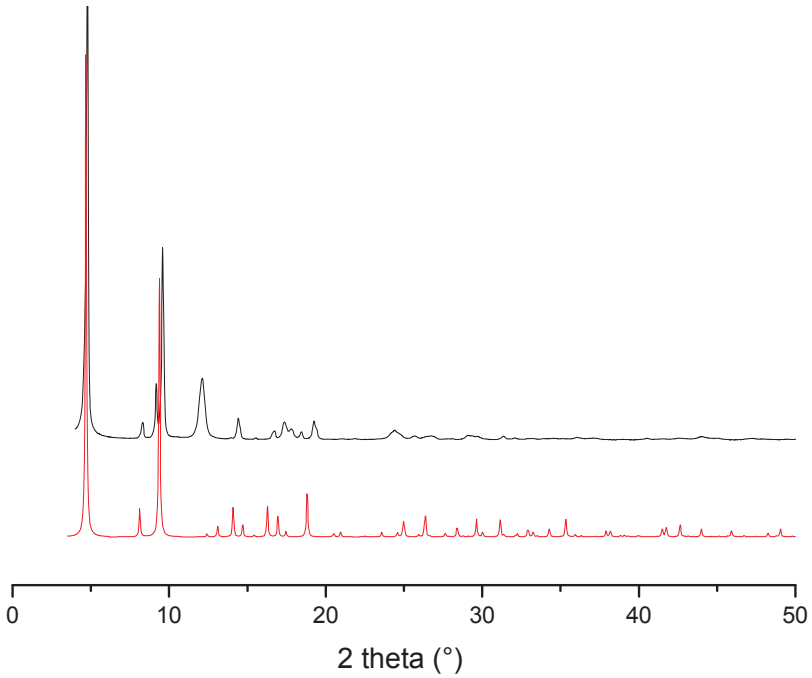

Figure 24. Powder X-ray diffraction patterns of MIL-68(Ga)-NH_2 (black line-top) and simulated MIL-68 (red-bottom).

V.2.2. Nitrogen physisorption

Nitrogen isotherm of MIL-68(Ga)-NH_2 shows a type II trend. Brunauer-Emmett-Teller (BET) surface area of MIL-68(Ga)-NH_2 is 385±3$m^2.g^{-1}$

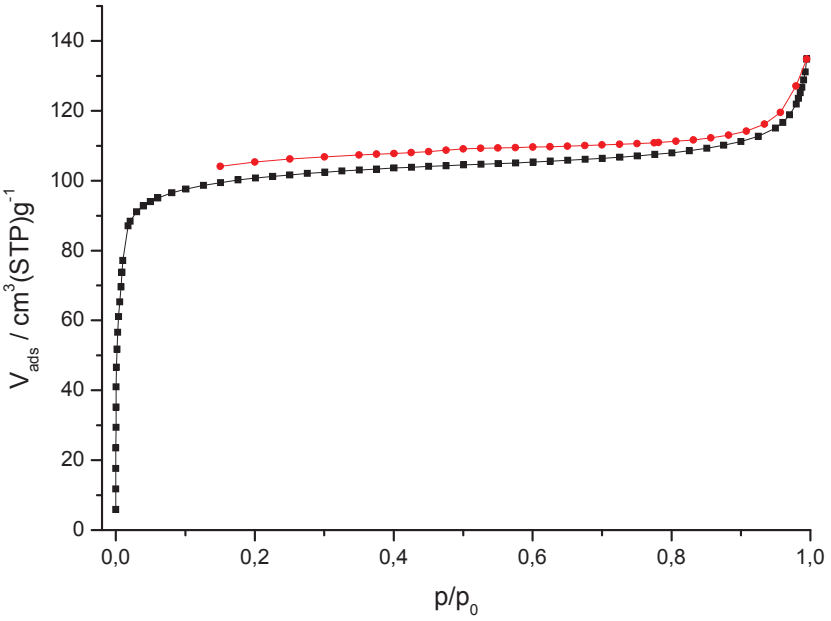

Figure 25. N_2 adsorption isotherm of MIL-68(Ga)-NH_2

V.2.3. TGA

For as synthesized Ga-MIL-68-NH_2 (black), three-step weight loss is observed. The first step corresponds to the release of the water from the pore. Then DMF molecules are evacuated around its boiling point (153°C). Last weight loss is due to the Structure collapsing and the formation of Gallium oxide Ga_2O_3. Measured formula is $Ga(OH)(abdc)_{0.74}$-0.54DMF-0.94water Activated Ga-MIL-68-NH_2 was washed of DMF and only shows the first and last weight loss (water removal and structure collapsing). $Ga(OH)(adbc)_{0.74}$-2.23water

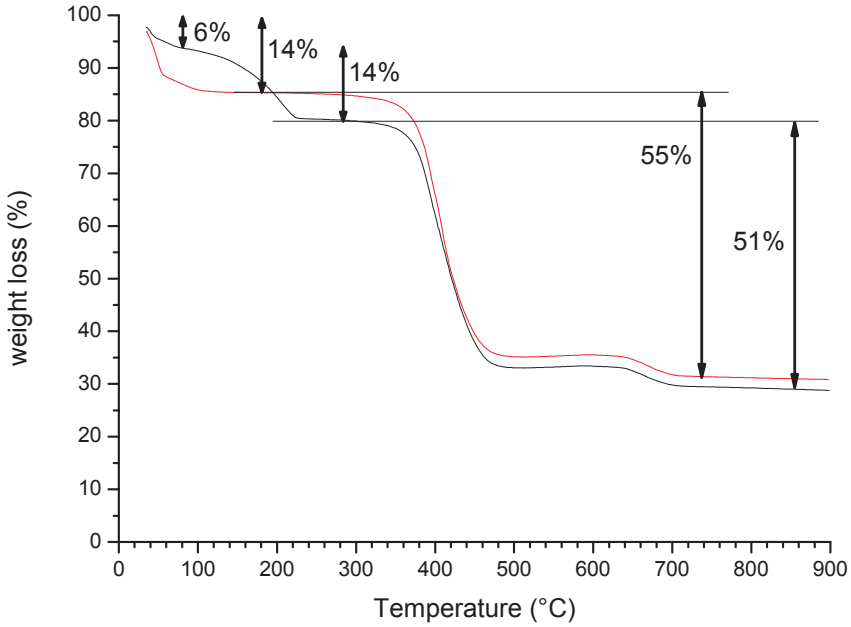

Figure 26. TGA of as MIL-68(Ga)-NH_2 (black line) and MIL-68(Ga)-NH_2 (red line)

V.2.4. ^{1}H liquid NMR

The ^{1}H NMR of the MIL-68(Ga)-NH_2 shows the aromatic protons of the abdc. Nevertheless traces of two other doublets (7.68 and 8.05 ppm) and a singlet (8.5 ppm) can be observed. It means that the environments of several amino groups have been modified in the synthesis (figure 27).

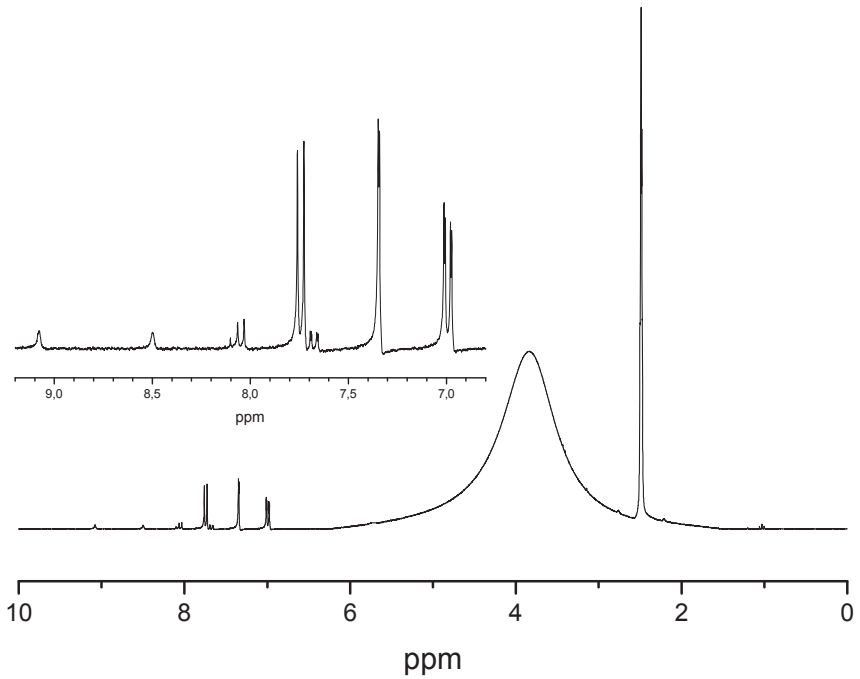

Figure 27. Liquid ^{1}H NMR spectra of MIL-68(Ga)-NH_2.

V.2.5. DRIFT spectroscopy

DRIFT spectroscopy of the materials was performed. Results are similar to those obtain on MIL-68(Ga)-NH_2 (figure 22 and 28).

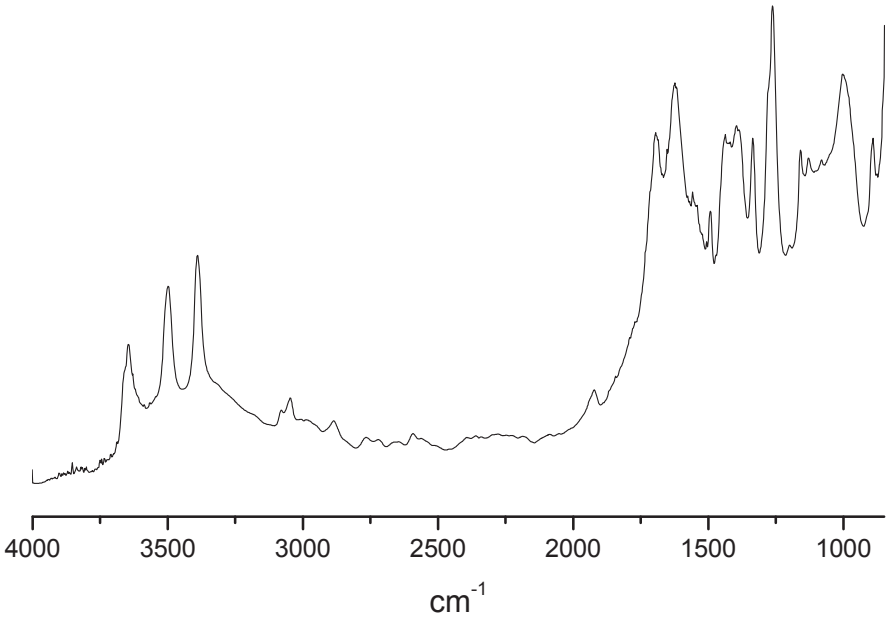

Figure 28. DRIFT spectra of MIL-68(Ga)-NH_2.

The band at 3650 cm^{-1} is attributed to the bridging OH in the chains of trans corner-

sharing $GaO_4(OH)_2$ octahedra. symmetric and asymmetric stretching of the primary amine are found at 3500 and 3380cm^{-1}.

V.2.6 SEM

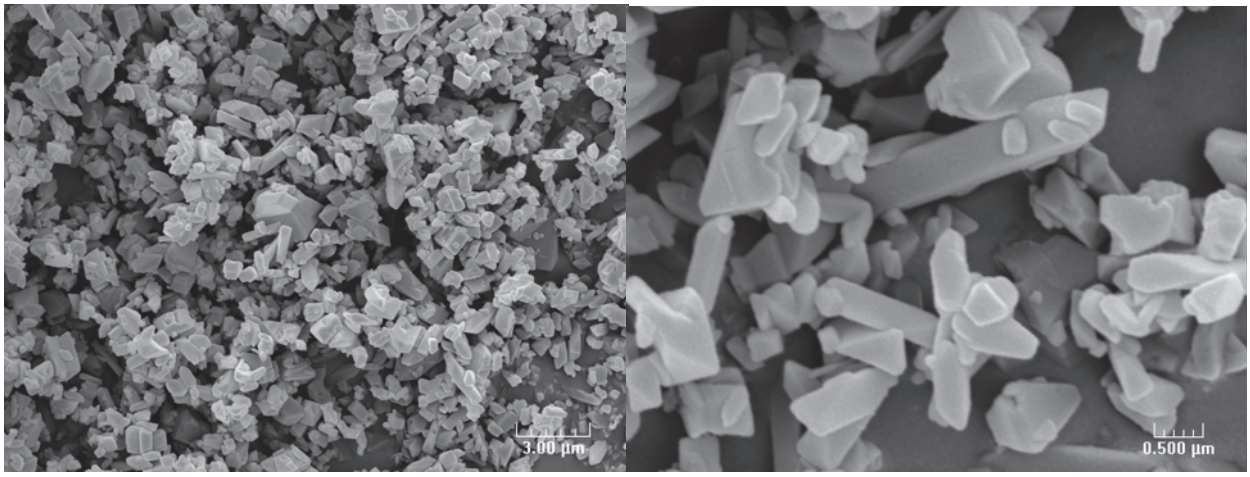

Figure 29. SEM image of the MIL-68(Ga)-NH_2

As shown on the SEM picture, MIL-68(Ga)-NH_2 powder is constituted of elongated crystal with size between 0.3 and 3µm.

VI. Unraveling the origin of the activity of amine functionalised Metal-Organic Frameworks in the catalytic synthesis of cyclic carbonates from epoxide and CO_2

(*ChemCatChem*., **2012**, DOI: 10.1002/cctc.201200288)

VI.1. Introduction

The conversion of carbon dioxide (CO_2) into bulk chemicals at lower energy cost is a scientific and technologic challenge [10, 11].

Acid-base pair catalysts are interesting for such applications as they can perform concerted reactions. The adsorption of CO_2 occurs on the basic sites to form activated species; then epoxide coordinates onto the neighbouring acidic site and ring-opening occurs by a nucleophilic attack of the activated species. An example of rational design of acid-base catalysts are amine functionalised mesoporous Ti(Al)-SBA-15[12]. Ratnasamy and co-workers show a "volcanic plot" of the reaction rate as a function of amine basicity, with secondary amines being the optima. They suggest that CO_2 is too weakly activated on primary amines whereas it is too strongly

adsorbed on tertiary amine. Hence, moderate CO_2 adsorption on amine functionalised acid solids appears as good catalyst candidates for this reaction.

It is generally acknowledged that Metal Organic Frameworks (MOF) are appropriate materials to design single site acid-base catalysts [13-15]. In a spectroscopic study on MOF, Gascon *et al* showed the functionalization of MOF-5 by an amino substituant (2-amino-1,4-benzenedicarboxylate), also known as IRMOF-3. The amino group acts as a electron donor (Lewis base) on CO_2 [16]. This "amino effect" on the CO_2 adsorption was experimentally observed on various MOFs and later confirmed by ab initio calculations [17-20]. The concept of concerted reactions on acid-base MOF has been reported by Baiker in the synthesis of propylene carbonate with amino containing mixed-linker MIL-53 co-catalyzed by tetraalkylammonium halides[21]. A turnover frequency of 400 h^{-1} was measured in solvent free condition. Another significant example is the activity of amino functionalized UiO-66 in the cross-aldol reaction reported by De Vos[22].

Hence, we anticipitate that the use of MOF exhibiting acid-base pairs, such as a Brønsted acid MOF functionalised with NH_2, could lead to catalyst candidates for carbonate synthesis from CO_2. In this work we elucidate the role of the NH_2 functionalization of MIL-68(In)-NH_2[23] as a catalyst for the synthesis of styrene carbonate from styrene oxide and CO_2.

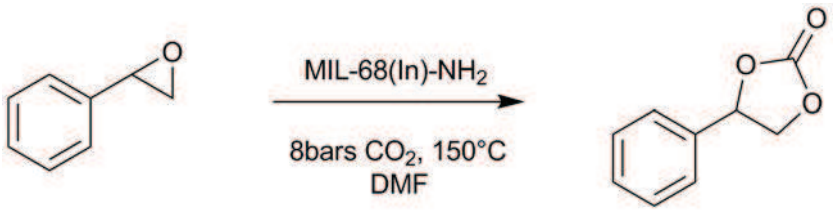

Scheme 30. Synthesis of styrene carbonate from styrene oxide

VI.2. Catalytic test: styrene carbonate synthesis

Preliminary screening of amino MOF was carried out with the following conditions. Styrene oxide (0.2 mL, 210.4 mg, 1.75 mmol) and anhydrous DMF (1.8mL, 1699.2 mg, 23.25 mmol) were loaded in a 3 mL glass vial. The typical amount of catalyst was 50 mg. The system was heated at 150°C under magnetic stirring (1000 rt/min), then the reaction was conducted by introducing 8 bars of CO_2 into the vial. Styrene oxide and styrene carbonate concentrations were determined by GC analysis of the samples using toluene as an external standard. In all experiments, no by-product was observed. The catalytic tests were repeated independently two or

three times in order to estimate the reproducibility and accuracy of the results. Test duration of 8 hours was chosen in order to have the best TOF (figure 31).

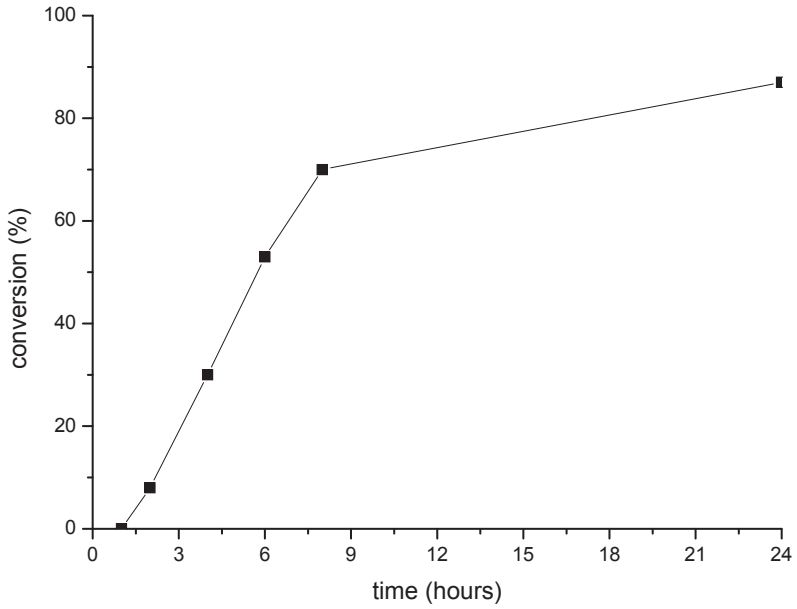

Figure 31. Styrene oxide conversion as function of time with MIL-68(In)-NH_2 catalyst.

Results are reported in Table 1 and compared with a blank experiments conducted without catalyst and tetramethylammonium bromide- a known active and selective homogeneous catalyst [24]. The only candidate which shows activity is the MIL-68(In). The styrene oxide conversion is clearly enhanced by NH_2 functionalization. It increases from about 39% (+/- 3%) for MIL-68(In) to 71% (+/-3%) for MIL-68(In)-NH_2.

Table 3. Catalytic activity. [b], [c] and [d]: independent catalytic tests. [a] : conversion and TOF calculated after 8hours

Catalyst	Styrene oxide conversion (%)[a]	TOF (h^{-1})[a]
blank	8	-
Tetramethylammonium bromide	87	0.78
MIL-53(Al)-NH2	Traces	-
MIL-53(Ga)-NH2	17	

MIL-68 (In) [b]	42	0.54
MIL-68 (In) [c]	36	0.47
MIL-68(In)-NH_2[b]	74	1.06
MIL-68(In)-NH_2[c]	68	0.97
MIL-68(In)-NH_2[d]	70	1.00
MIL-68(In)-NH_2 (recycled)	53	0.76

After a catalytic run, MIL-68(In)-NH_2 was removed from the reaction mixture by centrifugation (4000 rpm) and washed by an overnight dichloromethane soxhlet extraction. At this point the dried material was ready to reuse in a second test. In this case, conversion decreased from 74% to 53%. This slight decrease in activity could be explained by reactant blocked in the 1D channel of the MOF even after the recycling process. Even though the XRD pattern of the material after the test was identical to that of the fresh one (Figure 32), surface area (BET) decreases significantly from 1100 to 720 m2/g. The analysis of digested catalysts by ^1H NMR indicates a broad signal at 7.3ppm which corresponds to the aromatic protons of reactant and product which remain in the pores (Figure 33). We can estimate by integration that one molecule blocked for ten linkers. We can assume that it may block the access of 1D channel to N_2 as reflected by the lower BET.

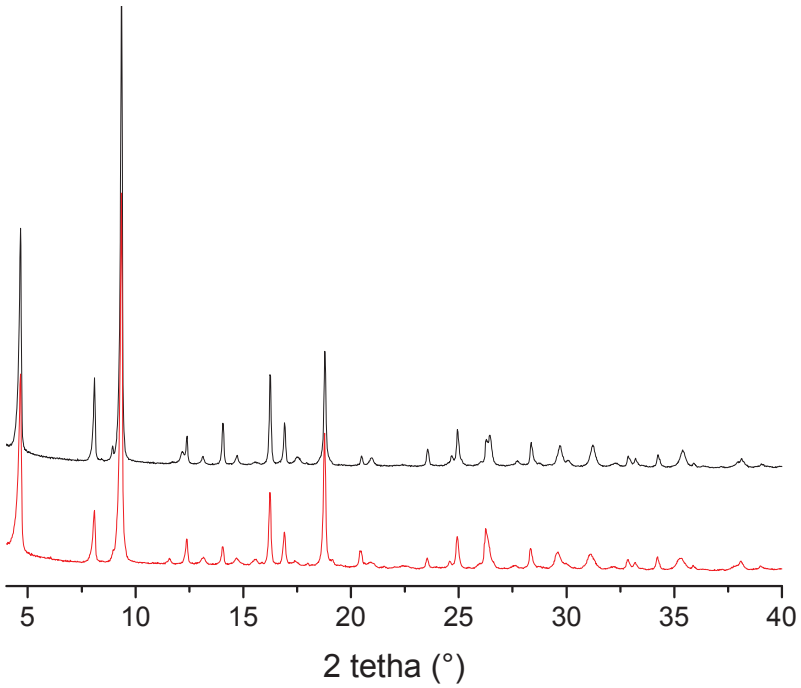

Figure 32. XRD pattern of MIL-68(In)-NH_2 before (bottom/red line) and after (top/black line) the carbonate synthesis.

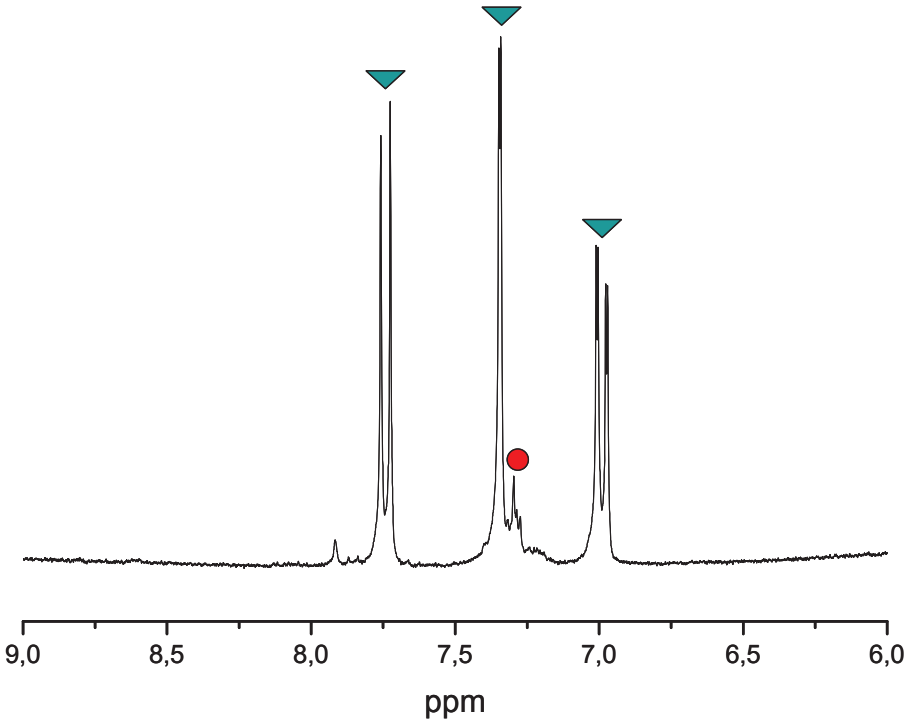

Figure 33. NMR spectra of MIL-68(In)-NH_2 after the carbonate synthesis and a DCM soxhlet.

The two doublets and the singulet marked with blue triangles are the aromatic protons of the linker. Broad signal at 7.3ppm (red circle) is protons of reactant and product which remain after reactivation procedure.

Catalytic tests carried out in other high boiling point solvents (chlorobenzene and DMSO) exhibit conversion values below 5%. Additionaly, slight conversion was obtained in DMF without catalysts (blank test, see Table 1). This indicates that DMF has a role in the reaction mechanism. It could be suspected that products of DMF degradation such as dimethylamine act as catalytic species [25]. However, no decomposition products were detected with NMR in the reaction mixture after test.

VI.3. Evaluation of the acid/base properties

Ab-initio calculations were carried out for the evaluation of the effect of the amino functionlisation on the acid-base properties. Figure 34 depicts the structures of MIL-68(In)-NH_2 optimised by Density Functional Theory (DFT) calculations. these calculations were performed using a periodic plane-wave method as implemented in VASP 5.2.[26] The exchange-correlation functional was treated within the generalised gradient approximation (GGA) parameterised by Perdew, Burke and Ernzernhof PBE,[27] and the electron-ion interaction was described by the projector augmented wave (PAW) scheme[28] with an energy cutoff of 400 eV. Energies were calculated with the 1x1x3 Kpoints mesh. Dispersion corrections were systematically included to energies and forces, within the DFT-D2 method of Grimme[29]. Full optimisation of structures was performed, until forces on each atom in each direction were inferior to 2.10^{-2} eV.$Å^{-1}$. Atomic charges were calculated by Bader charge analysis[30, 31], with an increased cutoff (500 eV) and fine FFT grid (250x420x80 points).

Amino groups were substituted on each linker, starting from MIL-68(In), and were arbitrarily placed so as to limit their interaction as much as possible. This class of MOFs is characterised by a one-dimensional rod-shaped structure with channels of two sizes: large hexagonal channels (LC) and tight triangular channels (TC). The $InO_4(OH)_2$ octahedral units are trans-connected through the hydroxyl groups to form an infinite chain. DFT suggests that the OH groups are tilted (out of the In-O-In plane) (Figure 34).

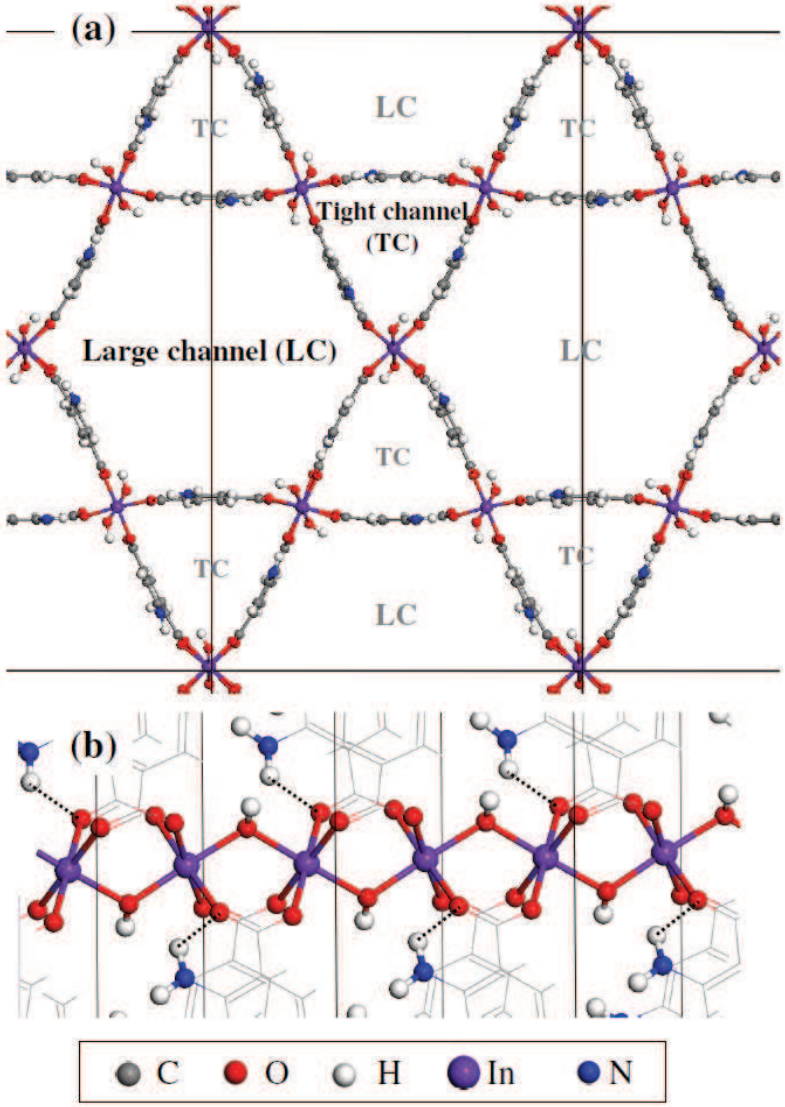

Figure 34. MIL-68(In)-NH_2: a) view of the lattice and the channels, b) view of the In chains; carbon and hydrogen atoms bonded to carbons are represented in line for the sake of clarity.

The acidity of $InO_4(OH)_2$ octahedral units was quantified by DFT calculations of the adsorption of basic probe molecules (CO, NH_3) on MIL-68(In) and MIL-68(In)-NH_2. Regarding CO, the traditional C adduct, -OH•••CO, was modeled to account for the acidity of the proton, as per the usual assumption. Table 2 reports the corresponding adsorption energies. Sites located in the tight and large channels exhibit comparable adsorption energies for both probes, even if the adsorption is generally slightly more favourable in the tight channel, which was shown to arise from enhanced van der Waals stabilization in TC. Moreover, following NH_2 functionalisation of the framework, the adsorption is even slightly stronger; this can tentatively be assigned to the attractive effect of NH_2, which is likely to enhance the acidity of the proton. This is indicated by

a slightly increased mean Bader charge on the protons of the OH groups after NH_2 functionalisation (+0.63e instead of +0.61e), even if it was shown that the electrostatic charge of the proton is not the single parameter to rationalize its acidity[32]. Note that for a given adsorption site (LC or TC), the NH_2 functionalisation does not significantly affect the van der Waals contribution of the molecule/framework interaction.

Table 4. Adsorption energies of CO and ammonia ($kJ.mol^{-1}$) for MIL-68(In) and MIL-68(In)-NH_2, as evaluated by DFT calculations.

	MIL-68(In)	MIL-68(In)-NH_2
Adsorbed molecule	Large/tight channel	Large/tight channel
CO	-22 / -32	-28/-35
Ammonia	-59 / -67	-73/-78

Ammonia was not protonated in any case; however, adsorption energies are significantly negative and are comparable to calculations performed on amorphous aluminosilicates (even upon removal of the dispersion component, which was not included in previous reports)[33]. The adsorption strength nevertheless remains more favourable on zeolites.[34] These results prove that MIL-68(In) presents mild Brønsted acidity that is slightly promoted upon NH_2 functionalisation. This acidity is even higher than that evaluated on other carboxylate based MOFs (MIL-53(Al) and IM-19)[35]. In a later study, we showed that bridging μ_2(OH) in MIL-53 (Ga, Al) exhibit weak to moderate Brønsted acidity that can be correlated to the acid mechanism of aromatic alkylation[35].

It has been already reported that substitution on the linker can modify the electronic structure and or density of the inorganic backbone of the MOF and thus the catalytic properties associated with acid sites. For examples, Gascon et al have reported the modification of the band gap of IRMOF solids by substitution on different linker[36]. Garcia et al have shown a similar effect on the UiO-66 when substituted with NH_2 for the photocatalytic production of H_2 [37].

The interactions of CO_2 with MIL-68(In) and MIL-68(In)-NH_2 were investigated by CO_2 adsorption and DRIFT measurements. Carbon dioxide adsorption measurements were carried out for the identification the mode of CO_2 activation on MIL-68(In)-NH_2. MIL-68(In)-NH_2 has a higher affinity for CO_2 adsorption than does its analogue with no amino group (Figure 35).

Henry constants for CO_2 for MIL-68(In) and MIL-68(In)-NH_2 are, respectively, 0.029 and 0.048 mmol.g^{-1}.kPa^{-1}, which gives a ratio of 1.69.

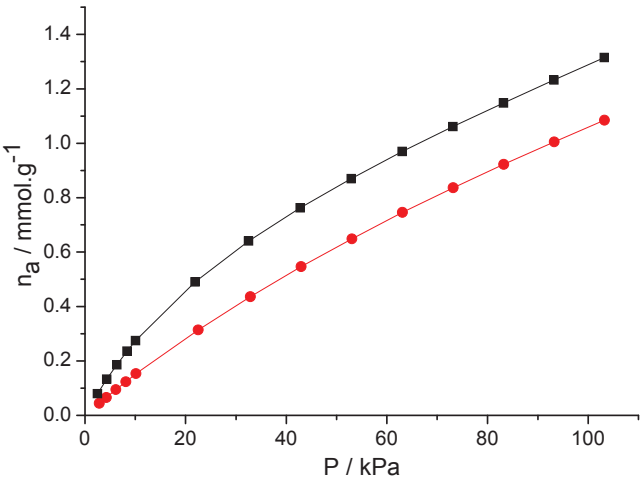

Figure 35. CO_2 adsorption isotherm of MIL-68(In) (red line - round dot) and MIL-68(In)-NH_2 (black line - square dot).

The enhancement of the Henry constant is in good agreement with molecular modelling studies performed by other groups on MIL-53(Al)-NH_2.[18, 20] In a similar fashion to MIL-68, MIL-53 possesses a rod-like structure with $AlO_4(\mu_2OH)_2$ units. Density Functional Theory (DFT) simulations showed that CO_2 are physisorbed on H-bonds, mainly on the μOH, and that carbamate species cannot be formed whatever the pressure. On the other hand, CO_2 adsorption enthalpies calculated by the Grand Canonical Monte Carlo method at low coverage (at 0.01 bar) on MIL-53(Al) and MIL-53(Al)-NH_2 reveal a slightly higher heat of adsorption for the amine: -23.2kJmol^{-1} versus -27.5kJmol^{-1} [20]. We can therefore conclude that CO_2 is weakly activated on MIL-68 samples without carbamate formation for the amine functionalised MIL-68(In)-NH_2. In addition, DRIFT analysis of the MIL-68(In)-NH_2 sample at 25°C under CO_2 flow did not show any modification of the bands at 3500 and 3390 cm^{-1} which correspond to the symmetric and asymmetric stretching of the primary amine (Figure 36). This confirms that no carbamate species were formed through the NH_2-CO_2 interaction.[18, 38, 39]

Additionaly, it has been reported that DMF may activate carbon dioxyde and stabilized the carbonate intermediate by elongated C-O bond as observed by the Yamada group[40]. This combined Brønsted acid and Lewis base co-catalyst has proven to be highly efficient in the synthesis of carbonate[21, 41, 42].

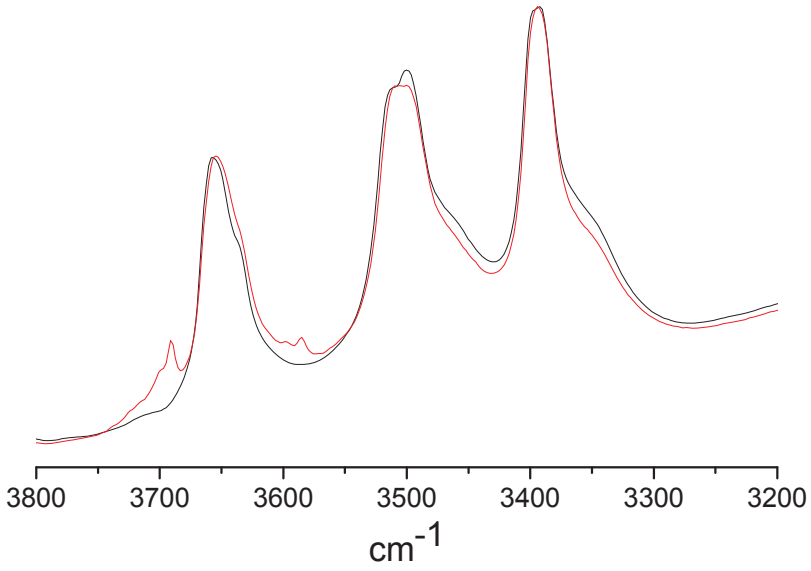

Figure 36. DRIFT spectra of MIL-68(In)-NH_2 at 25°C under Argon (black line) and CO_2 steam (red line). Peaks at 3585 and 3690 cm^{-1} are remaining gas signals after CO_2 background removal.

VII. Conclusions

We synthetized and fully characterized four amino substituted MOF. The synthesis of MIL-53-NH_2 and MIL-68-NH_2 was extended to Gallium metal and two new MOF were obtained. The choice of solvent is crucial to determine which structure will be form. Hydrothermal synthesis forms the MIL-53 structure when solvothermal synthesis in DMF forms the MIL-68 structure. Unfortunately Gallium based MIL-53 and MIL-68 showed a decrease in the adsorption properties and MIL(In)-68-NH_2 and MIL(Al)-53-NH_2 have been selected to performed the PSM experiments.

Then reactivity of amino functionalized MOF has been studied. We have shown that the synthesis of cyclic carbonate from CO_2 and styrene oxide can be accomplished through the intrinsic properties of MOFs in presence of DMF. MIL-68 shows moderate Brønsted acidity, while CO_2 is not dissociated into carbamate on NH_2 site. This study shows that electronic effect prevails for substituted MIL-68 catalysts. Surprisingly, the substitution with amine increases the interaction of the MOF with basic probe molecules as calculated by DFT.

Hence, we show that the gain in catalytic activity arises from the enhanced Brønsted acidity which originates from the linker substitution. Simultaneously, DMF seems to act as a co-catalyst and activated the carbon dioxide. We believe that this finding open new perspective in

the rational design of MOF in catalysis by applying approaches used in the development of molecular catalyst.

VIII. References

[1] G. Chaplais, A. Simon-Masseron, F. Porcher, C. Lecomte, D. Bazer-Bachi, N. Bats and J. Patarin, *Physical Chemistry Chemical Physics*, **2009**, **11**, 5241-5245.

[2] C. Volkringer, T. Loiseau, N. Guillou, G. Ferey, E. Elkaim and A. Vimont, *Dalton Transactions*, **2009**, 2241-2249.

[3] C. Volkringer, M. Meddouri, T. Loiseau, N. Guillou, J. Marrot, G. Ferey, M. Haouas, F. Taulelle, N. Audebrand and M. Latroche, *Inorg. Chem.*, **2008**, **47**, 11892-11901.

[4] T. Ahnfeldt, D. Gunzelmann, T. Loiseau, D. Hirsemann, J. r. Senker, G. Férey and N. Stock, *Inorganic Chemistry*, **2009**, **48**, 3057-3064.

[5] S. Marx, W. Kleist, J. Huang, M. Maciejewski and A. Baiker, *Dalton Trans.*, **2010**, **39**, 3795-3798.

[6] T. Ahnfeldt, D. Gunzelmann, T. Loiseau, D. Hirsemann, J. r. Senker, G. Ferey and N. Stock, *Inorganic Chemistry*, **2009**, **48**, 3057-3064.

[7] T. Loiseau, C. Serre, C. Huguenard, G. Fink, F. Taulelle, M. Henry, T. Bataille and G. Férey, *Chemistry – A European Journal*, **2004**, **10**, 1373-1382.

[8] S. Couck, J. F. M. Denayer, G. V. Baron, T. Rémy, J. Gascon and F. Kapteijn, *J. Am. Chem. Soc.*, **2009**, **131**, 6326-6327.

[9] M. Savonnet, D. Bazer-Bachi, N. Bats, J. Perez-Pellitero, E. Jeanneau, V. Lecocq, C. Pinel and D. Farrusseng, *J. Am. Chem. Soc.*, **2010**, **132**, 4518-4519.

[10] T. Sakakura, J.-C. Choi and H. Yasuda, *Chem. Rev.*, **2007**, **107**, 2365-2387.

[11] T. Sakakura and K. Kohno, *Chem. Comm.*, **2009**, 1312-1330.

[12] R. Srivastava, D. Srinivas and P. Ratnasamy, *Microporous Mesoporous Mater.*, **2006**, **90**, 314-326.

[13] D. Farrusseng, S. Aguado and C. Pinel, *Angew. Chem., Int. Ed.*, **2009**, **48**, 7502-7513.

[14] M. Savonnet, S. Aguado, U. Ravon, D. Bazer-Bachi, V. Lecocq, N. Bats, C. Pinel and D. Farrusseng, *Green Chem.*, **2009**, **11**, 1729-1732.

[15] M. Savonnet, A. Camarata, J. Canivet, D. Bazer-Bachi, N. Bats, V. Lecocq, C. Pinel and D. Farrusseng, *Dalton Trans.*, **2012**, **41**, 3945-3948.

[16] J. Gascon, U. Aktay, M. D. Hernandez-Alonso, G. P. M. van Klink and F. Kapteijn, *J. Catal.*, **2009**, **261**, 75-87.

[17] B. Arstad, H. Fjellvåg, K. Kongshaug, O. Swang and R. Blom, *Adsorption*, **2008**, **14**, 755-762.

[18] E. Stavitski, E. A. Pidko, S. Couck, T. Remy, E. J. M. Hensen, B. M. Weckhuysen, J. Denayer, J. Gascon and F. Kapteijn, *Langmuir*, **2011**, **27**, 3970-3976.

[19] J. G. Vitillo, M. Savonnet□, G. Ricchiardi and S. Bordiga, *ChemSusChem*, **2011**, **4**, 1281-1290.

[20] A. Torrisi, R. G. Bell and C. Mellot-Draznieks, *Cryst. Growth Des.*, **2010**, **10**, 2839-2841.

[21] W. Kleist, F. Jutz, M. Maciejewski and A. Baiker, *Eur. J. Inorg. Chem.*, **2009**, **2009**, 3552-3561.

[22] F. Vermoortele, R. Ameloot, A. Vimont, C. Serre and D. De Vos, *Chem. Comm.*, **2011**, **47**, 1521-1523.

[23] FR Patent 09/05.107, M. Savonnet, D. Bazer-Bachi, C. Pinel, V. Lecocq, N. Bats and D. Farrusseng, 2009.
[24] V. Calo, A. Nacci, A. Monopoli and A. Fanizzi, *Org. Lett.*, **2002**, **4**, 2561-2563.
[25] J. Muzart, *ChemInform*, **2009**, **40**, no-no.
[26] G. Kresse and J. Hafner, *Phys. Rev. B: Condens. Matter*, **1994**, **49**, 14251-14269.
[27] J. P. Perdew, K. Burke and M. Ernzerhof, *Phys. Rev. Lett.*, **1996**, **77**, 3865-3868.
[28] G. Kresse and D. Joubert, *Phys. Rev. B: Condens. Matter*, **1999**, **59**, 1758-1775.
[29] S. Grimme, *J. Comput. Chem.*, **2006**, **27**, 1787-1799.
[30] G. Henkelman, A. Arnaldsson and H. Jonsson, *Comput. Mater. Sci*, **2006**, **36**, 354-360.
[31] E. Sanville, S. D. Kenny, R. Smith and G. Henkelman, *J. Comput. Chem.*, **2007**, **28**, 899-908.
[32] F. Leydier, C. Chizallet, D. Costa and P. Raybaud, *Chem. Comm.*, **2012**, **48**, 4076-4078.
[33] C. Chizallet and P. Raybaud, *ChemPhysChem*, **2010**, **11**, 105-108.
[34] T. Bucko, J. Hafner and L. Benco, *J. Chem. Phys.*, **2004**, **120**, 10263-10277.
[35] U. Ravon, G. Chaplais, C. Chizallet, B. Seyyedi, F. Bonino, S. Bordiga, N. Bats and D. Farrusseng, *ChemCatChem*, **2010**, **2**, 1235-1238.
[36] J. Gascon, M. D. Hernandez-Alonso, A. R. Almeida, G. P. M. van Klink, F. Kapteijn and G. Mul, *Chemsuschem*, **2008**, **1**, 981-983.
[37] C. G. Silva, I. Luz, F. X. Llabres i Xamena, A. Corma and H. Garcia, *Chem. Eur. J.*, **2010**, **16**, 11133-11138.
[38] R. Srivastava, D. Srinivas and P. Ratnasamy, *J. Catal.*, **2005**, **233**, 1-15.
[39] J. Zhang, S. Zhang, K. Dong, Y. Zhang, Y. Shen and X. Lv, *Chem. Eur. J.*, **2006**, **12**, 4021-4026.
[40] Y. Sugawara, W. Yamada, S. Yoshida, T. Ikeno and T. Yamada, *J. Am. Chem. Soc.*, **2007**, **129**, 12902-12903.
[41] X.-B. Lu, X.-J. Feng and R. He, *Appl. Catal., A*, **2002**, **234**, 25-33.
[42] X.-B. Lu, Y.-J. Zhang, B. Liang, X. Li and H. Wang, *J. Mol. Catal. A.*, **2004**, **210**, 31-34.

Chapter 4

Control of the amino site density in Metal-organic frameworks

I. Introduction

Metal-organic frameworks are essentially functional materials[1-6]. The porous framework can be decorated with various organic moieties without undergoing significant structural changes. Such solids are usually referred to isoreticular structures. Among the different isoreticular MOFs, we can cite the IRMOF,[7, 8] the MIL-53,[9] the $Cu_2(Lx)(H_2O)_2$,[10] and the ZIF series displaying GME,[11] RHO[12] and LTA[13] topologies. Starting from a precursor solution containing 2-aminobenzene-1,4-dicarboxylate (abdc) instead of benzene-1,4-dicarboxylate linker (bdc), various MOFs with a pending $-NH_2$ function have been obtained, such as the Zn_4O(abdc) or IRMOF-3,[14] CAU-1,[15] MIL-53-NH_2[16], MIL-68-NH_2[17, 18] and UMCM-1-NH_2.[19] These materials are of particular interest, since the amino function enables the insertion of complex moieties using post-modification techniques.[18, 20-22]

Few properties are essential to design an efficient heterogeneous catalyst: it should have a sufficient thermal and chemical stability and reactant should easily access to the active site. According to these considerations MIL-53(Al) seems to be an appropriate material. It is stable until 500°C, under acidic conditions and can adopts a large pore configuration under thermal and pressure stimuli.

Nevertheless the MIL-53(Al) analogue with amino terephthalic acid linker instead of terephthalic acid (MIL-53(Al)-NH_2) does not possess the same properties. Its thermal stability decreases and the material possess a permanent narrow pore structure. Furthermore the full functionalization of amino MOF limits the diffusion of reactant within the pore (especially in 1D pore). The interaction of two amino groups from neighbouring linker cannot be excluded which make more complex the control design of isolated catalytic sites.

An alternative is the use of sophisticated porous materials known as multivariate functional MOFs (also known as MixMOFs) which can be designed using a synthesis method that starts from solutions composed of two or more different linkers. The ratio of each linker has a strong influence on the intrinsic properties of the materials. Therefore adsorption and separation performances of such solids can be finely tuned. Anyway the homogeneous repartition of the different linkers is questionable.

In this chapter, the different multivariate functional MOFs already published will be described. Focus will be given on MIL-53(Al) and MIL-68(In) “mixed linkers”. We will show that adsorption/desorption isotherms and thermodiffraction studies on MIL-53 flexible structures can indirectly characterize the homogeneity of MOFs made from a mixture of linkers. Breathing

pressures and temperatures for a series of MIL-53(Al) functionalized with amino tags were measured as a function of the amino content. The linear relationship between the CO_2 breathing pressure and the amino content in the MIL-53(Al) structure clearly illustrates the homogeneity of the crystallites composition; in other words, all crystallites have the same abdc:bdc ratio. On the other hand, the functionalization of MIL-53(Al) with low amino content (10% abdc) results in a profound modification of the breathing properties triggered by the temperature. Much higher temperatures are required for full conversion of the np (narrow pore) to the lp (large pore) phase. We also suggest an interplay between coexisting np and lp microcrystalline domains that may "smooth" the breathing properties at the macroscopic level. This "mixed linkers" strategy was extended to the precipitation synthesis of MIL-68(In) and a rigid MOF was synthesized with 20% of amino functionalized linker in the structure.

II. State of the Art of "mixed linkers" MOF

II.1. CID 5/6

The Kitagawa group showed that the degree of flexibility of MOF materials made from two different linkers (e.g., CID-5/6) can be monitored by adsorption measurements.[23] CID-5 [Zn(5-NO_2-ip)(bpy)] exhibits gate opening phenomena (i.e. it becomes porous) beyond a threshold water pressure, whereas CID-6 [Zn(5-MeO-ip)(bpy)] is intrinsically porous. Hence, for a particular process, it seems possible to engineer the gate opening/breathing properties of MOFs by finely tuning the linker functionalities and their relative amount in the crystals[24]. To exclude the possibility that the powder was just the mixture of pure crystals of CID-5 and CID-6, X-ray powder diffraction was performed on a single crystal of CID-5/6 and the structure was solved. The simulated powder X-ray pattern and the experimental pattern are similar which prove the macroscopic homogeneity of the solid.
CID-5 does not adsorb either CO_2 and CH_4 and CID-6 adsorb both. Finally the multivariate CID-5/6 gets the best of both two materials and absorbs selectively the CO_2.

II.2. MOF-5

Very large single crystals (~5-10 mm^3), isoreticular to MOF-5, containing two to eight different linkers, have been synthesized by Yaghi and coworkers using a self-assembly method under solvothermal conditions.[14] In such a concept, a random distribution of the different functions would result in a combinatorial functional sequence, providing pores with distinct

properties. Although the authors demonstrated no change in the crystal composition on a millimeter scale, they did not exclude the presence of microscopic domains exhibiting a composition different from the average in the whole crystal. In a separate study on the incorporation of the abdc linker into MOF-5,[25, 26] the presence of both linkers in the crystallites (1-10µm) was confirmed by high-resolution PXRD. Other authors, however, showed that crystal growth rates for the Zn_4O(bdc-X) system might depend not only on the linker, but also on the X substituent (X=I,Br). In this latter case, a radial distribution of the linker composition can be found, the crystal center being halogen rich, while the surface becoming poor.[27]

II.3 MIL-53(Al)

Baiker *et al*.[28] have synthesized a series of "mixed" MIL-53(Al) materials with the general formula $Al(OH)(bdc)_{1-n}(abdc)_n$, where the terephthalate linker (bdc) is partially substituted by aminoterephthalate (abdc). Using high-resolution PXRD, the authors concluded that the mixed frameworks are homogeneous. Notwithstanding this fact, the presence of microdomains with different compositions and/or a composition gradient from crystallite center to the surface could not be ruled out.

III. Homogeneity of flexible MIL-53(Al) containing mixed linkers

(*Dalton Trans*., **2011**, 40, 11359-11361)
(*J. Mater. Chem*., **2012**, 22, 10287-10293)
(*J. Phys. Chem*. C., **2012**, 116, 9507-9516)

Techniques to characterize crystallite homogeneity of MOFs containing two different linkers are imperatively needed, especially for MOFs made of abdc, which are excellent platforms for the introduction of additional functions by post-modification.[18, 20-22]
Herein, we show that adsorption/desorption isotherms and thermodiffraction studies of flexible structures can indirectly characterize the homogeneity of MOFs made from a mixture of linkers. Breathing pressures and temperatures for a series of MIL-53(Al) functionalized with amino tags, i.e. $Al(OH)(bdc)_{1-n}(abdc)_n$, have measured as a function of the amino content (i.e. bdc : abdc ratio).

III.1. Synthesis

Six different samples, including $Al(OH)(bdc)_n$ (e.g., MIL-53(Al)), $Al(OH)(abdc)_n$, (e.g., MIL-53(Al)-NH_2) and mixed $Al(OH)(bdc)_{1-n}$ $(abdc)_n$, were prepared and purified using a modified synthesis protocol based on Stock et al. (Scheme 1).[16]

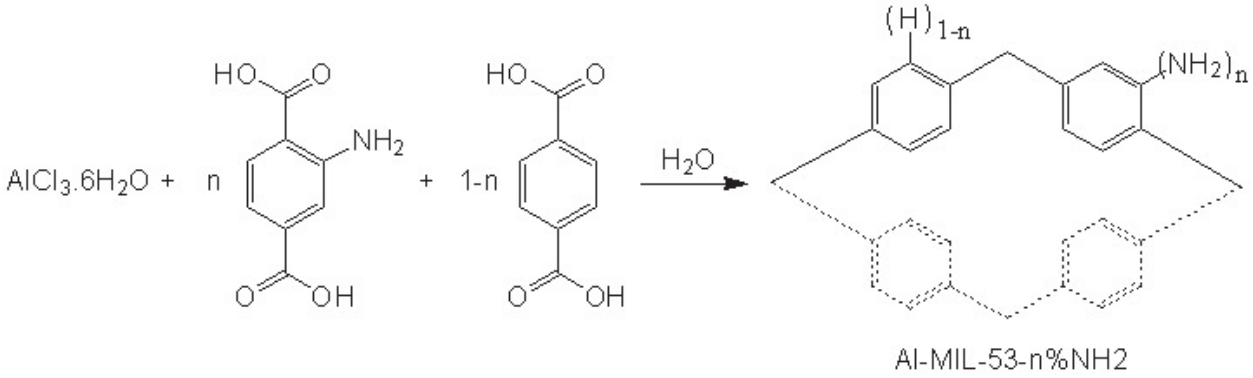

Figure 1. Synthesis of $Al(OH)(bdc)_{1-n}$ $(abdc)_n$.

Briefly, solutions containing 1.931 g (8 mmol) of aluminum chloride hexahydrate ($Al(Cl)_3 \cdot 6H_2O$), 8 mmol of benzene-1,4-dicarboxylate and 2-aminobenzene-1,4-dicarboxylate with different molar ratios (0, 11.1, 20, 50, 66.7 and 100% abdc) and 30 mL deionized water were introduced into a 48- mL Teflon-lined autoclave and subjected to solvothermal synthesis at 150°C for 9 h. After the synthesis, the solids were separated from water by centrifugation at 4000 rpm for 5 min. To remove any excess linker trapped within the porous network, the as-synthesized products were placed in an autoclave with 30 mL anhydrous DMF and heated at 150°C for 24 h.[28] The solvent was then substituted by fresh DMF and the solvothermal treatment was repeated twice. Afterwards, the DMF-containing solids were submitted to dichloromethane Soxhlet-extraction for 20 h to remove DMF. Finally, the solids were dried at 100°C for 9 h at reduced pressure to obtain powdered MIL-53(Al) (A), MIL-53(Al)-11.1%NH_2 (B), MIL-53(Al)-20%NH_2 (C), MIL-53(Al)-50%NH_2 (D), MIL-53(Al)-66.7%NH_2 (E) and MIL-53(Al)-NH_2 (F) samples.

III.2. Results

III.2.1. Composition by liquid ^{1}H- NMR

^{1}H-NMR spectra were recorded as described in chapter 3 (II.3.4). Due to their high

chemical stability, the relative bdc and abdc contents in the different MIL-53(Al)-NH_2 materials were quantified after digestion in a 1% HF/d_6-DMSO solution. The composition was computed using the area ratio of a given proton from each ligand.

For MIL-53(Al) (sample A), ^{1}H-NMR spectra shows a unique singlet corresponding to the four equivalent aromatic protons belonging to terephthalic acid (δ=8.02 ppm). In contrast, the spectrum of MIL-53(Al)-NH_2 (sample F) consists of two doublets (Hb-δ=7 ppm and Hc-δ=7.75 ppm; J=33 Hz) and a singlet (Ha-δ=7.35 ppm) (Scheme 2).

By increasing the abdc content in the starting solution (from A to F), we observe a progressive increase of the ^{1}H-NMR signals associated to the abdc linker (Figure 1). A linear correlation between the solid composition and the starting solution can be established (Table 1).

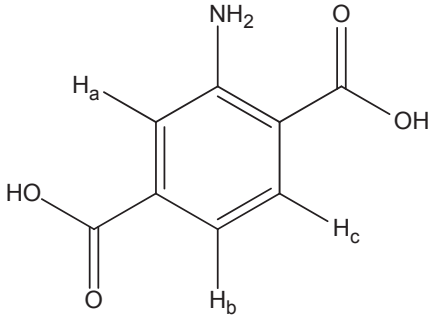

Figure 2. Aromatic protons of the abdc linker.

Table 1 Composition data of Al(OH)$(abdc)_n(bdc)_{1-n}$ samples.

Sample	% abdc in the solution	% abdc measured by ^{1}H NMR
A	0	0
B	11.1	10 ± 2
C	20	18 ± 2
D	50	49 ± 2
E	66.6	62 ± 5
F	100	100

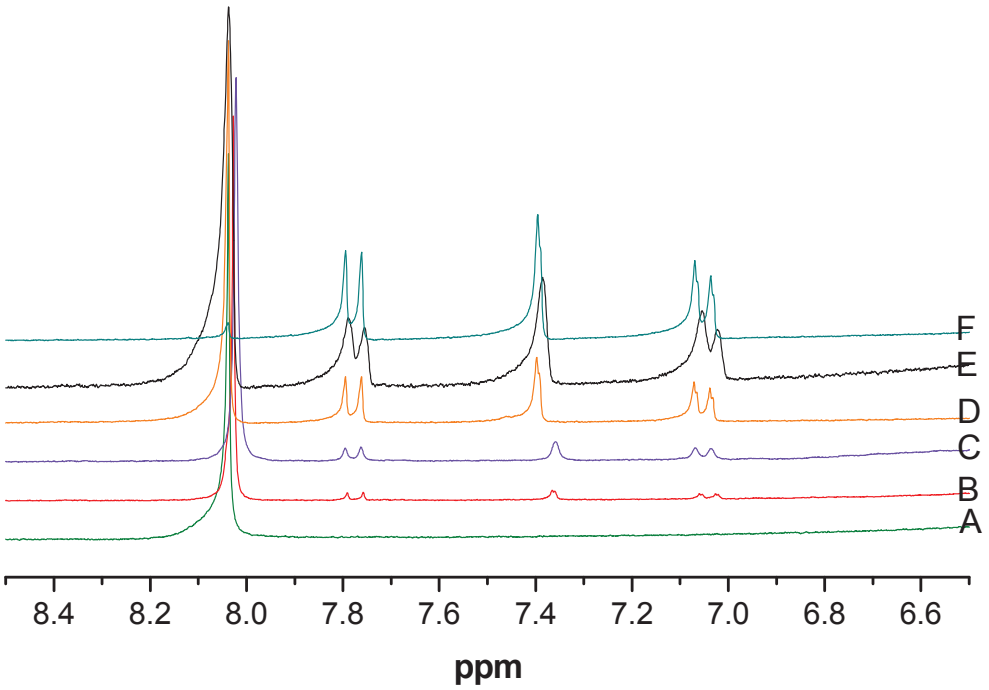

Figure 3. ^{1}H-NMR spectra of digested mixed-ligand Al-MIL-53.

In addition, for all samples, the absence of residual amounts of terephthalic acid and DMF is confirmed by liquid ^{1}H-NMR, solid-state ^{13}C-NMR (chapter 3) and DRIFT. We can thus conclude that the actual composition of the frameworks corresponds to the results given by the digestion-liquid ^{1}H-NMR technique.

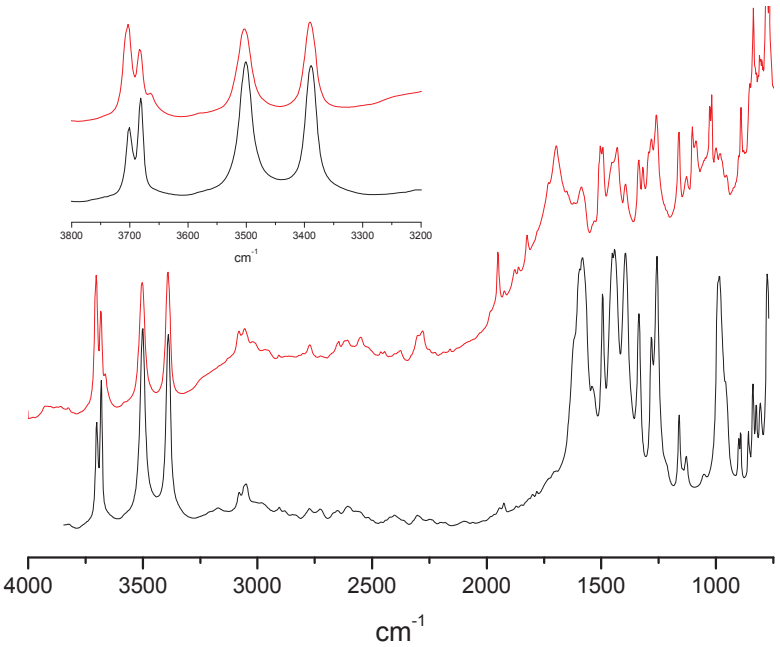

Figure 4. Drift spectrum of MIL-53(Al)-NH_2 (F-black line/bottom) and MIL-53(Al)-20%NH_2 (C-red line/top) after one hour desorption at 100°C.

The adsorption bands at 3500 and 3390 cm^{-1} correspond to the symmetric and asymmetric stretching of the primary amine. The doublet at 3660 and 3700cm-1 is due to the bridging OH in the chains of trans corner-sharing $AlO_4(OH)_2$ octahedra[29].The broad signals between 3100 and 2500 cm^{-1} are due to the hydroxyl group in the presence of NH_2 group. Large signals between 1600 and 1300 cm^{-1} are carboxylic acid function. The C=O band of free acid and DMF are not observed[16].

III.2.2. Crystallite morphology

SEM on $Al(OH)(bdc)_{1-n}(abdc)_n$ samples was carried out with a Stereoscan 260 SEM microscope. All samples exhibit a platelet-like morphology with a mean size about 1 µm. For samples with low abdc content, we can observe submicronic rounded particles that aggregate on top of the platelets. Noteworthy, MIL-53(Al)-NH_2 (F) shows very high particle homogeneity in terms of shape and size (Figure 5).

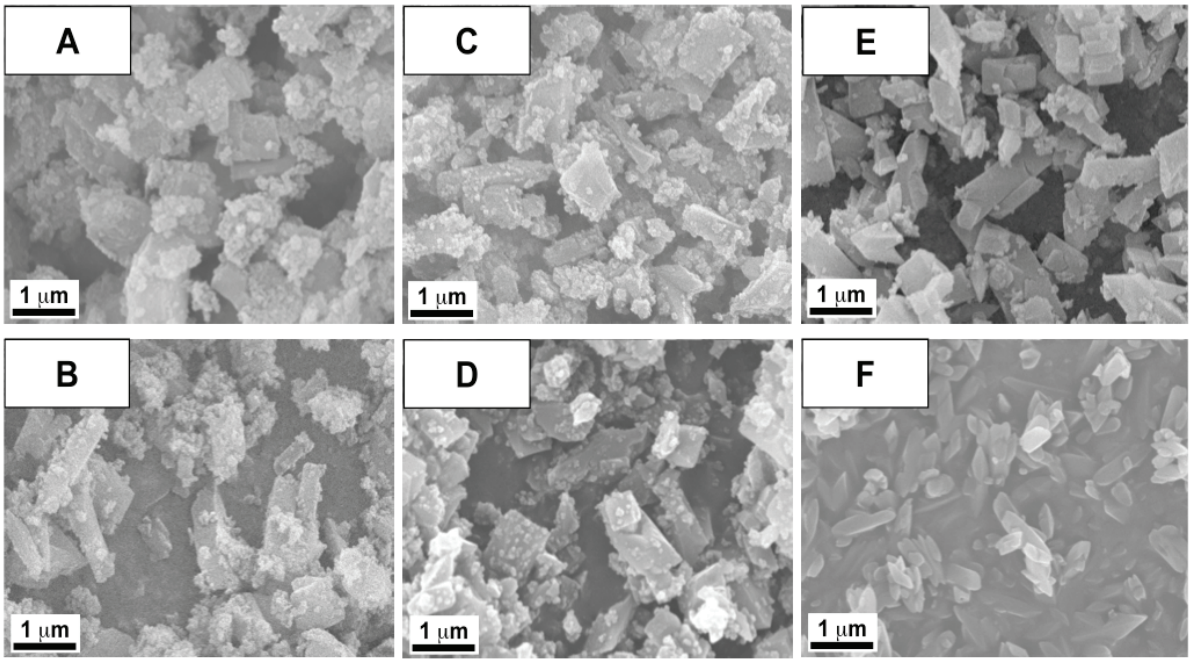

Figure 5. SEM micrographs of samples A-F.

III.2.3. N_2 physisorption

Nitrogen physisorption isotherms were measured at 77.4 K using a Micromeritics 2020 apparatus. Prior to the measurements, the samples were activated under secondary vacuum at 150°C for 24 h. Specific surface areas were calculated using the BET equation (p/p_o=0.05-0.25) on the adsorption branch, unless otherwise specified.

Except for MIL-53(Al)-NH_2 (F), the solids from A to E show a type-I isotherm for N_2 physisorption (Figure 6 top). The microporous volumes (t-plot method) and BET surface areas are in the same range and correspond to values reported in the literature for Al-MIL-53 (Table 2).[30, 31] The adsorption isotherm for the Al(OH)(abdc) solid (sample F) shows an S-shaped profile and a desorption branch displaying a type-I behaviour. This unusual sorption pattern with a large hysteresis loop has already been reported for pure MIL-53(Al)-NH_2[16]. The lower pore volume (0.37 $cm^3 \cdot g^{-1}$) and BET surface area (940 $m^2 \cdot g^{-1}$) of this sample are in good agreement with a shrinking of the unit cell as computed by DFT modelling.[32]

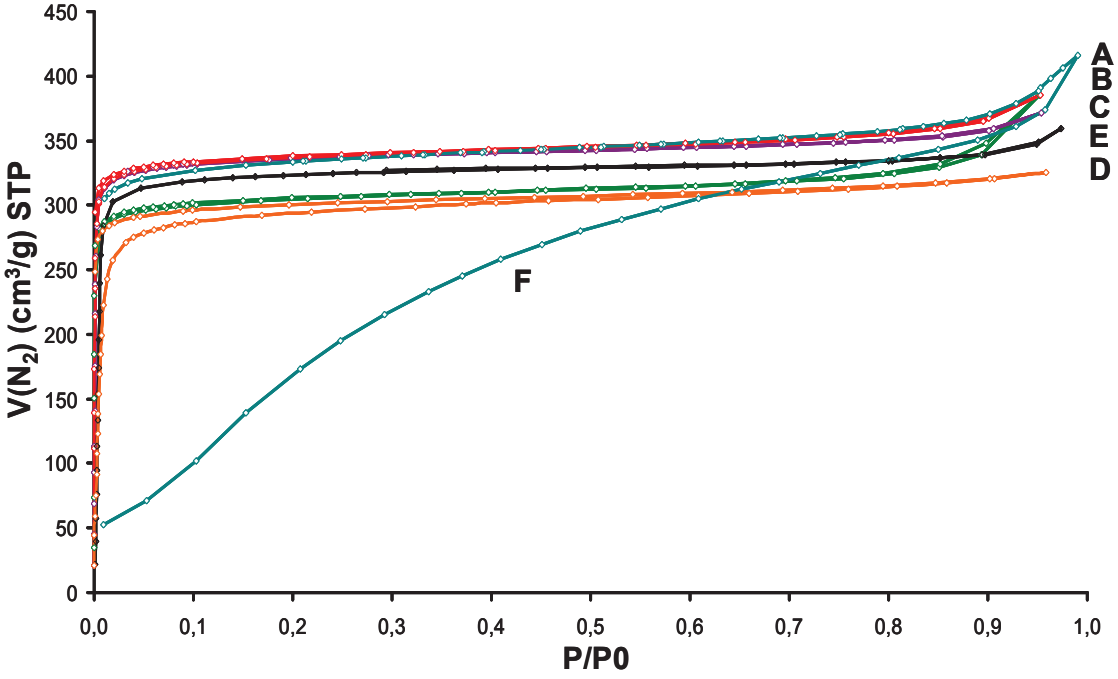

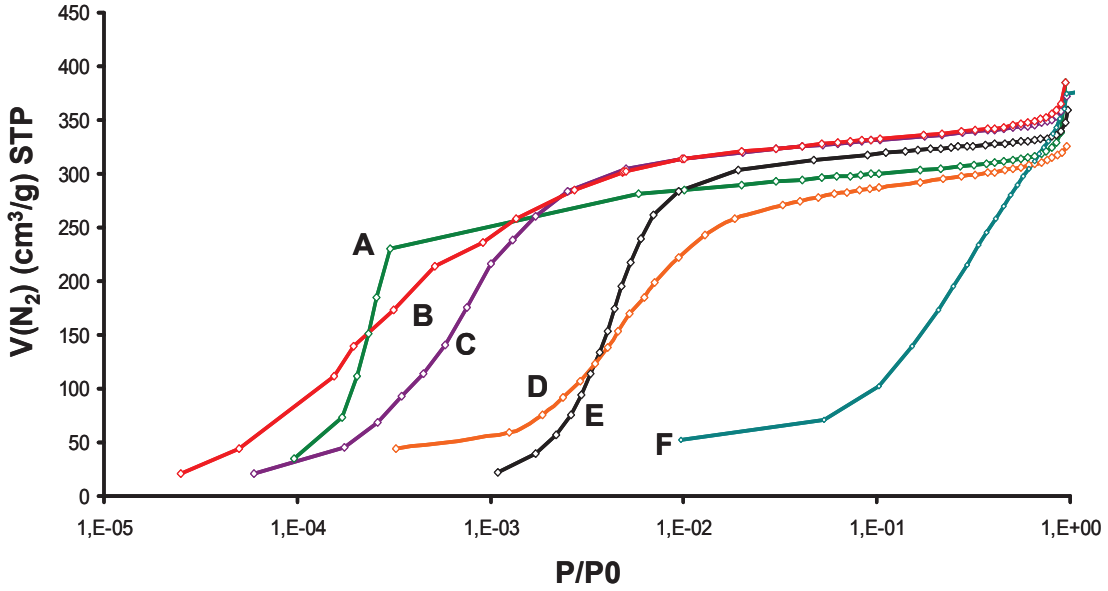

Figure 6. Nitrogen adsorption/desorption isotherms at 77 K (linear scale): A (green line), B (red line), C (purple line), D (orange line), E (black line) and F (turquoise line). On top, high-pressure region; on bottom, highly resolved isotherms at low pressures.

Table 2. Textural properties of $Al(OH)(abdc)_n(bdc)_{1-n}$ samples as inferred from N_2 adsorption/desorption at 77.4 K.

Sample	% abdc measured	V_{micro} † [$cm^3 \cdot g^{-1}$]	S_{BET} [$m^2 \cdot g^{-1}$]
A	0	0.51	1041
B	10±2	0.48	1048
C	18±2	0.51	1090
D	49±2	0.46	1100
E	62±5	0.50	1017
F	100	0.37	940#

† computed by the t-plot method, # computed from the desorption branch

By plotting the adsorbed N_2 volume as a function of the logarithm of the relative pressure (see Figure 6 bottom), we observe that the pressure at which the N_2 uptake begins depends mainly on the abdc content. The N_2 uptake is shifted to higher pressures as the amine content increases. We attribute this trend to a decrease of the N_2 affinity with the degree of amino-substitution in the MIL-53(Al)_lp framework rather than to a variation of the pore size.

III.2.4. CO_2 adsorption properties

CO_2 adsorption/desorption isotherms were measured on a BELSORP-HP microvolumetric apparatus at 30°C. The samples were outgassed under vacuum (~10^{-4} mbar) at 150°C for 12 h before the measurements.

Figure 7 plots the CO_2 adsorption-desorption isotherms at 30°C on the different amino-functionalized MIL-53(Al) samples prepared in this study. As already reported for pure MIL-53(Al) and MIL-53(Al)-NH_2, all samples display two distinct adsorption steps assigned, respectively, to lp→np and np→lp phase transitions at low and high CO_2 pressures.[32] Regardless of the amine loading, a plateau level of ~2 mmol·g^{-1} is attained for the different samples corresponding to ~0.5 CO_2 per μ-OH[33, 34]. This result suggests that an equal number of adsorption sites for the np phase for all samples.

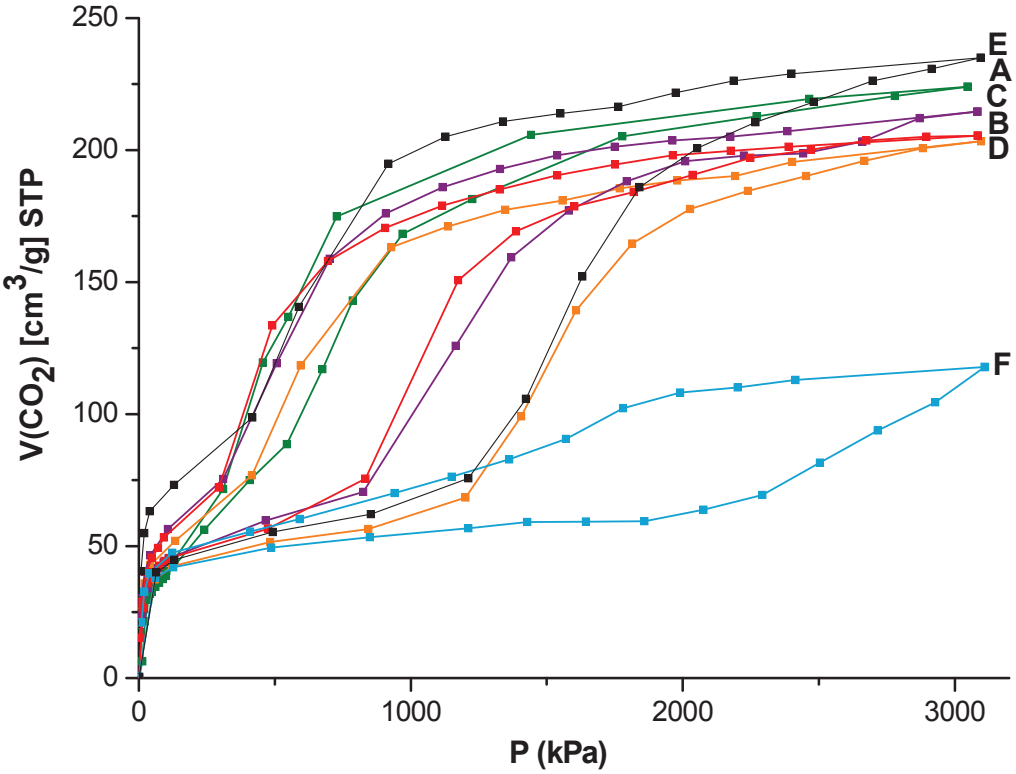

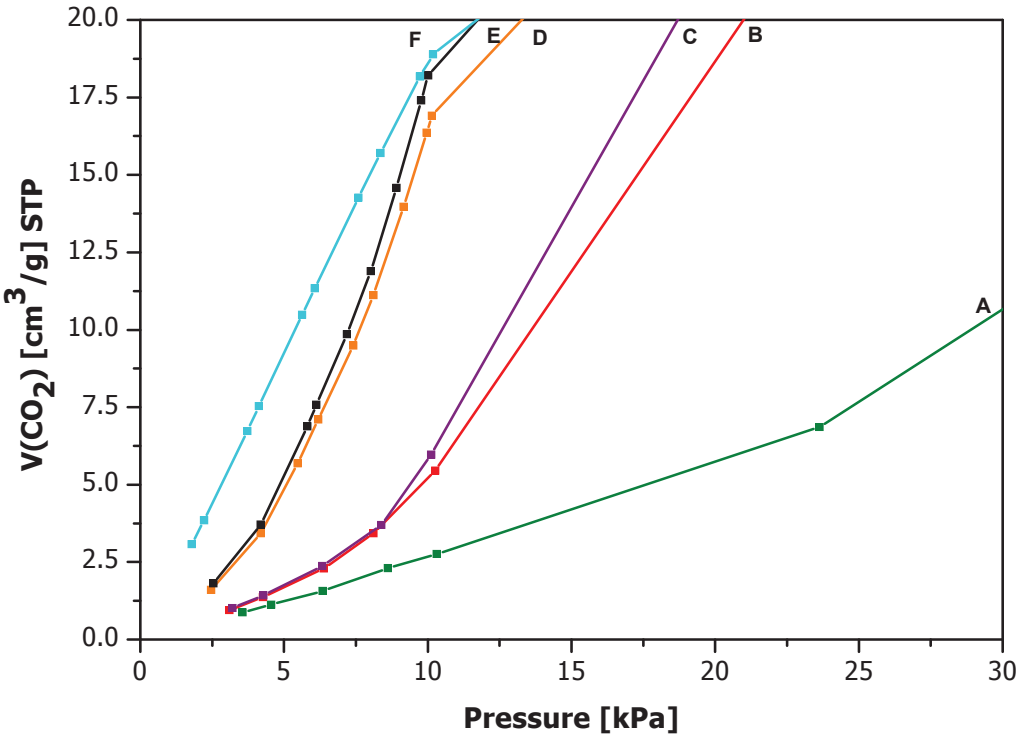

Figure 7. CO_2 physisorption isotherms at 30ºC of $Al(OH)(abdc)_n(bdc)_{1-n}$ samples: A (green line), B (red line), C (purple line), D (orange line), E (black line) and F (turquoise line).

At low pressure (<100 kPa), we see a linear correlation of the Henry constant with the abdc content (Table 3 and Figure 8). This can be explained on the basis of the higher heat of CO_2 adsorption on the amino-functionalized samples through formation of hydrogen bonds with pending amines and bridging μ-OH groups.[32] Note that the meaning of Henry constant should to be considered with care for soft porous crystals. Indeed, we have shown the absence of a genuine Henry's region in pure MIL-53(Al)-NH_2 and MIL-68(In)-NH_2 solids.[35] In this study, we consider the initial slope of the isotherm as the Henry constant although the selected Henry regions were not strictly linear. Nevertheless, this constant is a relevant descriptor of the surface-substrate interaction. At higher pressure (>100 kPa), the breathing pressure corresponding to the second transition increases with the abdc content from a value of 665 kPa for Al(OH)(bdc) (A) to 1770 kPa for Al(OH)(abdc) (F). This observation suggests a higher stabilization of the np structure with the degree of amine functionalization due to an increasing number of hydrogen bonds.[32]

Table 3. CO_2 adsorption data of $Al(OH)(abdc)_n(bdc)_{1-n}$ samples.

Sample	% abdc measured	P_{G1} / P_{G2}[‡] [kPa]	H[§] [$cm^3(STP)\cdot g^{-1}\cdot kPa^{-1}$]
A	0	1665	0.27
B	10±2	740	0.36
C	18±2	960	0.44
D	49±2	1110	0.93
E	62±5	1260	1.39
F	100	1770	1.96

[‡] phase transition pressures (30ºC) upon CO_2, [§] Henry constant for CO_2

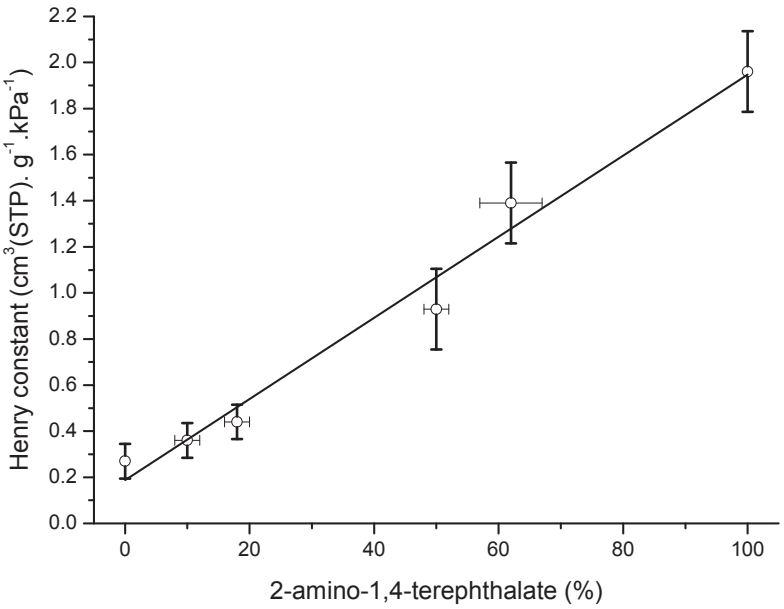

Figure 8. Evolution of the Henry constant for CO_2 adsorption as a function of the abdc content for $Al(OH)(abdc)_n(bdc)_{1-n}$.

III.2.5. Temperature-dependent XRD patterns

Powder X-ray diffraction patterns were recorded using a Panalytical X'Pert Pro MPD (Bragg–Brentano geometry, reflection mode) equipped with a secondary graphite monochromator (CuK alpha, wavelength 0.154184 nm) and a 1-dimensional multistrip detector (X'Celerator, 127 channels on 2.1°). The samples were mounted in an atmosphere-controlled Anton Paar XRK 900 reactor chamber. The temperature-regulated glass-ceramic sample holder was open to allow gas to flow through the sample (synthetic air 40 $mL\cdot min^{-1}$). Heating was

performed up to 480°C at a rate of 2°C·min^{-1}. XRD data at the desired temperature were collected after 10 min. The XRD measurements were carried out with an automatic variable divergence slit (8 mm irradiated length) at 127 min per scan (0.0334° 2Θ and 512 s per step) and converted into fixed slit mode.

The unit cell parameters of the np and lp phases were calculated by using whole powder pattern fitting (Fullprof code[36]) starting from crystal data of MIL-53(Al)_lt and MIL-53(Al)_ht.[31] The ratio of the np-lp phases is determined using the area of the main diffraction line of the phases, namely the (110) line at about 11.95° (2θ) for the np phase and the (011) line at about 8.72° (2θ) for the lp phase.

Temperature-dependent powder X-ray diffraction was performed on Al(OH)(abdc)$_n$(bdc)$_{1-n}$ samples (A-D and F) under ambient air (i.e. in the presence of moisture, Figure 6). Strong discrepancies in the breathing pressures are observed. A characteristic np→lp phase transition can be detected at 60°C for Al(OH)(bdc), whereas this structural change is not observed for Al(OH)(abdc). At intermediate abdc contents, the phase transition spreads over a wide range of temperatures that depends on the abdc content. For samples B, C and D, both np and lp phases coexist over a certain temperature range.

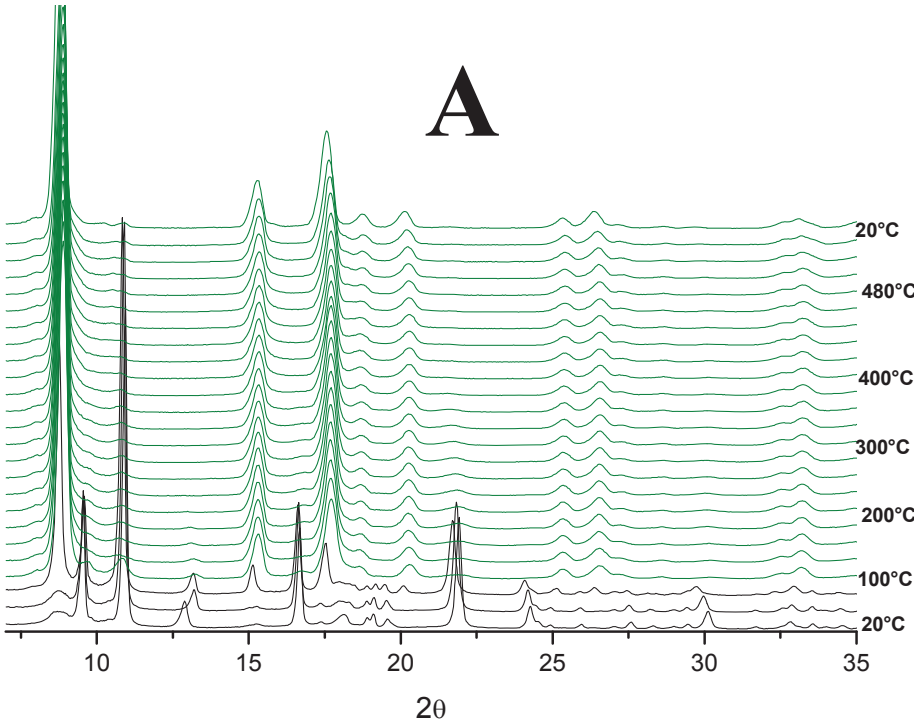

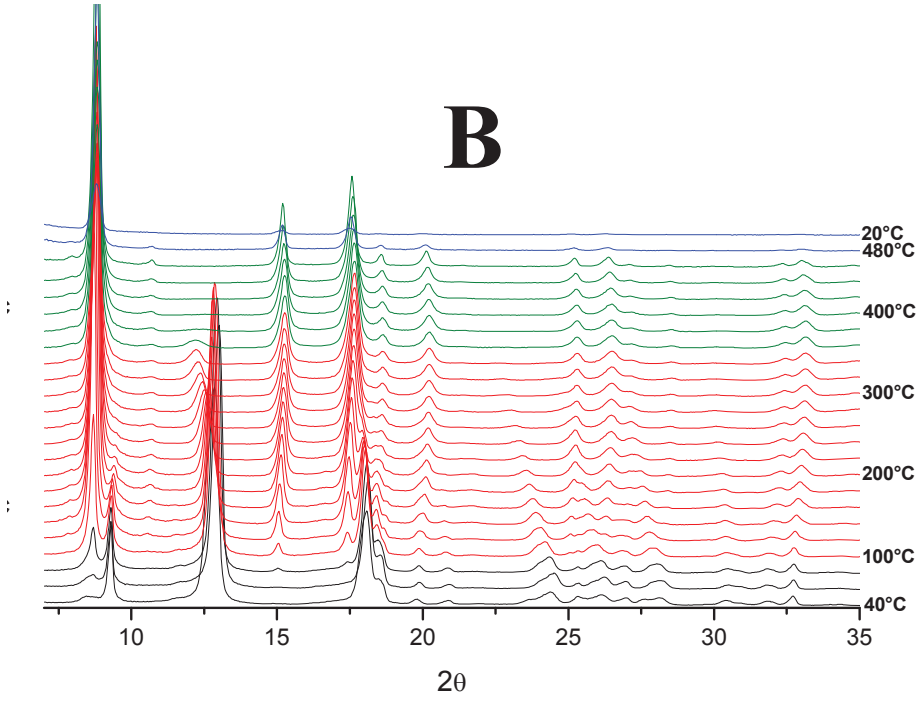
B
20°C
480°C
400°C
300°C
200°C
100°C
40°C
10
15
20
25
30
35
2θ

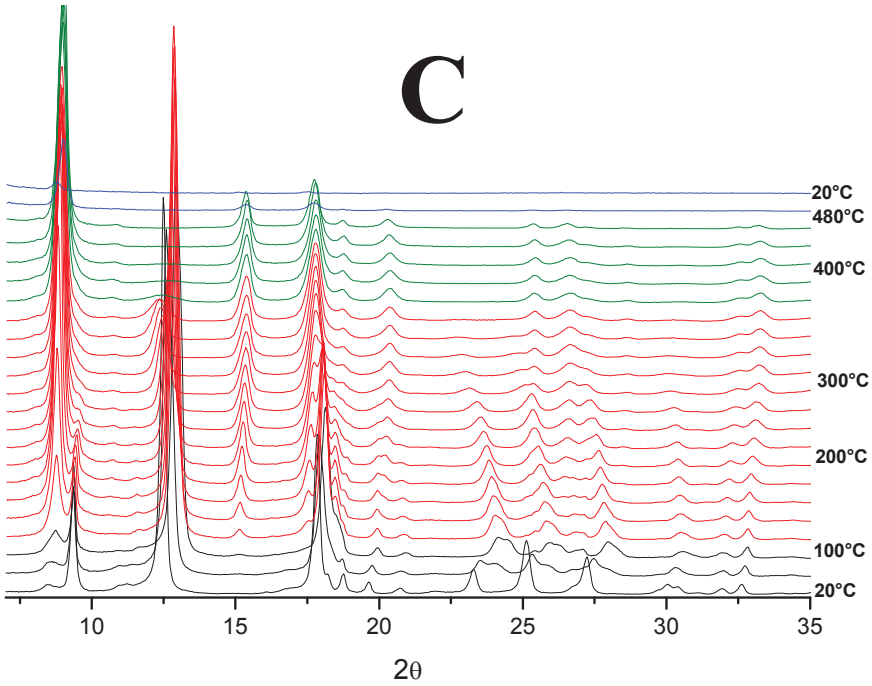
C
20°C
480°C
400°C
300°C
200°C
100°C
20°C
10
15
20
25
30
35
2θ

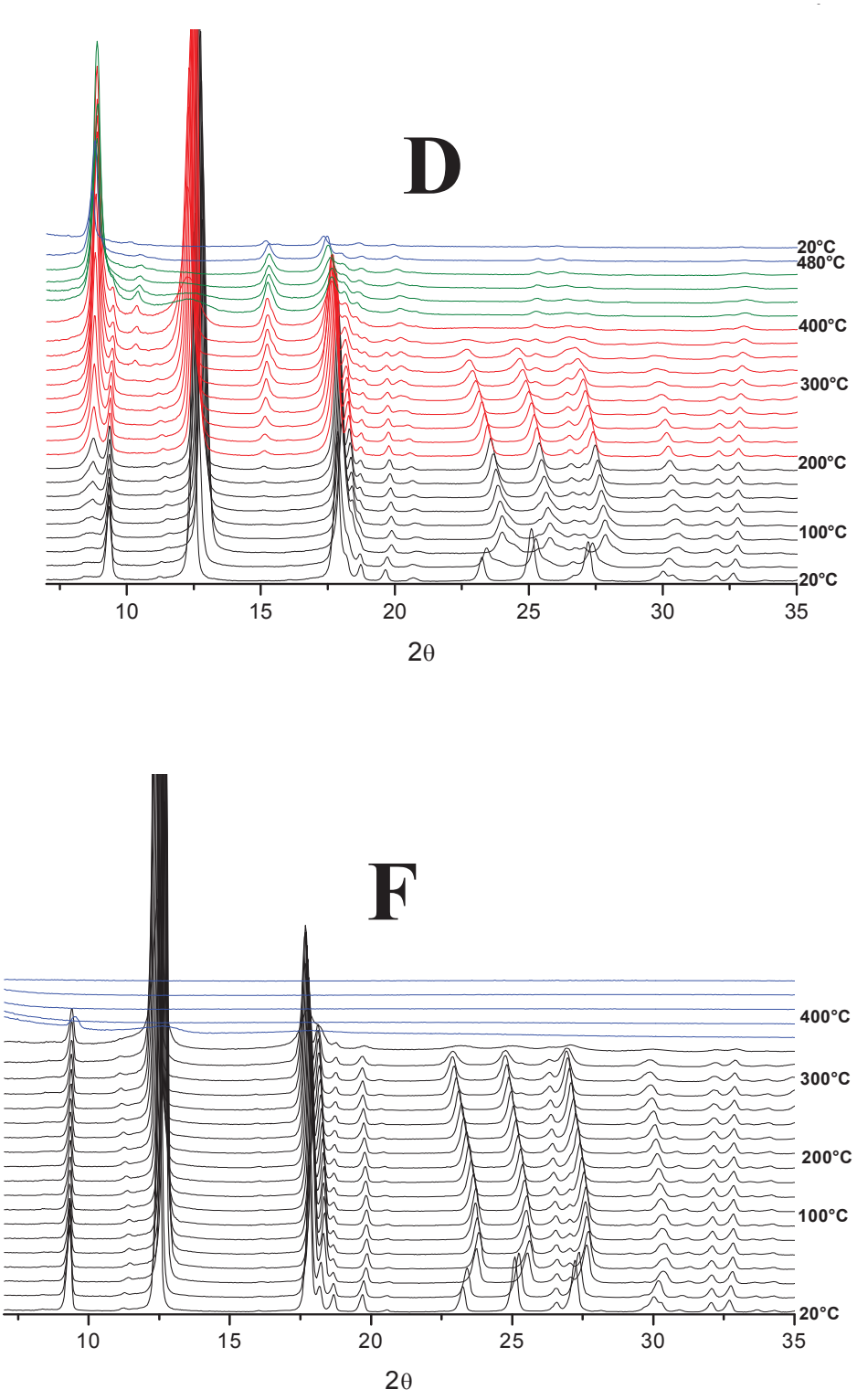

Figure 9. Thermodiffractograms of A, B, C, D and F. Key: single np phase (black), single lp phase (green), simultaneous presence of np and lp phases (red), amorphous phase (blue).

The ratio between the lp and np phases can be evaluated through the refinement of PXRD datas. These values must be considered carefully, since PXRD is not generally viewed as very

appropriate for performing quantitative measurements on samples with a mixture of phases. Nevertheless, the measurements and calculations are accurate enough to observe different trends for the samples. The relative amounts of the lp phase of the different samples are reported as a function of the temperature in Figure 10. Obviously, the phase transition is facilitated for samples with low abdc content. The breathing temperatures to attain a 1:1 mixture of np-lp phases are approximately 125°C, 175°C and 375°C, respectively, for samples (B), (C) and (D). Even at low abdc contents (sample B), we can still observe the presence of the np phase at high temperature (Table 4).

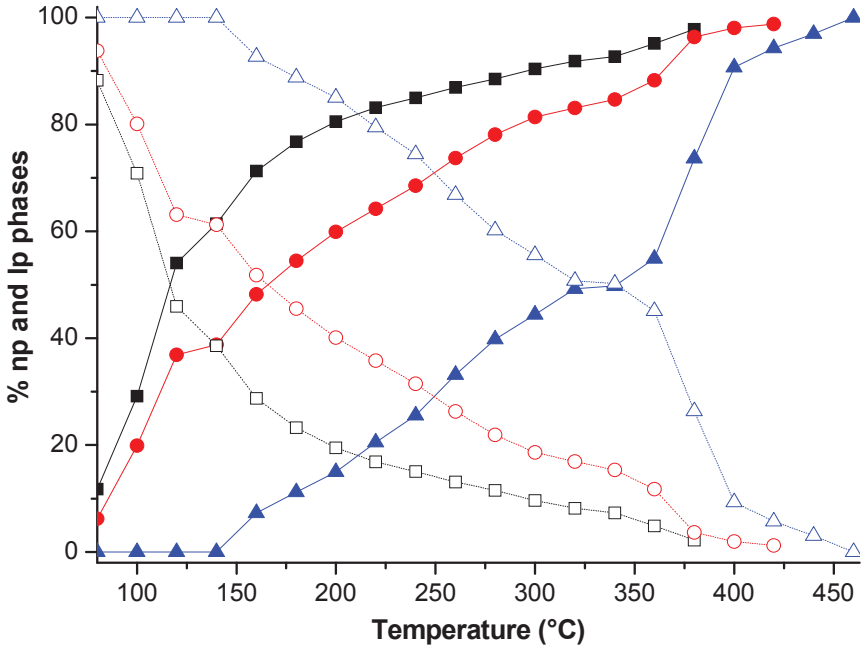

Figure 10. Evolution of the np (empty symbols)-lp (filled symbols) phase ratio as a function of temperature for B (square), C (circle) and D (triangle) samples.

Table 4. Behavior of $Al(OH)(abdc)_n(bdc)_{1-n}$ samples as a function of temperature.

Sample	% abdc measured	Temperature of disappearance of the np phase [°C]	Temperature of appearance of the lp phase [°C]	Collapsing temperature [ºC]
A	0	60	60	>480
B	10±2	360	100	480
C	18±2	380	100	480
D	49±2	380	200	480
F	100	n.a.	n.a.	380

The evolution of the unit cell parameters of the np and lp phases as a function of the temperature has also been investigated. For Al(OH)(bdc) (sample A), the unit cell volume of the lp phase keeps almost constant, showing a slight decrease from 1415 $Å^3$ at 100°C to 1410 $Å^3$ at 480°C. In contrast, the temperature has a much more complex effect on the unit cell parameters for the abdc-containing samples. For example, the evolution of the unit cell volume with temperature is shown for samples (B) and (C) (Figure 11). For both samples, the unit cell volume of the lp phase decreases first from 1440 $Å^3$ at 100°C to 1415 $Å^3$ at 350°C. From 350°C onwards, the unit cell volume increases abruptly. Note that this temperature corresponds to the disappearance of the np phase for the samples. On the other hand, the unit cell volume of the np phase increases linearly with the temperature until this phase disappears.

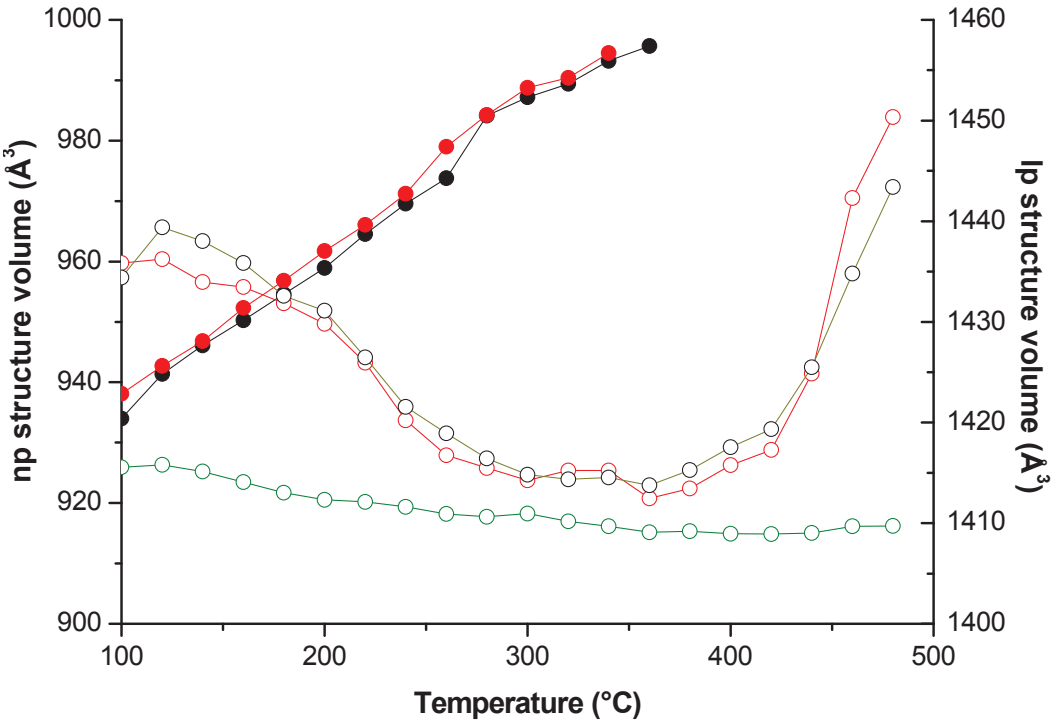

Figure 11. Evolution of the cell volume of the np and lp phases as a function of temperature. Key: np structure (filled circle), lp structure (empty circle). (A) (green), B (black) and C (red).

III.3 Discussion

In general, adsorption-desorption isotherms are used to characterize structural properties of microporous materials. Under conditions approaching substrate condensation and/or saturation, the total microporous volume can be evaluated. For all samples, the volumes

correspond to the values expected. We can therefore rule out the presence of significant amount of non-porous phases such as aluminates. Furthermore, the evolution of the gas uptake at low pressure (in Henry's region) makes possible to characterize the surface chemistry of the porous materials by measuring host-guest interactions. The linear relationship between the Henry's constant and the abdc content that is observed for CO_2 adsorption provides a clear evidence of the homogeneity of the samples at the microdomain level. This trend is further confirmed by the characteristic breathing pressures for CO_2 adsorption at high pressure (P_{CO2}>100 kPa), increasing with the amino content. It is worth mentioning that a mechanical mixture of separate Al-MIL-53 and MIL-53(Al)-NH_2 crystallites would result in a two-step adsorption isotherm in the respective "breathing" regions. For this reason, we rule out the presence of discrete crystallites of different phases. (figure 12).

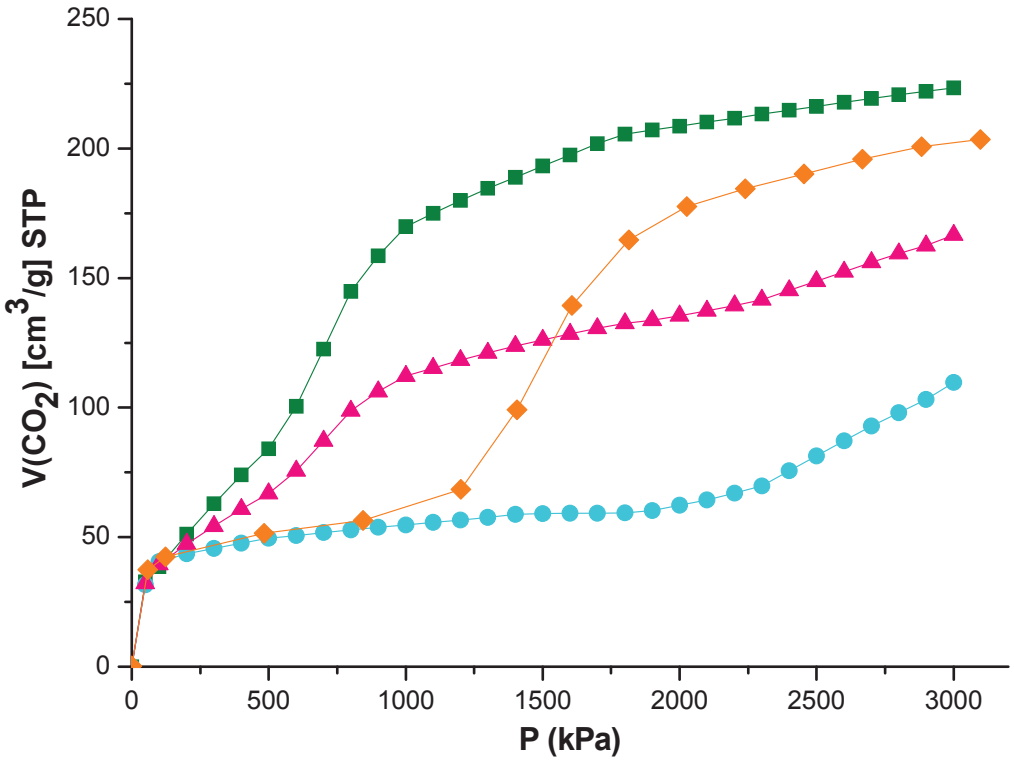

Figure 12. Calculated CO2 isotherm of a stoichiometric mixture of MIL-53(Al) and MIL-53(Al)-NH_2 (pink triangle).
MIL-53(Al) (green square), MIL-53(Al)-NH_2 (Blue round) and MIL-53(Al)-50%NH_2 (orange losange) are also showed for comparison.

It is noteworthy that the CO_2 gate opening pressure measured on the pure Al(OH)(abdc) sample (F), 1770 kPa, differs significantly from the value of 1200 kPa reported by Gascon *et al.*[32, 33] However the CO_2 uptake at 3000 kPa approaches ~6 mmol.g^{-1} for this sample, which is in good agreement with Gascon *et al.*[32] We believe that such different isotherm profiles may arise

from different crystallite sizes originating from different synthesis recipes. In this study, isolated crystallites of very regular shape and size (0.5-1 µm) have been obtained starting from $AlCl_3$ as the precursor. Nevertheless, the pre-treatment procedure can affect the initial respective amounts of lp-np phases for the samples. Slight but significant modifications of N_2 isotherm profiles were reported by Stock *et al*[16] on MIL-53(Al)-NH_2 by performing several cyclic measurements. Obviously, further investigations are required especially for the pure MIL-53(Al)-NH_2 sample to discern about the structure of this solid.

The simultaneous presence of np and lp phases over a broad range of temperatures, as observed here for B-D samples, was already reported for MIL-53(Ga).[37] Whereas the pure MIL-53(Al) framework transforms readily into the lp phase at low temperature (T=50°C), the MIL-53(Ga) analogue still shows the np phase at T=220°C. In turn, the simultaneous presence of both np and lp phases in abdc-containing MIL-53(Al) cannot be exclusively ascribed to a hypothetical lack of homogeneity of linker distribution within the frameworks. Indeed thermodiffractograms of a stoichiometric mixture of MIL-53(Al) and MIL-53(Al)-NH_2 has been calculated (Figure 13) and present a completely different profile than MIL-53(Al)-50%NH_2 (D).

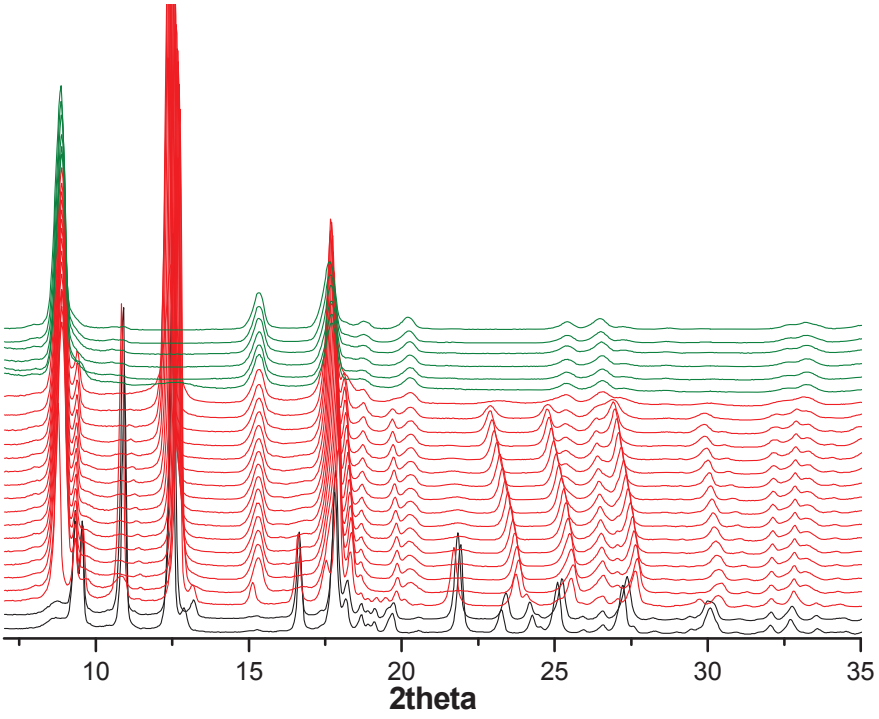

Figure 13. Calculated thermodiffractograms of a stoichiometric mixture of Al-MIL-53 and MIL-53(Al)-NH_2.

Moreover, the temperature-evolution profile of the np and lp unit cell volumes might

suggest an interplay between crystalline microdomains (Figure 11). It seems clear that the unit cell volume of the lp phase increases abruptly when the np phase disappears (and is converted into the lp phase). We suggest that the crystallites could consist of np and lp X-ray microdomains and that the np phase coerces a strain on the lp phase preventing it from a free expansion.

IV. MIL-68(In), a "mixed linkers" MOF synthesized by precipitation method

In order to evaluate the influence of the amino grafting rate, MIL-68(In)-20%NH_2 have been synthesized and characterized. This material will be used in chapter 5 as starting materials for post-functionalization.

IV.1. Synthesis

Indium nitrate (1 203.3mg, 4mmol), abdc (144.9mg, 0.8mmol) and bdc (531.2mg, 3.2mmol) were dissolved in DMF (30ml). The reaction mixture was stirred for 5 minutes then a solution of 4-diazabicyclo[2.2.2] octane (DABCO) (897.4mg, 8mmol) in DMF (10ml) were added. The reaction mixture was stirred for 120 minutes at room temperature. The obtained precipitate was washed with DMF in an autoclave at 150 °C overnight follow by a dichloromethane soxhlet during 24h.

IV.2 Characterization

IV.2.1 Composition by liquid ^{1}H-NMR

NMR of the fully digested MIL-68(In)-20%NH_2 reveals a molecular percentage of 16.7%. This result is slightly lower than the 20% introduce in the mixture. It seems the terephthalic linker reacted a little bit faster than the amino analogue in presence of base.

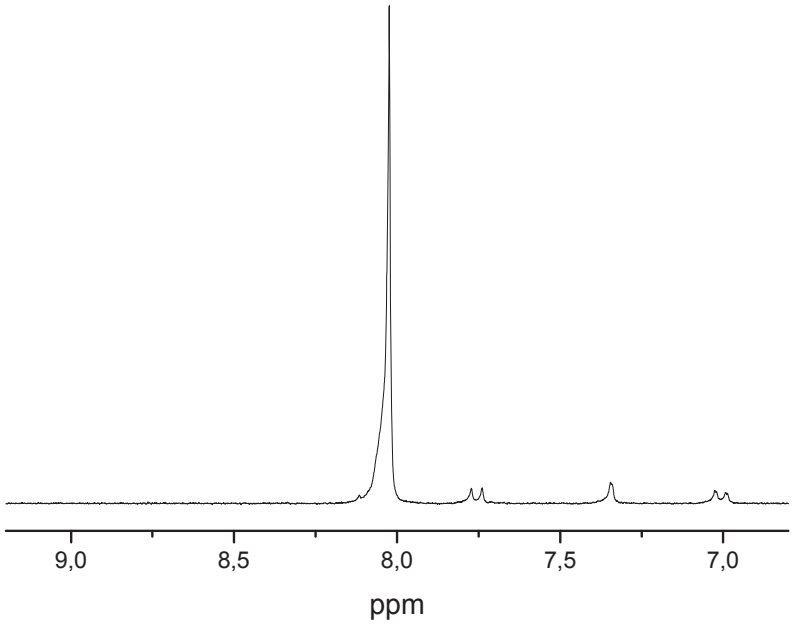

Figure 14. NMR spectrum aromatic protons of MIL-68(In)-20%NH_2.

IV.3.4. ^{1}H liquid NMR

^{1}H NMR of the digested materials was performed. Results are identical to those previously published [17, 38] and confirmed that the MOFs are empty of any organic solvant or remaining reactants (figure 15).

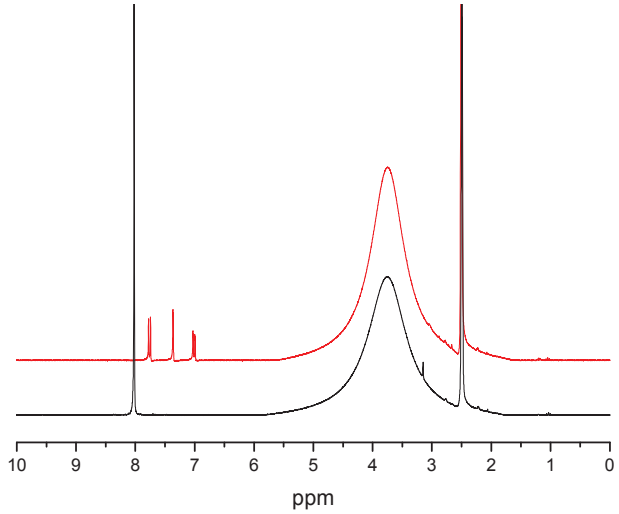

Figure 15. Liquid ^{1}H NMR spectrum of MIL-68(In) (bottom-black line) and MIL-68(In)-NH_2 (top-red line).

IV.2.2 PXRD pattern

The X-ray diffraction patterns of MIL-68(In) and MIL-68(In)-NH_2 are identical and

correspond to a structure discovered by Ferey *et al*[38] (figure 16).

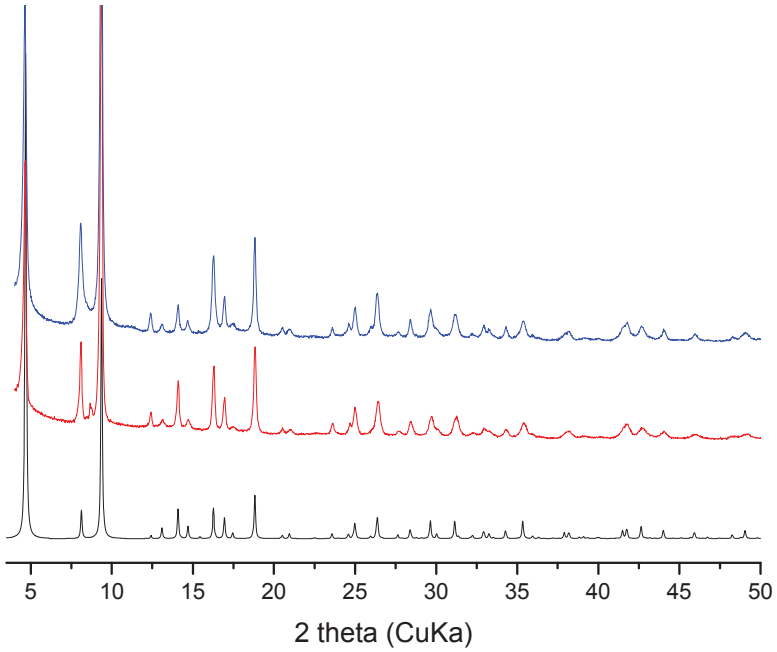

Figure 16. Powder X-ray diffraction patterns of simulated MIL-68(In) (black-bottom), experimental MIL-68(In) (red, middle) and experimental MIL-68(In)-NH2 (blue, top)

MIL-68(In)-20%NH_2 has the same XRD pattern than is fully functionalized analogue.

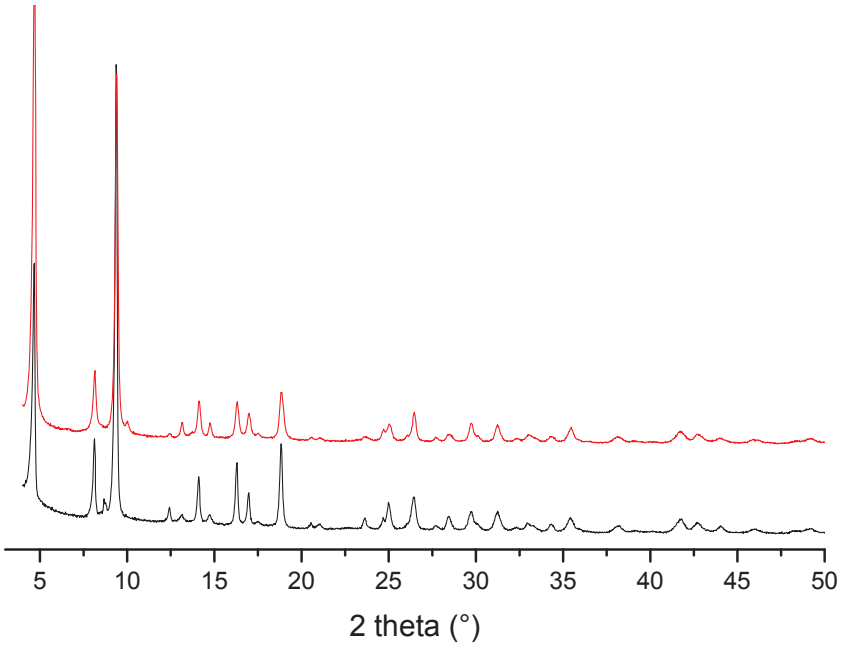

Figure 17. XRD pattern of MIL-68(In)-20%NH_2 (red line/top) and MIL-68(In)-NH_2 (black line/bottom).

IV.2.3 Nitrogen physisorption

Nitrogen isotherm of MIL-68(In)-20%NH_2 shows a type II trend. BET surface areas of MIL-68(In)-20%NH_2 is 1182m^2/g which is very close to the MIL-68(In)-NH_2 BET surface areas (1120 m^2/g).

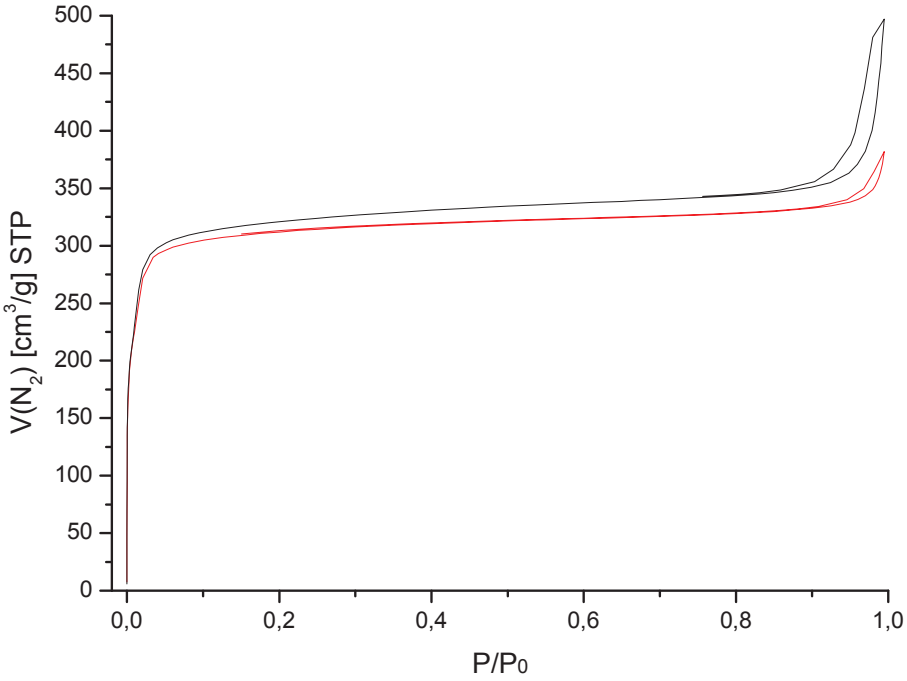

Figure 18. Nitrogen isotherm of MIL-68(In)-20%NH_2 (red line) and MIL-68(In)-NH_2 (black line)

IV.2.4 DRIFT spectroscopy

DRIFT spectroscopy was performed on MIL-68(In)-20%NH_2 and MIL-68(In)-NH_2. Both present the characteristic signals of MIL-68. Nevertheless the ratio amino signal area/ hydroxyl signal area is small in the case of MIL-68(In)-20%NH_2 compare to its fully functionalized analogue.

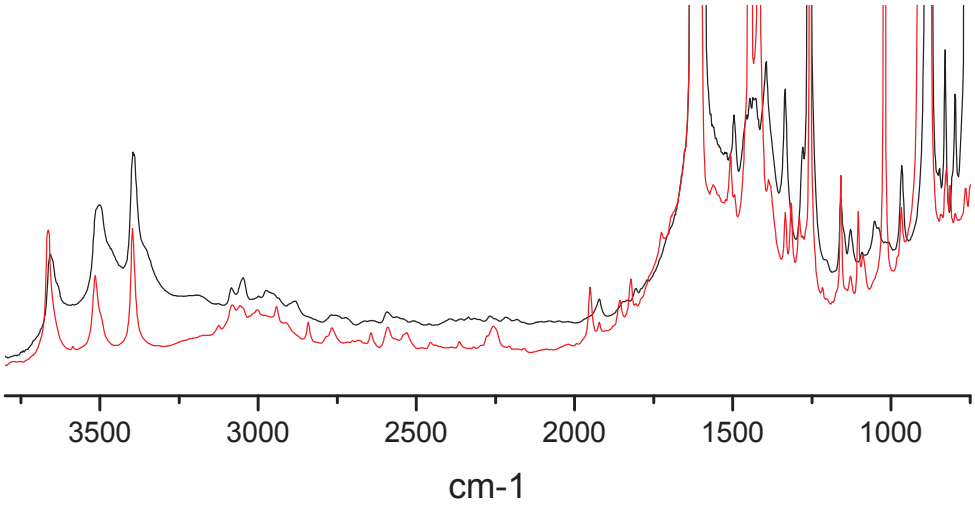

Figure 19. DRIFT pattern of MIL-68(In)-20%NH_2 (red line, bottom) and MIL-68(In)-NH_2 (black line, top).

IV.2.5 TGA

MIL-68(In)-20%NH_2 show slightly higher stability than MIL-68(In)-NH_2. MIL-68(In)-20%NH_2 collapsed at 395°C instead of 355°C for MIL-68(In)-NH_2. The weight lost between 20 and 100°C correspond to the evaporation of the water contained on the surface and in the pores (2 and 4%). The weight loss of 53-54% correspond to the removal of the organic linker and the formation of the Indium(III) oxide.

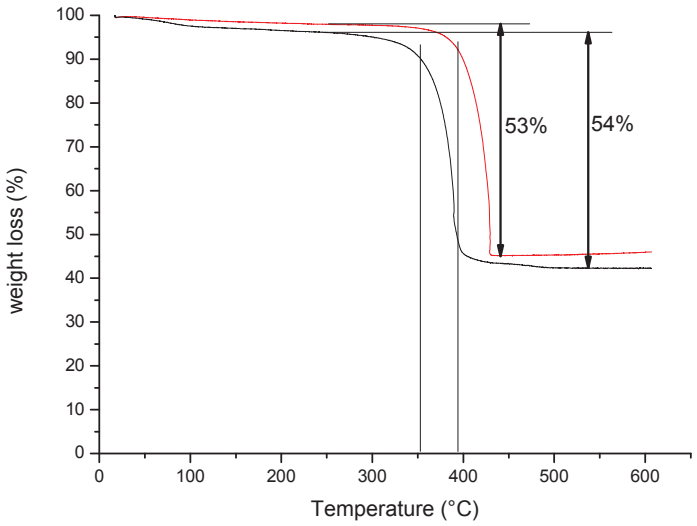

Figure 20. TGA curve of MIL-68(In)-20%NH_2 (red line) and MIL-68(In)-NH_2 (black line).

IV.3 Discussion

The synthesis of multivariable MOF can thus be extended to the precipitation synthesis. It seems that the terephthalic linker reacts a slightly faster than the amino analogue in the presence of base. MIL-68(In)-20%NH_2 has the same structure and BET surface area than other MIL-68 materials. TGA shows that the decrease of the abdc content from 100% to 16.7% increase by 40°C the collapsing temperature.

V. Conclusions

We have shown that the breathing pressure and temperature can characterize the homogeneity of flexible MOFs formulated as microcrystalline powders. The linear trends between the breathing pressure and the amine content in the Al-MIL-53 structure clearly indicate the homogeneity of the crystallite composition, i.e. the microcrystallites have the same abdc:bdc ratio. On the other hand, adsorption techniques cannot rule out the presence of a linker distribution at a microcrystalline level. The application of highly spatially resolved techniques to address this question will undoubtedly represent a breakthrough for the characterization of functionalized MOFs such as "mixed linkers" MOFs or post-modified MOFs.

We have also shown that the functionalization of MIL-53(Al) with a small amount of amine groups (i.e., 10% abdc) results in a profound modification of the breathing properties triggered by the temperature. Much higher temperatures are required for the full conversion of the np into the lp phase, in agreement with a previous DFT modeling study.[32] We also suggest a possible interaction between coexisting np and lp microcrystalline domains that might "smooth" the breathing properties at the macroscopic level.

This "mixed linkers" strategy has been extended to precipitation synthesis and In-MIL-68-20%NH_2 has been synthesized. The use of base modify the reactivity of the linkers and the abdc:bdc ratio in the solid is slightly lower than in the synthesis mixture.

VI. References

[1] G. Ferey, *Chem. Soc. Rev.*, **2008**, **37**, 191-214.
[2] G. Ferey and C. Serre, *Chem. Soc. Rev.*, **2009**, **38**, 1380-1399.
[3] S. Kitagawa and K. Uemura, *Chem. Soc. Rev.*, **2005**, **34**, 109-119.
[4] J. A. R. Navarro, E. Barea, A. Rodriguez-Diéguez, J. M. Salas, C. O. Ania, J. B. Parra, N. Masciocchi, S. Galli and A. Sironi, *J. Am. Chem. Soc.*, **2008**, **130**, 3978-3984.
[5] S. Horike, S. Shimomura and S. Kitagawa, *Nat Chem*, **2009**, **1**, 695-704.

[6] D. Farrusseng, *Metal-Organic Frameworks: Applications from Catalysis to Gas Storage*, WILEY-VCH, 2011.
[7] O. M. Yaghi, M. O'Keeffe, N. W. Ockwig, H. K. Chae, M. Eddaoudi and J. Kim, *Nature*, **2003**, **423**, 705-714.
[8] N. L. Rosi, J. Eckert, M. Eddaoudi, D. T. Vodak, J. Kim, M. O'Keeffe and O. M. Yaghi, *Science*, **2003**, **300**, 1127-1129.
[9] T. Devic, P. Horcajada, C. Serre, F. Salles, G. Maurin, B. a. Moulin, D. Heurtaux, G. Clet, A. Vimont, J.-M. Grenèche, B. L. Ouay, F. Moreau, E. Magnier, Y. Filinchuk, J. m. Marrot, J.-C. Lavalley, M. Daturi and G. Férey, *J. Am. Chem. Soc.*, **2009**, **132**, 1127-1136.
[10] K. Seki and W. Mori, *The Journal of Physical Chemistry B*, **2002**, **106**, 1380-1385.
[11] R. Banerjee, H. Furukawa, D. Britt, C. Knobler, M. O'Keeffe and O. M. Yaghi, *J. Am. Chem. Soc.*, **2009**, **131**, 3875-3877.
[12] W. Morris, B. Leung, H. Furukawa, O. K. Yaghi, N. He, H. Hayashi, Y. Houndonougbo, M. Asta, B. B. Laird and O. M. Yaghi, *J. Am. Chem. Soc.*, **2010**, **132**, 11006-11008.
[13] J. Pérez-Pellitero, H. Amrouche, F. R. Siperstein, G. Pirngruber, C. Nieto-Draghi, G. Chaplais, A. Simon-Masseron, D. Bazer-Bachi, D. Peralta and N. Bats, *Chem. Eur. J.*, **2010**, **16**, 1560-1571.
[14] H. Deng, C. J. Doonan, H. Furukawa, R. B. Ferreira, J. Towne, C. B. Knobler, B. Wang and O. M. Yaghi, *Science*, **2010**, **327**, 846-850.
[15] F. Hinterholzinger, C. Scherb, T. Ahnfeldt, N. Stock and T. Bein, *Physical Chemistry Chemical Physics*, **2010**, **12**, 4515-4520.
[16] T. Ahnfeldt, D. Gunzelmann, T. Loiseau, D. Hirsemann, J. r. Senker, G. Férey and N. Stock, *Inorg. Chem.*, **2009**, **48**, 3057-3064.
[17] M. Savonnet, D. Bazer-Bachi, N. Bats, J. Perez-Pellitero, E. Jeanneau, V. Lecocq, C. Pinel and D. Farrusseng, *Journal of the American Chemical Society*, **2010**, **132**, 4518-4519.
[18] M. Savonnet, E. Kockrick, A. Camarata, D. Bazer-Bachi, N. Bats, V. Lecocq, C. Pinel and D. Farrusseng, *New J. Chem.*, **2011**, **35**, 1892-1897.
[19] K. K. Tanabe and S. M. Cohen, *Angew. Chem.-Int. Edit.*, **2009**, **48**, 7424-7427.
[20] J. Canivet, S. Aguado, G. Bergeret and D. Farrusseng, *Chem. Comm.*, **2011**, **47**, 11650-11652.
[21] Z. Q. Wang and S. M. Cohen, *Chem. Soc. Rev.*, **2009**, **38**, 1315-1329.
[22] Z. Q. Wang and S. M. Cohen, *J. Am. Chem. Soc.*, **2007**, **129**, 12368-+.
[23] T. Fukushima, S. Horike, Y. Inubushi, K. Nakagawa, Y. Kubota, M. Takata and S. Kitagawa, *Angew. Chem., Int. Ed.*, **2010**, **49**, 4820-4824.
[24] T. Lescouet, E. Kockrick, G. Bergeret, M. Pera-Titus and D. Farrusseng, *Dalton Trans.*, **2011**, **40**, 11359-11361.
[25] W. Kleist, M. Maciejewski and A. Baiker, *Thermochim. Acta*, **2009**, **499**, 71-78.
[26] W. Kleist, F. Jutz, M. Maciejewski and A. Baiker, *Eur. J. Inorg. Chem.*, **2009**, **2009**, 3552-3561.
[27] A. D. Burrows, L. C. Fisher, C. Richardson and S. P. Rigby, *Chem. Comm.*, **2011**.
[28] S. Marx, W. Kleist, J. Huang, M. Maciejewski and A. Baiker, *Dalton Trans.*, **2010**, **39**, 3795-3798.
[29] S. Couck, J. F. M. Denayer, G. V. Baron, T. Rémy, J. Gascon and F. Kapteijn, *J. Am. Chem. Soc.*, **2009**, **131**, 6326-6327.
[30] S. Biswas, T. Ahnfeldt and N. Stock, *Inorg. Chem.*, **2011**, **50**, 9518-9526.
[31] T. Loiseau, C. Serre, C. Huguenard, G. Fink, F. Taulelle, M. Henry, T. Bataille and G. Férey, *Chem. Eur. J.*, **2004**, **10**, 1373-1382.
[32] E. Stavitski, E. A. Pidko, S. Couck, T. Remy, E. J. M. Hensen, B. M. Weckhuysen, J. Denayer, J. Gascon and F. Kapteijn, *Langmuir*, **2011**, **27**, 3970-3976.
[33] A. Boutin, S. Couck, F. X. Coudert, P. Serra-Crespo, J. Gascon, F. Kapteijn, A. H. Fuchs and J. F. M. Denayer, *Microporous Mesoporous Mat.*, **2010**, **140**, 108-113.
[34] A. Boutin, F. o.-X. Coudert, M.-A. Springuel-Huet, A. V. Neimark, G. Férey and A. H. Fuchs, *J. Phys. Chem. C*, **2010**, **114**, 22237-22244.
[35] M. Pera-Titus, M. Savonnet and D. Farrusseng, *The Journal of Physical Chemistry C*, **2010**, **114**, 17665-17674.

[36] Y. M. Juan and E. Kaxiras, *Pysi. Rev B*, **1993**, **48**, 14944-14952.
[37] C. Volkringer, T. Loiseau, N. Guillou, G. Ferey, E. Elkaim and A. Vimont, *Dalton Trans.*, **2009**, 2241-2249.
[38] C. Volkringer, M. Meddouri, T. Loiseau, N. Guillou, J. Marrot, G. Ferey, M. Haouas, F. Taulelle, N. Audebrand and M. Latroche, *Inorg. Chem.*, **2008**, **47**, 11892-11901.

Chapter 5

Alternative pathway for the synthesis of isocyanato and urea-functionalised metal-organic frameworks

I. Introduction

Many post-functionalization approaches have been developed for MOFs; they range from simple condensation reactions to more complex methods involving protection/deprotection steps[1, 2]. Examples of the latter are post-modification methods used in polymer science (click chemistry)[3, 4] and biochemistry (peptide coupling).[5]

MOFs constructed from 2-aminoterephthalate, such as IRMOF-3,[3, 4] and hereafter referred to as amino MOFs, are the most common starting platforms for post-synthesis because they can easily be obtained as long as their unfunctionalised counterparts exist. Currently, we can account for at least nine different amino MOF structures: UMCM-1-NH_2,[6] IRMOF-3,[7] DMOF-1(-NH_2),[8] MOF-LIC-1,[9] MIL-68(-NH_2)[4], MIL-53(-NH_2)[10], UiO-66(-NH_2)[11], MIL-101(-NH_2)[10, 12] and MIL-125(-NH_2)[13]. Another important advantage is the low cost of 2-aminoterephthalic acid, which enables the preparation of large quantities of MOFs on the laboratory scale. Amino MOFs nevertheless present a major drawback for their post-functionalisation: reactivity is limited due to the relatively weak nucleophilicity of the amino substituent on the aromatic ring. Strongly electrophilic molecules such as acid anhydrides, acyl chlorides or isocyanates must therefore be used to carry out such chemical reactions[1, 14-16]. Unfortunately, only a few of these molecules are commercially available. Also, in the case of condensation with acyl chloride, the liberation of hydrogen chloride strongly damages the structure of most MOFs.

An alternative strategy is to convert the amino groups into a more reactive functionality. This approach has already been developed by Cohen *et al*., who reported the transformation of the NH_2 group into an isocyanate group using a diphosgene treatment.[17] The presence of the isocyanate group facilitates the grafting of a large library of amines or alcohols to form ureas and carbamates. Nevertheless, this diphosgene-based reaction can be applied only to the most stable MOFs, such as Al-MIL-53-NH_2. In fact, the hydrogen chloride produced during the reaction is generally detrimental to the structural integrity of the MOF.

Following this idea of increasing substituent reactivity, we converted the amino group into an azido group in order to enable click chemistry reactions. A simple method was devised to form azido MOFs by the reaction of tert-butylnitrite (tBuONO) and trimethylsilyl azide ($TMSN_3$) on amino MOFs.[3, 4] This substitution allows the one-pot synthesis of a combinatorial library of post-modified MOFs with diverse functions[18]. Recently, Kitagawa *et al*. described a soft method to activate the azido groups of a functionalised MOF (CID-N_3) under ultraviolet irradiation and make them react with oxygen. The authors concluded that this method could be generalised for use with other guest molecules such as CO in order to form isocyanato groups[19]. This approach

presents two main advantages compared to previously-described post-functionalisation methods: (i) it requires no solvent and (ii) no purification is required to remove organic by-products. Nevertheless, the simplicity of this procedure is compromised by the complex synthesis of 5-azidoisophthalic acid linker through the use of hazardous sodium azide.

To the best of our knowledge, there is no generic method of obtaining an isocyanate-grafted MOF starting from an amino structure. In this article, we describe in a step-by-step fashion the post-functionalisation of four amino MOFs into azido, isocyanato and finally urea MOFs (respectively, steps I, II and III in Scheme 1). Al-MIL-53 was chosen in order to permit a comparison with previously-published results obtained for functionalised MIL-53. In addition, In-MIL-68 was selected because its sensitivity makes it unsuitable for the diphosgene route (Scheme 1; route IV). Finally, two mixed-ligand MOFs based on the MIL-53 and MIL-68 structures were synthesised in order to control site density. The aminoterephthalate linker (abdc) was partially substituted by terephthalate (bdc) to form a homogeneous material of molar ratio abdc:bdc = 1:4[20, 21]. The percentage of functional group per linker is provided at the end of material names (*e.g.*, Al-MIL-53-20%NCO or In-MIL-68-20%NCO). Finally, we evaluated the efficiency of each transformation and compared it to the state of the art.

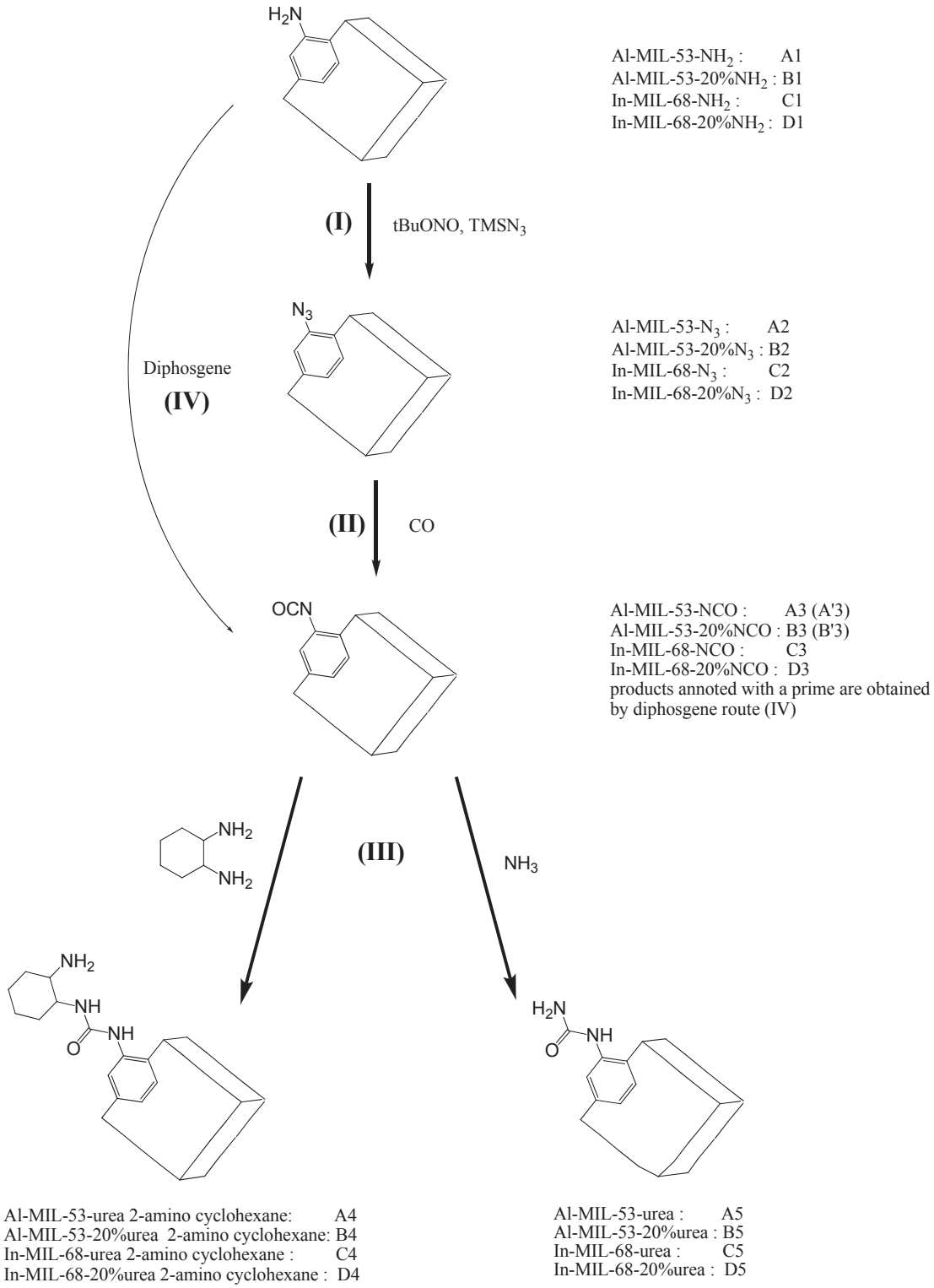

Scheme 1. Alternative pathway for the synthesis of isocyanato and urea-functionalised metal-organic frameworks.

II. Experimental

II.1. Synthesis

A typical azido synthesis was carried out to form the following MOFs: Al-MIL-53-N_3, **A2**; In-MIL-68-N_3; **B2**; Al-MIL-53-20%N_3, **C2** and In-MIL-68-20%N_3, **D2**. In this procedure, freshly dried Al-MIL-53-NH_2 (**A1),** In-MIL-68-NH_2 (**B1**), Al-MIL-53-20%NH_2 (**C1**) and In-MIL-68-20%NH_2 (**D1)** (200 mg, 0.73 mmol equiv of -NH_2) were placed into a vial (10 mL capacity) with 3.0 mL of solvent (THF), 1.5 mL (12.65 mmol) of tBuONO and 1.4 mL (10.64 mmol) of $TMSN_3$. Samples were left to react for 6 hours at room temperature to produce the azido MOFs. The reaction was quenched by decanting the solvent. Excess reactants were removed by washing three times in THF followed by three times in CH_2Cl_2. Drying at room temperature yielded yellowish powders[3, 4, 18].

Al-MIL-53-NH_2 (**A'3**) and Al-MIL-53-20%NH_2 (**B'3**) were prepared by the synthesis reported by Cohen *et al.*[17] Diphosgene (0.5 mL, 4.14 mmol) was added to stirred suspensions of **A1** and **B1** (200 mg, 0.73 mmol equivalent of -NH_2) in THF (5 mL). After 15 h, solids were removed by centrifugation, washed three times with fresh THF and dried at reduced pressure[17].

Isocyanato MOFs (Al-MIL-53-NCO: **A3**, In-MIL-68-NCO: **B3**, Al-MIL-53-20%NCO: **C3** and In-MIL-68-20%NCO: **D3**) were synthesised by allowing the reaction of CO gas with the dried MOF powders. The transformations were followed in a Diffuse Reflectance Infrared Fourier Transform (DRIFT) apparatus. **A2**, **B2**, **C2** and **D2** were placed in the DRIFT cell and desorbed at 100°C overnight under argon. The temperature was raised to 150°C prior to the introduction of flowing CO (22 mL/min). After 24 hours, the reaction was stopped and the products were collected.

Al-MIL-53-20%urea 2-amino cyclohexane (**B4**) and In-MIL-68-20%urea 2-amino cyclohexane (**D4**) were synthesised by adding (1*R*,2*R*)-1,2-diaminocyclohexane (0.5 mL, 4.16 mmol) to 200 mg **B3** and **D3**, respectively, in dried acetonitrile (4 mL). Mixtures were stirred and heated at 40°C for at least 48 h. The resulting solids were washed three times with fresh acetonitrile, and then DCM Soxhlet extractions were performed for 20 h.

The synthesis of Al-MIL-53-20%urea (**B5**) and In-MIL-68-20%urea (**D5**) was conducted in the DRIFT apparatus in order to characterise the transformations over time by treating **B3 and D3** at 90°C with an argon flow containing 1% NH_3 over a 24-hour period.

II.2. Analysis

All NMR spectra were recorded with the same automated procedure for routine analysis using a Bruker Avance 250 spectrometer operating at 250 MHz for ^{1}H. The spectra were calibrated using the DMSO signal. Due to their high chemical stability, the Al-MIL-53 samples were digested in a 1% HF/DMSO-d_6 solution. In-MIL-68 materials were digested under the same conditions for purposes of comparison. Powder X-ray diffraction patterns were recorded using a Bruker D-5005 diffractometer (Bragg–Brentano geometry, graphite monochromator, Cu Kα radiation). Nitrogen isotherm measurements were performed at –196°C using a Belsorp Mini system (Bel Japan). Prior to the measurement, the samples were activated overnight under vacuum at 100°C. Specific surface areas were calculated using the Brunauer, Emmett and Teller (BET) equation. DRIFT spectra were measured at 25°C under argon flow using a Thermo Scientific Nicolet 8700 FT-IR spectrometer equipped with a MCT detector and a high temperature reaction chamber with ZnSe windows (Harrick). Prior to the measurement, the sample was activated at 100°C for 5 h. Thermogravimetric analysis (TGA) was performed with a SETARAM apparatus (Setsys Evolution 12-TG-DTA mode). Measurements were carried out under a flow of synthetic air (50 mL/min) with a 2°C/min heating ramp from room temperature to 600°C. The mass spectra were recorded on a hybrid quadrupole time-of-flight mass spectrometer (MicroTOFQ-II, Bruker Daltonics, Bremen) with an Electrospray Ionization ion source. The gas flow of spray gas is 0,6bar and the capillary voltage is 4,5kV. The solutions are infused at 180µL/h in a mixture of solvents (methanol/dichloromethane/water 45/40/15). The mass range of the analysis is 50-1000m/z and the calibration was done with sodium formate.

III. Results and discussion

The synthesis of isocyanate-functionalised MOFs and the grafting of amine upon them can be summarised as follows: synthesis of amino MOFs, conversion into azides (I), transformation into isocyanate moieties (II) and condensation with amines to form urea groups (III). For each stage, materials were fully characterised and selectivity was evaluated. The analytical results of the isocyanato MOFs obtained by this method are compared to those of the products synthesised by diphosgene treatment.

III.1. Step I: Transformation of amino MOFs into azido-functionalised MOFs

Amino MOFs (**A1** to **D1**) were successively treated by tert-butyl nitrite and $TMSN_3$ in THF to form azido MOFs (**A2** to **D2**). After reaction and workup, DRIFT spectra reveal an almost total disappearance of amine bands and the appearance of a new band at about 2110 cm^{-1} that is characteristic of the asymmetric stretching of N=N=N bonds (Figure 1).[17]

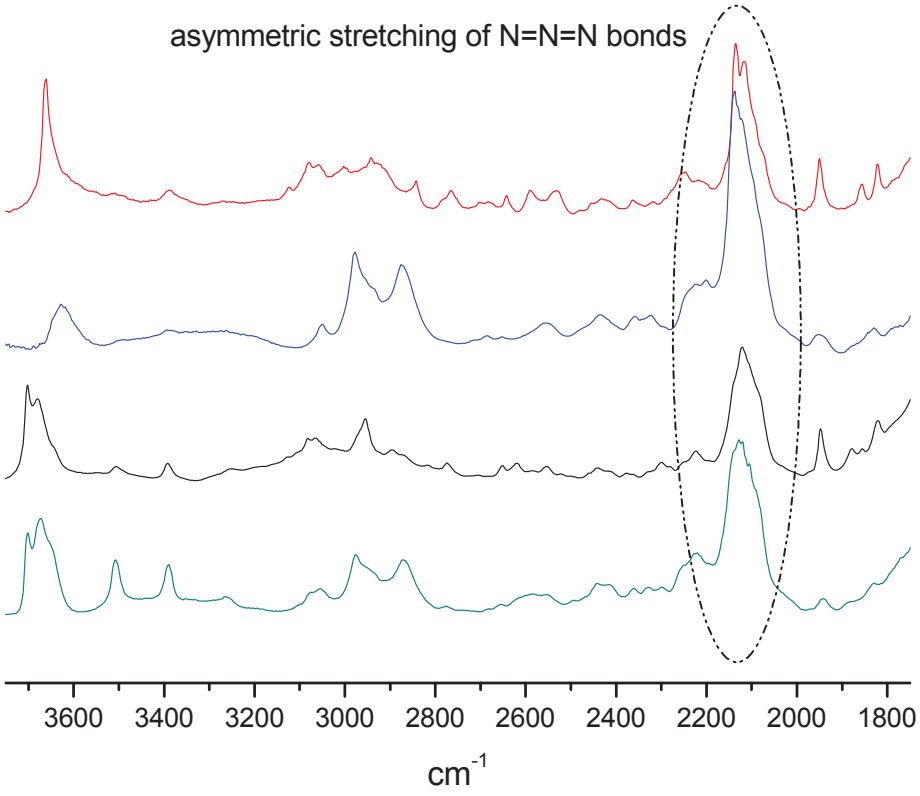

Figure 1. DRIFT spectra of **A2, B2, C2** and **D2** (from bottom to top).

An excellent method of quantifying the organic environment consists in observing the protons of the terephthalic linker through liquid state ^1H NMR spectroscopy following sample digestion. Indeed, the modification of the terephthalic ligand substitution strongly affects the chemical shift of aromatic protons. Amino MOF present two doublets (7 ppm, H_b and 7.75 ppm, H_c) and a singlet (7.35 ppm, H_a) that correspond to the three aromatic protons of 2-aminoterephthalic acid, as labelled in Scheme 2.

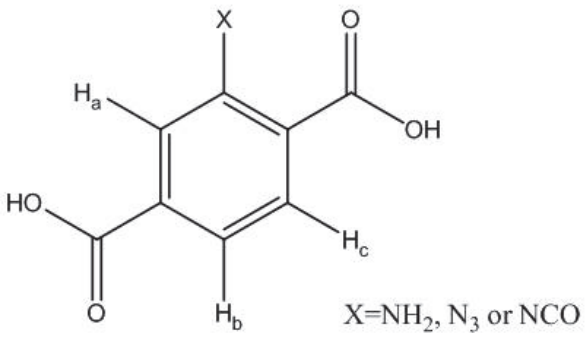

Scheme 2. Aromatic protons of substituted ligands

For the MOFs with 20% functionalised linker, the NMR spectra show an extra singlet at 8.02 ppm, which corresponds to the aromatic protons of pure terephthalic acid. Post-functionalisation conversions were also quantified by liquid ^{1}H NMR spectroscopy. Azido MOFs present a broad signal at around 7.75 ppm that corresponds to the superposition of the signals of the three aromatic protons. The integration of the different signals provides the conversion (Figure 2).

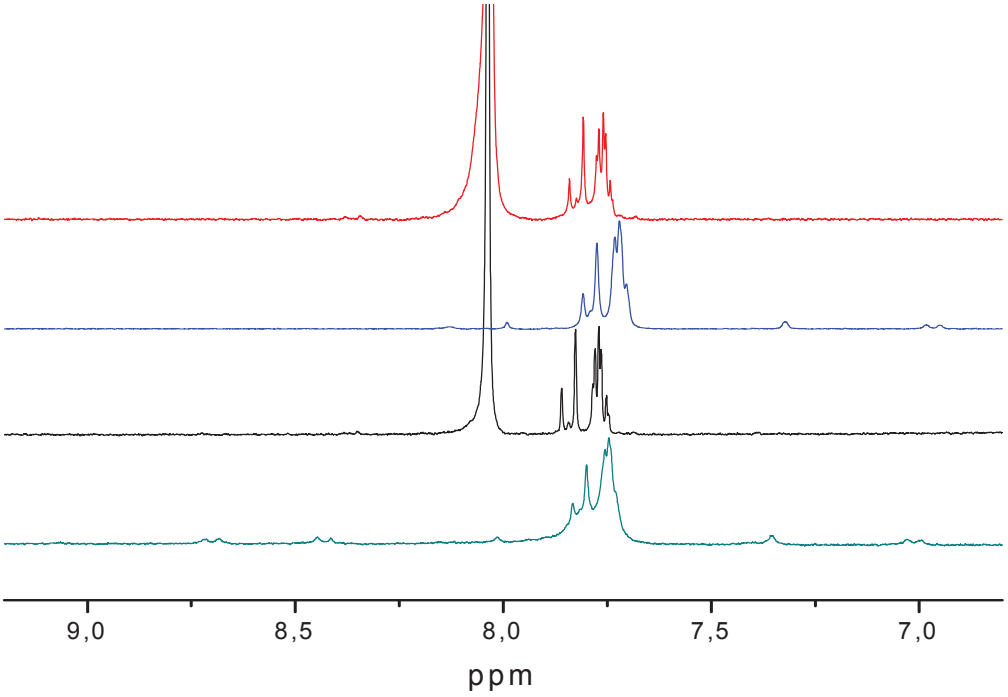

Figure 2. ^{1}H NMR spectrum of (from bottom to top) **A2**, **B2**, **C2** and **D2**.

Nearly complete conversions (95-100%) were obtained for all samples. Nevertheless, the signals that correspond to the stretching of amino species remain in the DRIFT spectra. In contrast to NMR, however, DRIFT spectroscopy is not a quantitative method, which means that the area of the amine signals cannot be compared to the area of the other signals. Moreover, no decrease in crystallinity was observed by PXRD after transformation (Figure 3).

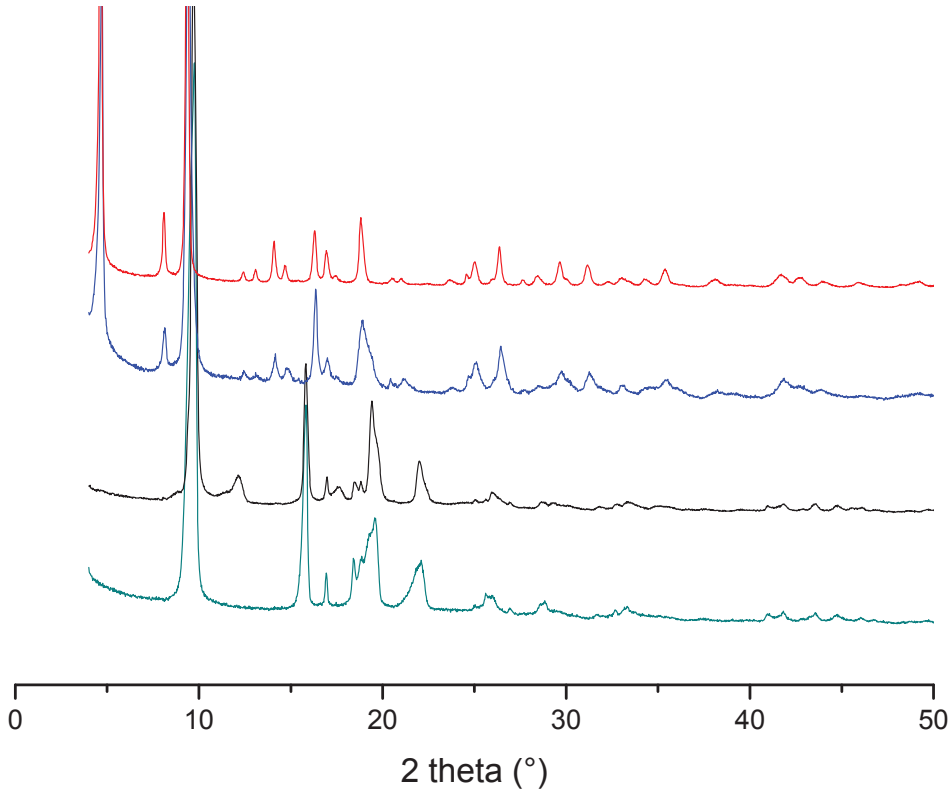

Figure 3. XRD pattern of (from bottom to top) A2, B2, C2 and D2.

Thermogravimetric analyses performed on **A2**, **B2**, **C2** and **D2** show a sharp exothermic peak at 150°C corresponding to the transformation of the azide into nitrene species (Figure 4). This temperature was consequently chosen for carrying out the transformation of azides into isocyanates.

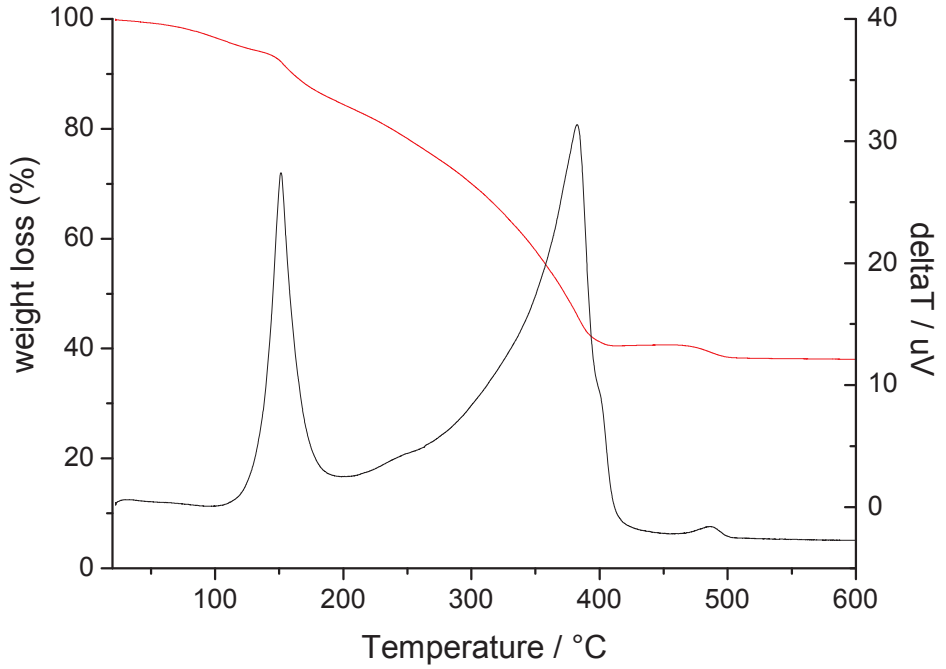

Figure 4. TGA of **C2** under synthetic air. Weight (red line) and temperature variation (black line)

III. 2. Step II: Transformation of azido MOFs into isocyanato MOFs

The transformation of azide-substituted MOFs (**A2** to **D2**) into their isocyanate analogues (**A3** to **D3**) by reaction with CO was followed *in operando* using the DRIFT apparatus. The DRIFT cell chamber was heated to 150°C, a constant flow of carbon monoxide was introduced and spectra were recorded at various times. These spectra revealed a decrease in the azide band (2110 cm^{-1}) and the appearance of a band at 2275 cm^{-1} attributed to the asymmetric stretching of the N=C=O bonds. Reactions carried out at a somewhat lower temperature (140°C) present either no conversion or very slow kinetics.

The conversion of the **A2** sample into isocyanate **A3** occurred over the first two hours. The azide signal decreases continuously for 24 hours until disappearing entirely. We also observed a modification in the amine signals during the first half hour.

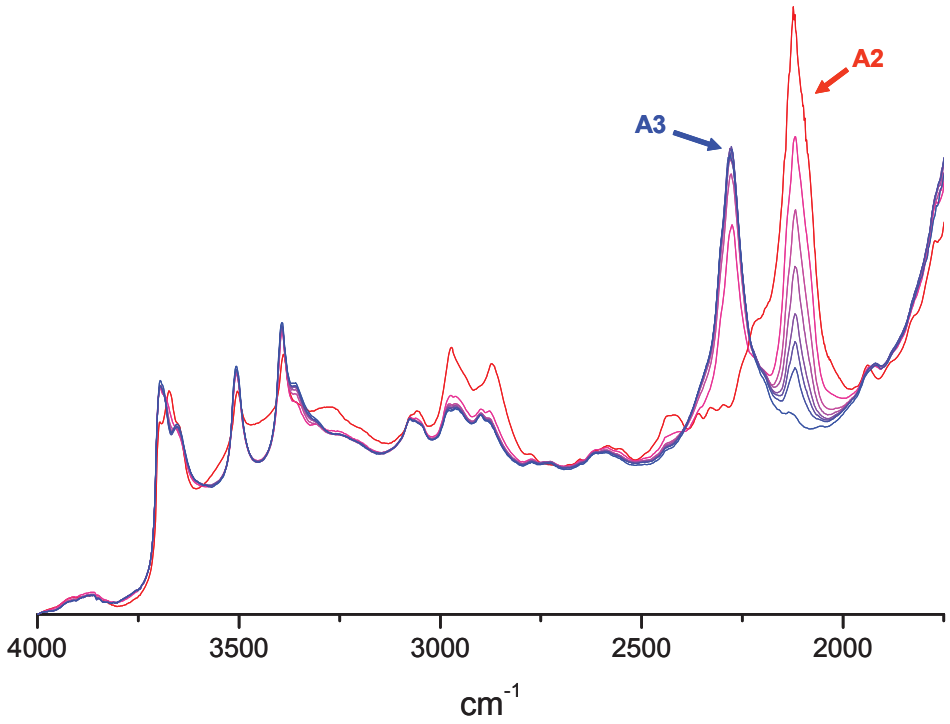

Figure 5. DRIFT spectra of the transformation of **A2** into **A3** at 150°C under CO flow. Spectra were recorded (from red to blue) at 0, 30, 75, 120, 180, 240, 330 and 1320 minutes.

It is noteworthy that DRIFT spectroscopy is a method of surface analysis, meaning that only the upper layer of the sample powder is studied. For this reason, each sample was extracted from the DRIFT cell after transformation, the sample powder was homogenised with a spatula, and then it was replaced in the DRIFT apparatus. A decrease in the isocyanate signal is observed in this situation (Figure 6).

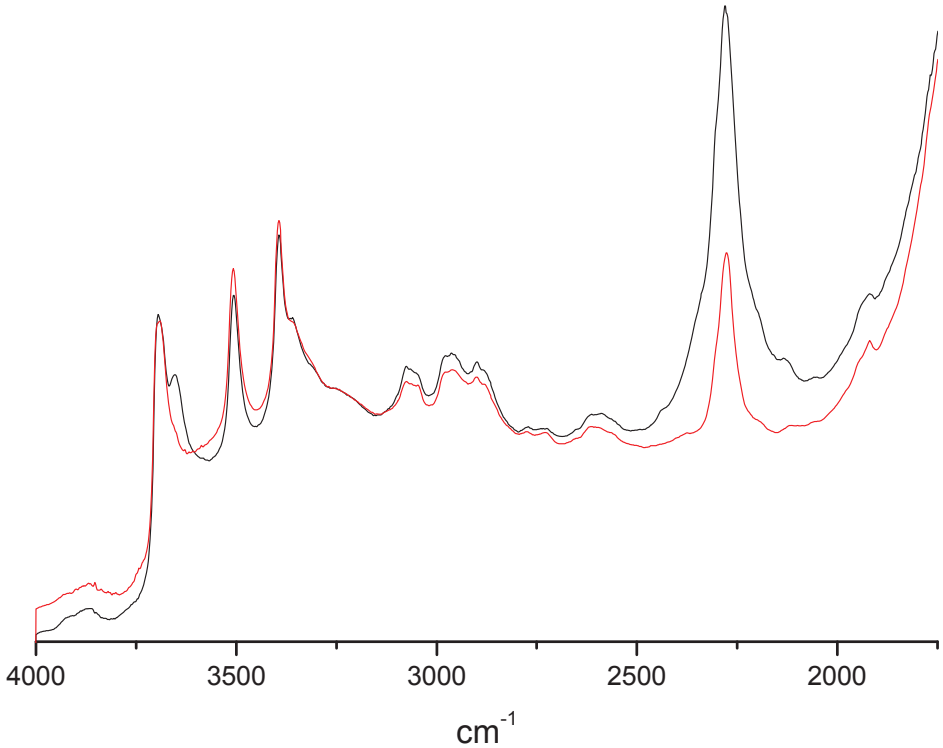

Figure 6. DRIFT spectra of **A3** at 100°C under Argon flow. In black, surface layer and in red, mixed sample.

We observed that the crystalline integrity of **A3** is preserved (Figure 7).

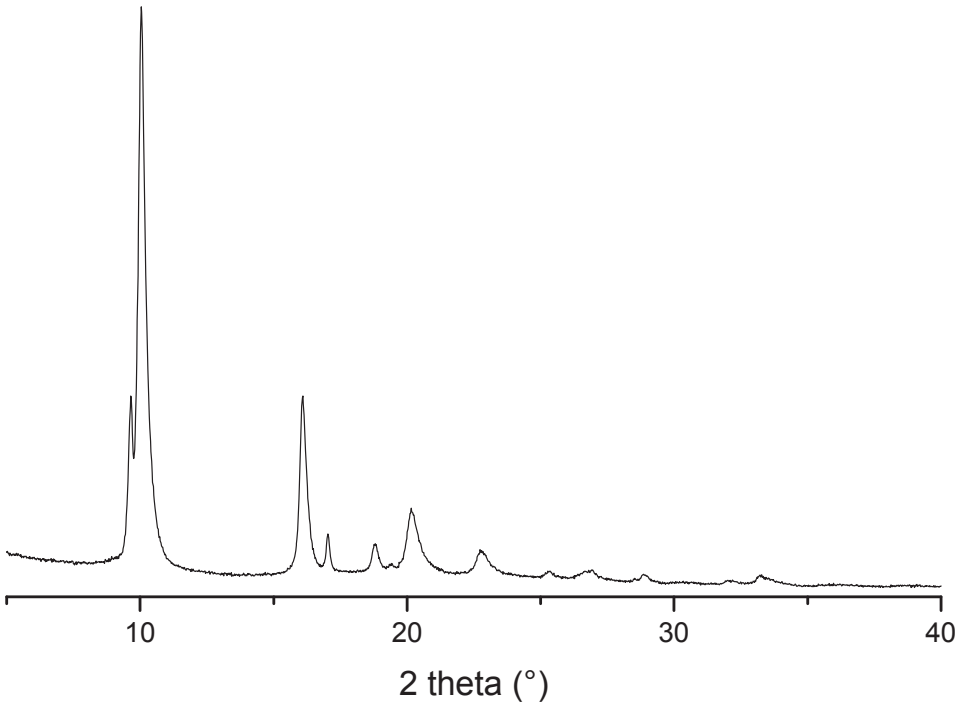

Figure 7. XRD pattern of **A3**

^{1}H NMR analysis nevertheless reveals only traces of isocyanate signals (Figure 8). The main products are 2-aminoterephthalic acid and the bare terephthalic linker (peak at 8.02 ppm). For comparison, we prepared Al-MIL-53-NCO (**A'3**) and Al-MIL-53-20%NCO (**B'3**) by the method described by Cohen *et al.*[17] using diphosgene (Scheme 1, route IV). The ^{1}H NMR spectrum of isocyanate-substituted MOF **A'3** shows two doublets (7.6ppm, H_b and 8ppm, H_c) and a singlet (7.6ppm, H_a).

The transformation of **A3** has a very low selectivity. DRIFT spectroscopy proves that isocyanate species are formed (mainly on the DRIFT cell surface) but it is principally side reactions that take place.

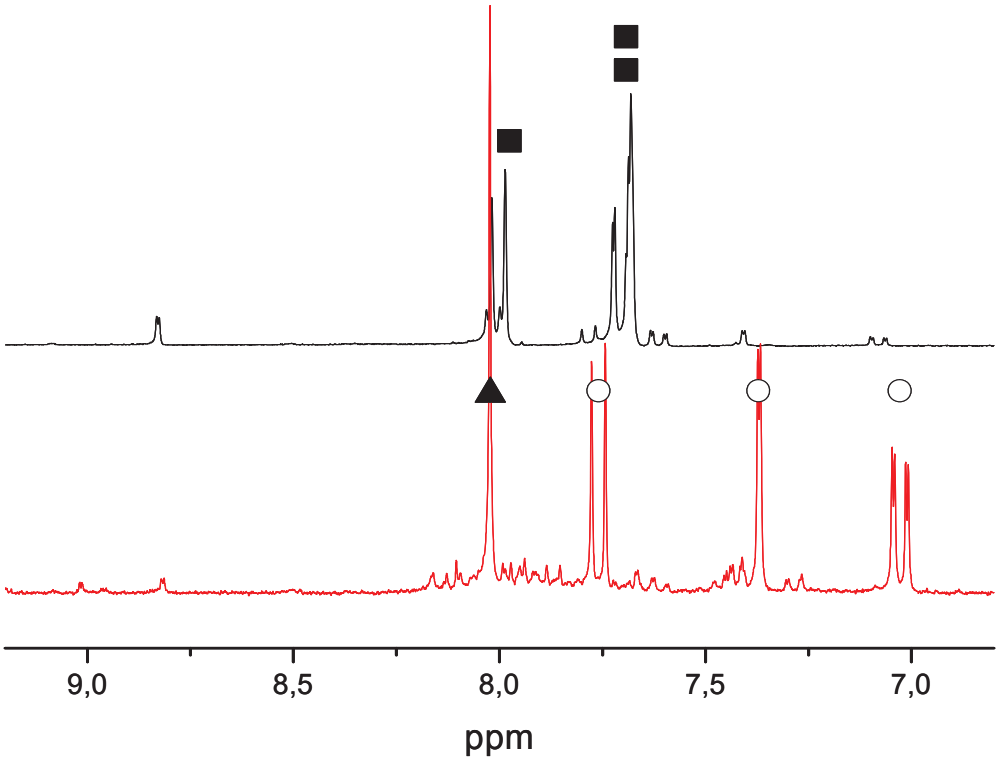

Figure 8. ^{1}H NMR spectra of **A3** (red line, bottom) and **A'3** (black line, top). Isocyanato terephthalic protons are indicated with squares, terephthalic acid protons with a triangle and amino terephthalic protons with circles.

The DRIFT analysis of **C2** presents a different profile. The azide band decreases by only 60% after 24 hours. Here, the azide signal seems to be a superposition of several bands (Figure 9). There are at least two types of azide with two peaks. As no azide is observed by ^{1}H NMR, the higher wavenumber species must be present only on the outer layer of the sample. The band with the lower wavenumber should, however, have a much smaller molar absorption coefficient. This

means that the initial decay of the 2100 cm^{-1} band is related to a drastic change in azide concentration. This observation is consistent with the degradation kinetics of azide groups as observed by TGA.

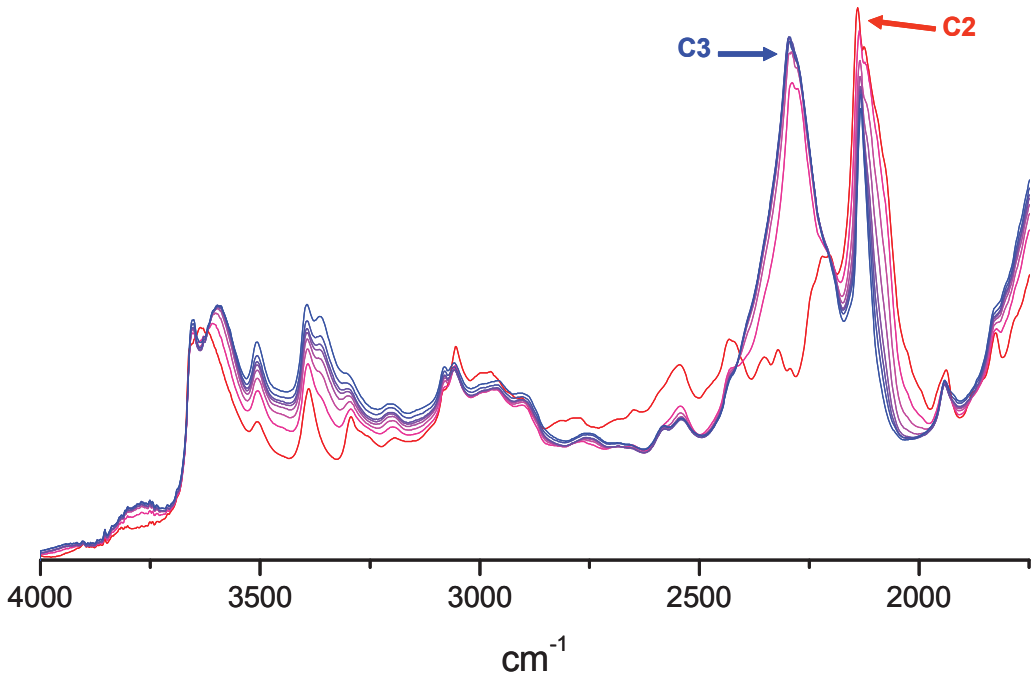

Figure 9. DRIFT spectra of the transformation of **C2** at 150°C under CO flow. Spectra were recorded (from red to blue) at 0, 30, 75, 120, 180, 240, 330 and 1360 minutes.

The **C3** material was analysed by XRD just after conversion. Figure 10 shows the evolution of the XRD spectra of **C3** within minutes of its extraction from the DRIFT cell. As time increases, the peaks broaden and their intensities decrease, indicating a loss of crystallinity. **C3** obtained under CO flow is stable only under dry gas flow, as it seems that its substituents undergo intermolecular reaction in the presence of atmospheric moisture.

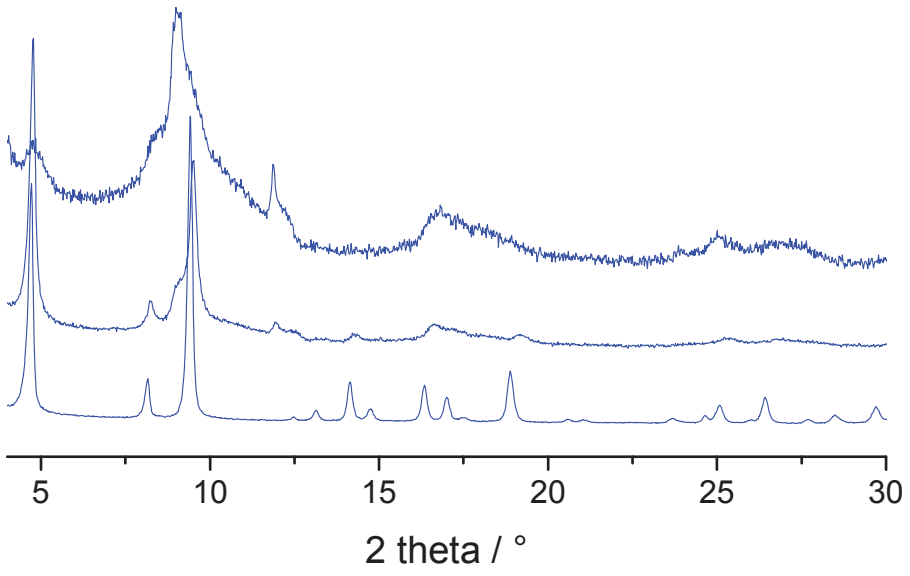

Figure 10. PXRD pattern of (from bottom to top) **D3**, **C3** after 3 minutes under air and **C3** after 6 minutes under air.

The ^{1}H NMR spectrum of **C3** shows the same by-products as for **A3**. According to the DRIFT spectra, maximum conversion into isocyanate is reached after 90 min (Figures 5 and 9). The azide signal nevertheless continues to decrease over 24 hours. It seems that azide groups continue to be transformed into nitrene species but radicals are not converted into isocyanate. This phenomenon can be explained by the formation of isocyanate at the entry of the 1D channel, which blocks access to CO molecules and prevents further conversion.

A consequence of the accumulation of nitrene species within the pore could be side reactions such as the formation of a diazo bridge when two nitrene groups react with each other. Azo compounds such as azobisisobutyronitrile (AIBN) could easily be degraded to form nitrogen and radicals. Upon contact with atmospheric moisture or in the digestion solution, these radicals would form the bare terephthalic acid observed by NMR. Furthermore, any unreacted nitrene would react with labile protons to form amino groups. Based on structure visualisation, the distance between two substituents present on the same wall is less than 3Å. It therefore appears possible for two adjacent functionalised linkers to react with each other.

In the case of **C3**, In-MIL-68 presents a structure too sensitive to withstand these intramolecular reactions, which leads to the collapse of this structure under contact with air (Figure 10).

A mixed-linker strategy may be helpful in producing a material in which the substituent groups are too far from each other to react. Al-MIL-53-20%N_3 (**B2**) and In-MIL-68-20%N_3 (**D2**) were

converted into NCO-substituted species with the same CO method. Conversions are of the same order as those obtained with the fully-functionalised MOFs, and these materials are still crystalline after days in air (**D3** in Figures 10 and **B3** in Figure 14).

For samples **B2** and **D2**, isocyanate formation follows similar kinetics to those of their fully-functionalised analogues (**A2** and **C2**). All of the isocyanate groups are formed within the first two hours, but the azide signal continues to decrease in the following 20 hours (Figures 11 and 12).

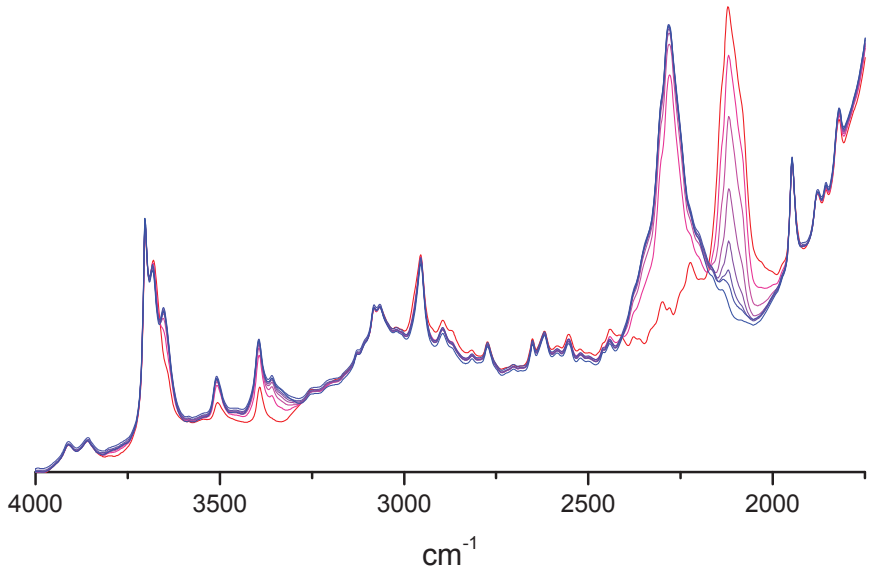

Figure 11. DRIFT spectra of the transformation of **B2** at 150°C under CO flow. Spectrums were record (from red to blue) at 0, 30, 75, 120, 180, 240, 330 and 1320 minutes.

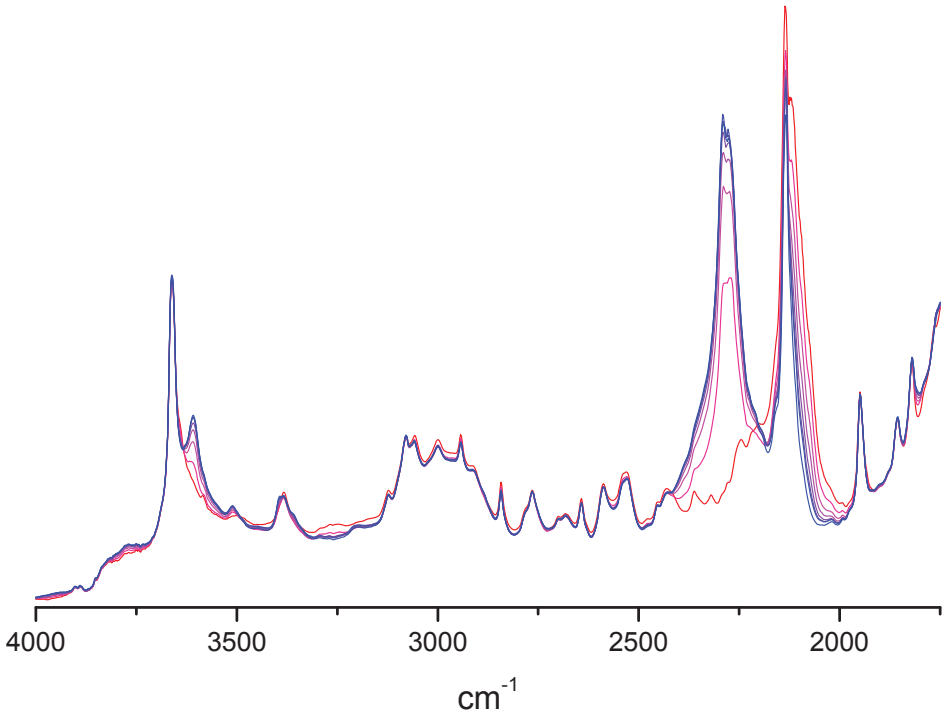

Figure 12. DRIFT spectra of the transformation of **D2** at 150°C under CO flow.

The ^{1}H NMR spectra of samples **B3** and **D3** are consistent with those of **A'3** and **B'3**, the isocyanate MOFs synthesised using the diphosgene method. Full selectivity into isocyanate was obtained only with **D3**. For **B3**, the transformation of the azide into an isocyanate group is accompanied by the formation of an amino group (Figure 13).

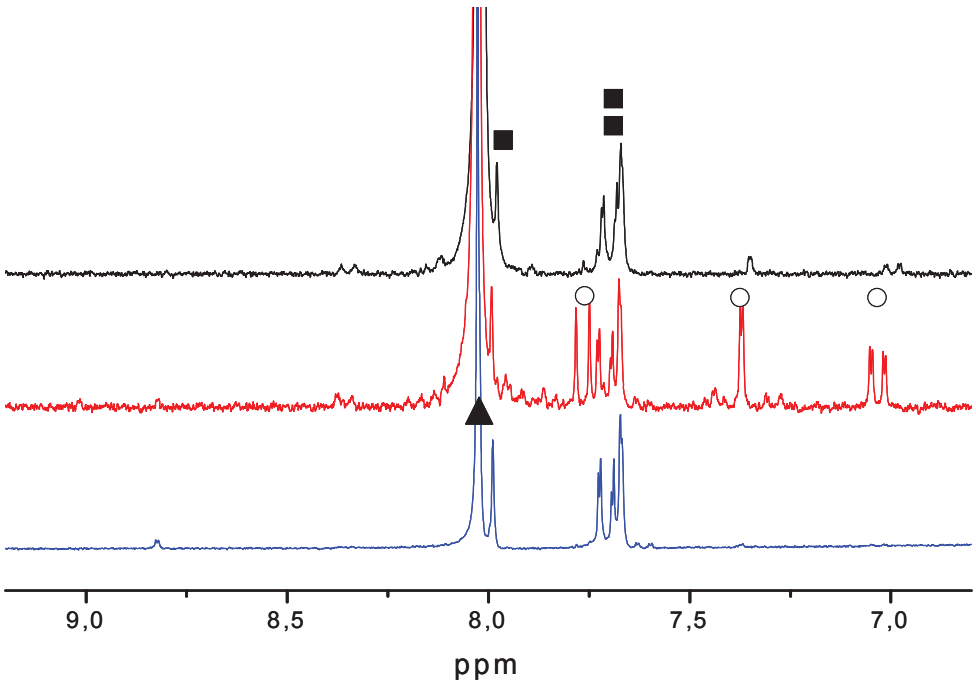

Figure 13. ^{1}H NMR spectra of (from bottom to top) **B'3**, **B3** and **D3**. Isocyanato terephthalic protons are indicated with squares, terephthalic acid protons with a triangle and amino terephthalic protons with circles.

The XRD pattern of the **A'3** sample is the same as that observed by Cohen *et al.*[17] (Figure 14).

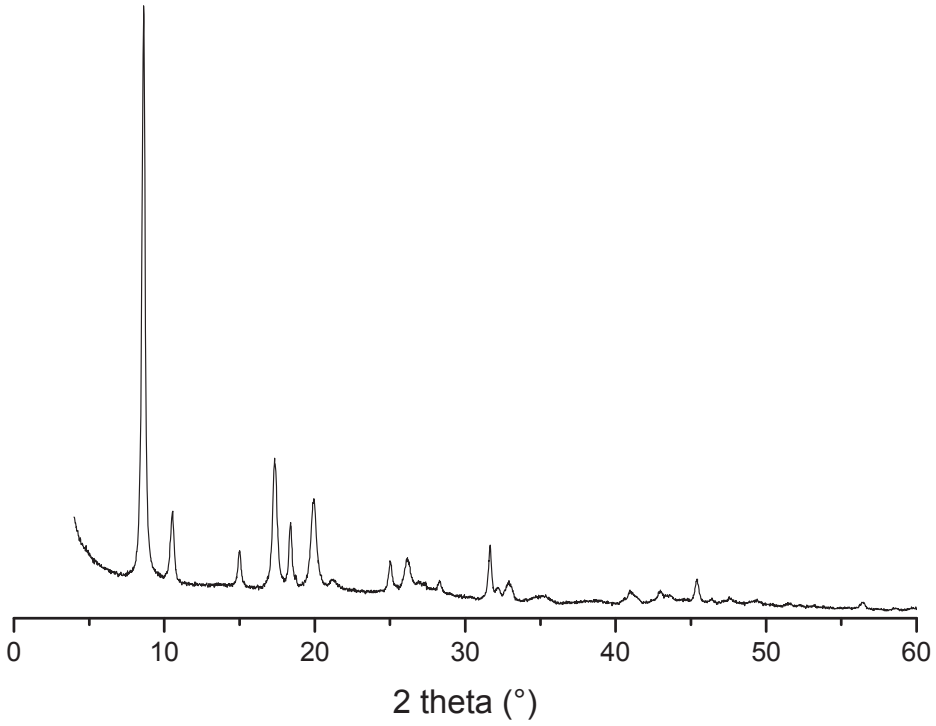

Figure 14. XRD pattern of **A'3**

This diffractogram corresponds to the orthorhombic structure with large pores[22]. The post-functionalisation of amino groups increases the intramolecular repulsion force (bulk and/or electronic), leading to a structure with larger pores. Meanwhile, samples **B'3** and **B3** present different diffractograms, with peaks at 8.7, 15 and 17° corresponding to an *e.g.*, **B1**) (Figure 15). Our team has previously demonstrated that the use of mixed ligands could facilitate the transition from a narrow-pore form to a large-pore form with Al-MIL-53[20, 21]. A decreased number of functionalised groups may reduce intramolecular interaction, aiding in the transition of **B3** and **B'3** from large pores to narrow pores.

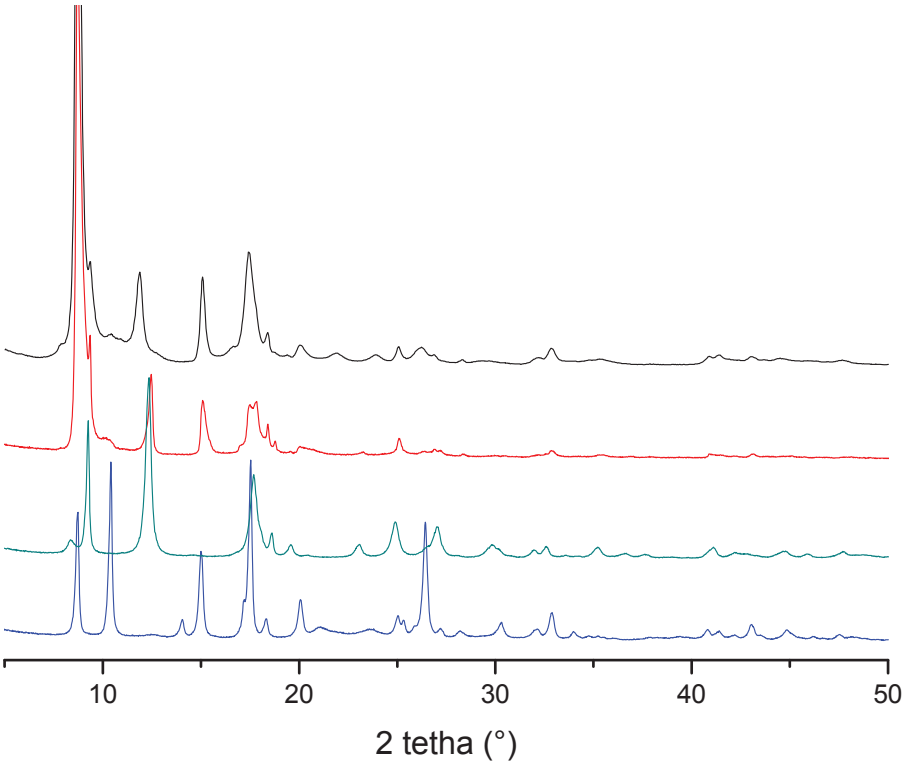

Figure 15. XRD pattern of (from bottom to top) as-synthesised **B1** (blue line), activated **B1** (cyan line), **B3** (red line) and **B'3** (black line).

TGA curves of **B3** and **D3** display the same behaviour as with amino MOFs, with water desorption below 100°C and structural collapse at 435 and 375°C, respectively. The Al-MIL-53-20%NCO samples obtained by the diphosgene route (**B'3**) or by CO treatment (**B3**) present the same TGA curve (Figure 16).

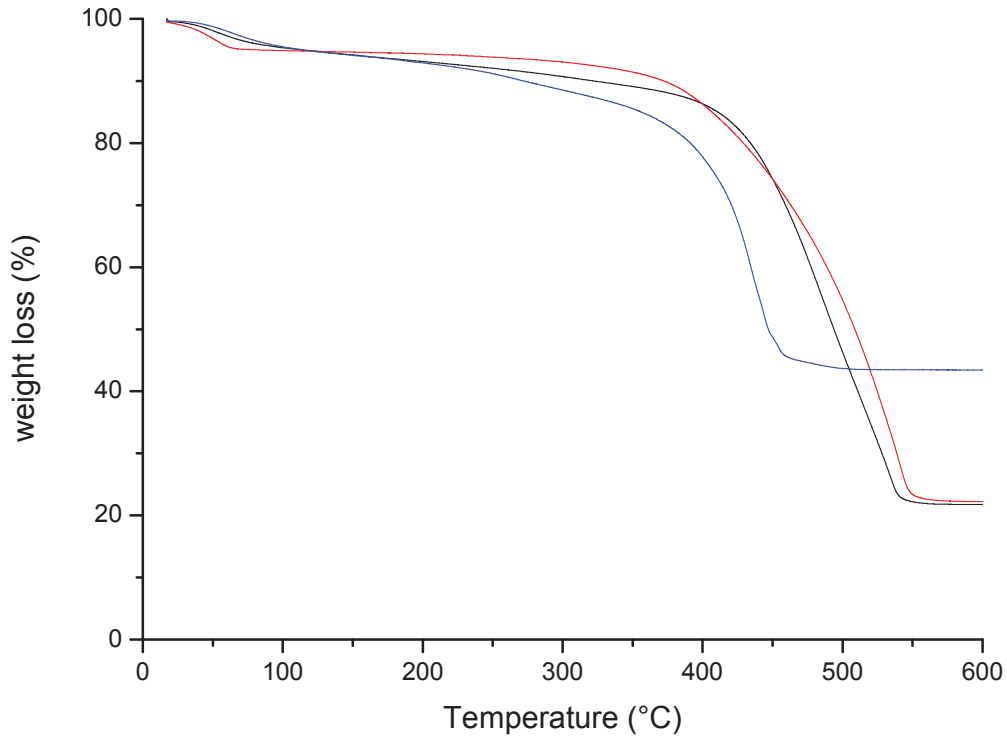

Figure 16. TGA of **B'3** (black line), **B3** (red line) and **D3** (blue line) under synthetic air.

The comparison of XRD, DRIFT, ^{1}H NMR and TGA analyses with isocyanate-functionalised Al-MIL-53 obtained by diphosgene treatment proves beyond a doubt that isocyanate MOFs have been synthesised. We can suggest that the breathing properties of the **B3** material do not allow it to maintain sufficient distance between nitrene substituents. Furthermore, the flexibility of MIL-53 favours strong host-guest interaction. Traces of water can remain after the desorption process and ultimately react with the nitrene. This may explain why the selectivity toward the isocyanate product is only 56%.

III. 3. Step III: Transformation of isocyanato MOFs B3 and D3 into urea-functionalised MOFs B4, D4, B5 and D5.

The condensation of amine on isocyanate-functionalised MOFs was first carried out in the gas phase in order to allow DRIFT monitoring. When azide DRIFT signals stopped decreasing, **B3** and **D3** were flushed at 90°C with a flow of 1% ammonia in argon, leading to ureas **B5** and **D5**. The DRIFT spectra showed a slow decrease in the isocyanate signal and a strong modification of the amine bands. The shoulder that appears at 3350 cm^{-1} corresponds to the amine stretching of an amide group (Figure 17 and Figure 18).[23]

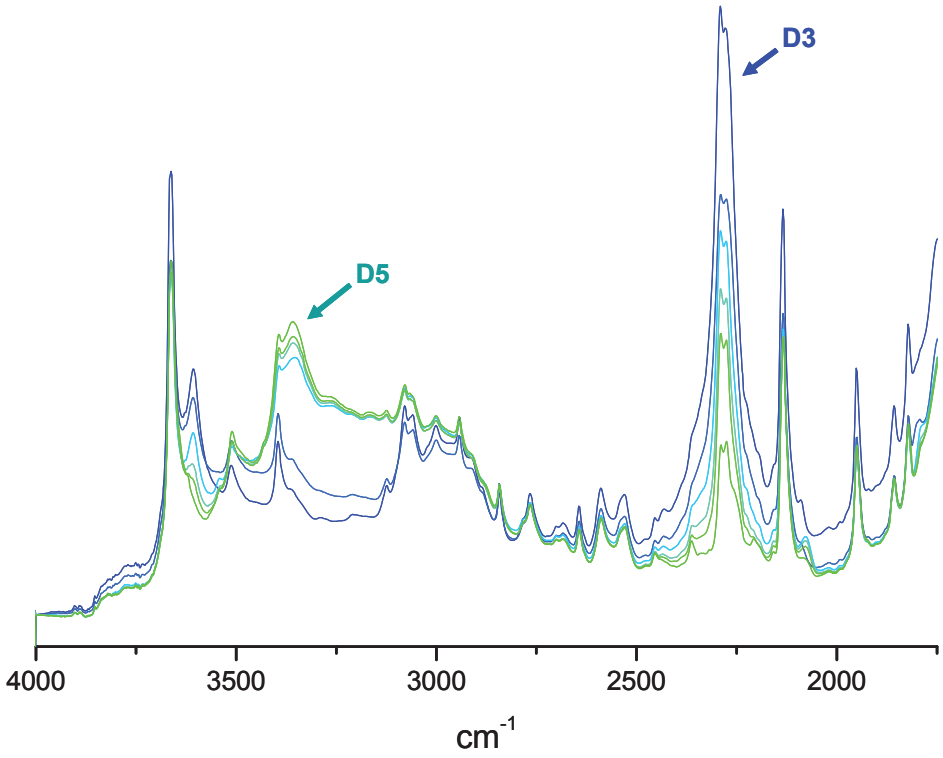

Figure 17. DRIFT spectra of the transformation of **D3** into **D5** at 90°C under ammonia flow (1% in argon).

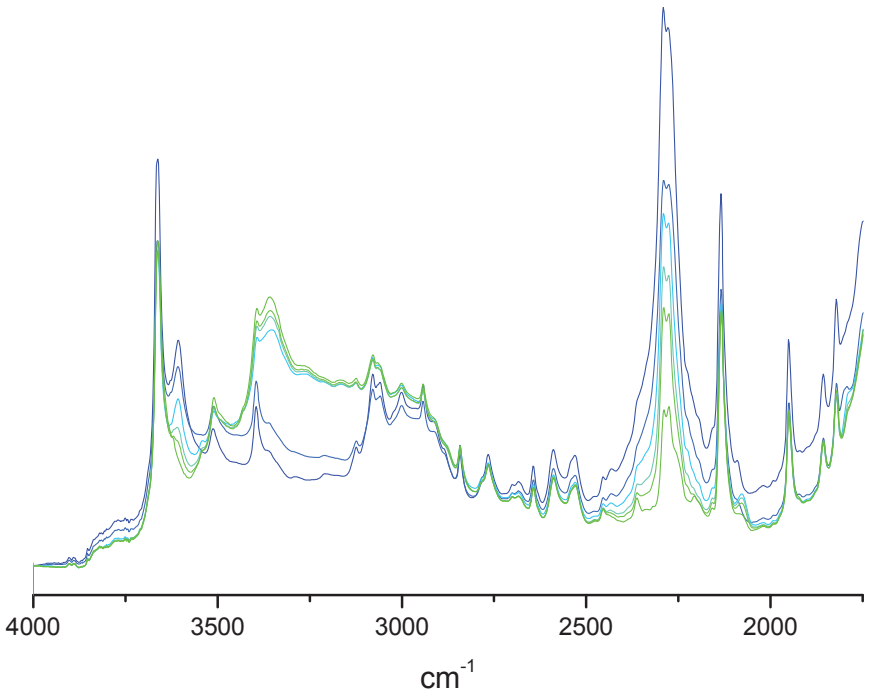

Figure 18. DRIFT spectra of the transformation of **B3** into **B5** at 90°C under ammonia flow (1% in Argon).

The conversion of isocyanate MOFs into ureas is confirmed by ^{1}H NMR (Figure 19). The disappearance of the broad isocyanate signal is accompanied by the rise of two doublets (7.47 ppm, H_b and 7.95 ppm, H_c) and a singlet (8.8 - 9ppm, H_a) (Scheme 2). The aromatic proton in the α position of the substituent is strongly shifted by the transformation of the isocyanate into the urea group.

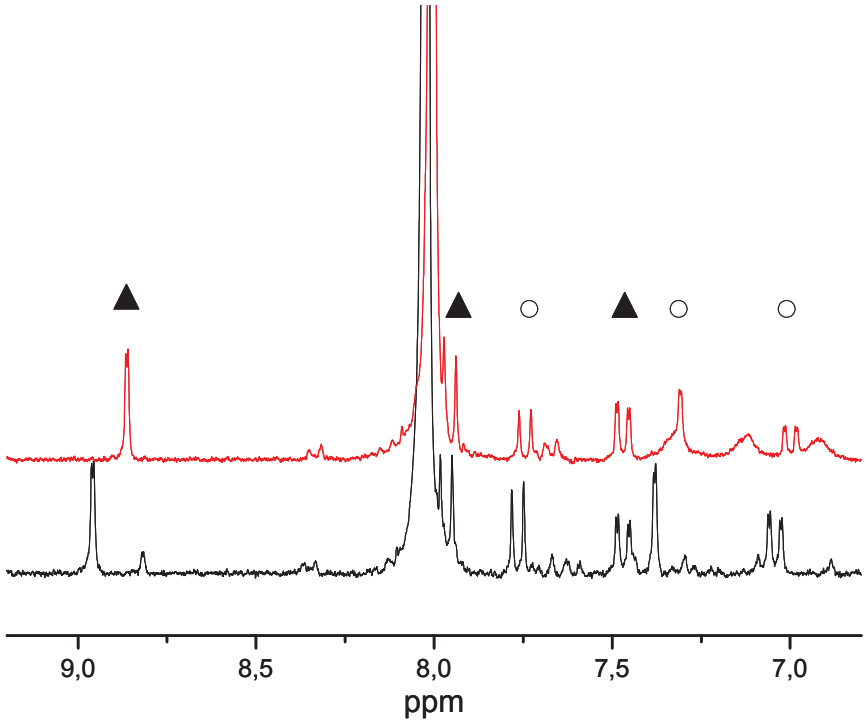

Figure 19. ^{1}H NMR spectra of (from bottom to top) **B5** and **D5**. Urea terephthalic protons are indicated with triangles and amino terephthalic protons with circles.

Urea MOFs were also obtained in liquid phase synthesis by reacting **B3** and **D3** with diamino cyclohexane in acetonitrile to yield **B4** and **D4**. As with **B5** and **D5,** the dried solids present the aromatic proton of the substituted terephthalic linker (Figure 20).

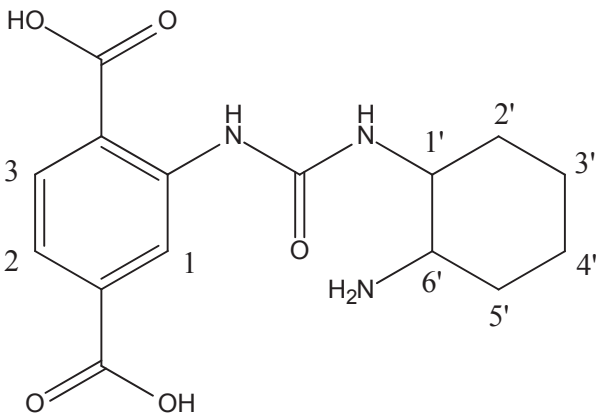

^{1}H NMR (250 MHz, d6-DMSO):
δ= 8.83 (s, 1H, 1), 8.05 (d, 1H, 3), 7.62 (d, 1H, 2), 3.55 (s, 1H, 1'), 3.03 (s, 1H, 6'), 1.96 and 1.66 (m, 4H, 2' and 5'), 1.26 (m, 4H, 3' and 4')

Scheme 3. ^{1}H NMR shift of urea aminocyclohexane substituted MOF.

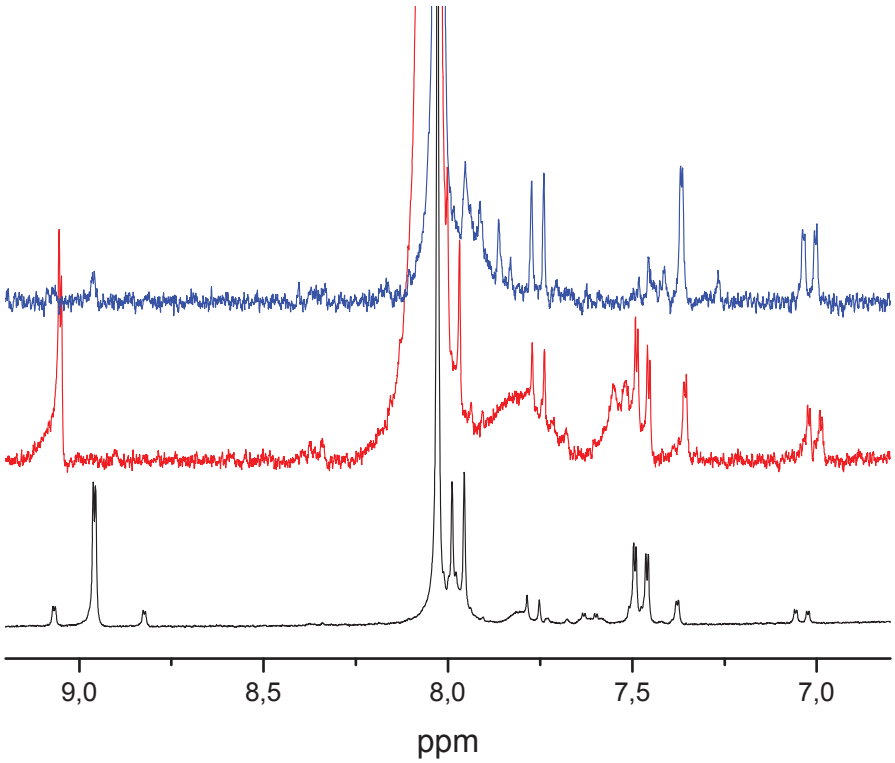

Figure 20. ^{1}H NMR spectrum of (from bottom to top) **B'4**, **D4** and **B4** (aromatic region).

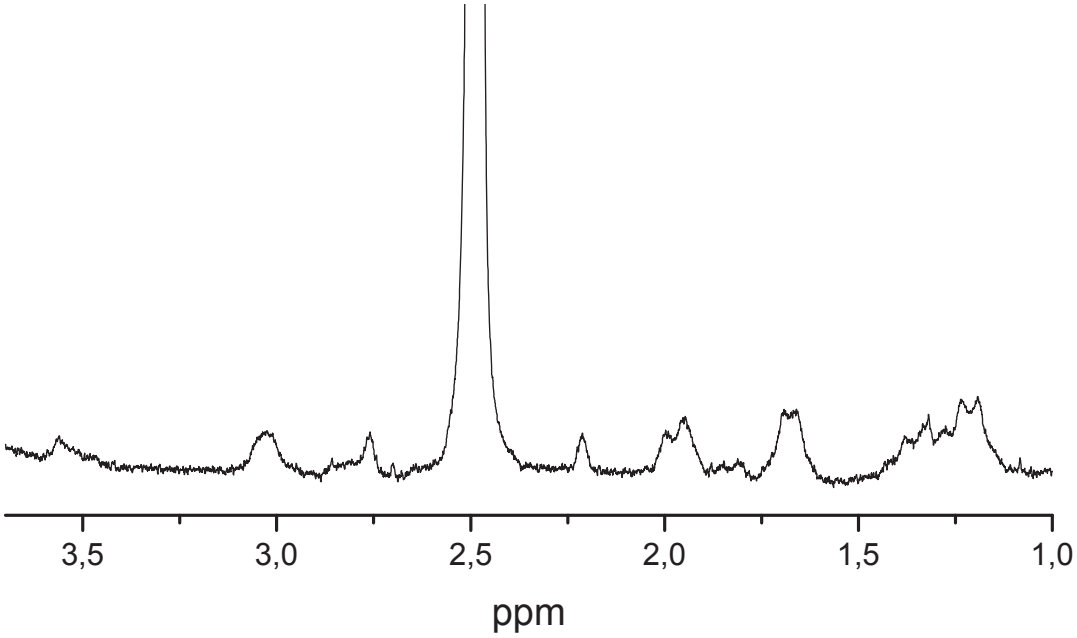

Figure 21. ^{1}H NMR spectra of **B4** (aliphatic region)

The aliphatic protons of the cyclohexane group give signals at 3.55 ppm (singlet, 1H), 3.03 ppm (singlet, 1H), 1.96 and 1.66 ppm (multiplet, 4H) and 1.26 ppm (multiplet, 4H) (Figure 21). The integrations of the cyclohexane protons and the terephthalic acid protons are identical and prove that no free amine remains after DCM Soxhlet extraction. The selectivity of the transformation into urea as determined by integration of the ^{1}H NMR signals is roughly 70%.

Electrospray ionisation mass spectroscopy performed on digested samples confirmed the presence of the expected molecular ions (Figures 22 to 26). Amino-, isocyanate- and azide-substituted linker molecular ions appeared under negative ionisation at m/z = 182 and 206. Triple protonated 2-aminocyclohexane urea-substituted linker can be observed under positive ionisation at m/z = 322.

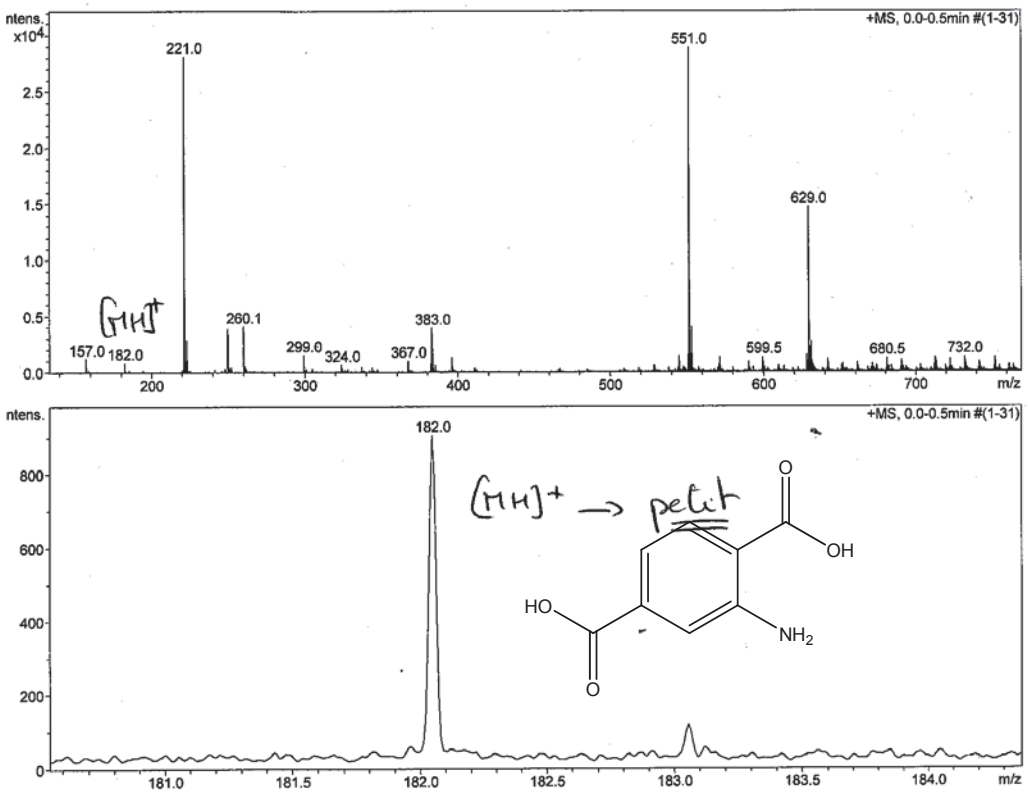

Figure 22. ESI-MS (negative mode) of **B1**

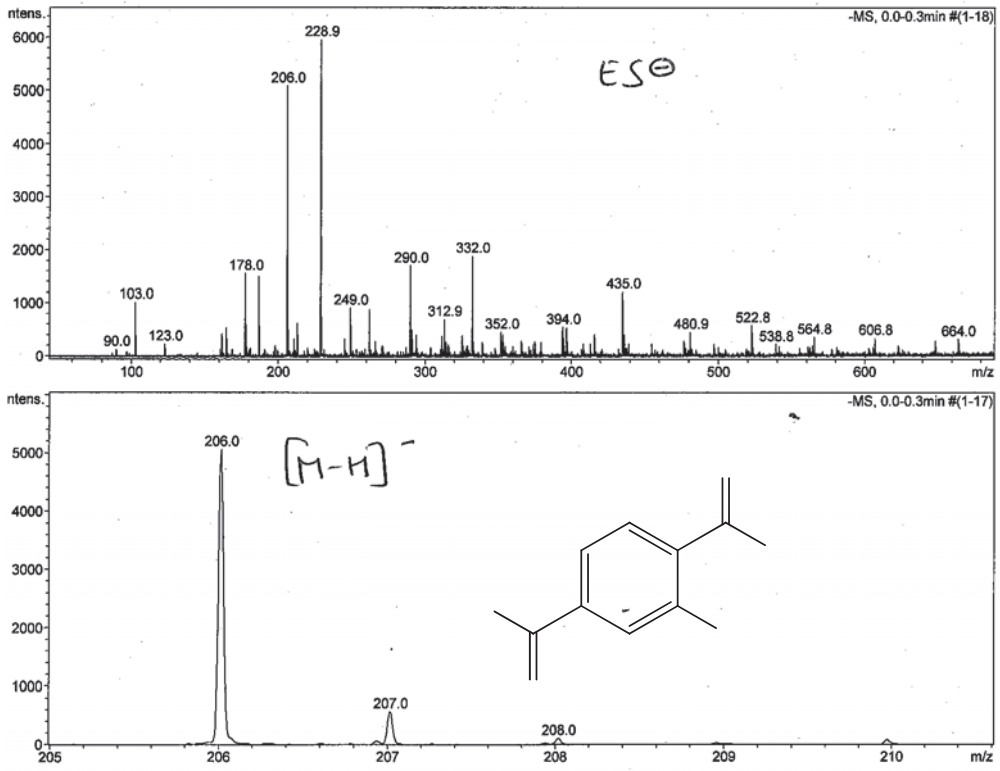

Figure 23. ESI-MS (negative mode) of **B2**

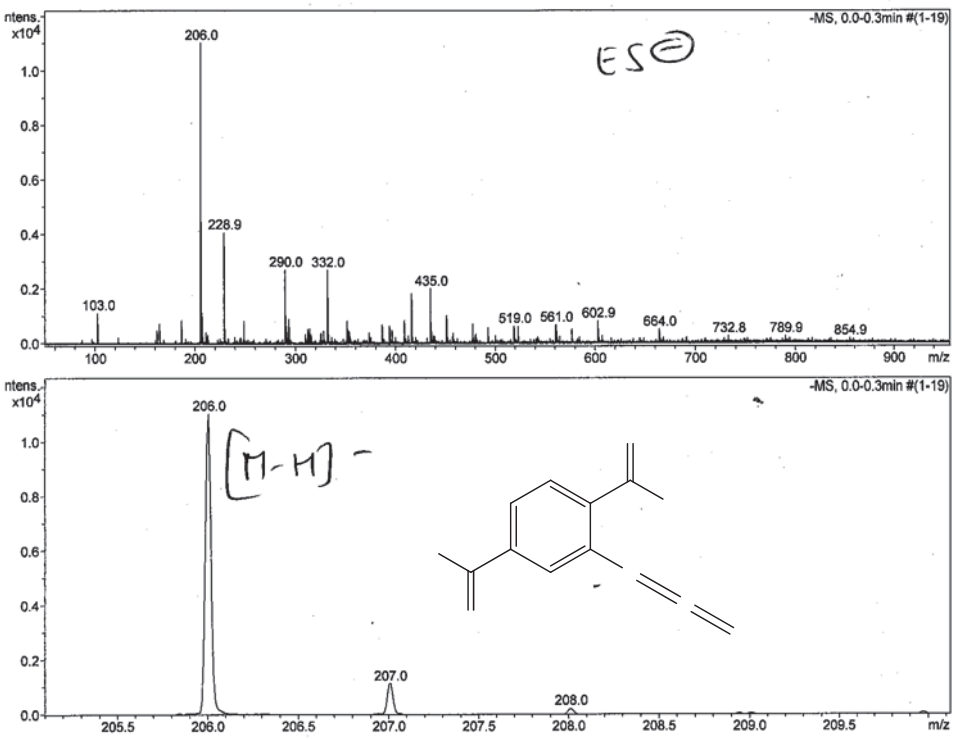

Figure 24. ESI-MS (negative mode) of **B3'**

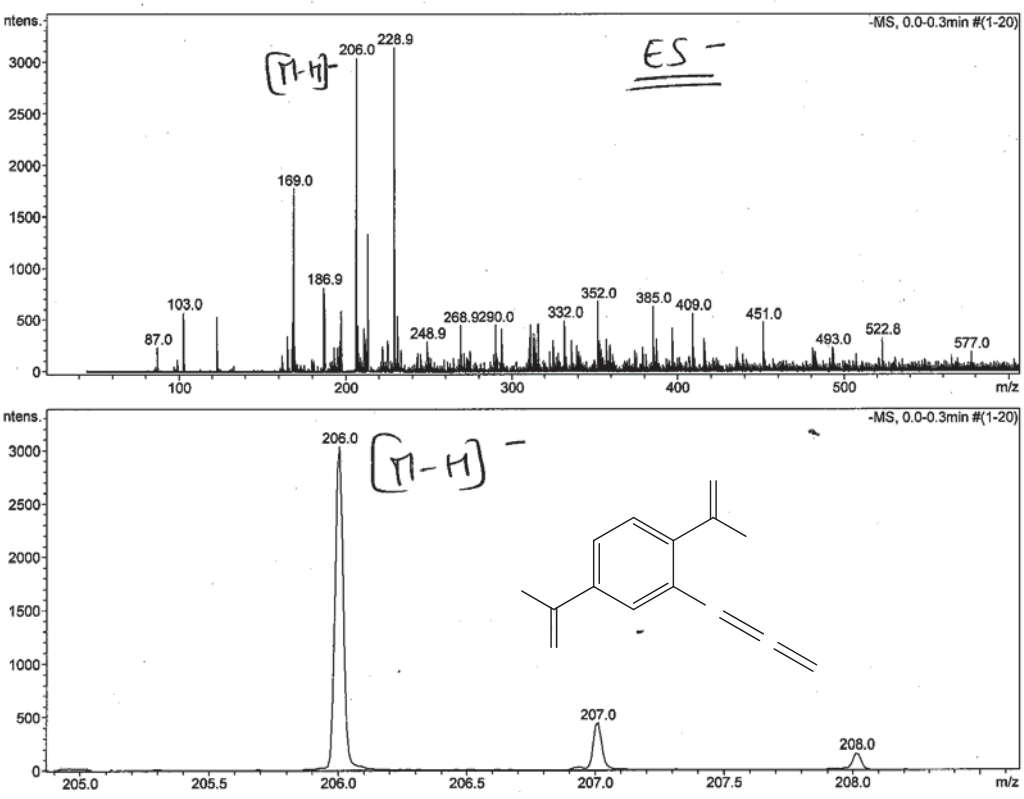

Figure 25. ESI-MS (negative mode) of **B3**

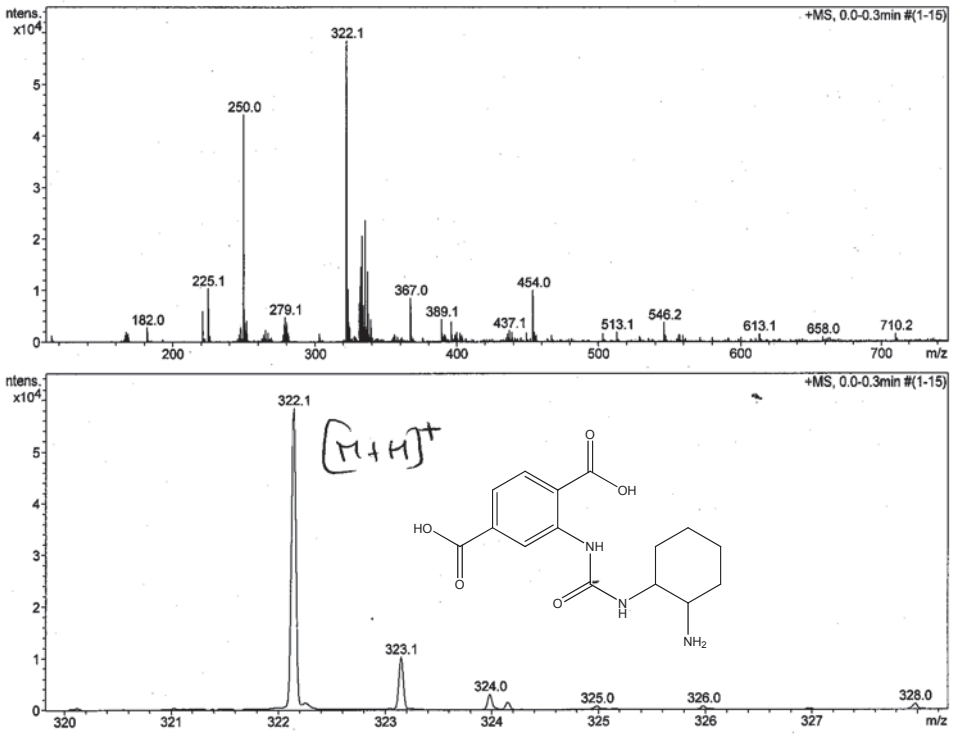

Figure 26. ESI-MS (positive mode) of **B4**

SEM images of Al-MIL-53 and In-MIL-68 respectively show crystallites (around 1 μm) and aggregated particles (0.2 μm) (Figures 27 to 31).

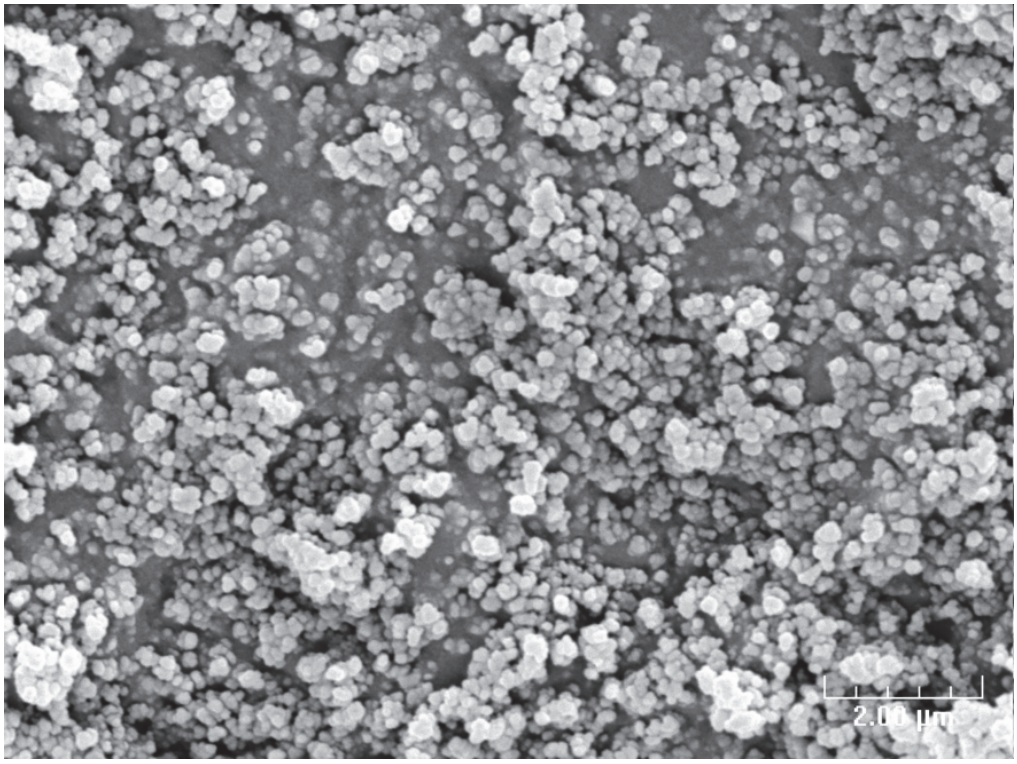

Figure 27. SEM image of **D3**

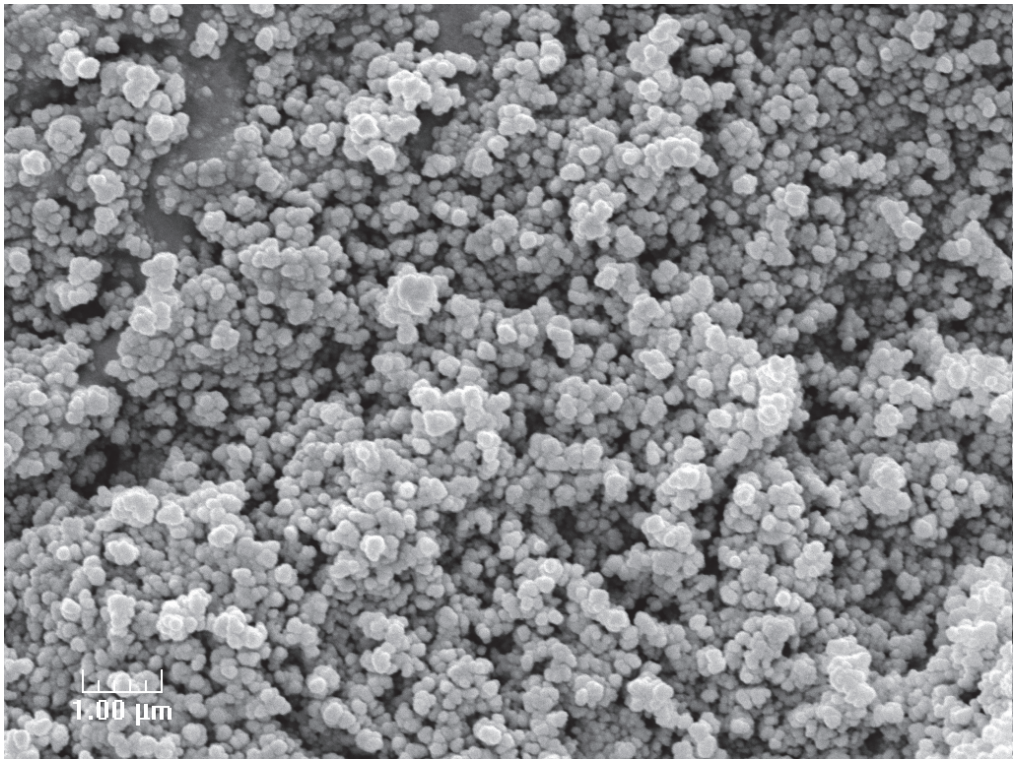

Figure 28. SEM image of **D4**

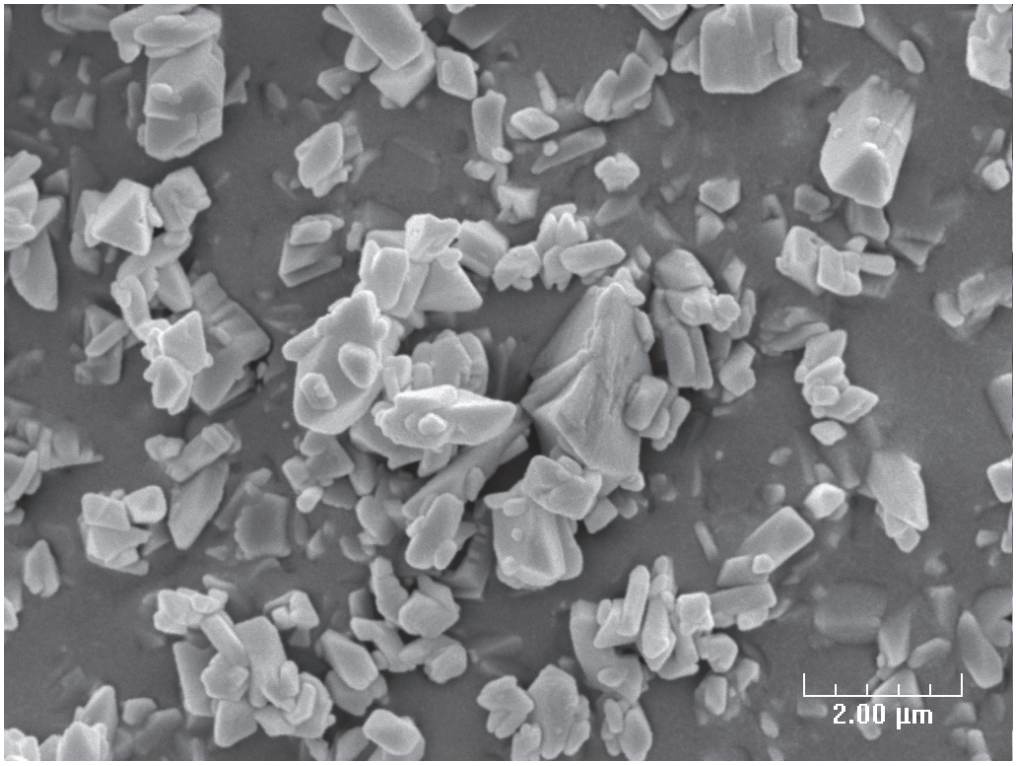

Figure 29. SEM image of **B3**

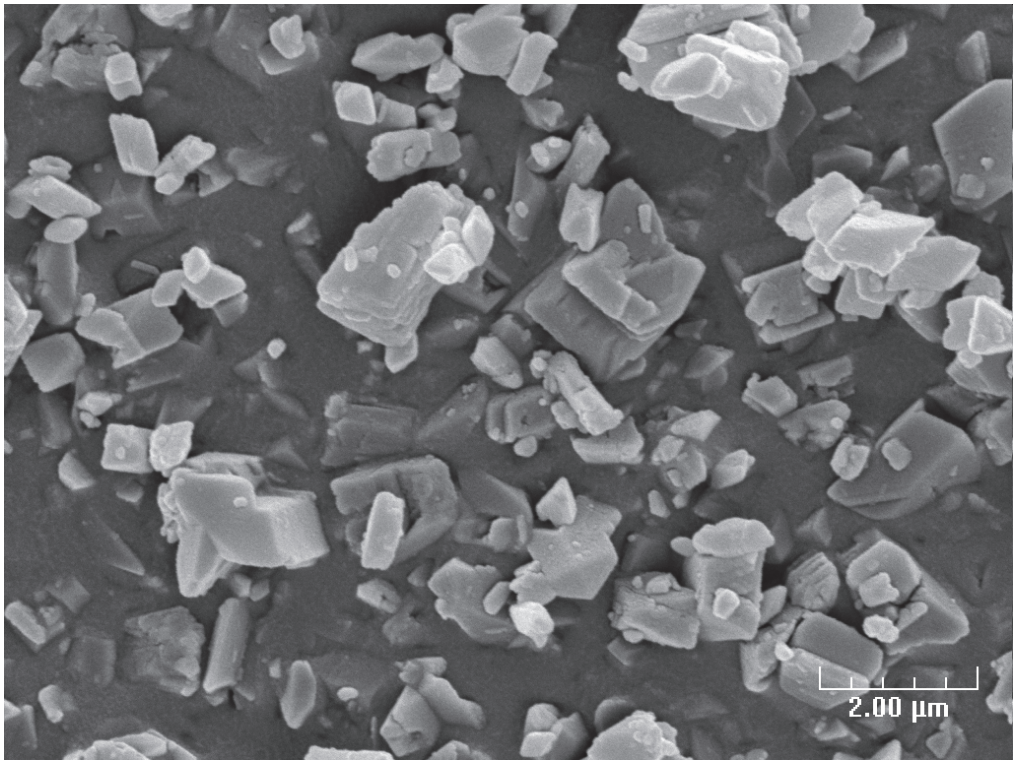

Figure 30. SEM image of **B3'**

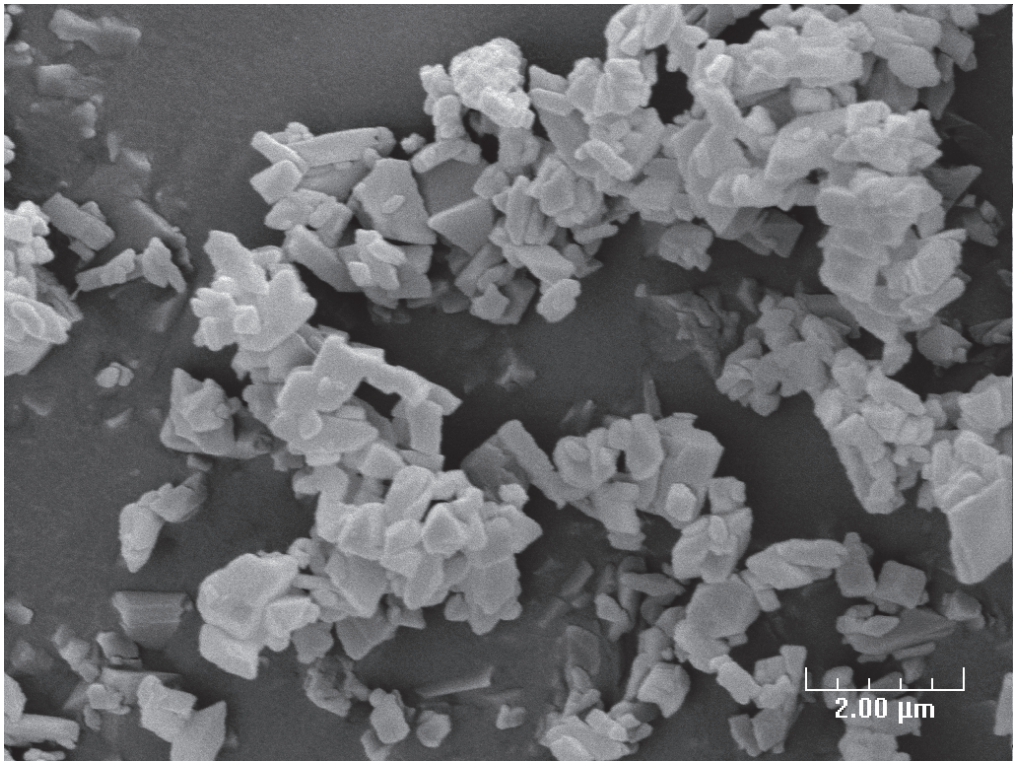

Figure 31. SEM image of **B4**

The BET surface area and microporous volume of **B3**, **D3**, **B4**, **D4**, **B5** and **D5** were measured. Each post-functionalisation step provokes a decrease in BET surface area and microporous volume (Table 1 and Figures 32 and 33).

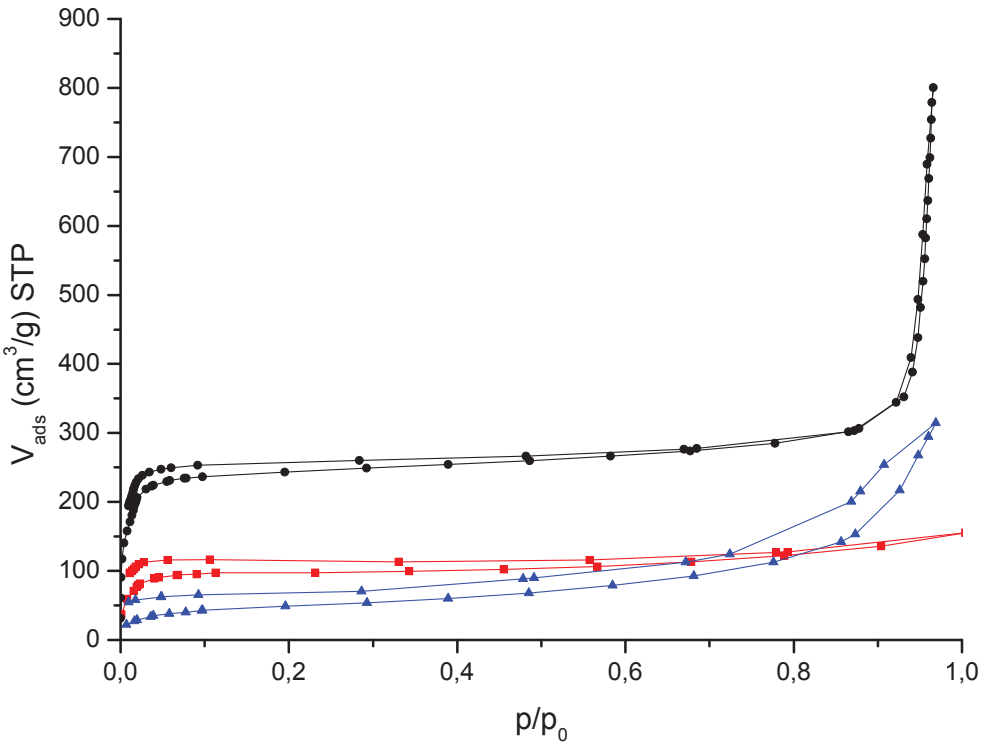

Figure 32. nitrogen isotherms at 77K of **D3** (black circles), **D4** (blue triangles) and **D5** (red square).

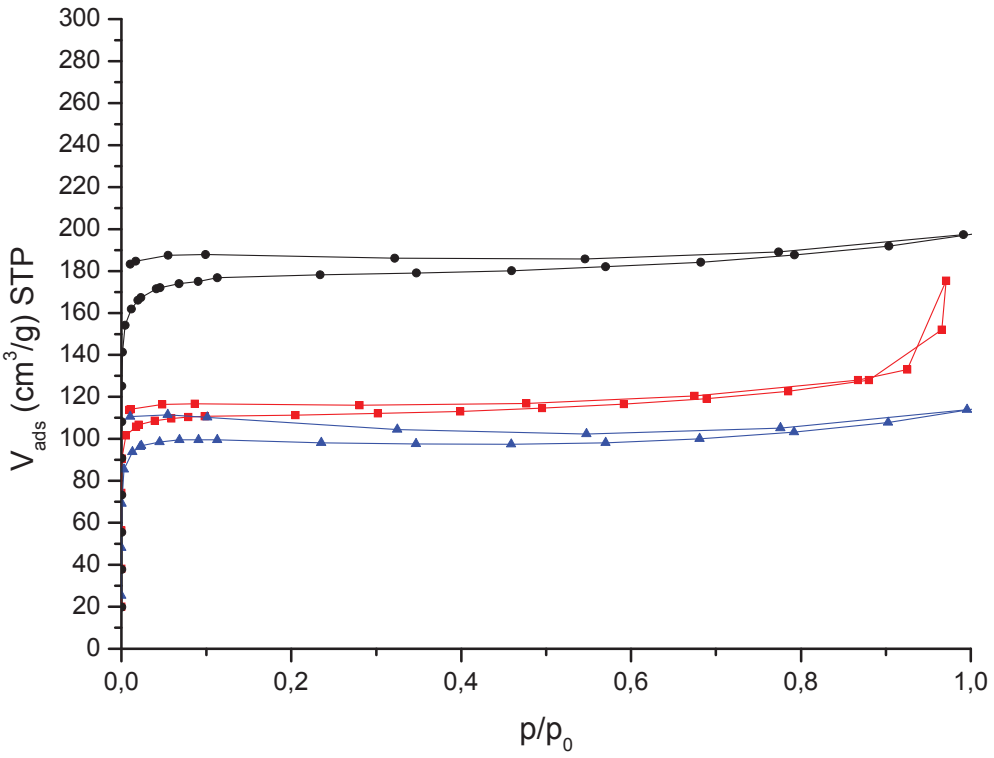

Figure 33. nitrogen isotherms at 77K of **B3** (black circles), **B4** (blue triangles) and **B5** (red square).

Table 1. N_2 physisorption results of isocyanate- and urea-functionalised MOFs.

	S_{BET} ($m^2 \cdot g^{-1}$)	V_{micro} ($cm^3 \cdot g^{-1}$)
B3	684	157
B4	385	88
B5	379	87
D3	872	200
D4	178	45
D5	391	90

The various post-functionalisation steps do not affect the integrity of the framework. No structural modification throughout the different treatments is observed on SEM images, and diffractograms show that mixed-linker MOFs retain high crystallinity (Figure 34).

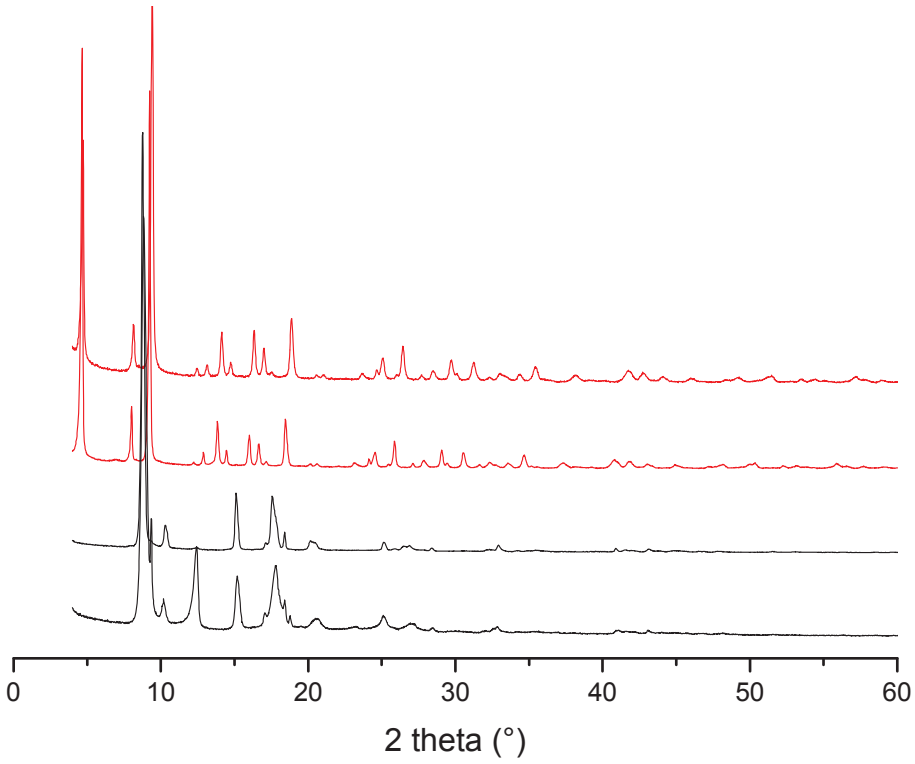

Figure 34. XRD pattern of (from bottom to top) **B4**, **B5**, **D4** and **D5**.

IV. Conclusions

Al-MIL-53-20% (**B**) and In-MIL-68-20% (**D**) remain porous at each step, and even bulky amino cyclohexane-substituted MOFs maintain a degree of porosity sufficient to allow the diffusion of species within the pores.

All of the selected amino MOFs were converted into their azido analogues with 100% yield. Unfortunately, only traces of isocyanate moieties are detected in fully-functionalised MOFs (**A** and **C**) after activation of azide into nitrene and reaction with carbon monoxide. This might be due to side reactions involving nitrene species. Indeed, the activated substituents of linkers within the same channel are close enough to react together to give mainly terephthalic and aminoterephthalic linkers. Diluting functionalised linkers with bare linkers during MOF synthesis decreases the density of functionalised groups within the pores, which in turn reduces the likelihood of having neighbouring nitrenes. Indium-based MIL-68 with 20% functionalised linkers (**D**) shows 100% conversion and selectivity toward isocyanate with no decrease in porosity or crystallinity. On the other hand, aluminium-based MIL-53 with 20% functionalised linkers presents only 56% selectivity for isocyanate. An explanation for the side reactions in this case can be that structural breathing brings together reactive groups on opposite walls of the same 1D channel.

The diphosgene route allows the synthesis of isocyanate-substituted Al-MIL-53 from the amino form in one step without the formation of nitrene species. This method is preferable when an acid-resistant material is used.

The two isocyanate MOFs (**B** and **D**) were converted into ureas by reaction with amines in both liquid and gas phases. Selectivities toward urea moieties were about 70%, with amino groups formed as side products.

Table 2. Selectivity* throughout the post-functionalisation steps.

	Amino into azido MOF	Azido into isocyanato MOF	Isocyanato into urea-functionalised MOF
A	100%	Trace	-
B	100%	56%	40%
C	100%	Structural collapse	-
D	100%	100%	70%

*Selectivity from amino form measured by integration on ^{1}H NMR spectra. Conversions into urea were established by integration on the **B5** and **D5** ^{1}H NMR spectra.

At each step of the post-functionalisation, mixed-linker carboxylate MOFs present optimal thermal stability and reactivity. Amino-functionalised MOFs are highly stable, but they can be converted easily only if electrophilic reactants such as acid anhydrides, acyl chlorides or isocyanates are used. These molecules rarely present nucleophilic groups because they can condense onto themselves. The inability to furnish potentially chelating groups is a limitation for grafting organometallics in a controlled environment.

An azide-functionalised MOF is an efficient platform for click chemistry. Triazole groups, even functionalised ones, could then be grafted onto the MOF through the reaction of azide groups with an alkyne. Unfortunately, the azide groups have a very low stability. Furthermore, in the case of a Cu-catalysed click reaction, copper traces remained inside the pore after reaction[24].

Isocyanate-functionalised MOFs have intermediate features (Table 3), with thermal stability similar to that of amino-functionalised MOFs. As an isocyanate group is relatively electrophilic, a large library of amines or alcohols[17] could be condensed onto it.

Table 3. Thermal stability and examples of reactants for each post-functionalisation step.

	Thermal Stability*	Reactants
20%NH_2 MOFs (**B1** and **D1**)	435 / 395°C	Acid anhydride[25] Acyl chloride[15] Isocyanate[26]
20%N_3 MOFs (**B2** and **D2**)	150 / 150°C	Alkyne[3, 4, 18]
20%NCO MOFs (**B3** and **D3**)	435 / 375°C	Amine*,[17] Alcohol[17]

*This work

This work presents a soft, two-step method of synthesising an isocyanate-substituted MOF from its amino analogue. It appears that the transformation of azide into isocyanate presents side reactions that limit selectivity. Through the use of a mixed-linker approach, acceptable selectivity has been maintained and isocyanate-substituted In-MIL-68 and Al-MIL-53 have been synthesised. We have demonstrated that the MOF structure should ideally be more rigid than flexible in order to successfully confront the highly reactive nitrene species. Isocyanate-functionalised MOFs could therefore react with amines to form urea groups. This soft generic method could be extended to a large library of reactants and MOFs and could provide new perspectives in the grafting of elaborate organometallics for catalysis.

V. References

[1] S. M. Cohen, *Chemical Reviews*, **2012**, **112**, 970-1000.
[2] J. Canivet and D. Farrusseng, *ChemCatChem*, **2011**, **3**, 823-826.
[3] M. Savonnet, D. Bazer-Bachi, N. Bats, J. Perez-Pellitero, E. Jeanneau, V. Lecocq, C. Pinel and D. Farrusseng, *Journal of the American Chemical Society*, **2010**, **132**, 4518-4519.
[4] M. Savonnet, E. Kockrick, A. Camarata, D. Bazer-Bachi, N. Bats, V. Lecocq, C. Pinel and D. Farrusseng, *New J. Chem.*, **2011**, **35**, 1892-1897.
[5] J. Canivet, S. Aguado, G. Bergeret and D. Farrusseng, *Chemical Communications*, **2011**, **47**, 11650-11652.
[6] K. Koh, A. G. Wong-Foy and A. J. Matzger, *Angew. Chem.-Int. Edit.*, **2008**, **47**, 677-680.
[7] M. Eddaoudi, J. Kim, N. Rosi, D. Vodak, J. Wachter, M. O'Keefe and O. M. Yaghi, *Science*, **2002**, **295**, 469-472.
[8] D. N. Dybtsev, H. Chun, S. Yoon, D. Kim and K. Kim, *J. Am. Chem. Soc.*, **2004**, **126**, 32-33.
[9] J. S. Costa, P. Gamez, C. A. Black, O. Roubeau, S. J. Teat and J. Reedijk, *European Journal Of Inorganic Chemistry*, **2008**, 1551-1554.
[10] S. Bauer, C. Serre, T. Devic, P. Horcajada, J. Marrot, G. Ferey and N. Stock, *Inorganic Chemistry*, **2008**, **47**, 7568-7576.
[11] F. Vermoortele, R. Ameloot, A. Vimont, C. Serre and D. De Vos, *Chemical Communications*, **2011**, **47**, 1521-1523.
[12] M. Hartmann and M. Fischer, *Microporous and Mesoporous Materials*, **2012**.
[13] M. A. Moreira, J. o. C. Santos, A. F. P. Ferreira, J. M. Loureiro, F. Ragon, P. Horcajada, P. G. Yot, C. Serre and A. E. Rodrigues, *Langmuir*, **2012**, **28**, 3494-3502.
[14] S. J. Garibay, Z. Wang, K. K. Tanabe and S. M. Cohen, *Inorganic Chemistry*, **2009**, **48**, 7341-7349.
[15] M. Savonnet, S. Aguado, U. Ravon, D. Bazer-Bachi, V. Lecocq, N. Bats, C. Pinel and D. Farrusseng, *Green Chemistry*, **2009**, **11**, 1729-1732.
[16] Z. Q. Wang and S. M. Cohen, *Chemical Society Reviews*, **2009**, **38**, 1315-1329.
[17] C. Volkringer and S. M. Cohen, *Angewandte Chemie International Edition*, **2010**, **49**, 4644-4648.
[18] M. Savonnet, A. Camarata, J. Canivet, D. Bazer-Bachi, N. Bats, V. Lecocq, C. Pinel and D. Farrusseng, *Dalton Transactions*, **2012**, **41**, 3945-3948.
[19] H. Sato, R. Matsuda, K. Sugimoto, M. Takata and S. Kitagawa, *Nat Mater*, **2010**, **9**, 661-666.
[20] T. Lescouet, E. Kockrick, G. Bergeret, M. Pera-Titus, S. Aguado and D. Farrusseng, *Journal of Materials Chemistry*, **2012**.
[21] T. Lescouet, E. Kockrick, G. Bergeret, M. Pera-Titus and D. Farrusseng, *Dalton transactions (Cambridge, England : 2003)*, **2011**, **40**, 11359-11361.
[22] T. Ahnfeldt, D. Gunzelmann, T. Loiseau, D. Hirsemann, J. r. Senker, G. Férey and N. Stock, *Inorganic Chemistry*, **2009**, **48**, 3057-3064.
[23] G. Socrates, *Infrared characteristic group frequencies, Tables and charts*, Wiley, London, 1994.
[24] M. Savonnet, J. Canivet, S. Gambarelli, L. Dubois, D. Bazer-Bachi, V. Lecocq, N. Bats and D. Farrusseng, *CrystEngComm*, **2012**, **14**, 4105-4108.
[25] Z. Wang and S. M. Cohen, *Journal of the American Chemical Society*, **2009**, **131**, 16675-16677.
[26] E. Dugan, Z. Wang, M. Okamura, A. Medina and S. M. Cohen, *Chemical Communications*, **2008**, 3366-3368.

Experimental

I. Characterization techniques

I.1 Thermogravimetric (TG) analysis

Thermogravimetric analysis was performed with a SETARAM apparatus (Setsys Evolution 12 - TG-ATD mode). Measurements were carried out under a flow of synthetic air (50ml/min) with a 2°C/min heating ramp from room temperature to 600°C.

I.2 ^{1}H Nuclear Magnetic Resonance (^{1}H –NMR)

^{1}H-NMR spectra were recorded on a Bruker Avance 250 spectrometer operating at 250 MHz using an automated procedure for routine analysis. The spectra were calibrated using the deuterium signals of DMSO. Amino-MOF samples are commonly digested and dissolved in HF/DMSO-d_6 solution (0.8ml of HF (30% in water) in 25ml of DMSO-d_6

I.3 Diffuse-Reflectance Infrared Fourier Transform (DRIFT) Spectroscopy

Diffuse-Reflectance Infrared Fourier Transform (DRIFT) spectrum was measured at 25°C under argon flow using Thermo Scientific Nicolet 8700 FT-IR spectrometer, equipped with a MCT detector. Prior to the measurement, the samples were desorbed at 100°C under argon flow for 4 h and cooled at 25°C for measurements.

I.4 Powder X-ray diffraction (XRD)

Powder X-ray diffraction patterns were recorded using a Bruker D-5005 diffractometer (Bragg–Brentano geometry, graphite monochromator, Cu Kα radiation).

I.5 Elemental analysis (ICP-OES)

Elemental analysis was measured by Inductively Coupled Plasma Optical Emission Spectroscopy (ICP-OES). The samples were dissolved in a boiling sulphuric and nitric acid mixture under reflux conditions and metal contents were analyzed using ICP-OES Activa spectrometer (Jobin-Yvon).

I.6 N_2 and CO_2 Physisorption

Nitrogen and CO_2 physisorption isotherms were measured at 77K using a Micromeretics 2020 apparatus. Prior to the measurement, the samples were activated in primary vacuum at 100°C for 24 hours. Specific surface areas were calculated using the BET equation (p/p_o = 0.05-0.2).

CO_2 physisorption isotherms were measured at 303K using a Belsorp Max system (Bel Japan). Prior to the measurement, the samples were activated in vacuum at 100°C for 24 hours.

I.7 Field Emission Scanning Electron Microscopy (FESEM)

FESEM and EDS-analysis (Energy Dispersive Spectrometer) were carried out with a Stereoscan 260 SEM with EDX analysis system using SE (Secondary Electrons) and BSE (Backscattered Electrons) detectors, respectively. Elemental analyses using EDX were obtained as a mean value of five measurements in a magnification of 3000.

II. Synthesis

II.1 Phthalocyanine Encapsulated in MIL-101

II.1.1 MIL-101

Mesoporous MIL-101 was prepared and purified by a modified synthesis introduced by *Ferey et al.*[1] A solution containing 2.4 g chromium nitrate nonahydrate ($Cr(NO_3)_3 \cdot 9 \cdot H_2O$) (Sigma-Aldrich), 1.50 g 1,4-benzenedicarboxylic acid (bdc) (Sigma-Aldrich), 0.30 ml of hydrofluoric acid (40 % in water) (Sigma-Aldrich) and 30 ml deionised H_2O was introduced in a 48 ml Teflon-liner autoclave and was heated to 493 K for 9 h (heating ramp 25K/h). After a cooling period of 8 h, the reaction mixture was filtered through a large pore fritted glass filter to eliminate excess of recrystallised terephthalic acid. The product was separated from water by centrifugation at 4000 rpm for 20 min. In order to remove incorporated 1,4-benzenedicarboxylic acid, the as-synthesized product was first treated in 100 ml of ammonium fluoride solution in water/ethanol 1:1 v/v (3.7 g NH_4F) for 24 h at 70 °C. Afterwards the halide salt excess was washed by an aqueous soxhlet-extraction for 20 h. Finally, the solid was dried at 423 K for 9 h under reduced pressure to obtain activated, fine powdered MIL-101.

II.1.2 Synthesis of pthhalocyanine complexes

The preparation of metal phthalocyanine complexes was performed according to published procedures: $FePc(COOH)_4$[2], $FePc^tBu_4$ [3], $(FePc^tBu_4)_2N$ [4], $FePc(SO_3H)_4$ [5], $FePcF_{16}$ [6], $RuPcF_{16}$ [7], $CoPc(COOH)_8$[8].

II.1.3 Encapsulation of phthalocyanine complexes inside MIL-101

The MPc–MOF composite materials were prepared by wet infiltration of the deep blue-colored MPc solutions into Cr–MIL-101. 25 mg of $MPcF_{16}$ (M=Fe, Ru) or $(FePc^tBu_4)_2N$ complexes were dissolved in 25 ml of acetone or dichloromethane, respectively. 250 mg of activated MIL-101 were added to the intense blue coloured solution and continuously stirred for 72 h. After complete solvent evaporation the composite materials were washed with solvent (acetone or DCM), stirred for 2 h and centrifuged at 4000 rpm for 20 min several times until the solutions remain colourless. Finally, solids were dried under air for 4 h at 423 K followed by drying under reduced pressure overnight at the same temperature to obtain activated catalyst systems.

II.2 MIL-53 Synthesis

II.2.1 MIL-53(Al)-NH2 Synthesis

MIL-53(Al)-NH_2 was prepared and purified using a modified synthesis protocol based on Stock et al[9]. Solutions containing 1.931 g (8 mmol) of aluminum chloride hexahydrate (Sigma-Aldrich), 8 mmol of 2-aminobenzene-1,4-dicarboxylate (abdc) (Sigma-Aldrich) and 30 mL deionized H_2O were introduced into a 48- mL Teflon-lined autoclave and subjected to solvothermal synthesis at 150°C for 9 h. After the synthesis, product was separated from water by centrifugation at 4000 rpm for 5 min. To remove any excess linker trapped within the porous network, the as-synthesized product was placed in an autoclave with 30 mL anhydrous N,N-dimethylformamide (DMF) and heated at 150°C for 24 h.[10] The solvent was then substituted by fresh DMF and the solvothermal treatment was repeated twice. Afterwards, the DMF-containing solid was submitted to dichloromethane (DCM) Soxhlet-extraction for 20 h to remove DMF. Finally, the solids were dried at 100°C for 9 h under reduced pressure to obtain MIL-53(Al)-NH_2 as a yellow powder.

II.2.2 MIL-53(Ga)-NH2 Synthesis

MIL-53(Ga)-NH_2 could be obtained by a solvothermal method analogous to the one described by Stock et al[9] or by a precipitation method. Solutions containing 2.046 g (8 mmol) of Gallium nitrate hydrate (Sigma-Aldrich), 8 mmol of 2-aminobenzene-1,4-dicarboxylate (Sigma-Aldrich) and 30 mL deionized H_2O were introduced into a 48- mL Teflon-lined autoclave and subjected to solvothermal synthesis at 110°C for 48h. In the precipitation procedure, Gallium nitrate and 2-aminoterephthalic acid were solvated in water. The reaction mixtures were stirred for 5 minutes, and then a solution of triethylamine (Et_3N, 2 equivalents, Sigma-Aldrich) in water was added. After stirring for 120 minutes at room temperature, the resulting precipitates were filtered, washed intensively with water and dried. Products of the both two methods were purified by three DMF extractions and a DCM soxhlet.

II.3 MIL-68 Synthesis

II.3.1 MIL-68(In)-NH2 Synthesis

MIL-68(In)-NH_2 was obtained by precipitation[11] in a Pyrex beaker (capacity 100 mL) starting from a mixture of 4.82 mL (4.14 mmol) of 0.86 M indium nitrate in anhydrous N,N-dimethylformamide (DMF) and 10.06 mL (3.32 mmol) of 0.33 M 2-aminoterephthalic acid in DMF. The reaction mixture was stirred for 5 minutes, then 4.83 mL (6.67 mmol) of 1.38 M 4-diazabicyclo[2.2.2] octane (DABCO) in DMF were added. The reaction mixtures were stirred for 120 minutes at room temperature. The precipitates obtained were washed with DMF at 160°C followed by a dichloromethane Soxhlet extraction for 24 h in order to remove remaining free acid. The resulting mass of dried MIL-68(In)-NH_2 was 880 mg.

II.3.2 MIL-68(Ga)-NH2 Synthesis

As for MIL-53(Ga)-NH_2, MIL-68(Ga)-NH_2 can be obtained by solvothermal or precipitation synthesis. Solutions containing 2.046 g (8 mmol) of Gallium nitrate hydrate , 8 mmol of 2-aminobenzene-1,4-dicarboxylate and 30 mL anhydrous DMF (THF gives identical result) were introduced into a 48- mL Teflon-lined autoclave and subjected to solvothermal synthesis at 110°C for 48 h. In the precipitation procedure, Gallium nitrate and 2-aminoterephthalic acid were solvated in DMF. The reaction mixtures were stirred for 5 minutes,

and then a solution of triethylamine (Et_3N) in DMF was added. After stirring for 120 minutes at room temperature, the resulting precipitates were filtered and dried. Products of both methods were purified by three DMF extractions at 150°C and a DCM soxhlet. The activated solid was dried under vaccum to give 860mg of an off-white powder.

II.4 mixed linkers MOF Synthesis

II.4.1 Mixed linkers MIL-53(Al) Synthesis

Six different samples, including $Al(OH)(bdc)_n$ (e.g., MIL-53(Al)), $Al(OH)(abdc)_n$, (e.g., MIL-53(Al)-NH_2) and mixed $Al(OH)(bdc)_{1-n}$ $(abdc)_n$, were prepared and purified using a modified synthesis protocol based on Stock et al. (Scheme 1).[9]

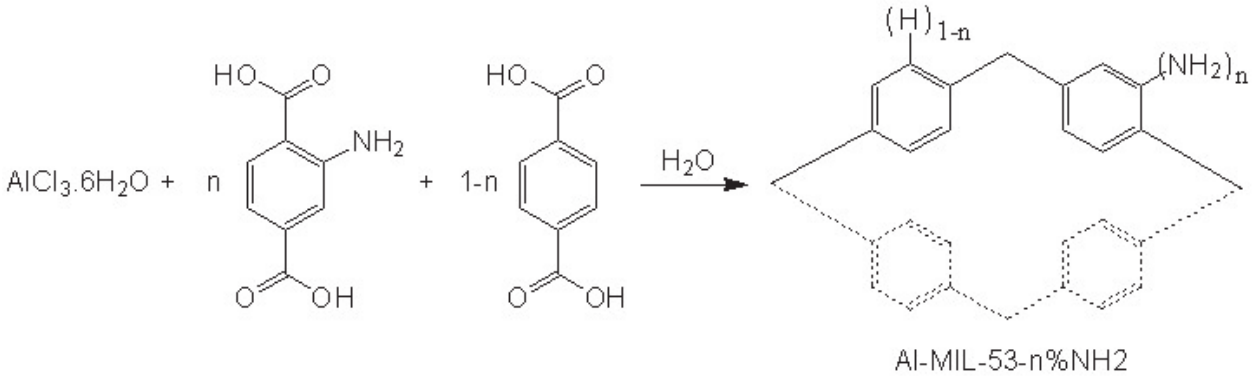

Scheme 1. Synthesis of $Al(OH)(bdc)_{1-n}$ $(abdc)_n$.

Solutions containing 1.931 g (8 mmol) of aluminum chloride hexahydrate ($Al(Cl)_3 \cdot 6H_2O$), 8 mmol of benzene-1,4-dicarboxylate and 2-aminobenzene-1,4-dicarboxylate with different molar ratios (0, 11.1, 20, 50, 66.7 and 100% abdc) and 30 mL deionized water were introduced into a 48- mL Teflon-lined autoclave and subjected to solvothermal synthesis at 150°C for 9 h. After the synthesis, the solids were separated from water by centrifugation at 4000 rpm for 5 min. To remove any excess linker trapped within the porous network, the as-synthesized products were placed in an autoclave with 30 mL anhydrous DMF and heated at 150°C for 24 h.[10] The solvent was then substituted by fresh DMF and the solvothermal treatment was repeated twice. Afterwards, the DMF-containing solids were submitted to dichloromethane Soxhlet-extraction for 20 h to remove DMF. Finally, the solids were dried at 100°C for 9 h at reduced pressure to obtain powdered MIL-53(Al), MIL-53(Al)-11.1%NH_2, MIL-53(Al)-20%NH_2, MIL-53(Al)-50%NH_2, MIL-53(Al)-66.7%NH_2 and MIL-53(Al)-NH_2 samples.

II.4.2 Mixed linkers MIL-68 (In) Synthesis

Indium nitrate (1 203.3mg, 4mmol), abdc (144.9mg, 0.8mmol) and bdc (531.2mg, 3.2mmol) were dissolved in DMF (30ml). The reaction mixture was stirred for 5 minutes then a solution of 4-diazabicyclo[2.2.2] octane (DABCO) (897.4mg, 8mmol) in DMF (10ml) were added. The reaction mixture was stirred for 120 minutes at room temperature. The obtained precipitate was washed with DMF in an autoclave at 150 °C overnight follow by a dichloromethane soxhlet during 24h.

II.5. Post synthetic modification

II.5.1 Azido functionalized MOF synthesis

A typical azido synthesis was carried out to form the following MOFs: Al-MIL-53-N_3, In-MIL-68-N_3, Al-MIL-53-20%N_3 and In-MIL-68-20%N_3. In this procedure, freshly dried Al-MIL-53-NH_2**,** In-MIL-68-NH_2, Al-MIL-53-20%NH_2 and In-MIL-68-20%NH_2 (200 mg, 0.73 mmol equiv of -NH_2) were placed into a vial (10 mL capacity) with 3.0 mL of solvent (THF), 1.5 mL (12.65 mmol) of tBuONO and 1.4 mL (10.64 mmol) of $TMSN_3$. Samples were left to react for 6 hours at room temperature to produce the azido MOFs. The reaction was quenched by decanting the solvent. Excess reactants were removed by washing three times in THF followed by three times in CH_2Cl_2. Drying at room temperature yielded yellowish powders[11-13].

II.5.2 isocyanato functionalized MOF synthesis (diphosgene route)

Al-MIL-53-NCO and Al-MIL-53-20%NCO were prepared by the synthesis reported by Cohen *et al.*[14] Diphosgene (0.5 mL, 4.14 mmol) was added to stirred suspensions of Al-MIL-53-NH_2 and Al-MIL-53-20%NH_2 (200 mg, 0.73 mmol equivalent of -NH_2) in THF (5 mL). After 15 h, solids were removed by centrifugation, washed three times with fresh THF and dried at reduced pressure[14].

II.5.3 isocyanato functionalized MOF synthesis (CO route)

Isocyanato MOFs (Al-MIL-53-NCO, In-MIL-68-NCO, Al-MIL-53-20%NCO and In-MIL-68-20%NCO) were synthesised by allowing the reaction of CO gas with the dried MOF powders.

The transformations were followed in a Diffuse Reflectance Infrared Fourier Transform (DRIFT) apparatus. Al-MIL-53-N_3, In-MIL-68-N_3, Al-MIL-53-20%N_3 and In-MIL-68-20%N_3 were placed in the DRIFT cell and desorbed at 100°C overnight under argon. The temperature was raised to 150°C prior to the introduction of flowing CO (22 mL/min). After 24 hours, the reaction was stopped and the products were collected.

II.5.4 urea functionalized MOF synthesis

Al-MIL-53-20%urea 2-amino cyclohexane and In-MIL-68-20%urea 2-amino cyclohexane were synthesised by adding (1*R*,2*R*)-1,2-diaminocyclohexane (0.5 mL, 4.16 mmol) to 200 mg Al-MIL-53-20%NCO and In-MIL-68-20%NCO, respectively, in dried acetonitrile (4 mL). Mixtures were stirred and heated at 40°C for at least 48 h. The resulting solids were washed three times with fresh acetonitrile, and then DCM Soxhlet extractions were performed for 20 h.

The synthesis of Al-MIL-53-20%urea and In-MIL-68-20%urea was conducted in the DRIFT apparatus in order to characterise the transformations over time by treating Al-MIL-53-20%NCO and In-MIL-68-20%NCO at 90°C with an argon flow containing 1% NH_3 over a 24-hour period.

III. Catalysis

III.1 Tetralin oxidation

Catalytic tetralin oxidation under static pressure was carried out in parallel reactors with eight pressure stable micro-reaction-vessels (3 ml) inside a temperature-controlled steel vessel. In a typical reaction a mixture of 2.5 ml of tetralin and 1 mg of the pure complexes or 5 mg of the MIL-101 supported complex systems was placed into the batch reactor and heated under continuously stirring at 900 rpm to the desired temperature (50-130 °C) under static oxygen or synthetic air pressure up to 6-10 bar for 1 to 24 h. After cooling down to room temperature, the reaction mixtures were depressurized and centrifuged. The conversion and selectivity of the oxidation reactions were subsequently analyzed by gas chromatography (GC) using a HP-5 capillary column and a flame ionization detector (FID).

III.2 Oxidation of adamantane-1,3-d_2

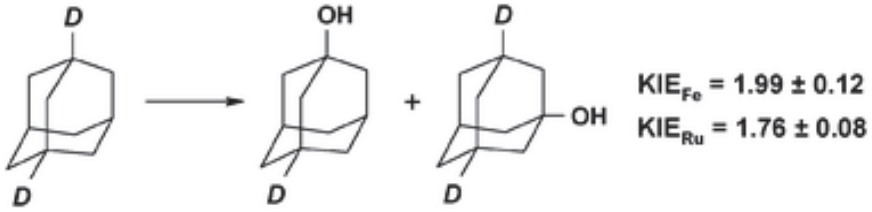

Scheme 2. The oxidation of adamantane-1,3-d_2

Adamantane-1,3-d_2 (Ad-d_2) was prepared as previously described[15]. Ad-d_2 (3.4 mg) was dissolved in 2.5 mL of acetonitrile and 5 mg of the $FePcF_{16}$–MIL-101 or $RuPcF_{16}$–MIL-101 materials were added. The resulting mixture was stirred at 90 °C at 8 bars of dioxygen for 6 h in the parallel batch reactors applied for tetralin oxidation. The reaction products were analyzed by GC-MS method (Hewlett Packard 5973/6890 system ; electron impact ionization at 70 eV, He carrier gas, 30 m x 0.25 mm cross-linked 5 % PHME (0.25 µm coating) capillary column, HP-5MS). The exact isotopic composition of 1-adamantanol was calculated by integration of all scans of the 1-adamantanol peak since AdOH-d_1 and AdOH-d_2 were partially separated on the GC column. KIEs were obtained from the intensities of molecular peak at m/z=154 (for AdOH-d_2) and m/z=153 (for AdOH-d_1) after correction on natural ^{13}C abundance (1.08 % x 10 carbon atoms = 10.8 %).

III.3 Styrene carbonate synthesis

Styrene oxide (0.2 mL, 210.4 mg, 1.75 mmol) and anhydrous DMF (1.8mL, 1699.2 mg, 23.25 mmol) were loaded in a 3 mL glass vial. The typical amount of catalyst was 50 mg. The system was heated at 150°C under magnetic stirring (1000 rt/min), then the reaction was conducted by introducing 8 bars of CO_2 into the vial. Styrene oxide and styrene carbonate concentrations were determined by GC analysis of the samples using toluene as an external standard. In all experiments, no by-product was observed. The catalytic tests were repeated independently two or three times in order to estimate the reproducibility and accuracy of the results. Test duration of 8 hours was chosen in order to have the best TOF.

IV. References

[1] G. Ferey, C. Mellot-Draznieks, C. Serre, F. Millange, J. Dutour, S. Surble and I. Margiolaki, *Science*, **2005**, **309**, 2040-2042.
[2] A. Sorokin, A. Robert and B. Meunier, *J. Am. Chem. Soc.*, **1993**, **115**, 7293-7299.
[3] J. Metz, O. Schneider and M. Hanack, *Inorg. Chem.*, **1984**, **23**, 1065-1071.
[4] A. B. Sorokin, E. V. Kudrik and D. Bouchu, *Chem. Commun.*, **2008**, 2562-2564.
[5] J. H. Weber and D. H. Busch, *Inorg. Chem.*, **1965**, **4**, 469-&.
[6] J. G. Jones and M. V. Twigg, *Inorg. Chem.*, **1969**, **8**, 2018-&.
[7] K. J. Balkus, M. Eissa and R. Levado, *J. Am. Chem. Soc.*, **1995**, **117**, 10753-10754.
[8] S. A. Mikhalenko, L. I. Solov'eva and E. A. Luk'yanets, *Russ. J. Gen. Chem.*, **2004**, **74**, 451-459.
[9] T. Ahnfeldt, D. Gunzelmann, T. Loiseau, D. Hirsemann, J. r. Senker, G. Férey and N. Stock, *Inorganic Chemistry*, **2009**, **48**, 3057-3064.
[10] S. Marx, W. Kleist, J. Huang, M. Maciejewski and A. Baiker, *Dalton Trans.*, **2010**, **39**, 3795-3798.
[11] M. Savonnet, D. Bazer-Bachi, N. Bats, J. Perez-Pellitero, E. Jeanneau, V. Lecocq, C. Pinel and D. Farrusseng, *J. Am. Chem. Soc.*, **2010**, **132**, 4518-4519.
[12] M. Savonnet, A. Camarata, J. Canivet, D. Bazer-Bachi, N. Bats, V. Lecocq, C. Pinel and D. Farrusseng, *Dalton Transactions*, **2012**, **41**, 3945-3948.
[13] M. Savonnet, E. Kockrick, A. Camarata, D. Bazer-Bachi, N. Bats, V. Lecocq, C. Pinel and D. Farrusseng, *New J. Chem.*, **2011**, **35**, 1892-1897.
[14] C. Volkringer and S. M. Cohen, *Angewandte Chemie International Edition*, **2010**, **49**, 4644-4648.
[15] J. G. Jones and M. V. Twigg, *Inorg. Chem.*, **1969**, **8**, 2018-&.

Conclusions

Le large choix de métaux et de ligands pour la synthèse de Metal-Organic Frameworks permet la formation d'un nombre infini de structures et de compositions. Néanmoins la stabilité des MOFs et leurs propriétés acides modérées sont de fortes limitations pour être compétitif par rapport aux matériaux poreux déjà utilisés en catalyse (pétrochimie, raffinage). C'est pourquoi il convient d'explorer les nouvelles propriétés de ces matériaux. Cette thèse a pour but d'utiliser la modularité des MOFs pour les rapprocher des catalyseurs biologiques avec qui ils partagent de nombreuses qualités. Cette dernière partie résume les différents résultats obtenus lors de cette thèse puis discute des travaux en cours et à réaliser pour finaliser un catalyseur hétérogène biomimétique des enzymes.

Afin d'obtenir des MOFs présentant un effet de confinement similaire aux enzymes, nous avons essayé la synthèse de MOF à partir de biomolécules. L'histidine, un acide aminé, ou encore la phthalocyanine, molécule inspirée des porphyrines, furent utilisées. Malheureusement l'utilisation de ces réactifs sophistiqués n'aboutit qu'à des matériaux amorphes ou non poreux. Aussi, d'autres méthodes furent appliquées.

L'encapsulation irréversible de catalyseurs organométalliques au sein des pores des MOFs apparut comme une alternative pour combiner l'activité du catalyseur et la sélectivité induite par la taille de pore. Le Chapitre 2 décrit l'imprégnation de perfluorophthalocyanines complexées au fer et au ruthénium dans le MOF MIL-101(Cr). L'évaluation de l'activité des ces matériaux dans l'oxydation catalytique de la tétraline sous oxygène montre que le TON du catalyseur encapsulé est environ dix fois plus important que celui mesuré en milieu homogène. De plus une modification de la sélectivité est observée. Cela peut être expliqué à la fois par un effet de confinement mais également par la dispersion des catalyseurs dans les pores qui évite la désactivation des complexes par formation de dimères. Néanmoins les liaisons non-covalentes entre le catalyseur et le support ne permettent pas la conception contrôlée d'un environnement similaire aux sites actifs des enzymes.

La post-fonctionnalisation est une méthode efficace pour greffer de façon covalente des groupes organiques aux ligands de la structure. De nombreuses réactions de condensation furent ainsi appliquées en post-traitement sur les MOFs. Les MOFs les plus communément utilisés pour la post-fonctionnalisation possèdent des fonctions amino sur leurs ligands. Ces « amino » MOFs ont l'avantage de pouvoir être synthétisés dès que leurs équivalents non fonctionnalisés existent. Le chapitre 3 décrit la synthèse est la caractérisation de quatre MOFs

portant des groupes amino. Le MIL-53(Al)-NH_2 fut choisi pour son extrême stabilité thermique et chimique ainsi que pour sa flexibilité lors de l'adsorption de molécules semblable à l'interaction réactif-structure des enzymes. Le MIL-68(In)-NH_2 est un MOF rigide élaboré au sein de notre institut. Sa stabilité chimique modérée permet de prouver la généricité des méthodes de traitements appliqués au MIL-53 (Al)-NH_2. Ces deux structures décrites dans la littérature furent étendues avec l'utilisation du gallium et deux nouveaux MOFs furent synthétisés. Le MIL-53(Ga)-NH_2 et MIL-68(Ga)-NH_2 furent synthétisés par méthode hydrothermale et précipitation. Il apparaît que le choix du solvant est ici primordial pour obtenir la structure voulue. Du fait de la faible porosité des MOFs à base de gallium, seuls le MIL-53(Al)-NH_2 et le MIL-68(In)-NH_2 sont conservés dans les travaux des chapitres suivants.

Afin de comprendre si la fonction amino pouvait posséder des propriétés basiques qui pourrait théoriquement réaliser un mécanisme concerté avec le centre métallique acide, ces amino MOFs furent testés dans la synthèse catalytique de carbonate à partir d'oxyde de styrène sous pression de dioxyde de carbone. Il apparaît que le MIL-68(In)-NH_2 possède une activité et que celle-ci est supérieure à celle de son équivalent non aminé. Des expériences DRIFT ainsi que de la modélisation DFT prouvent que le groupe amino ne dissocie pas le CO_2 en carbamate comme dans le cas des bases fortes. Il s'avère néanmoins que cette substitution augmente l'acidité de Brønsted du complexe $InO_4(OH)_2$ par effet électronique.

La diminution de la densité de site fonctionnalisé au sein des MOFs est essentielle afin de créer des sites isolés qui n'interagissent pas avec l'environnement des pores voisins. La stratégie « mixed linker » MOF qui consiste à diluer le ligand aminé avec son analogue non fonctionnalisé apporte une solution à ce problème. Néanmoins rien ne pouvait prédire une répartition homogène des substituants dans la structure.

Le Chapitre 4 décrit la synthèse de plusieurs MIL-53(Al) avec différent taux de fonctionnalisation. Les différents matériaux furent étudiés en adsorption et diffraction de rayons-X en température afin de déterminer à quelle pression et température ceux-ci changeaient de structure et « ouvraient » leurs pores. La linéarité entre la pression d'ouverture et le taux de greffage est un indice de l'homogénéité de ces matériaux. Les microcristaux possèdent en effet le même rapport ligand amino/ ligand non fonctionnalisé. De plus ces expériences ont montré qu il était possible de contrôler la pression d'ouverture de ces « mixed

linker » MOFs et donc leur flexibilité. Ceci est un premier pas vers des matériaux présentant des propriétés contrôlées de reconnaissance moléculaire.
Enfin cette méthode fut étendue à la synthèse du MIL-68(In). La présence de substituant sur les ligands diminue généralement la résistance thermique des matériaux. Cette stratégie nous a également permis de conserver des stabilités proches de celles des matériaux non fonctionnalisés.

Beaucoup de travaux sur la post-fonctionnalisation de MOFs proposent la condensation de réactifs sur les groupes amino présents dans les MOFs. Néanmoins la faible nucléophilie de ces groupes obligent l'utilisation d'électrophiles forts comme les chlorure d'acide, les anhydrides ou les isocyanates. Malheureusement peu de ces réactifs sont commercialement disponibles et leur condensation libère des espèces acides dans le milieu qui peuvent endommager la structure du MOF (chlorure d'acide et anhydrides).
Le chapitre 5 décrit une nouvelle méthode pour transformer les amino MOFs en isocyanato MOFs. La réactivité des substituants passe alors d'une nucléophilie modéré à une électrophilie élevée et diverses amines peuvent y être greffées. Cette post-fonctionnalisation est possible grâce à la transformation des groupes amino en azides. Les groupes azides sont alors activés thermiquement en nitrenes qui réagissent avec du monoxyde de carbone pour former les groupes isocyanates. Le suivi *in situ* dans un appareil DRIFT de la transformation des azido MOFs en isocyanato MOFs permet de mieux mesurer la cinétique de la réaction. La non linéarité de la disparition des azides et l'apparition des groupes isocyanates indiquent l'accumulation de radicaux dans les pores. Ces radicaux peuvent réagir entre eux et former des produits secondaires. Cette observation est confirmée par la sélectivité de la réaction qui passe de presque 0% pour les MOFs entièrement fonctionnalisés à 100% dans le cas du MIL-68(In) dont seulement 20% des ligands portent la fonctions NH_2. La diminution de la densité de site actif grâce à la stratégie « mixed linker » est cruciale pour obtenir les fonctions isocyanates. Enfin des amines furent condensées avec succès en phase gazeuse et en phase liquide pour former des groupes urées.
La seule méthode précédemment publiée pour la transformation d'amino MOFs en isocyanato MOFs utilisait un traitement au diphosgène et n'était applicable que sur le super stable MIL-53(Al). Nous avons ici mis au point une méthode sans solvant et généralisable à un large panel de structure.

Perspectives :

Cette étude montre qu'il est possible de contrôler les flexibilités ou encore les propriétés (acides et basiques) de MOF par la fonctionnalisation des ligands. Les pores peuvent être décorés grâce à la condensation de diverses amines afin de reproduire un environnement similaire aux sites catalytiques des enzymes. Néanmoins l'utilisation des centres métalliques de la structure comme site actif peut poser plusieurs problèmes. L'accès des réactifs au métal peut être limité du fait de l'encombrement stérique. De plus le changement de coordination lors du cycle catalytique peut être préjudiciable pour la structure. Il est donc intéressant de complexer les métaux sur les fonctions organiques greffées sur les ligands. Des précurseurs de palladium et du cuivre furent imprégnés sur plusieurs de nos MOFs dont les ligands portent des fonctions urée aminobenzène et urée aminocyclohexane. Ils sont actuellement analysés par MET, XPS, RPE (cuivre) et RMN à hauts champs afin de prouver et déterminer la coordination du complexe. Enfin des molécules chirales comme le (1S,2S)-(+)-1,2-diaminocyclohexane furent greffées ouvrant des perspectives en catalyse énantiosélective.

Nous apportons ici des outils pour la conception de MOF dont les pores ont un environnement proche des enzymes. Néanmoins il parait essentiel dans un second temps de faire appel aux outils de la modélisation et à des biologistes et de se focaliser sur un site enzymatique en particulier. La modélisation DFT est un outil de calcul puissant pour évaluer la configuration la plus probable des substituants dans les pores (Figure) et ainsi comprendre le mécanisme d'interactions substrats-structure.

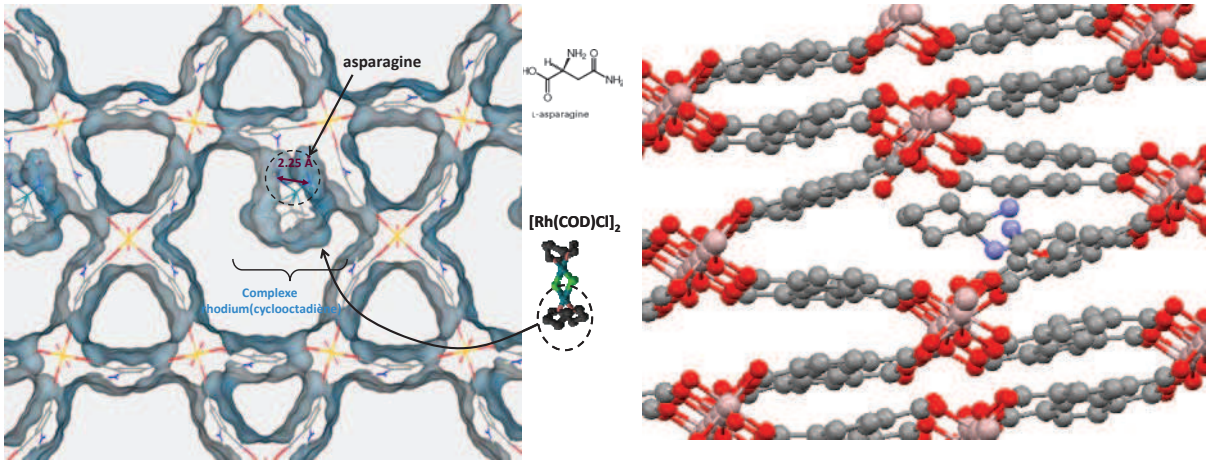

Figure. Modélisation DFT d'un complexe rhodium cyclooctadiène greffé sur un MOF fonctionnalisé à la L-asparagine (à gauche). Modélisation du substituant urée amino cyclohexane dans un pore de MIL-53(Al) (à droite).

Enfin des systèmes artificiels, récemment obtenus par auto assemblage d'urées fonctionnalisé par des macrocycles ou par des imidazole[1, 2] et formant des canaux possédant une polarité unique ont montré des aptitudes pour le transport de protons ou de molécules d'eau similaires aux protéines naturelles (protéines Influenza A M2 et aquaporins). Grâce à la possibilité de fonctionnaliser les canaux des MOFs avec des groupes organiques organisées, des propriétés de conductivité identiques peuvent être espérées.

[1] M. Barboiu, *Chem. Commun.*, **2010**, **46**, 7466-7476.
[2] Y. Le Duc, M. Michau, A. Gilles, V. Gence, Y.-M. Legrand, A. van der Lee, S. Tingry and M. Barboiu, *Angew. Chem. Int. Ed.*, **2011**, **50**, 11366-11372.

Appendix

I. Crystal data of the MIL-53(Al) "mixed linker" (Chapter 4)

Table 1. Crystal data for A (MIL-53(Al))

	Structure lt, np, monoclinic Cc SG 9					Structure ht, lp, orthorhombic			
Temperature	a (Å)	b(Å)	c(Å)	Bêta	V(Å)3	a (Å)	b(Å)	c(Å)	V(Å)3
°C	19,5130	7,6120	6,5760	104,24	946,8	6,6085	16,6750	12,8130	1412,0
80						6,6240	16,7871	12,7463	1417,4
100						6,6180	16,7728	12,7525	1415,6
120						6,6171	16,7538	12,7708	1415,8
140						6,6155	16,7477	12,7725	1415,1
160						6,6142	16,7393	12,7719	1414,1
180						6,6117	16,7359	12,7702	1413,0
200						6,6099	16,7292	12,7722	1412,3
220						6,6089	16,7283	12,7727	1412,1
240						6,6070	16,7258	12,7739	1411,6
260						6,6051	16,7227	12,7737	1410,9
280						6,6039	16,7189	12,7764	1410,6
300						6,6032	16,7242	12,7764	1410,9
320						6,6031	16,7237	12,7702	1410,2
340						6,6021	16,7180	12,7721	1409,7
360						6,6003	16,7128	12,7740	1409,1
380						6,6001	16,7109	12,7769	1409,2
400						6,5995	16,7026	12,7821	1409,0
420						6,5975	16,6817	12,8018	1408,9
440						6,5932	16,6178	12,8604	1409,0
460						6,5869	16,5647	12,9199	1409,7
480						6,5798	16,5216	12,9680	1409,7

Table 2. Crystal data for B (MIL-53(Al)-11.1%NH_2)

	Structure lt, np, monoclinic Cc SG 9					Structure ht, lp, orthorhombic			
Temperature	a (Å)	b(Å)	c(Å)	Bêta	V(Å)3	a (Å)	b(Å)	c(Å)	V(Å)3
°C	19,5130	7,6120	6,5760	104,24	946,8	6,6085	16,6750	12,8130	1412,0
25	19,590	7,628	6,597	104,67	953,7				
40	19,559	7,345	6,594	104,72	916,2				
60	19,684	7,295	6,619	104,95	918,3				
80	19,705	7,337	6,623	105,09	924,5				
100	19,751	7,395	6,629	105,26	934,0	6,653	16,821	12,818	1434,4
120	19,779	7,443	6,633	105,41	941,4	6,656	16,837	12,843	1439,4
140	19,767	7,488	6,633	105,51	946,1	6,654	16,837	12,836	1438,0
160	19,753	7,532	6,632	105,63	950,3	6,650	16,835	12,825	1435,8
180	19,768	7,572	6,629	105,85	954,6	6,648	16,815	12,815	1432,6
200	19,761	7,618	6,631	106,13	958,9	6,644	16,823	12,804	1431,1
220	19,778	7,651	6,633	106,07	964,5	6,636	16,808	12,789	1426,5
240	19,775	7,691	6,630	105,97	969,6	6,628	16,795	12,771	1421,6
260	19,761	7,741	6,620	105,92	973,8	6,623	16,786	12,764	1418,9
280	19,963	7,776	6,608	106,37	984,1	6,619	16,779	12,754	1416,4
300	19,956	7,830	6,585	106,36	987,2	6,614	16,773	12,754	1414,8

320	19,987	7,886	6,547	106,49	989,4	6,613	16,765	12,758	1414,4
340	20,038	7,929	6,521	106,55	993,2	6,613	16,766	12,759	1414,5
360	20,123	7,935	6,514	106,82	995,6	6,612	16,769	12,751	1413,8
380						6,617	16,778	12,748	1415,3
400						6,621	16,779	12,760	1417,6
420						6,624	16,773	12,776	1419,4
440						6,634	16,785	12,802	1425,5
460						6,645	16,818	12,838	1434,8
480						6,655	16,870	12,857	1443,4

Table 3. Crystal data for C (MIL-53(Al)-20%NH_2)

	Structure lt, np, monoclinic Cc SG 9					Structure ht, lp, orthorhombic			
Temperature	a (Å)	b(Å)	c(Å)	Bêta	V(Å)3	a (Å)	b(Å)	c(Å)	V(Å)3
°C	19,5130	7,6120	6,5760	104,24	946,8	6,6085	16,6750	12,8130	1412,0
25	19,602	7,661	6,593	104,77	957,3				
40	19,719	7,555	6,606	105,31	949,2				
60	19,729	7,364	6,617	105,20	927,8				
80	19,760	7,392	6,623	105,31	933,1	6,650	16,697	12,845	1426,26
100	19,776	7,427	6,625	105,41	938,1	6,650	16,870	12,799	1435,86
120	19,792	7,455	6,631	105,51	942,7	6,653	16,836	12,823	1436,24
140	19,789	7,491	6,631	105,62	946,8	6,651	16,846	12,798	1433,95
160	19,795	7,535	6,633	105,72	952,3	6,652	16,844	12,793	1433,47
180	19,796	7,576	6,631	105,81	956,8	6,653	16,837	12,783	1431,84
200	19,808	7,617	6,629	105,95	961,7	6,648	16,835	12,775	1429,81
220	19,799	7,657	6,628	105,98	966,1	6,639	16,822	12,768	1425,93
240	19,848	7,694	6,618	106,06	971,2	6,631	16,823	12,732	1420,21
260	19,956	7,731	6,611	106,30	979,0	6,626	16,818	12,714	1416,76
280	19,976	7,779	6,601	106,35	984,2	6,622	16,802	12,722	1415,48
300	19,990	7,832	6,582	106,38	988,7	6,617	16,797	12,723	1414,27
320	20,007	7,887	6,546	106,49	990,4	6,616	16,791	12,739	1415,23
340	20,087	7,919	6,525	106,64	994,5	6,615	16,792	12,740	1415,24
360						6,614	16,804	12,709	1412,47
380						6,619	16,814	12,699	1413,44
400						6,624	16,812	12,713	1415,76
420						6,624	16,802	12,733	1417,27
440						6,634	16,819	12,771	1424,87
450						6,657	16,878	12,838	1442,32
460						6,661	16,968	12,832	1450,35

Table 4. Crystal data for D (MIL-53(Al)-50%NH_2)

	Structure lt, np, monoclinic Cc SG 9					Structure ht, lp, orthorhombic			
Temperature	a (Å)	b(Å)	c(Å)	Bêta	V(Å)3	a (Å)	b(Å)	c(Å)	V(Å)3
°C	19,5130	7,6120	6,5760	104,24	946,8	6,6085	16,6750	12,8130	1412,0
25	19,675	7,669	6,588	105,07	959,8				
40	19,724	7,593	6,599	105,40	952,9				
60	19,779	7,421	6,619	105,45	936,5				

80	19,810	7,428	6,630	105,54	939,9				
100	19,809	7,454	6,632	105,61	943,1				
120	19,811	7,476	6,633	105,69	945,8				
140	19,805	7,508	6,634	105,76	949,3	6,632	16,551	13,063	1433,8
160	19,795	7,540	6,633	105,81	952,6	6,636	16,606	12,948	1427,0
180	19,796	7,572	6,633	105,89	956,2	6,642	16,739	12,800	1423,0
200	19,804	7,609	6,634	106,00	961,0	6,653	17,044	12,637	1433,0
220	19,807	7,648	6,634	106,07	965,7	6,636	16,807	12,721	1418,8
240	19,809	7,687	6,633	106,16	970,2	6,634	16,811	12,687	1414,9
260	19,817	7,726	6,632	106,27	974,7	6,639	16,912	12,607	1415,5
280	19,822	7,768	6,642	106,49	980,6	6,637	16,772	12,620	1404,7
300	19,863	7,841	6,654	106,65	992,8	6,639	16,834	12,680	1417,2
320	19,876	7,881	6,649	106,79	997,0	6,647	16,953	12,597	1419,6
340	19,913	7,929	6,653	106,92	1005,0	6,650	16,966	12,620	1423,7
360	19,979	7,962	6,658	107,07	1012,6	6,650	16,963	12,657	1427,7
380						6,650	16,951	12,814	1444,6
400						6,650	16,907	12,788	1437,9
420						6,641	16,870	12,827	1437,2
440						6,617	16,615	13,044	1434,1
460						6,590	16,464	13,200	1432,2
480						6,581	16,404	13,252	1430,6

Table 5. Crystal data for F (MIL-53(Al)-NH_2)

	Structure lt, np, monoclinic Cc SG 9					Structure ht, lp, orthorhombic			
Temperature	a (Å)	b(Å)	c(Å)	Bêta	V(Å)3	a (Å)	b(Å)	c(Å)	V(Å)3
°C	19,5130	7,6120	6,5760	104,24	946,8	6,6085	16,6750	12,8130	1412,0
25	19,7677	7,6680	6,5982	105,56	963,5				
40	19,7674	7,6077	6,5994	105,73	955,3				
60	19,7888	7,5030	6,6094	105,83	944,1				
80	19,8380	7,4924	6,6282	105,93	947,3				
100	19,8398	7,5121	6,6290	105,97	949,9				
120	19,8537	7,5267	6,6294	106,06	952,0				
140	19,8506	7,5538	6,6298	106,12	955,0				
160	19,8516	7,5807	6,6315	106,19	958,4				
180	19,8556	7,6084	6,6338	106,26	962,1				
200	19,8583	7,6370	6,6352	106,32	965,7				
220	19,8594	7,6661	6,6361	106,37	969,4				
240	19,8652	7,6979	6,6378	106,46	973,4				
260	19,8661	7,7298	6,6394	106,53	977,4				
280	19,8653	7,7597	6,6396	106,57	981,0				
300	19,8667	7,7892	6,6392	106,63	984,4				
320	19,8727	7,8118	6,6410	106,68	987,6				

II. COSY 1H NMR of In-MIL-20%NH_2 (D1), In-MIL-20%N_3 (D2), In-MIL-20%NCO (D3) and In-MIL-20%urea 2-amino cyclohexane (D4) (Chapter 5)

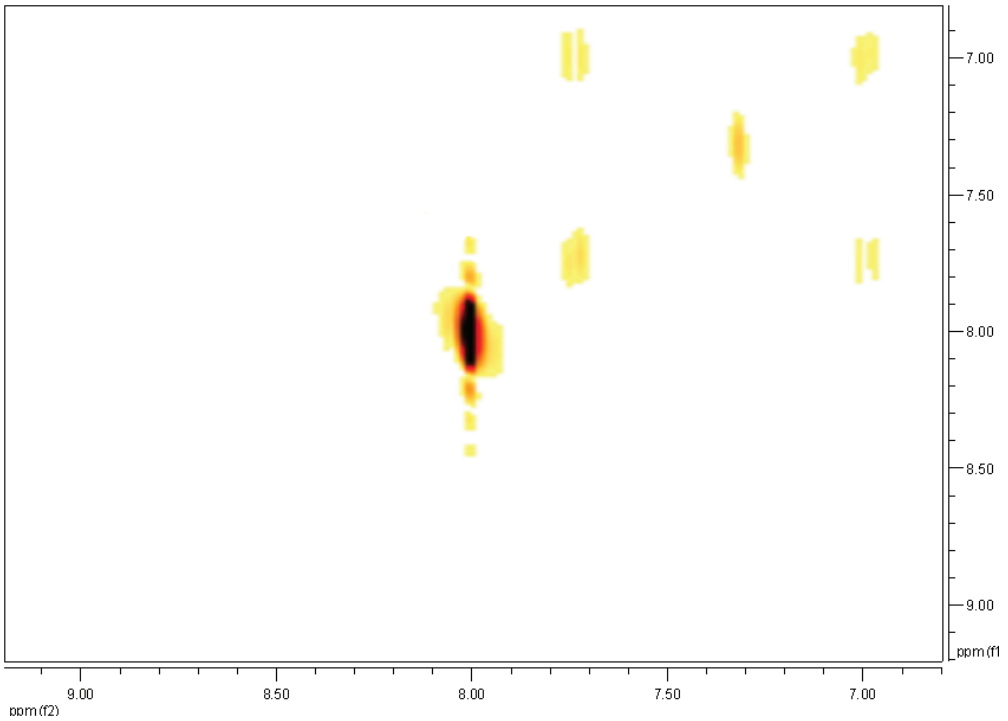

Figure 1. 2D ^{1}H NMR (COSY) of D1

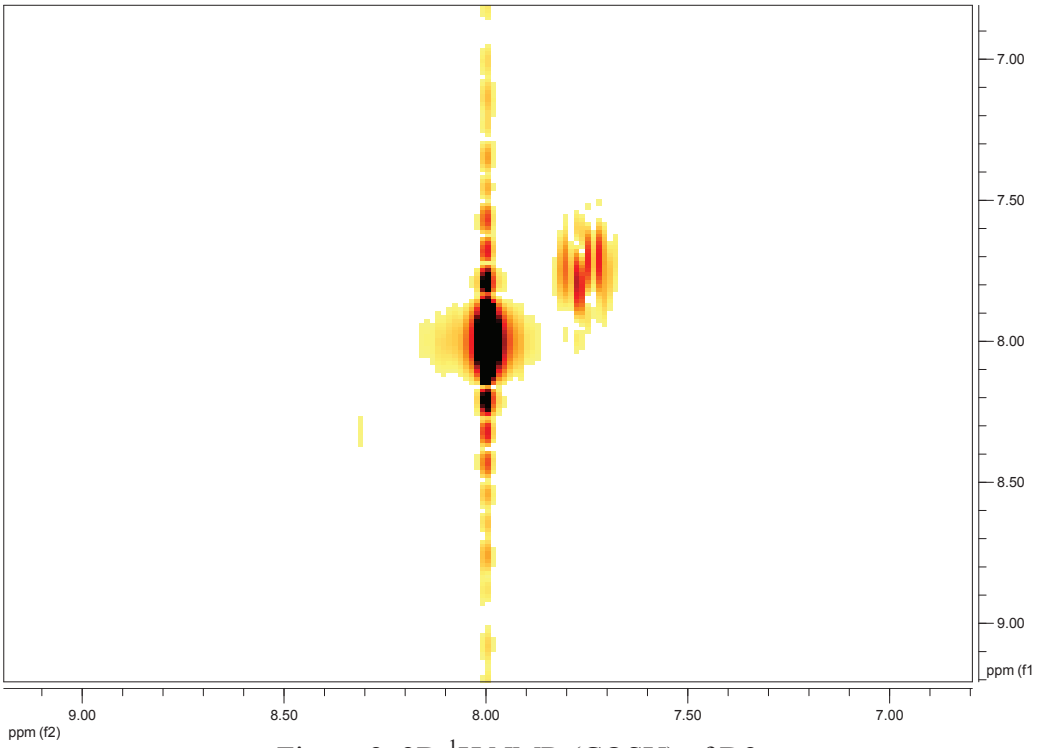

Figure 2. 2D ^{1}H NMR (COSY) of D2

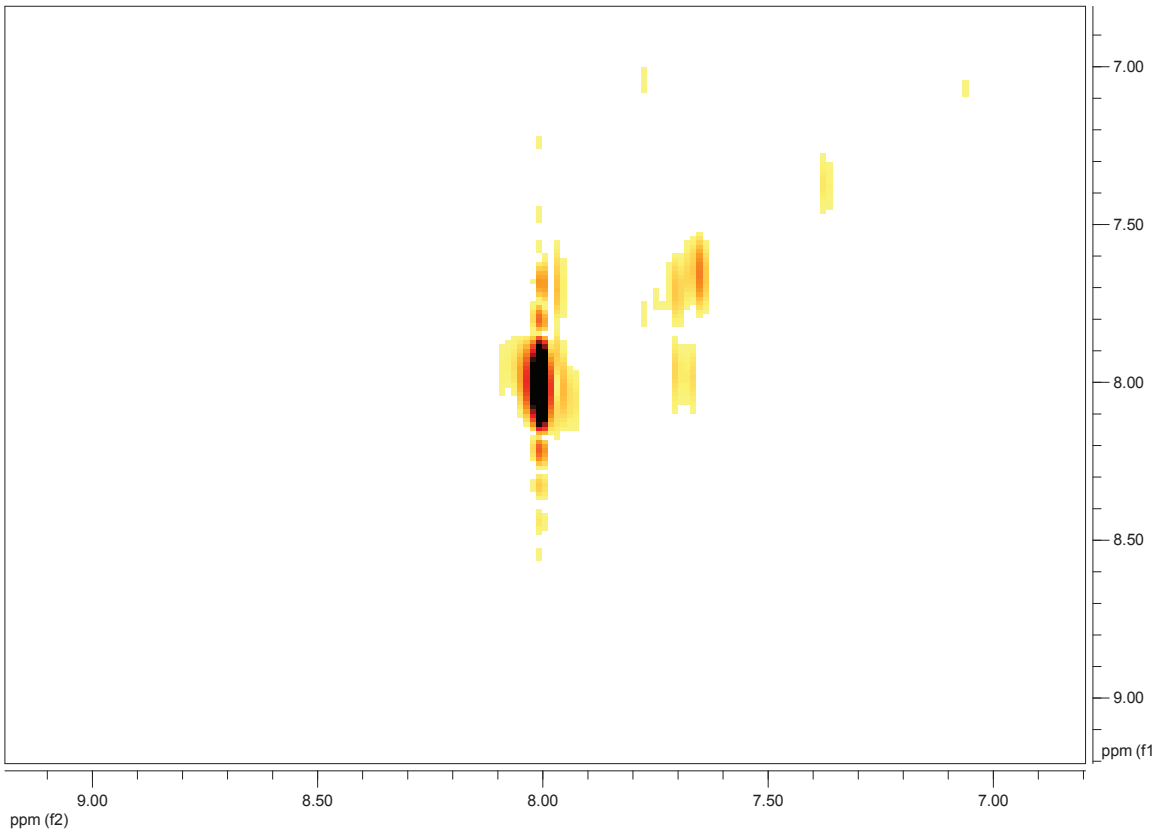

Figure 3. 2D ^{1}H NMR (COSY) of D3

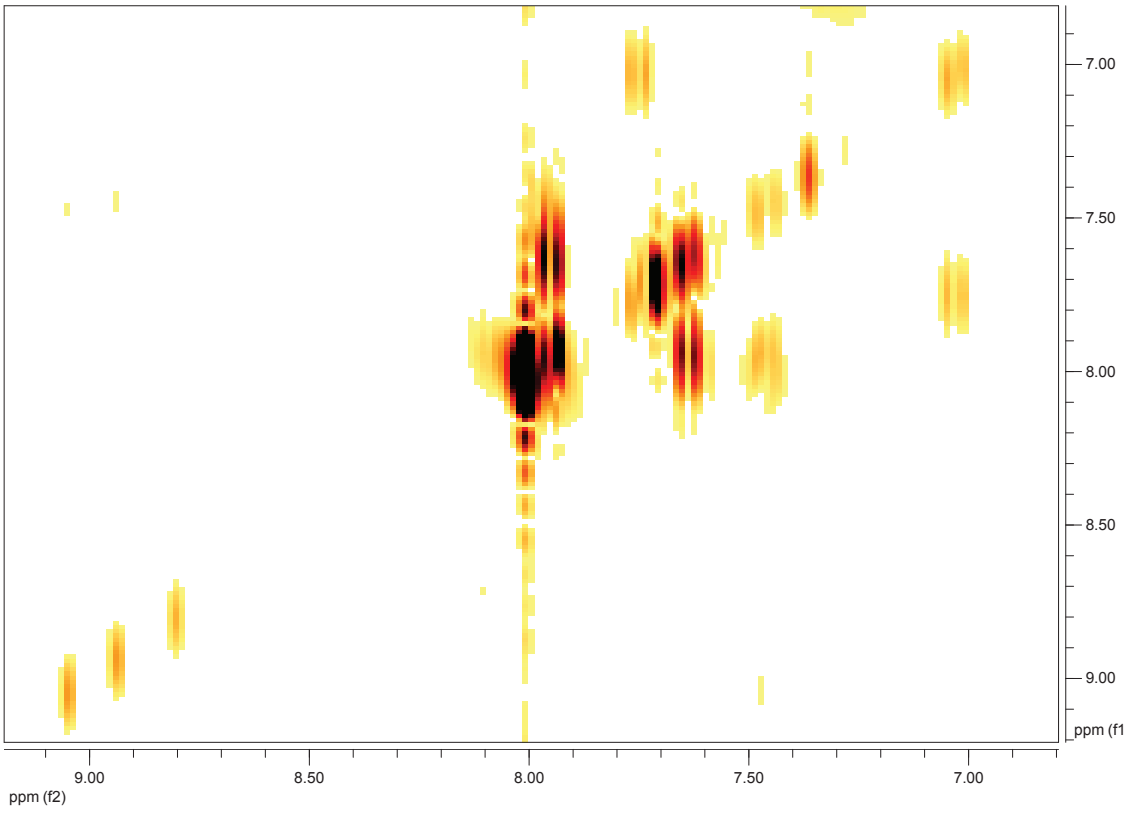

Figure 4. 2D ^{1}H NMR (COSY) of D4

Publications

1.

Synergistic effects of encapsulated phthalocyanine complexes in MIL-101 for the selective aerobic oxidation of tetralin, Emanuel Kockrick , Tristan Lescouet , Evgeny V. Kudrik , Alexander B. Sorokin and David Farrusseng, *Chem. Commun*., **2011**,47, 1562-1564
Times cited: 8

2.

Homogeneity of flexible metal–organic frameworks containing mixed linkers, Tristan Lescouet , Emanuel Kockrick , Gérard Bergeret , Marc Pera-Titus , Sonia Aguado and David Farrusseng, *J. Mater. Chem*., **2012**,22, 10287-10293
Times cited: 1

3.

Engineering MIL-53(Al) flexibility by controlling amino tags, Tristan Lescouet , Emanuel Kockrick , Gerard Bergeret , Marc Pera-Titus and David Farrusseng, *Dalton Trans*., **2011**,40, 11359-11361
Times cited: 7

4.

Quantitative Characterization of Breathing upon Adsorption for a Series of Amino-Functionalized MIL-53, M. Pera-Titus , T. Lescouet , S. Aguado , and D. Farrusseng, *J. Phys. Chem. C*, **2012**, 116 (17), pp 9507–9516

5.

The Origin of the Activity of Amine-Functionalized Metal–Organic Frameworks in the Catalytic Synthesis of Cyclic Carbonates from Epoxide and CO_2, Tristan Lescouet, Dr. Céline Chizallet, Dr. David Farrusseng, *ChemCatChem*, Article first published online: 21 AUG **2012**, DOI: 10.1002/cctc.201200288

6.

Transition metal loaded silicon carbide-derived carbons with enhanced catalytic properties, Lars Borchardt, Frédéric Hasché, Martin R. Lohe, Martin Oschatz, Franz Schmidt, Emanuel Kockrick, Christoph Ziegler, Tristan Lescouet, Alicja Bachmatiuk, Bernd Büchner, David

Farrusseng, Peter Strasser, Stefan Kaskel, *Carbon*, Volume 50, Issue 5, April **2012**, Pages 1861–1870

7.

Soft synthesis of isocyanate-functionalised metal–organic frameworks, Jenny G. Vitillo, Tristan Lescouet, Marie Savonnet, David Farrusseng and Silvia Bordiga, *Dalton Trans*., **2012**, DOI: 10.1039/ c2dt31977b, accepted

8.

Alternative Pathway for the Synthesis of Isocyanate- and Urea-Functionalised Metal-Organic Frameworks, Tristan lescouet, Jenny G. Vitillo, David Farrusseng and Silvia Bordiga, *Journal of Materials Chemistry*, **2012**, submitted

Synergistic effects of encapsulated phthalocyanine complexes in MIL-101 for the selective aerobic oxidation of tetralin†

Emanuel Kockrick, Tristan Lescouet, Evgeny V. Kudrik, Alexander B. Sorokin and David Farrusseng*

Received 15th October 2010, Accepted 11th November 2010
DOI: 10.1039/c0cc04431h

Metal phthalocyanine complexes encapsulated in MIL-101, and used as "ship-in-a-bottle" catalysts, show outstanding TONs in the aerobic oxidation of tetralin.

Over the last decade, metal–organic frameworks (MOFs) have been introduced as a new class of heterogeneous catalyst systems.[1–7] Rapid progress is being made in developing MOF-based catalysts for selective oxidation of hydrocarbons. One approach consists in designing MOFs that possess metallic clusters with catalytic centers.[8–11] Corma *et al.* have investigated Cu-pymo and Co-ZIF-9, in which the clusters are responsible for the selective oxidation of tetralin in air.[12] Another approach resides in using MOFs as a host matrix to support the catalyst, as in the case of zeolites.[13] Thanks to their cage-type structures, faujasite (FAU) zeolites in particular can encapsulate "nano" catalysts, but the small size of the FAU cavities (0.74 nm) prevents the hosting of large catalytic systems. The use of activated carbons or mesoporous silica can permit the insertion of large systems, but leaching can easily take place, posing a problem for the retention of guest species. In contrast, MIL-101, which exhibits a 3D pore system with calibrated cavities of 2.9 nm and 3.4 nm,[14,15] presents a very promising pore structure for the development of supported metallic or oxide complexes as "ship-in-a-bottle" catalysts. Such an approach has recently been undertaken to encapsulate inorganic clusters such as polyoxometalates,[14,16–18] metallic nanoparticles[13,19,20] and molecular catalysts.[21–23]

Metal phthalocyanine complexes (MPc) exhibit outstanding performance as oxidation catalysts.[24,25] Recently, our group showed that a bulky N-bridged diiron phthalocyanine complex, $(FePc^tBu_4)_2N$, allows the selective oxidation of methane, benzene and alkylaromatics.[26–28] The EXAFS structural determination indicates a linear $Fe^{+3.5}(\mu\text{-}N)Fe^{+3.5}$ unit with equivalent Fe–N distances (1.65 Å) and a 3.33 Å distance between parallel Pc planes.[29] Unfortunately, MPc usually self-assemble to oligomer structures in solution through π stacking, which strongly limits their catalytic applications in homogeneous processes.[30] To overcome this issue, silica- and zeolite-supported MPc have therefore been developed.[31–35]

IRCELYON, Université Lyon I, CNRS, 2 av. Albert Einstein, F-69626 Villeurbanne, France.
E-mail: david.farrusseng@ircelyon.univ-lyon1.fr;
Fax: +33 4 72 33 53 99; Tel: +33 4 72 44 53 65

† Electronic supplementary information (ESI) available: Synthetic details, activity, selectivity and TON of MPc complexes in aerobic tetralin oxidation, X-ray powder diffraction patterns, diffuse reflectance UV-VIS spectra, and N_2-physisorption isotherms and EDS spectra of composite catalysts. See DOI: 10.1039/c0cc04431h

The objective of this work is to encapsulate large MPc in cavities of MIL-101 for the selective oxidation of tetralin into 1-tetralone, a diesel fuel additive and an intermediate for the synthesis of agricultural chemicals.[12] To the best of our knowledge, this is the first report on the synergistic effect of the confinement of molecular catalysts in porous MOFs.

A catalytic screening of different unsupported metal phthalocyanine catalysts in aerobic tetralin oxidation (Table S1, ESI†) has enabled the identification of two different perfluorinated complexes ($MPcF_{16}$, M = Fe, Ru) and the bulky dimer, $(FePc^tBu_4)_2N$, which were selected for encapsulation. The activities and selectivities are presented in Table 1. This reaction was performed in parallel batch reactors at 8 bar of O_2 at 90 °C with a substrate-to-MPc molar ratio of 36 000 : 1. The products were analyzed by GC and GC-MS. The TONs of the molecular catalysts follow the order $(FePc^tBu_4)_2N > RuPcF_{16} > FePcF_{16}$. Interestingly, similar selectivities toward 1-tetralone were obtained for the three molecular complexes.

The MPc–MOF composite materials were prepared by wet infiltration of the deep blue-colored MPc solutions into Cr–MIL-101 with a maximal theoretical complex loading inside the MOF of 9 wt%. After slow evaporation of the solvent (acetone for $MPcF_{16}$ and CH_2Cl_2 for $(FePc^tBu_4)_2N$), any complexes not strongly bound to the host MOFs were removed by intensive washing until the filtrate remained colorless. The actual complex loading for the perfluorinated complexes inside the MIL-101 was determined by ICP-OES measurements to be 2.1 wt% and 3.6 wt% for $FePcF_{16}$ and $RuPcF_{16}$, corresponding to approximately 0.8 and 1.2 complexes per large pore respectively. Considering also the access to the smaller pores, the total pore filling would correspond to an average of app. 0.3 ($FePcF_{16}$) and 0.4 ($RuPcF_{16}$). A higher loading of 5.2 wt% is obtained for the $(FePc^tBu_4)_2N$ dimeric complex. This last result was also confirmed by diffuse reflectance UV-VIS spectra of pristine

Table 1 Catalytic activity, selectivity and turnover numbers after 6 h for the applied phthalocyanine complexes used as homogeneous catalysts in tetralin oxidation

	Complexes		
	$(FePc^tBu_4)_2N$	$FePcF_{16}$	$RuPcF_{16}$
X^a [%]	25	21	38
$S_{one}{}^b$ [%]	69	68	70
TON[c]	7400	3400	5200

[a] Conversion of tetralin. [b] Selectivity toward 1-tetralone. [c] Turnover number after 6 h for 1-tetralol and 1-tetralone.

and complex loaded MOFs (Fig. S1, ESI†). In agreement with the literature, two adsorption maxima at 446 nm and 600 nm can be identified for the non-loaded MIL-101.[36] For the loaded materials, a shift of the peak maximum to around 615 nm was observed due to the presence of the Pc complexes.[32]

X-Ray powder diffraction and N_2 physisorption measurements demonstrate the stability of MIL-101 host materials after the encapsulation process, since similar diffraction patterns and isotherm shapes were obtained (Fig. S2 and S3, ESI†). As expected, the specific surface area and pore volume decrease for complex-containing MOF systems (Table 2).

For $RuPcF_{16}$@MIL-101, the total pore volume decreases by 16 % with respect to pure MIL-101, which is more than the weight loading of 3.6 wt%. This clearly shows that the complexes are incorporated into the porous structure and thus reduce the pore volume by preventing the N_2 from entering the cavities. Similar decreases in specific surface area and pore volume were also reported for nanoparticle and polyoxometalate functionalized MIL-101 materials.[16,20] For the bulky $(FePc^tBu_4)_2N$@MIL-101, the total pore volume decreases by only 5%, which corresponds to the weight gain of 5.2 wt% after loading. This indicates that the voluminous $(FePc^tBu_4)_2N$ complex is not incorporated into the mesoporous structure of the MIL-101. Indeed, the dimer ($\sim$2.0 $\times$ 2.0 nm) is too large to enter the hexagonal pore windows of the MIL-101 (1.47 $\times$ 1.6 nm).[14] It would appear that $(FePc^tBu_4)_2N$ complexes are strongly adsorbed at the outer surfaces of the crystallites and/or in macroporous cavities formed by MOF particle agglomeration.

The homogeneous distribution of different iron and ruthenium complexes inside the MIL-101 support was verified by EDS analysis (Fig. S4, ESI†).

The encapsulated perfluorinated complexes were tested in similar conditions with a tetralin-to-complex molar ratio of 147 000 : 1 for $FePcF_{16}$@MIL-101 and 92 000 : 1 for $RuPcF_{16}$@MIL-101, respectively. Note that pure MIL-101 shows no catalytic activity (Table 2). $FePcF_{16}$@MIL-101 and $RuPcF_{16}$@MIL-101 catalysts show very high TONs. The turnover number of $FePcF_{16}$@MIL-101 was 48 200 after 24 h, almost eight times higher than for the homogeneous $FePcF_{16}$ catalyst (TON = 6300). Significantly, the $FePcF_{16}$@MIL-101 catalyst provided a higher selectivity (up to 80 %) toward the desired 1-tetralone compared to the homogeneous $FePcF_{16}$ (68 %) at similar conversion. An analogous rise and change in selectivity was already reported for the hydroperoxide-mediated cyclohexane oxidation of zeolite-supported Ru complexes.[32]

Table 2 N_2 physisorption results and catalytic performance of incorporated MPc@MIL-101 after 6 h and 24 h

Pc@MIL-101	MIL-101	$N(FePc^tBu_4)_2$ @MIL-101	$FePcF_{16}$ @MIL-101[c]	$RuPcF_{16}$ @MIL-101
S_{BET}[a] [$m^2\ g^{-1}$]	2500	2450	2220	2120
V_P[b] [$cm^3\ g^{-1}$]	1.22	1.16	1.08	1.03
X [%]	0/—	4/—	17/33	34/48
S_{one}[d] [%]	—/—	79/—	80/80	62/74
TON[e]	0/—	5100/—	24 200/ 48 200	30 900/ 46 300
Size [nm $\times$ nm]	1.47 $\times$ 1.6[f]	$\sim$2.0 $\times$ 2.0[g]	$\approx$1.3 $\times$ 1.3[g]	$\approx$1.3 $\times$ 1.3[g]

[a] S_{BET} at p/p_0 = 0.05–0.2. [b] Total volume at p/p_0 = 0.95. [c] Conversion of tetralin. [d] Selectivity toward 1-tetralone. [e] Turnover number after 6 h/24 h. [f] Hexagonal pore window of MIL-101. [g] Sizes of Pc complexes.

The higher activity for encapsulated complexes has previously been explained by the preclusion of the dimerization process by π stacking that is typically observed for homogeneous catalysts.[32] Previously published activities of up to 3000 TON d^{-1} are, however, significantly lower than those determined in the present study. To the best of our knowledge, this is the highest catalytic activity ever reported for homo- and heterogeneous tetralin oxidations. Note that the terminology of TON may be generally misused for metal-initiated free-radical oxidations. It expresses the activity in terms of the product (mol)/catalyst (mol) ratio, which is the indicator commonly used by the community.

In contrast, a limited conversion of up to 4 % was obtained for the $(FePc^tBu_4)_2N$@MIL-101 catalyst. In this case, the synergistic effects arising from the confinement in the pore do not take place. This is consistent with the hypothesis that $(FePc^tBu_4)_2N$ is not encapsulated within the mesoporous structure of the MIL-101. The observed residual conversion (4 %) may arise from the $(FePc^tBu_4)_2N$ complexes that are on or close to the external surface of the MIL crystallites and that are easily accessible for the tetralin.[14,37] This hypothesis is confirmed by similar TONs obtained for $(FePc^tBu_4)_2N$ (7400) and $(FePc^tBu_4)_2N$@MIL-101 (5100).

Compared to the homogeneous perfluorinated catalysts, an induction period of up to three hours was observed for the encapsulated systems (Fig. 1). A similar phenomenon was also obtained for Co–MOF catalyzed aerobic cyclohexene (MFU-1) and tetralin oxidations (Co-ZIF-9), respectively.[10,12]

A release of the complexes by progressive degradation of the host structure in the reaction medium could have led to an induction period, as found for drug delivery mechanisms.[38]

No leaching of the complexes was detected by UV-VIS as the reaction proceeded, however (pure phthalocyanine structures are soluble in the reaction medium). This further demonstrates the robustness of the host matrix and the strong adsorption of the complexes into the MOF porous structure.

In order to gain insight into the mechanism of this oxidation, we studied the kinetic isotope effect (KIE) on the oxidation of adamantane-1,3-d_2. This substrate is a useful probe to determine an *intra*-molecular KIE since it contains two equal tertiary C–H and two C–D bonds in the same molecule.[39] It should be noted that the reactivity of adamantane was much lower compared to tetralin. The analysis of the isotopic composition of the adamantanol-1 product directly provides an intrinsic KIE:

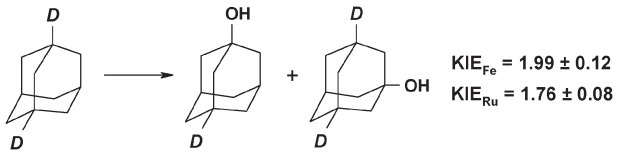

The KIE values were determined to be 1.99 $\pm$ 0.12 and 1.76 $\pm$ 0.08 for $FePcF_{16}$@MIL-101 and $RuPcF_{16}$@MIL-101, respectively. The KIE measured using $FePcF_{16}$ and $RuPcF_{16}$ in homogeneous solutions are similar: 1.94 $\pm$ 0.10 and 1.68 $\pm$ 0.11, respectively, suggesting that the same mechanism

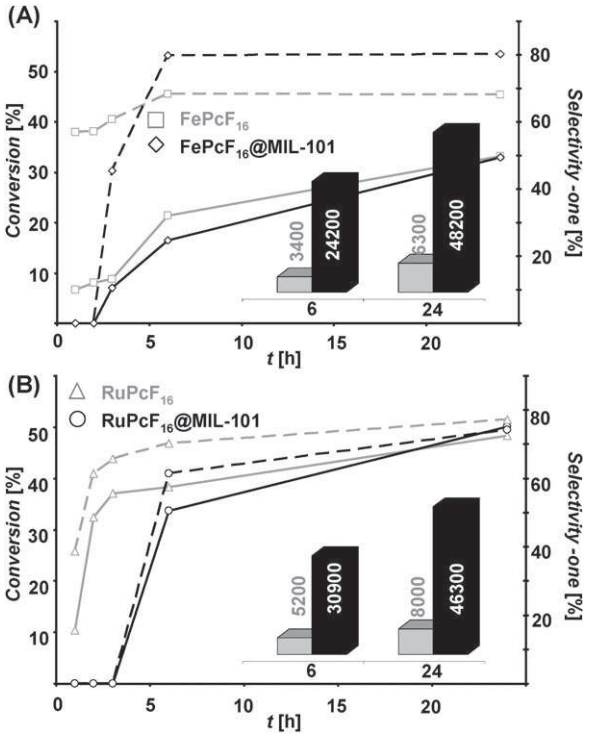

Fig. 1 Tetralin conversion (solid line) and selectivity toward 1-tetralone (dashed line) of homogeneous $FePcF_{16}$ and $RuPcF_{16}$ complexes (grey) and $FePcF_{16}$@MIL-101 (A) and $RuPcF_{16}$@MIL-101 (B) (black) with significantly lower catalyst contents (n(tetralin) : n(MPcF16) = 147 000 : 1 (Fe) and 92 000 : 1 (Ru)) compared to the non-incorporated complexes (36 000 : 1) explaining the clear difference in turnover numbers (TONs) after 6 h and 24 h (inset), respectively.

should be operating in homogeneous and heterogeneous systems. These low KIE values indicate the involvement of a radical mechanism in this reaction. The occurrence of an induction period and the detection of a small concentration of tetralinhydroperoxide by GC-MS over the course of tetralin oxidation are also consistent with a free radical mechanism of oxidation, as previously suggested elsewhere.[12]

In summary, this study demonstrates that the encapsulation of MPc in MIL-101 allows an activity increase of approximately one order of magnitude. This increase in activity may arise from the dispersion of the molecular complexes as isolated monomers in the nanopore cavities and/or from the confinement effects provided by the host porous structure. In contrast, the $(FePc^tBu_4)_2N$ dimer, which is too large to penetrate into the porous structure, does not show this synergistic effect.

We thank the ANR for financial support (ANR-08-BLANC-0183-01).

Notes and references

1 U. Mueller, M. Schubert, F. Teich, H. Puetter, K. Schierle-Arndt and J. Pastre, *J. Mater. Chem.*, 2006, **16**, 626–636.
2 D. Farrusseng, S. Aguado and C. Pinel, *Angew. Chem., Int. Ed.*, 2009, **48**, 7502–7513.
3 J. Y. Lee, O. K. Farha, J. Roberts, K. A. Scheidt, S. B. T. Nguyen and J. T. Hupp, *Chem. Soc. Rev.*, 2009, **38**, 1450–1459.
4 L. Q. Ma, C. Abney and W. B. Lin, *Chem. Soc. Rev.*, 2009, **38**, 1248–1256.
5 A. Corma, H. Garcia and F. X. Llabres i Xamena, *Chem. Rev.*, 2010, **110**, 4606–4655.
6 G. Ferey, *Chem. Soc. Rev.*, 2008, **37**, 191–214.
7 K. P. Lillerud, U. Olsbye and M. Tilset, *Top. Catal.*, 2010, **53**, 859–868.
8 K. Schlichte, T. Kratzke and S. Kaskel, *Microporous Mesoporous Mater.*, 2004, **73**, 81–88.
9 L. Alaerts, J. Wahlen, P. A. Jacobs and D. E. De Vos, *Chem. Commun.*, 2008, 1727–1737.
10 M. Tonigold, Y. Lu, B. Bredenkotter, B. Rieger, S. Bahnmuller, J. Hitzbleck, G. Langstein and D. Volkmer, *Angew. Chem., Int. Ed.*, 2009, **48**, 7546–7550.
11 P. Horcajada, S. Surble, C. Serre, D. Y. Hong, Y. K. Seo, J. S. Chang, J. M. Greneche, I. Margiolaki and G. Ferey, *Chem. Commun.*, 2007, 2820–2822.
12 F. X. Llabres i Xamena, O. Casanova, R. G. Tailleur, H. Garcia and A. Corma, *J. Catal.*, 2008, **255**, 220–227.
13 M. Sabo, A. Henschel, H. Froede, E. Klemm and S. Kaskel, *J. Mater. Chem.*, 2007, **17**, 3827–3832.
14 G. Ferey, C. Mellot-Draznieks, C. Serre, F. Millange, J. Dutour, S. Surble and I. Margiolaki, *Science*, 2005, **309**, 2040–2042.
15 D. Y. Hong, Y. K. Hwang, C. Serre, G. Ferey and J. S. Chang, *Adv. Funct. Mater.*, 2009, **19**, 1537–1552.
16 J. Juan-Alcaniz, E. V. Ramos-Fernandez, U. Lafont, J. Gascon and F. Kapteijn, *J. Catal.*, 2010, **269**, 229–241.
17 N. V. Maksimchuk, K. A. Kovalenko, S. S. Arzumanov, Y. A. Chesalov, M. S. Melgunov, A. G. Stepanov, V. P. Fedin and O. A. Kholdeeva, *Inorg. Chem.*, 2010, **49**, 2920–2930.
18 S. R. Bajpe, C. E. A. Kirschhock, A. Aerts, E. Breynaert, G. Absillis, T. N. Parac-Vogt, L. Giebeler and J. A. Martens, *Chem.–Eur. J.*, 2010, **16**, 3926–3932.
19 S. Hermes, M. K. Schroter, R. Schmid, L. Khodeir, M. Muhler, A. Tissler, R. W. Fischer and R. A. Fischer, *Angew. Chem., Int. Ed.*, 2005, **44**, 6237–6241.
20 A. Henschel, K. Gedrich, R. Kraehnert and S. Kaskel, *Chem. Commun.*, 2008, 4192–4194.
21 M. H. Alkordi, Y. L. Liu, R. W. Larsen, J. F. Eubank and M. Eddaoudi, *J. Am. Chem. Soc.*, 2008, **130**, 12639–12641.
22 S. Horike, S. Shimomura and S. Kitagawa, *Nat. Chem.*, 2009, **1**, 695–704.
23 R. Makiura, S. Motoyama, Y. Umemura, H. Yamanaka, O. Sakata and H. Kitagawa, *Nat. Mater.*, 2010, **9**, 565–571.
24 I. M. Geraskin, M. W. Luedtke, H. M. Neu, V. N. Nemykin and V. V. Zhdankin, *Tetrahedron Lett.*, 2008, **49**, 7410–7412.
25 A. B. Sorokin and E. V. Kudrik, *Catal. Today*, 2010, DOI: 10.1016/j.cattod.2010.1006.1020.
26 A. B. Sorokin, E. V. Kudrik and D. Bouchu, *Chem. Commun.*, 2008, 2562–2564.
27 E. V. Kudrik and A. B. Sorokin, *Chem.–Eur. J.*, 2008, **14**, 7123–7126.
28 U. Isci, P. Afanasiev, J. M. M. Millet, E. V. Kudrik, V. Ahsen and A. B. Sorokin, *Dalton Trans.*, 2009, 7410–7420.
29 P. Afanasiev, D. Bouchu, E. V. Kudrik, J. M. M. Millet and A. B. Sorokin, *Dalton Trans.*, 2009, 9828–9836.
30 P. E. Ellis and J. E. Lyons, *J. Chem. Soc., Chem. Commun.*, 1989, 1315–1316.
31 K. J. Balkus, Jr., A. G. Gabrielov, S. L. Bell, F. Bedioui, L. Roue and J. Devynck, *Inorg. Chem.*, 1994, **33**, 67–72.
32 K. J. Balkus, M. Eissa and R. Levado, *J. Am. Chem. Soc.*, 1995, **117**, 10753–10754.
33 J. M. Thomas, R. Raja, G. Sankar and R. G. Bell, *Nature*, 1999, **398**, 227–230.
34 A. B. Sorokin and A. Tuel, *Catal. Today*, 2000, **57**, 45–59.
35 A. B. Sorokin, S. Mangematin and C. Pergrale, *J. Mol. Catal. A: Chem.*, 2002, **182–183**, 267–281.
36 J. Kim, S. Bhattacharjee, K. E. Jeong, S. Y. Jeong and W. S. Ahn, *Chem. Commun.*, 2009, 3904–3906.
37 S. B. Lei, C. Wang, S. X. Yin, H. N. Wang, F. Xi, H. W. Liu, B. Xu, L. J. Wan and C. L. Bai, *J. Phys. Chem. B*, 2001, **105**, 10838–10841.
38 P. Horcajada, C. Serre, G. Maurin, N. A. Ramsahye, F. Balas, M. Vallet-Regi, M. Sebban, F. Taulelle and G. Ferey, *J. Am. Chem. Soc.*, 2008, **130**, 6774–6780.
39 A. Sorokin, A. Robert and B. Meunier, *J. Am. Chem. Soc.*, 1993, **115**, 7293–7299.

View Online / Journal Homepage / Table of Contents for this issue
Dynamic Article Links

Journal of Materials Chemistry

Cite this: J. Mater. Chem., 2012, 22, 10287

www.rsc.org/materials

PAPER

Homogeneity of flexible metal–organic frameworks containing mixed linkers†

Tristan Lescouet, Emanuel Kockrick, Gérard Bergeret, Marc Pera-Titus, Sonia Aguado and David Farrusseng*

Received 17th November 2011, Accepted 16th January 2012
DOI: 10.1039/c2jm15966j

Very sophisticated porous materials known as multivariate functional MOFs (also known as MixMOFs) can be designed using a synthesis method that starts from solutions composed of two or more different linkers. For this procedure to be successful, one must have access to techniques that characterize the homogeneity of MOF crystallites containing two different linkers. This is of particular relevance for MOFs made of 2-aminobenzene-1,4-dicarboxylate (abdc), which are excellent platforms for the introduction of additional functions by post-modification. In this paper, we show that adsorption/desorption isotherms and thermodiffraction studies on flexible structures can indirectly characterize the homogeneity of MOFs made from a mixture of linkers. Breathing pressures and temperatures for a series of MIL-53(Al) functionalized with amino tags, *i.e.* $Al(OH)(bdc)_{1-n}(abdc)_n$, were measured as a function of the amino content. The linear relationship between the CO_2 breathing pressure and the amine content in the MIL-53(Al) structure clearly illustrates the homogeneity of the crystallite composition; in other words, the crystallites have the same abdc : bdc ratio. On the other hand, the functionalization of MIL-53(Al) with low amine content (10% abdc) results in a profound modification of the breathing properties triggered by the temperature. Much higher temperatures are required for full conversion of the np (narrow pore) to the lp (large pore) phase. We also suggest an interplay between coexisting np and lp microcrystalline domains that may "smooth" the breathing properties at the macroscopic level.

Introduction

Metal–organic frameworks or porous coordination polymers are essentially functional materials.[1–6] The porous framework can be decorated with various organic moieties without undergoing significant structural changes. Such solids are usually referred to as isoreticular structures. Among the different isoreticular MOFs, we can cite the IRMOF,[7,8] the MIL-53,[9] the $Cu_2(Lx)(H_2O)_2$,[10] and the ZIF series displaying GME,[11] RHO[12] and LTA[13] topologies. Starting from a precursor solution containing 2-aminobenzene-1,4-dicarboxylate (abdc) instead of benzene-1,4-dicarboxylate linker (bdc), various MOFs with a pending $–NH_2$ function have been obtained, such as Zn_4O(bdc-NH_2) or IRMOF-3,[14] CAU-1,[15] IHM-2 (ref. 16) and UMCM.[17] These materials are of particular interest, since the amino function enables the insertion of complex moieties using post-modification techniques.[18–21]

The synthesis of multivariate functional MOFs starting from solutions composed of two or more different linkers is the latest development in the field. Very large single crystals (~5 to 10 mm^3), isoreticular to MOF-5, containing two to eight different linkers, have been synthesized using a self-assembly method under solvothermal conditions.[14] In such a concept, a random distribution of different functions would result in a combinatorial functional sequence, providing pores with distinct properties. Although the authors demonstrated no change in the crystal composition on a millimetre scale, they did not exclude the presence of microscopic domains exhibiting a composition different from the average in the whole crystal. In a separate study on the incorporation of the abdc linker into MOF-5 (made from benzene-1,4-dicarboxylate),[22,23] the presence of both linkers in the crystallites (1–10 μm) was confirmed by high-resolution PXRD. Other authors, however, showed that crystal growth rates for the Zn_4O(bdc-X) system might depend not only on the linker, but also on the X substituent (X = I, Br). In this latter case, a radial distribution of the linker composition can be found, the crystal center being halogen rich, while the surface becoming poor.[24]

Furthermore, it has been shown that the degree of flexibility of MOF materials made from two different linkers (*e.g.*, CID-5/6) can be monitored by adsorption measurements.[25] CID-5 [Zn(5-NO_2-ip)(bpy)] exhibits gate opening phenomena (*i.e.* it becomes porous) beyond a threshold water pressure, whereas CID-6 [Zn(5-MeO-ip)(bpy)] is intrinsically porous. Hence, for a particular process, it seems possible to engineer the gate opening/

University of Lyon, Institut de Recherches sur la Catalyse et l'Environnement de Lyon (IRCELYON), UMR 5256 CNRS—2 Av. Albert Einstein, 69626 Villeurbanne, France. E-mail: avid.farrusseng@ircelyon.univ-lyon1.fr; Fax: +33 (0)4 72 33 53 99; Tel: +33 (0)4 72 44 53 65

† Electronic supplementary information (ESI) available: Synthesis details, ^{1}H-NMR, powder X-ray diffraction and N_2 physisorption isotherms. See DOI: 10.1039/c2jm15966j

breathing properties of MOFs by finely tuning the linker functionalities and their relative amount in the crystals.[26]

Baiker *et al.*[27] have synthesized a series of "mixed" Al-MIL-53 materials with the general formula $Al(OH)(bdc)_{1-n}(abdc)_n$, where the terephthalate linker (bdc) is partially substituted by aminoterephthalate (abdc). Using high-resolution PXRD, the authors concluded that the mixed frameworks are homogeneous. Notwithstanding this fact, the presence of microdomains with different compositions and/or a composition gradient from the crystallite center to the surface could not be ruled out. Techniques to characterize crystallite homogeneity of MOFs containing two different linkers are imperatively needed, especially for MOFs made of abdc, which are excellent platforms for the introduction of additional functions by post-modification.[18–21]

Herein, we show that adsorption/desorption isotherms and thermodiffraction studies of flexible structures can indirectly characterize the homogeneity of MOFs made from a mixture of linkers. Breathing pressures and temperatures for a series of Al-MIL-53 functionalized with amino tags, *i.e.* $Al(OH)(bdc)_{1-n}(abdc)_n$, have been measured as a function of the amino content (*i.e.* bdc : abdc ratio).

Experimental

Synthesis of $Al(OH)(bdc)_{1-n}(abdc)_n$

Six different samples, including $Al(OH)(bdc)_n$ (*e.g.*, Al-MIL-53), $Al(OH)(abdc)_n$, (*e.g.*, Al-MIL-53-NH_2) and mixed $Al(OH)(bdc)_{1-n}(abdc)_n$, were prepared and purified using a modified synthesis protocol based on Stock *et al.* (Scheme 1).[28] Briefly, solutions containing 1.931 g (8 mmol) of aluminium chloride hexahydrate ($AlCl_3 \cdot 6H_2O$, Sigma-Aldrich, 99%), 8 mmol of benzene-1,4-dicarboxylate, 2-aminobenzene-1,4-dicarboxylate (Sigma-Aldrich, 98%) of different molar ratios (0, 11.1, 20, 50, 66.7 and 100% abdc) and 30 mL of deionized H_2O were introduced into a 48 mL Teflon-lined autoclave and subjected to solvothermal synthesis at 150 °C for 9 h. After the synthesis, the products were separated from water by centrifugation at 4000 rpm for 5 min. To remove any excess linker trapped within the porous network, the as-synthesized products were placed in an autoclave with 30 mL anhydrous DMF (Sigma Aldrich, 99.8%) and heated at 150 °C for 24 h.[27] The solvent was then substituted by fresh DMF and the solvothermal treatment was repeated twice. Afterwards, the DMF-containing solids were submitted to dichloromethane Soxhlet-extraction for 20 h to remove DMF. Finally, the solids were dried at 100 °C for 9 h at reduced pressure to obtain powdered Al-MIL-53 (A), Al-MIL-53-11.1%NH_2 (B), Al-MIL-53-20% NH_2 (C), Al-MIL-53-50%NH_2 (D), Al-MIL-53-66.7%NH_2 (E) and Al-MIL-53-NH_2 (F) samples.

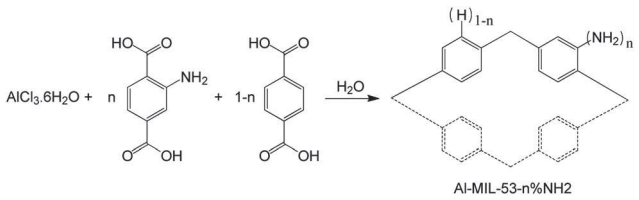

Scheme 1 Synthesis of $Al(OH)(bdc)_{1-n}(abdc)_n$.

Powder X-ray thermodiffraction

Powder X-ray diffraction patterns were recorded using a PANalytical X'Pert Pro MPD (Bragg–Brentano geometry, reflection mode) equipped with a secondary graphite monochromator (CuKα, wavelength 0.154184 nm) and a 1-dimensional multistrip detector (X'Celerator, 127 channels on 2.1°). The samples were mounted in an atmosphere-controlled Anton Paar XRK 900 reactor chamber. The temperature-regulated glass-ceramic sample holder was opened to allow the gas to flow through the sample (synthetic air 40 mL min^{-1}). Heating was performed up to 480 °C at a rate of 2 °C min^{-1}. XRD data at the desired temperature were collected after 10 min. The XRD measurements were carried out with an automatic variable divergence slit (8 mm irradiated length) at 127 min per scan (0.0334° 2q and 512 s per step) and converted into fixed slit mode.

The unit cell parameters of the np and lp phases were calculated by using whole powder pattern fitting (Fullprof code[29]) starting from crystal data of MIL-53(Al)_lt and MIL-53(Al)_ht.[30] The ratio of the np–lp phases is determined using the area of the main diffraction line of the phases, namely the (110) line at about 11.95° (2θ) for the np phase and the (011) line at about 8.72° (2θ) for the lp phase.

Liquid ^{1}H-NMR

^{1}H-NMR spectra were recorded on a Bruker Avance 250 spectrometer operating at 250 MHz using an automated procedure for routine analysis. The spectra were calibrated using the deuterium signals of DMSO. Due to their high chemical stability, the relative bdc and abdc contents in the different Al-MFI-53-NH_2 materials were quantified after digestion in a 1% HF/d_6-DMSO solution. The composition was computed using the area ratio of a given proton from each ligand (the signal at δ: 8.02 ppm belongs to the four aromatic protons of terephthalic acid, while the signals at δ: 7, 7.75 and 7.35 ppm correspond to the three aromatic protons of 2-aminobenzene-1,4-dicarboxylic acid).

Field emission scanning electron microscopy

FESEM on $Al(OH)(bdc)_{1-n}(abdc)_n$ samples was carried out with a Stereoscan 260 SEM microscope.

N_2 physisorption

Nitrogen physisorption isotherms were measured at 77.4 K using a Micromeritics 2020 apparatus. Prior to the measurements, the samples were activated under secondary vacuum at 150 °C for 24 h. Specific surface areas were calculated using the BET equation (p/p_0 = 0.05–0.25) on the adsorption branch, unless otherwise specified.

CO_2 adsorption/desorption

CO_2 adsorption/desorption isotherms were measured on a BELSORP-HP microvolumetric apparatus at 30 °C. The samples were outgassed under vacuum ($\sim 10^{-4}$ mbar) at 150 °C for 12 h before the measurements.

Results

Composition by liquid ^{1}H-NMR

For Al(OH)(bdc) (sample A), the aromatic zone of ^{1}H-NMR shows a unique singlet corresponding to the four equivalent aromatic protons belonging to terephthalic acid (δ: 8.02 ppm). In contrast, the spectrum of Al(OH)(abdc) consists of two doublets (Hb-δ: 7 ppm and Hc-δ: 7.75 ppm; $J = 33$ Hz) and a singlet (Ha-δ: 7.35 ppm) (Scheme 2).

By increasing the abdc content in the starting solution (from A to F), we observe a progressive increase of the ^{1}H-NMR signals associated with the abdc linker (Fig. 1). A linear correlation between the solid composition and the starting solution can be established (Table 1).

In addition, for all samples, the absence of residual amounts of abdc acid and DMF is confirmed by liquid ^{1}H-NMR, solid-state ^{13}C-NMR and Diffuse Reflectance IR (DRIFT) (see ESI†). We can thus conclude that the actual composition of the frameworks corresponds to the results given by the digestion-liquid ^{1}H-NMR technique.

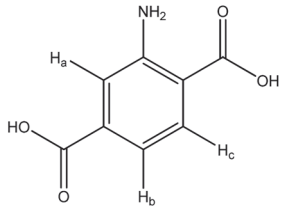

Scheme 2 Aromatic protons of the abdc linker.

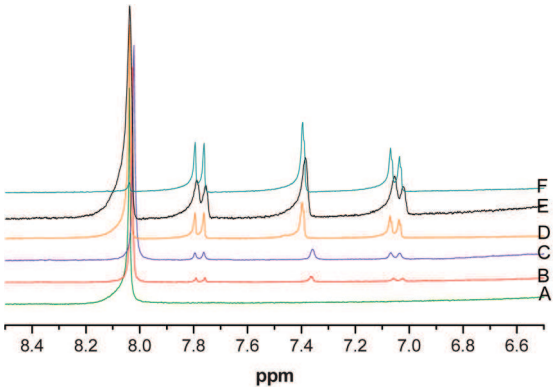

Fig. 1 ^{1}H-NMR spectra of digested mixed-ligand Al-MIL-53.

Table 1 Composition data of Al(OH)(abdc)$_n$(bdc)$_{1-n}$ samples

Sample	% abdc in the solution	% abdc measured by ^{1}H-NMR
A	0	0
B	11.1	10 ± 2
C	20	18 ± 2
D	50	49 ± 2
E	66.6	62 ± 5
F	100	100

Crystallite morphology

All samples exhibit a platelet-like morphology with a mean size of about 1 μm. For samples with a low abdc content, we can observe submicronic rounded particles that aggregate on top of the platelets. Noteworthy, Al(OH)(abdc) (F) shows very high particle homogeneity in terms of shape and size (Fig. 2).

N_2 physisorption

Except for Al(OH)(abdc) (F), the solids show a type-I isotherm for N_2 physisorption (Fig. 3, top). The microporous volumes (*t*-plot method) and BET surface areas are in the same range and correspond to values reported in the literature for Al-MIL-53 (Table 2).[30,31] The adsorption isotherm for the Al(OH)(abdc) solid (sample F) shows an S-shaped profile and a desorption branch displaying a type-I behaviour. This unusual sorption pattern with a large hysteresis loop has already been reported for

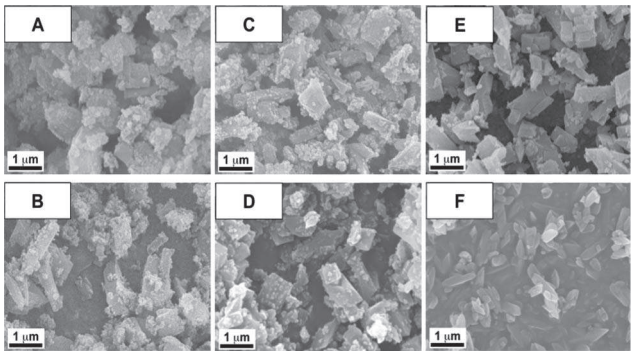

Fig. 2 SEM micrographs of samples A–F.

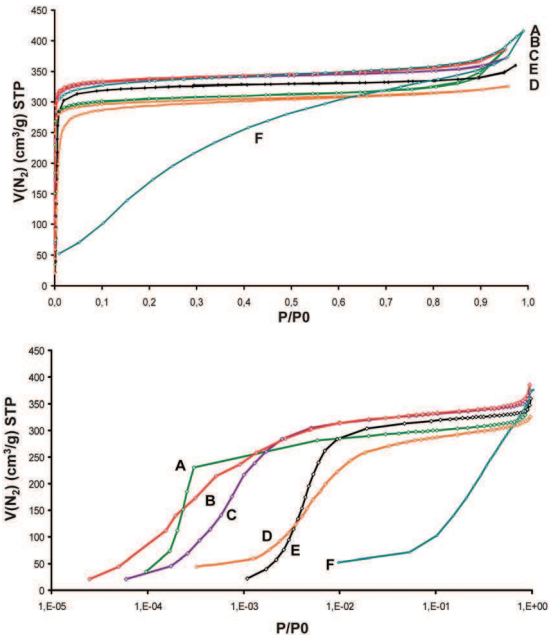

Fig. 3 Nitrogen adsorption/desorption isotherms at 77 K (linear scale): A (green line), B (red line), C (purple line), D (orange line), E (black line) and F (turquoise line). Top: high-pressure region; and bottom: highly resolved isotherms at low pressures.

Table 2 Textural properties of $Al(OH)(abdc)_n(bdc)_{1-n}$ samples as inferred from N_2 adsorption/desorption at 77.4 K

Sample	% abdc measured	V_{micro}[a]/cm^3 g^{-1}	S_{BET}/m^2 g^{-1}
A	0	0.51	1041
B	10 ± 2	0.48	1048
C	18 ± 2	0.51	1090
D	49 ± 2	0.46	1100
E	62 ± 5	0.50	1017
F	100	0.37	940[b]

[a] Computed by the *t*-plot method. [b] Computed from the desorption branch.

pure Al-MIL-53(NH_2).[28] The lower pore volume (0.37 cm^3 g^{-1}) and BET surface area (940 m^2 g^{-1}) of this sample are in good agreement with the shrinking of the unit cell as computed by DFT modelling.[32]

By plotting the adsorbed N_2 volume as a function of the logarithm of the relative pressure (see Fig. 3, bottom), we observe that the pressure at which the N_2 uptake begins depends mainly on the abdc content. The N_2 uptake is shifted to higher pressures as the amine content increases. We attribute this trend to a decrease of the N_2 affinity with the degree of amino-substitution in the Al-MIL-53_lp framework rather than to a variation of the pore size.

CO_2 adsorption properties

Fig. 4 plots the CO_2 adsorption–desorption isotherms at 30 °C of different amino-functionalized Al-MIL-53 samples prepared in this study. As already reported for pure Al-MIL-53 and Al-MIL-53-NH_2, all samples display two distinct adsorption steps assigned, respectively, to lp → np and np → lp phase transitions at low and high CO_2 pressures.[32] Regardless of the amine loading, a plateau level of ~2 mmol g^{-1} is attained for different samples corresponding to ~0.5 CO_2 per μOH.[33,34] This result suggests an equal number of adsorption sites for the np phase for all samples.

At low pressures (<100 kPa), we see a linear correlation of the Henry constant with the abdc content (Table 3 and Fig. 5). This observation can be explained on the basis of the higher heat of CO_2 adsorption on the amino-functionalized samples through formation of hydrogen bonds with pending amines and bridging μOH groups.[32] Note that the meaning of Henry constant should be considered with care for soft porous crystals. Indeed, we have shown the absence of a genuine Henry's region in pure Al-MIL-53-NH_2 and In-MIL-68-NH_2 solids.[35] In this study, we consider the initial slope of the isotherm as the Henry constant although the selected Henry regions were not strictly linear. Nevertheless, this constant is a relevant descriptor of the surface–substrate interaction. At higher pressures (>100 kPa), the breathing pressure corresponding to the second transition increases with the abdc content from a value of 665 kPa for Al(OH)(bdc) (A) to 1770 kPa for Al(OH)(abdc) (F). This observation suggests a higher stabilization of the np structure with the degree of amine functionalization due to an increasing number of hydrogen bonds.[32]

Temperature-dependent XRD patterns

Temperature-dependent powder X-ray diffraction was performed on $Al(OH)(abdc)_n(bdc)_{1-n}$ samples (A–D and F) under ambient air (*i.e.* in the presence of moisture, Fig. 6). Strong discrepancies in the breathing pressures are observed. A characteristic np → lp phase transition can be detected at 60 °C for Al(OH)(bdc), whereas this structural change is not observed for Al(OH)(abdc). At intermediate abdc contents, the phase transition spreads over a wide range of temperatures that depends on the abdc content. For samples B, C and D, both np and lp phases coexist over a certain temperature range.

The ratio between the lp and np phases can be computed through the refinement of PXRD results. These values must be considered carefully, since PXRD is not generally viewed as very appropriate for performing quantitative measurements on

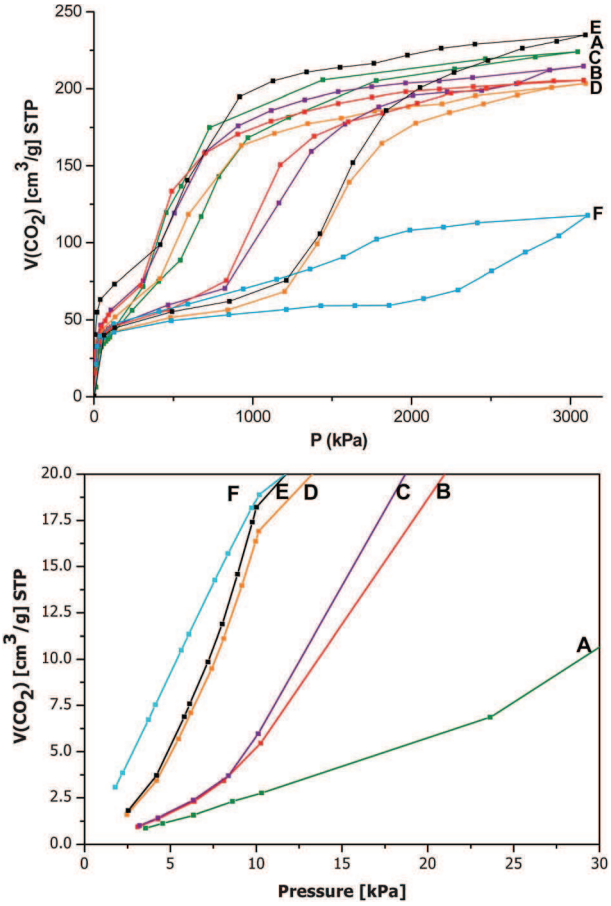

Fig. 4 CO_2 physisorption isotherms at 30 °C of $Al(OH)(abdc)_n(bdc)_{1-n}$ samples: A (green line), B (red line), C (purple line), D (orange line), E (black line) and F (turquoise line).

Table 3 CO_2 adsorption data of $Al(OH)(abdc)_n(bdc)_{1-n}$ samples

Sample	% abdc measured	P_{G1}/P_{G2}[a]/kPa	H[b]/cm^3 (STP) g^{-1} kPa^{-1}
A	0	1665	0.27
B	10 ± 2	740	0.36
C	18 ± 2	960	0.44
D	49 ± 2	1110	0.93
E	62 ± 5	1260	1.39
F	100	1770	1.96

[a] Phase transition pressures (30 °C) upon CO_2. [b] Henry constant for CO_2.

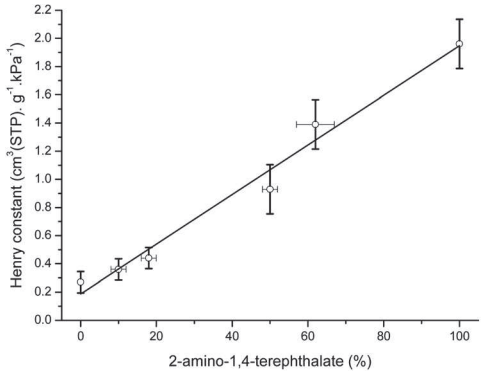

Fig. 5 Evolution of the Henry constant for CO_2 adsorption as a function of the abdc content for $Al(OH)(abdc)_n(bdc)_{1-n}$.

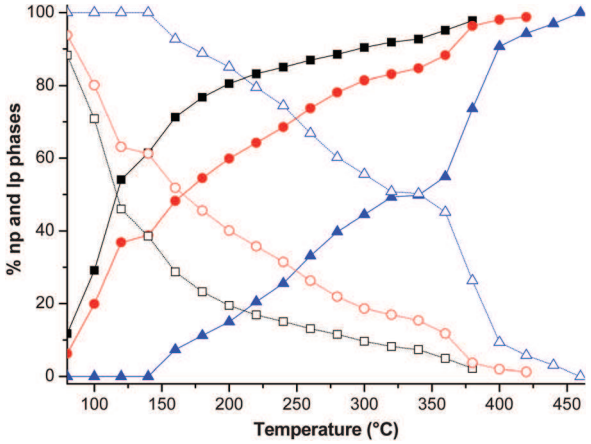

Fig. 7 Evolution of the np (empty symbols)–lp (filled symbols) phase ratio as a function of temperature for B (squares), C (circles) and D (triangles) samples.

samples with a mixture of phases. Nevertheless, the measurements and calculations are accurate enough to observe different trends for the samples. The relative amounts of the lp phase of different samples are reported as a function of the temperature in Fig. 7. Obviously, the phase transition is facilitated for samples with low abdc content. The breathing temperatures to attain a 1 : 1 mixture of np–lp phases are approximately 125 °C, 175 °C and 375 °C, respectively, for samples (B), (C) and (D). Nonetheless, even at low abdc contents (sample B), we can still observe the presence of the np phase at high temperature (Table 4).

The evolution of the unit cell parameters of the np and lp phases as a function of the temperature has also been investigated. For Al(OH)(bdc) (sample A), the unit cell volume of the lp phase remains almost constant, showing a slight decrease from 1415 Å^3 at 100 °C to 1410 Å^3 at 480 °C. In contrast, the temperature exerts a much more complex effect on the unit cell parameters for the abdc-containing samples (ESI†). As a matter of example, the evolution of the unit cell volume with temperature is shown for samples (B) and (C). For both samples, the unit cell volume of the lp phase decreases first from 1440 Å^3 at 100 °C to 1415 Å^3 at 350 °C. From 350 °C onwards, the unit cell volume increases abruptly. Note that this temperature corresponds to the disappearance of the np phase for the samples. On the other hand, the unit cell volume of the np phase increases linearly with the temperature until this phase disappears (Fig. 8).

Discussion

In general terms, adsorption–desorption isotherms are used to characterize structural properties of microporous materials. At conditions approaching substrate condensation and/or

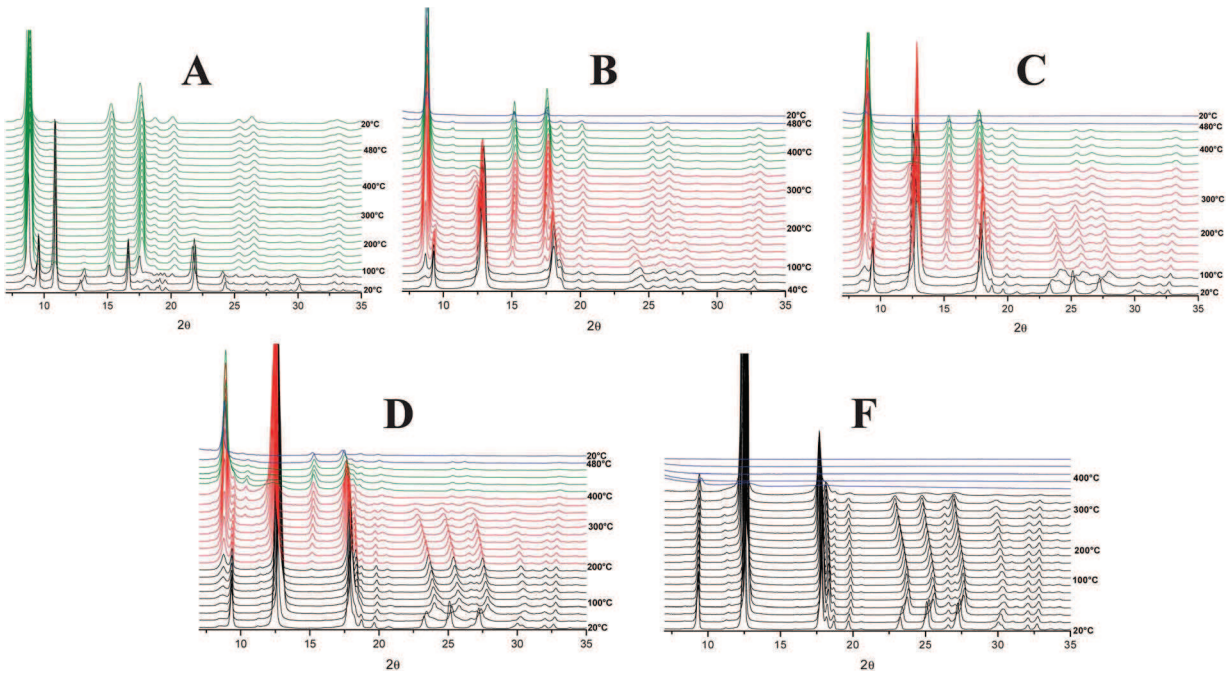

Fig. 6 Thermodiffractograms of A, B, C, D and F. Key: single np phase (black), single lp phase (green), simultaneous presence of np and lp phases (red), and amorphous phase (blue).

Table 4 Behavior of $Al(OH)(abdc)_n(bdc)_{1-n}$ samples as a function of temperature

Sample	% abdc measured	Temperature of disappearance of the np phase/°C	Temperature of appearance of the lp phase/°C	Collapsing temperature/°C
A	0	60	60	>480
B	10 ± 2	360	100	480
C	18 ± 2	380	100	480
D	49 ± 2	380	200	480
F	100	n.a.	n.a.	380

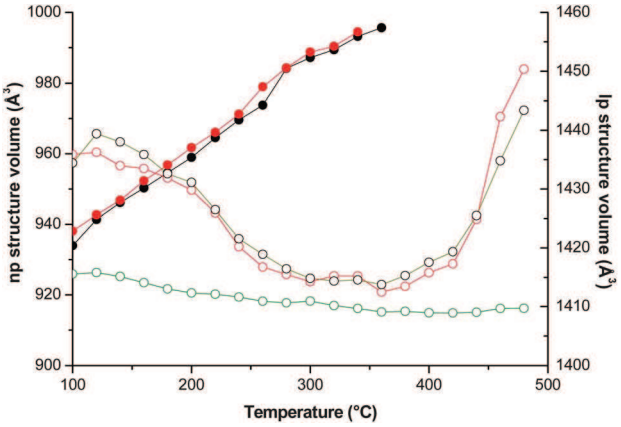

Fig. 8 Evolution of the pore volume of the np and lp phases as a function of temperature. Key: np structure (filled circles) and lp structure (empty circles). Samples (A) (green), B (black) and C (red).

saturation, the total microporous volume can be evaluated. For all samples, the volumes correspond to the values expected. We can therefore rule out the presence of a significant amount of non-porous phases such as aluminates. Furthermore, the evolution of the gas uptake at low pressure (in Henry's region) makes it possible to characterize the surface chemistry of the porous materials by measuring host–guest interactions. The linear relationship between the Henry's constant and the abdc content that is observed for CO_2 adsorption provides clear evidence of the homogeneity of the samples at the microdomain level. This trend is further confirmed by the characteristic breathing pressures for CO_2 adsorption at high pressure (P_{CO_2} > 100 kPa), increasing with the amine content. It is worth mentioning that a mechanical mixture of separate Al-MIL-53 and Al-MIL-53-NH_2 crystallites would result in a two-step adsorption isotherm in the respective "breathing" regions. For this reason, we rule out the presence of discrete crystallites of different phases.

It is noteworthy that the CO_2 gate opening pressure measured on the pure Al(OH)(abdc) sample (F), 1770 kPa, differs significantly from the value of 1200 kPa reported by Gascon *et al.*[32,33] Note however that the CO_2 uptake at 3000 kPa approaches ~6 mmol g^{-1} for this sample, which is in good agreement with Gascon *et al.*[32] We believe that such different isotherm profiles may arise from different crystallite sizes originating from different synthesis recipes. In this study, isolated crystallites of very regular shape and size (0.5–1 μm) have been obtained starting from $AlCl_3$ as the precursor. Nevertheless, we must recall that the pre-treatment procedure can affect the initial respective amounts of lp–np phases for the samples. Slight but significant modifications of N_2 isotherm profiles were reported by Stock *et al.*[28] on Al-MIL-53-NH_2 by performing several cyclic measurements. Obviously, further investigations are required especially for the pure Al-MIL-53-NH_2 sample to discern about the structure of this solid.

The simultaneous presence of np and lp phases over a broad range of temperatures as observed here for B–D samples was already reported for MIL-53(Ga).[36] Whereas the pure Al-MIL-53 framework transforms readily into the lp phase at a low temperature (T = 50 °C), the Ga-MIL-53 analogue still shows the np phase at T = 220 °C. In turn, the simultaneous presence of both np and lp phases in abdc-containing Al-MIL-53 cannot be exclusively ascribed to a hypothetical lack of homogeneity of linker distribution within the frameworks. Moreover, the temperature-evolution profile of the np and lp unit cell volumes might suggest an interplay between crystalline microdomains (Fig. 8). It seems clear that the unit cell volume of the lp phase increases abruptly when the np phase disappears (and is converted into the lp phase). We suggest that the crystallites could consist of np and lp X-ray microdomains and that the np phase exerts a strain on the lp phase preventing it from a free expansion.

Conclusions

In this paper, we have shown that the breathing pressure and temperature can characterize the homogeneity of flexible MOFs formulated as microcrystalline powders. The linear trends between the breathing pressure and the amine content in the Al-MIL-53 structure clearly indicate the homogeneity of the crystallite composition, *i.e.* the microcrystallites have the same abdc : bdc ratio. On the other hand, adsorption techniques cannot rule out the presence of a linker distribution at a microcrystalline level. The application of highly spatially resolved techniques to address this question will undoubtedly represent a breakthrough for the characterization of functionalized MOFs such as multivariate MOFs or post-modified MOFs.

We have also shown that the functionalization of Al-MIL-53 with a small amount of amine groups (*i.e.*, 10% abdc) results in a profound modification of the breathing properties triggered by the temperature. Much higher temperatures are required for the full conversion of the np into the lp phase, in agreement with a previous DFT modeling study.[32] We also suggest a possible interaction between coexisting np and lp microcrystalline domains that might "smooth" the breathing properties at the macroscopic level.

Acknowledgements

We thank the European Commission and the NANOMOF program (FP7-NMP).

Notes and references

1 G. Ferey, *Chem. Soc. Rev.*, 2008, **37**, 191–214.
2 G. Ferey and C. Serre, *Chem. Soc. Rev.*, 2009, **38**, 1380–1399.
3 S. Kitagawa and K. Uemura, *Chem. Soc. Rev.*, 2005, **34**, 109–119.

4 J. A. R. Navarro, E. Barea, A. Rodriguez-Diéguez, J. M. Salas, C. O. Ania, J. B. Parra, N. Masciocchi, S. Galli and A. Sironi, *J. Am. Chem. Soc.*, 2008, **130**, 3978–3984.
5 S. Horike, S. Shimomura and S. Kitagawa, *Nat. Chem.*, 2009, **1**, 695–704.
6 D. Farrusseng, *Metal-Organic Frameworks: Applications from Catalysis to Gas Storage*, WILEY-VCH, 2011.
7 O. M. Yaghi, M. O'Keeffe, N. W. Ockwig, H. K. Chae, M. Eddaoudi and J. Kim, *Nature*, 2003, **423**, 705–714.
8 N. L. Rosi, J. Eckert, M. Eddaoudi, D. T. Vodak, J. Kim, M. O'Keeffe and O. M. Yaghi, *Science*, 2003, **300**, 1127–1129.
9 T. Devic, P. Horcajada, C. Serre, F. Salles, G. Maurin, B. a. Moulin, D. Heurtaux, G. Clet, A. Vimont, J.-M. Greneche, B. L. Ouay, F. Moreau, E. Magnier, Y. Filinchuk, J. m. Marrot, J.-C. Lavalley, M. Daturi and G. Férey, *J. Am. Chem. Soc.*, 2009, **132**, 1127–1136.
10 K. Seki and W. Mori, *J. Phys. Chem. B*, 2002, **106**, 1380–1385.
11 R. Banerjee, H. Furukawa, D. Britt, C. Knobler, M. O'Keeffe and O. M. Yaghi, *J. Am. Chem. Soc.*, 2009, **131**, 3875–3877.
12 W. Morris, B. Leung, H. Furukawa, O. K. Yaghi, N. He, H. Hayashi, Y. Houndonougbo, M. Asta, B. B. Laird and O. M. Yaghi, *J. Am. Chem. Soc.*, 2010, **132**, 11006–11008.
13 J. Pérez-Pellitero, H. Amrouche, F. R. Siperstein, G. Pirngruber, C. Nieto-Draghi, G. Chaplais, A. Simon-Masseron, D. Bazer-Bachi, D. Peralta and N. Bats, *Chem.–Eur. J.*, 2010, **16**, 1560–1571.
14 H. Deng, C. J. Doonan, H. Furukawa, R. B. Ferreira, J. Towne, C. B. Knobler, B. Wang and O. M. Yaghi, *Science*, 2010, **327**, 846–850.
15 F. Hinterholzinger, C. Scherb, T. Ahnfeldt, N. Stock and T. Bein, *Phys. Chem. Chem. Phys.*, 2010, **12**, 4515–4520.
16 M. Savonnet, D. Bazer-Bachi, N. Bats, J. Perez-Pellitero, E. Jeanneau, V. Lecocq, C. Pinel and D. Farrusseng, *J. Am. Chem. Soc.*, 2010, **132**, 4518–4519.
17 K. K. Tanabe and S. M. Cohen, *Angew. Chem., Int. Ed.*, 2009, **48**, 7424–7427.
18 J. Canivet, S. Aguado, G. Bergeret and D. Farrusseng, *Chem. Commun.*, 2011, **47**, 11650–11652.
19 Z. Q. Wang and S. M. Cohen, *Chem. Soc. Rev.*, 2009, **38**, 1315–1329.
20 Z. Q. Wang and S. M. Cohen, *J. Am. Chem. Soc.*, 2007, **129**, 12368.
21 M. Savonnet, E. Kockrick, A. Camarata, D. Bazer-Bachi, N. Bats, V. Lecocq, C. Pinel and D. Farrusseng, *New J. Chem.*, 2011, **35**, 1892–1897.
22 W. Kleist, M. Maciejewski and A. Baiker, *Thermochim. Acta*, 2009, **499**, 71–78.
23 W. Kleist, F. Jutz, M. Maciejewski and A. Baiker, *Eur. J. Inorg. Chem.*, 2009, 3552–3561.
24 A. D. Burrows, L. C. Fisher, C. Richardson and S. P. Rigby, *Chem. Commun.*, 2011, **47**(12), 3380–3382.
25 T. Fukushima, S. Horike, Y. Inubushi, K. Nakagawa, Y. Kubota, M. Takata and S. Kitagawa, *Angew. Chem., Int. Ed.*, 2010, **49**, 4820–4824.
26 T. Lescouet, E. Kockrick, G. Bergeret, M. Pera-Titus and D. Farrusseng, *Dalton Trans.*, 2011, **40**, 11359–11361.
27 S. Marx, W. Kleist, J. Huang, M. Maciejewski and A. Baiker, *Dalton Trans.*, 2010, **39**, 3795–3798.
28 T. Ahnfeldt, D. Gunzelmann, T. Loiseau, D. Hirsemann, J. r. Senker, G. Férey and N. Stock, *Inorg. Chem.*, 2009, **48**, 3057–3064.
29 Y. M. Juan and E. Kaxiras, *Phys. Rev. B: Condens. Matter*, 1993, **48**, 14944–14952.
30 T. Loiseau, C. Serre, C. Huguenard, G. Fink, F. Taulelle, M. Henry, T. Bataille and G. Férey, *Chem.–Eur. J.*, 2004, **10**, 1373–1382.
31 S. Biswas, T. Ahnfeldt and N. Stock, *Inorg. Chem.*, 2011, **50**, 9518–9526.
32 E. Stavitski, E. A. Pidko, S. Couck, T. Remy, E. J. M. Hensen, B. M. Weckhuysen, J. Denayer, J. Gascon and F. Kapteijn, *Langmuir*, 2011, **27**, 3970–3976.
33 A. Boutin, S. Couck, F. X. Coudert, P. Serra-Crespo, J. Gascon, F. Kapteijn, A. H. Fuchs and J. F. M. Denayer, *Microporous Mesoporous Mater.*, 2010, **140**, 108–113.
34 A. Boutin, F. o.-X. Coudert, M.-A. Springuel-Huet, A. V. Neimark, G. Férey and A. H. Fuchs, *J. Phys. Chem. C*, 2010, **114**, 22237–22244.
35 M. Pera-Titus, M. Savonnet and D. Farrusseng, *J. Phys. Chem. C*, 2010, **114**, 17665–17674.
36 C. Volkringer, T. Loiseau, N. Guillou, G. Ferey, E. Elkaim and A. Vimont, *Dalton Trans.*, 2009, 2241–2249.

Dalton Transactions

Cite this: *Dalton Trans.*, 2011, **40**, 11359

www.rsc.org/dalton

COMMUNICATION

Engineering MIL-53(Al) flexibility by controlling amino tags†

Tristan Lescouet, Emanuel Kockrick, Gerard Bergeret, Marc Pera-Titus and David Farrusseng*

Received 7th September 2011, Accepted 19th September 2011
DOI: 10.1039/c1dt11700a

The flexibility of MIL-53(Al) can be tuned by adjusting the ratio of terephthalate and 2-amino terephthalate linkers incorporated into the framework during hydrothermal synthesis.

The latest generation of Porous Coordination Polymers (PCPs), also known as Metal–Organic Frameworks (MOFs), exhibit structural flexibility upon external stimuli such as temperature or pressure changes.[1–4] Gas adsorption on these materials is characterized by a prominent step (S-shaped isotherm) associated with a structural change promoted by guest–host accommodation. This inflection is usually accompanied by a marked hysteresis loop between the adsorption and desorption branches. This peculiar adsorption/desorption behaviour, usually termed "breathing" or "gate opening," arises from an intrinsic flexibility of the porous network.[5] Recent efforts have focused on engineering the breathing properties of the well-known $M^{3+}(OH)(bdc)$, also known as MIL-53(Al, Cr, Fe, Ga), discovered by Férey and coworkers at the Institut Lavoisier.[6–11] On the fundamental side, the predictive simulation of the breathing properties of Al(OH)(bdc) has made it possible to identify the pressure and temperature ranges over which the phase transformation occurs.[12–16] The effect of cation substitution (Al, Fe, Ga, Cr) on the breathing properties has been investigated.[17] Whereas the MIL-53(Al) framework transforms into the lp phase at low temperature (T = 50 °C), the analogous MIL-53(Ga) framework still shows the np phase at T = 220 °C. Recently, Kitagawa showed that the flexibility of CID-5/6 MOFs can be modulated by tuning the composition of two different linkers.[18] If one varies their relative ratio, the pressure at which the network begins expansion (the gate opening pressure) can be finely controlled. The synthesis of "mixed" MOFs with a random distribution of functional linkers has also been achieved for IRMOF systems.[19–23] Finally, a "mixed" MIL-53(Al) in which the terephthalate linker (bdc) is partially substituted by 2-aminobenzene-1,4-dicarboxylate (abdc) has been synthesized.[24] Notwithstanding, the effect of amino content on the flexibility of MIL-53(Al) was not reported.[15]

Herein, we report, for the first time, the influence of terephthalate linker functionalization by amino tags on the breathing and phase transition properties of MIL-53(Al). The breathing behavior of amino-MIL-53(Al) was assessed by modelling CO_2 adsorption/desorption isotherms and by conducting temperature-programmed X-ray diffraction measurements.

Both bdc and abdc linkers were introduced into the starting solution at different molar ratios prior to hydrothermal treatment, following the Stock protocol[25] (Fig. 1). After the synthesis, the samples were washed with boiling DMF followed by CH_2Cl_2 Soxhlet extraction in order to remove the organic acids.[24] The relative bdc and abdc contents in the resulting materials were quantified by liquid ^{1}H-NMR after digestion in a 1% HF/d_6-DMSO solution (Table 1). For the pure amino MIL-53(Al)-NH_2 (F), the absence of residual amounts of abdc acid and DMF in this sample was confirmed by ^{1}H, ^{13}C NMR and Diffuse Reflectance IR (see ESI†).

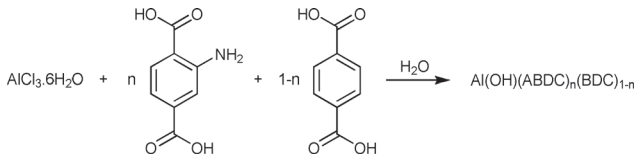

Fig. 1 Synthesis of Al-MIL-53 with different amino contents.

The six fresh MIL-53(Al)-NH_2 samples prepared here display the narrow pore (np) structure at ambient conditions (*i.e.*, in the presence of moisture). After treatment at 150 °C and 5.10^{-4} mbar for 12 h, N_2 isotherms at 77 K were recorded[25] (Table 1). The measured micropore volumes (*t*-plot method) fall into the range of 0.37–0.51 $cm^3\ g^{-1}$ with BET surface areas of 1000–1100 $m^2\ g^{-1}$. These data coincide with the range found in previous work for pure MIL-53(Al)[26] and pure amino MIL-53(Al)-NH_2.[25] As indicated by Stock,[25] we can observe for the pure amino MIL-53(Al)-NH_2 (F) a marked N_2 adsorption step (77 K) at low pressure, accompanied by a large hysteresis loop between the adsorption/desorption branches[25] (ESI†).

The CO_2 adsorption/desorption isotherms were recorded at 30 °C from 2 to 3200 kPa on a Belsorp Max system (Bel Japan). Prior to gas adsorption, the samples were degassed at 150 °C under 10^{-5} mbar for 12 h. For the sake of simplicity, only the adsorption branches are plotted in Fig. 2. Complete adsorption/desorption isotherms can be found in ESI.† As already reported for pure MIL-53(Al) and pure MIL-53(Al)-NH_2, all samples display two distinct adsorption steps assigned, respectively, to lp→np and np→lp

University of Lyon, Institut de Recherches sur la Catalyse et l'Environnement de Lyon (IRCELYON), UMR 5256 CNRS – 2 Av. Albert Einstein, 69626, Villeurbanne, France. E-mail: david.farrusseng@ircelyon.univ-lyon1.fr; Fax: +33 (0)4 72 33 53 99; Tel: +33 (0)4 72 44 53 65

† Electronic supplementary information (ESI) available: Synthesis details, ^{1}H NMR, powder X-ray diffraction and N_2 physisorption isotherms. See DOI: 10.1039/c1dt11700a

Table 1 Composition and adsorption data of Al(OH)(abdc)$_n$(bdc)$_{1-n}$ samples

Sample	%abdc theoretical	%abdc measured[a]	V_{micro}[b] (cm^3 g^{-1})	S_{BET}[b] (m^2 g^{-1})	P_{G1}/P_{G2}[d] (kPa)	H[e] (cm^3(STP) g^{-1} kPa^{-1})	ΔF lp->np (kJ mol^{-1})
A	0	0	0.51	1041	15/665	0.27	–3.3
B	11.1	10 ± 2	0.48	1048	10/740	0.36	–2.8
C	20	18 ± 2	0.51	1090	12/960	0.44	–3.6
D	50	49 ± 2	0.46	1100	7/1110	0.93	–5.6
E	66.6	62 ± 5	0.50	1017	8/1260	1.39	–6.8
F	100	100	0.37	940[c]	30/1770	1.96	–8.6

[a] Measured by NMR. [b] Measured by N_2 adsorption at 77.4 K. [c] Calculations made from the desorption branch. [d] Phase transition pressures (303 K) upon CO_2. [e] Henry constant for CO_2/ΔF np→lp: Phase transition energy upon CO_2. adsorption estimated by fitting Tóth and Freundlich, respectively, curves for the lp and np phase according to Coudert *et al.*[12] (data in kJ mol^{-1} of solid). Values accurate to within 15%.

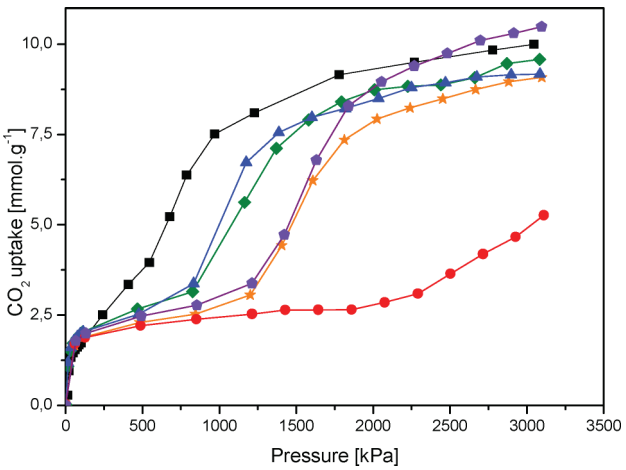

Fig. 2 CO_2 isotherm of Al(OH)(abdc)$_n$(bdc)$_{1-n}$ at 303 K for A (square), B (triangle), C (rhombus), D (star), E (pentagon) and F (circle). Desorption branches have been omitted for clarity.

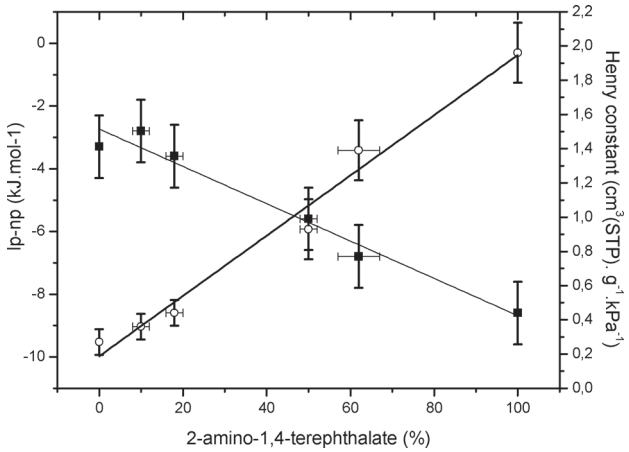

Fig. 3 Evolution of the Henry constant for CO_2 (empty cycle) and the second phase transition energy, lp to np (filled square) upon CO_2 adsorption as a function of the abdc content for Al(OH)(abdc)$_n$(bdc)$_{1-n}$. See Table 1 for corresponding data.

phase transitions at low and high CO_2 pressures.[27] Regardless of the amine loading, a plateau level of ~2 mmol g^{-1} is attained, corresponding to ~0.5 CO_2 per μOH.[16,28] This result suggests that all samples possess an equal number of adsorption sites for the np phase. At low pressures (<100 kPa), we can observe a linear correlation of the Henry constant with the abdc content (Table 1 and Fig. 3). This observation can be explained on the basis of a larger heat of adsorption for CO_2 through formation of hydrogen bonds with pending amino-tags and bridging μOH groups.[27] On the other hand, at higher pressure, the gate opening pressure increases with the abdc content from a value of 665 kPa for pure MIL-53(Al) (A) to 1770 kPa for pure MIL-53(Al)-NH_2 (F). This trend involves an increase of the np→lp phase transition free energy from 0.7 kJ mol^{-1} for the bare MIL-53(Al) to 9 kJ mol^{-1} for the pure MIL-53(Al)-NH_2 (see ESI†). From the plot in Fig. 3, we can observe that the phase transition energy is linearly correlated with the amino content.

It is noteworthy that the gate opening pressure measured on the pure MIL-53(Al)-NH_2 (F) sample, 1770 kPa, differs significantly from the value of 1200 kPa reported by Gascon *et al.*[27,28] Furthermore, the CO_2 uptake at 3000 kPa approaches ~6 mmol g^{-1} for MIL-53(Al)-NH_2 (F), which is in good agreement with Gascon *et al.*[26] We believe that such different isotherm profiles may arise from different crystallite sizes originating from different synthesis recipes. In this study, isolated crystallites of very regular shape and size (0.5 μm) were obtained starting from $AlCl_3$ as the precursor.

Temperature-dependent powder X-ray diffraction was performed on Al(OH)(abdc)$_n$(bdc)$_{1-n}$ samples (A–D and F) under an ambient air atmosphere (Fig. 4). A markedly different thermal behaviour is observed as a function of the abdc content. A characteristic np→lp phase transition can be detected at 60 °C for pure MIL-53(Al) (A), whereas this structural change is

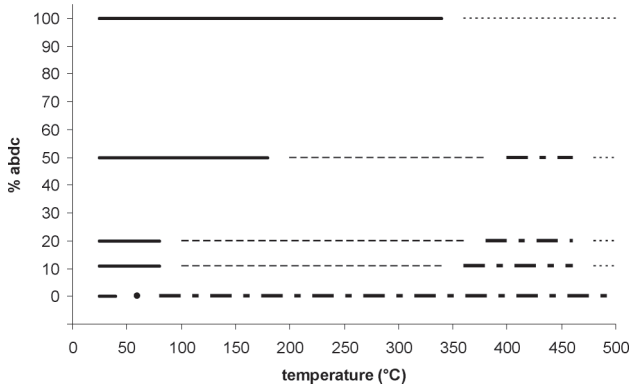

Fig. 4 Phase transition and collapse of Al(OH)(abdc)$_n$(bdc)$_{1-n}$ as a function of temperature; np monoclinic (thick line), lp orthorhombic (thick dash and dot line), mixture of np and lp (thin dash line), and collapse of the structure (thin dot line).

not observed for the pure MIL-53(Al)-NH_2 sample (F). For intermediate amine content, this phase transition temperature increases with the abdc content. It varies from 100–340 °C for sample B to 200–380 °C for sample D. The simultaneous presence of np and lp phases over a broad range of temperature was already reported for MIL-53(Ga).[17] Again, the higher thermal stability of the np phase in the abdc-rich samples arises from the stronger hydrogen bonding involving the NH_2 moieties and the $[AlO_6]_\infty$ group, as recently calculated.[27] In addition, we observe from PXRD that a structural collapse takes place at lower temperature as a function of the amino content. The lower thermal stability of amino-containing MIL-53 and UiO-66 with respect to the parent materials has already been reported.[24,29]

The linear trends observed, relating to the Henry constant and to phase transition energy as a function of the amino content, are clear evidence of the molecular-level homogeneity of the abdc and bdc linkers. Mixing of separate MIL-53(Al) and MIL-53(Al)-NH_2 crystallites can therefore be ruled out.

We have shown in this study that the adsorption and breathing properties of MIL-53(Al) can be tuned by the controlled substitution of terephthalate by aminoterephthalate linkers. We have provided, for the first time, quantitative structure–property relationships that could guide the engineering of MIL-53(Al) for drug delivery, sensor and separation applications.

Acknowledgements

We thank the European Commission and the NANOMOF program (FP7-NMP).

Notes and references

1 S. Kitagawa and K. Uemura, *Chem. Soc. Rev.*, 2005, **34**, 109–119.
2 J. A. R. Navarro, E. Barea, A. Rodriguez-Diéguez, J. M. Salas, C. O. Ania, J. B. Parra, N. Masciocchi, S. Galli and A. Sironi, *J. Am. Chem. Soc.*, 2008, **130**, 3978–3984.
3 G. Ferey, *Chem. Soc. Rev.*, 2008, **37**, 191–214.
4 S. Horike, S. Shimomura and S. Kitagawa, *Nat. Chem.*, 2009, **1**, 695–704.
5 G. Ferey and C. Serre, *Chem. Soc. Rev.*, 2009, **38**, 1380–1399.
6 P. L. Llewellyn, P. Horcajada, G. Maurin, T. Devic, N. Rosenbach, S. Bourrelly, C. Serre, D. Vincent, S. Loera-Serna, Y. Filinchuk and G. Férey, *J. Am. Chem. Soc.*, 2009, **131**, 13002–13008.
7 S. Bourrelly, P. L. Llewellyn, C. Serre, F. Millange, T. Loiseau and G. Férey, *J. Am. Chem. Soc.*, 2005, **127**, 13519–13521.
8 C. Serre, S. Bourrelly, A. Vimont, N. A. Ramsahye, G. Maurin, P. L. Llewellyn, M. Daturi, Y. Filinchuk, O. Leynaud, P. Barnes and G. Férey, *Adv. Mater.*, 2007, **19**, 2246–2251.
9 P. L. Llewellyn, S. Bourrelly, C. Serre, Y. Filinchuk and G. Férey, *Angew. Chem.*, 2006, **118**, 7915–7918.
10 N. A. Ramsahye, G. Maurin, S. Bourrelly, P. L. Llewellyn, C. Serre, T. Loiseau, T. Devic and G. Ferey, *J. Phys. Chem. C*, 2008, **112**, 514–520.
11 C. Serre, F. Millange, C. Thouvenot, M. Nogues, G. r. Marsolier, D. Louër and G. Férey, *J. Am. Chem. Soc.*, 2002, **124**, 13519–13526.
12 F. o.-X. Coudert, M. Jeffroy, A. H. Fuchs, A. Boutin and C. Mellot-Draznieks, *J. Am. Chem. Soc.*, 2008, **130**, 14294–14302.
13 A. M. Walker, B. Civalleri, B. Slater, C. Mellot-Draznieks, F. Cora, C. M. Zicovich-Wilson, G. Roman-Perez, J. M. Soler and J. D. Gale, *Angew. Chem., Int. Ed.*, 2010, **49**, 7501–7503.
14 A. Torrisi, R. G. Bell and C. Mellot-Draznieks, *Cryst. Growth Des.*, 2010, **10**, 2839–2841.
15 A. Torrisi, C. Mellot-Draznieks and R. G. Bell, *J. Chem. Phys.*, 2010, 132.
16 A. Boutin, F. o.-X. Coudert, M.-A. Springuel-Huet, A. V. Neimark, G. Férey and A. H. Fuchs, *J. Phys. Chem. C*, 2010, **114**, 22237–22244.
17 C. Volkringer, T. Loiseau, N. Guillou, G. Ferey, E. Elkaim and A. Vimont, *Dalton Trans.*, 2009, 2241–2249.
18 T. Fukushima, S. Horike, Y. Inubushi, K. Nakagawa, Y. Kubota, M. Takata and S. Kitagawa, *Angew. Chem., Int. Ed.*, 2010, **49**, 4820–4824.
19 A. D. Burrows, L. C. Fisher, C. Richardson and S. P. Rigby, *Chem. Comm.*, 2011.
20 K. Koh, A. G. Wong-Foy and A. J. Matzger, *Chem. Commun.*, 2009, 6162–6164.
21 W. Kleist, F. Jutz, M. Maciejewski and A. Baiker, *Eur. J. Inorg. Chem.*, 2009, 3552–3561.
22 H. Deng, C. J. Doonan, H. Furukawa, R. B. Ferreira, J. Towne, C. B. Knobler, B. Wang and O. M. Yaghi, *Science*, 2010, **327**, 846–850.
23 W. Kleist, M. Maciejewski and A. Baiker, *Thermochim. Acta*, 2010, **499**, 71–78.
24 S. Marx, W. Kleist, J. Huang, M. Maciejewski and A. Baiker, *Dalton Trans.*, 2010, **39**, 3795–3798.
25 T. Ahnfeldt, D. Gunzelmann, T. Loiseau, D. Hirsemann, J.r. Senker, G. Férey and N. Stock, *Inorg. Chem.*, 2009, **48**, 3057–3064.
26 T. Loiseau, C. Serre, C. Huguenard, G. Fink, F. Taulelle, M. Henry, T. Bataille and G. Férey, *Chem.–Eur. J.*, 2004, **10**, 1373–1382.
27 E. Stavitski, E. A. Pidko, S. Couck, T. Remy, E. J. M. Hensen, B. M. Weckhuysen, J. Denayer, J. Gascon and F. Kapteijn, *Langmuir*, 2011, **27**, 3970–3976.
28 A. Boutin, S. Couck, F. X. Coudert, P. Serra-Crespo, J. Gascon, F. Kapteijn, A. H. Fuchs and J. F. M. Denayer, *Microporous Mesoporous Mater.*, 2011, **140**, 108–113.
29 M. Kandiah, M. H. Nilsen, S. Usseglio, S. Jakobsen, U. Olsbye, M. Tilset, C. Larabi, E. A. Quadrelli, F. Bonino and K. P. Lillerud, *Chem. Mater.*, 2010, **22**, 6632–6640.

THE JOURNAL OF PHYSICAL CHEMISTRY C

Article

pubs.acs.org/JPCC

Quantitative Characterization of Breathing upon Adsorption for a Series of Amino-Functionalized MIL-53

M. Pera-Titus,* T. Lescouet, S. Aguado, and D. Farrusseng

Université de Lyon, Institut de Recherches sur la Catalyse et l'Environnement de Lyon (IRCELYON), UMR 5256 CNRS - Université Lyon 1, 2, Av. A. Einstein, 69626 Villeurbanne Cedex, France

Supporting Information

ABSTRACT: This work presents the synthesis of MIL-53(Al) metal−organic frameworks with different terephthalate/2-aminoterephthalate linker ratios incorporated into the framework during hydrothermal synthesis. In all cases, the materials show prominent S-shaped isotherms upon CO_2 adsorption that can be attributed to sorbate-induced breathing phenomena involving two narrow-to-large-pore phase transitions. However, the breathing properties of the MIL-53(Al) materials (i.e., the relative stability of the np phase) are modified by adjusting the terephthalate/2-aminoterephthalate ratio. As a consequence, the pressure at which the second np → lp phase transition occurs, as well as Henry's constant for CO_2 adsorption, are directly associated with the number of amino-modified linkers. The different N_2 and CO_2 adsorption/desorption patterns have been successfully reproduced through the formulation of thermodynamic isotherms, providing direct information about energy heterogeneity of the solid/sorbate system and a direct characterization of the phase transition zone for breathing systems.

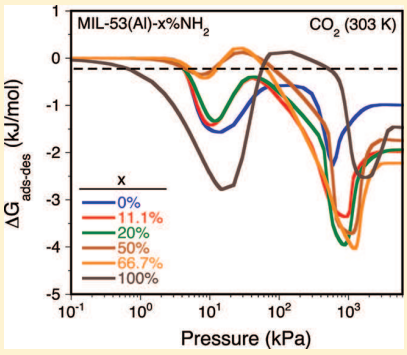

1. INTRODUCTION

Soft porous crystals (SPCs) exhibiting dynamic structural flexibility upon external stimuli such as variations of pressure, temperature, or electric field are the last generation of porous solids.[1−3] They consist of bi(multi)stable crystalline materials with long-range order and possess a structural transformability which is allowed by a panel of weak secondary bonds (e.g., Π−Π stacking, hydrogen bonds, van der Waals interactions). Structural transformations usually take place upon guest adsorption or removal from the network. This property is attractive for the design of new generations of adsorbents,[4,5] catalysts,[6] and sensors.[7]

The above stated structural changes in SPCs translate into anomalous adsorption patterns characterized by eye-catching inflections and hysteresis loops in the adsorption/desorption curves. If the structure is relatively rigid, these transformations are moderate. A case example is ZIF-8, where partial swing of the imidazolate linkers can be achieved by low-pressure N_2 adsorption at 77.4 K,[8] leading to a significant increase of the accessible pore volume and the size of 6-ring windows. A remarkably different situation is encountered for highly flexible frameworks, where a net expansion/shrinking of the unit cell occurs. In this case, the material can display abrupt but reversible phase transitions between metastable states upon guest accommodation, involving either amorphous-to-crystal or crystal-to-crystal transformations being at the origin of the striking "gate opening" and "breathing" phenomena.[1,9,10] As a consequence, the isotherms usually display outstanding inflections, which are accompanied by marked hysteresis loops between the adsorption and desorption branches.

A paradigmatic example of prominent structural transitions in SPCs can be found in the MIL-53 family. The MIL-53 framework consists of parallel 1D M(OH) chains (M = Al^{3+}, Cr^{3+}, Fe^{3+}, Ga^{3+}) based on trans-corner-shared $MO_4(OH,F)_2$ octahedra cross-linked by 1,4-benzene-dicarboxylate (terephthalate, bdc) ligands to form linear diamond-shaped channels.[11,12] The temperature and guest-responsive properties of MIL-53 depend to a great extent on the metal cation: the MIL-53(Al) structure evolves in a spontaneous and nongradual fashion between a narrow-pore (np) monoclinic and large-pore (lp) orthorhombic phase upon guest accommodation and water loss at ∼60 °C,[13,14] whereas the MIL-53(Fe,Ga) analogues show little expansion until 150 °C (Fe) and 200 °C (Ga), even after dehydration, due to the formation of a highly stable np phase.[15−17] Bistability in MIL-53 is promoted by strong sorbate−sorbate interactions in the framework, acting as a backbone for an onset of symmetric interactions with μ-OH surface groups.[18,19] Water[11] and CO_2[19−21] adsorption in MIL-53(Cr,Al) (and to a lesser extent C1−C9 alkanes[22,23]) results in two abrupt lp → np and np → lp phase transitions at near-room temperature starting from the lp phase for the outgassed sample (i.e., sorbate-free). For MIL-53(Al), this transition is accompanied by a prominent inflection in the CO_2 isotherm (S-shaped) at about 6 bar and 304 K,[24] involving a unit cell volume expansion of about 38%. This particular sorption behavior opposes to the typical type I or even type V[25] patterns

Received: December 7, 2011
Revised: April 10, 2012
Published: April 11, 2012

   dx.doi.org/10.1021/jp2117856 | J. Phys. Chem. C 2012, 116, 9507−9516

displayed by "rigid" MOFs in the presence of strong sorbate−sorbate interactions.

In addition to the metal cation, Kitagawa and co-workers[26] have shown that the flexibility of SPCs (CID-5/6 in their case) can be modulated by tuning the relative amount of two different linkers. By varying their relative ratio, the pressure at which the network begins expansion can be finely tuned. MIL-53(Al) can be functionalized with free-standing amino groups pointing to the pores starting from 2-amino-1,4-benzenedicarboxylate (abdc) ligand instead of terephthalic acid during hydrothermal synthesis.[27−29] Couck et al.[27] have shown that the amino function can shift the np → lp phase transition pressure upon CO_2 adsorption from 6 bar for the bare MIL-53(Al) to ca. 13 bar at room temperature for pure MIL-53(Al)-NH_2.

The physical basis for such different behavior can be found in the improved sorbate/sorbent interactions in the MIL-53 framework. Remarkably, Torrisi et al.[30] have shown in a recent computational study (DFT) that amine functionalization of benzene linkers improves the adsorption affinity for CO_2 through intermolecular interactions between C and lone electron pairs of NH_2. Stavitsky et al.[31] have also provided IR evidence supported by DFT calculations that CO_2 adsorption on pure MIL-53(Al)-NH_2 proceeds via physisorption with surface OH and NH_2 groups, but neither carbamates nor (bi)carbonate species are formed (i.e., no stable bonds are formed). In a short communication,[32] we have reported the possibility of finely tuning the flexibility of MIL-53(Al) by varying the relative amount of 2-amino-1,4-benzenedicarboxylate/1,4-benzenedicarboxylate ligands within the structure.

The great diversity of MOF structures and sorption patterns makes necessary the development of suitable isotherm models describing properly gas adsorption in flexible MOFs. At first glance, this task is not straightforward, since classical adsorption models address rigid materials with negligible guest-promoted strains. This shortcoming combined with the extremely large specific surfaces offered by some MOFs pose obvious questions on the compatibility of the BET theory for measuring specific surfaces[33,34] and the classical Dubinin−Radushkevic (DR) and Dubinin−Astakhov (DA) isotherms.

In this paper, we show a quantitative thermodynamic approach for inferring the intrinsic flexibility in SPCs, as an attempt to provide a tool for classifying SPCs in a quantitative and rational manner. The different sorption patterns can be reproduced through the formulation of "thermodynamic isotherms" using a reduced set of affinity and energy heterogeneity parameters, which can be regarded as descriptors of flexibility. Recently, we applied this method to two different flexible MOFs.[35,36] We present here the application of such an approach to N_2 and CO_2 adsorption on a series of MIL-53(Al) samples with different degrees of amine functionalization. This approach enables a quantitative characterization of the flexibility on MOF materials with small structural differences.

2. EXPERIMENTAL SECTION

2.1. Synthesis of Pure and Mixed Amino-MIL-53(Al). All chemicals, supplied by Sigma-Aldrich, were used as received: aluminum chloride hexahydrate ($AlCl_3 \cdot 6H_2O$, 99%), benzene-1,4-dicarboxylate (bdc, 98%), 2-aminobenzene-1,4-dicarboxylate (abdc, 98%), and *N*,*N*′-dimethylformamide (DMF, 99.8%).

Pure MIL-53(Al) and MIL-53(Al)-NH_2, as well as four mixed-ligand MIL-53(Al)-*x*%NH_2 samples (*x* = 10−70%), were prepared and purified following the synthetic approach reported in previous studies[32,37] and adapted from Stock and co-workers.[38] Briefly, solutions containing 1.931 g (8 mmol) of $AlCl_3 \cdot 6H_2O$, 8 mmol of bdc and abdc in different molar ratios (0, 11.1, 20, 50, 66.7, and 100% of abdc), and 30 mL of deionized water were introduced to a 48 mL Teflon-lined autoclave and subjected to hydrothermal synthesis at 150 °C for 9 h (see reaction scheme in Figure SI1, Supporting Information). After cooling, the products were separated from water by centrifugation at 4000 rpm for 5 min. In order to remove the remaining abdc and bdc ligands in solution, the as-synthesized products were placed in an autoclave with 30 mL DMF and heated at 150 °C for 24 h. Then, the solvent was replaced by fresh DMF and the solvothermal treatment was repeated twice.

After the synthesis, DMF was removed by Soxhlet extraction with dichloromethane for 20 h and the solid was dried at 100 °C for 9 h at reduced pressure to obtain fine powdered MIL-53(Al) (A), MIL-53(Al)-11.1%NH_2 (B), MIL-53(Al)-20%NH_2 (C), MIL-53(Al)-50%NH_2 (D), MIL-53(Al)-66.7%NH_2 (E), and MIL-53(Al)-NH_2 (F).

The relative bdc and abdc content in the resulting materials was quantified by liquid ^{1}H NMR after digestion in a 1% HF/d_6-DMSO solution. For the pure amino MIL-53(Al)-NH_2 (F), the absence of residual abdc acid and DMF was confirmed by liquid ^{1}H NMR, solid ^{13}C NMR, and DRIFT spectroscopy.

2.2. Measurement of N_2 and CO_2 Adsorption/Desorption Isotherms. N_2 adsorption/desorption isotherms were measured at 77.4 K on a Micromeritics ASAP 2010 M apparatus. Care was taken of the absence of diffusional limitations in the adsorption measurements. In the low-pressure region ($10^{-5} < P/P_0 < 10^{-2}$), the adsorption measurements were carried out by doses of 3−6 cm^3(STP)/g. Prior to the measurements, the samples were outgassed under secondary vacuum (5×10^{-4} mbar) at 423 K for 12 h.[38] BET specific surfaces were determined on the adsorption branch (unless otherwise stated) at $5 \times 10^{-3} \leq P/P_0 \leq 0.25$, and the micropore volume was calculated using the t-plot method.

CO_2 adsorption/desorption isotherms were recorded at 303 K in the range 2−3200 kPa on a Belsorp HP equipment (Bel Japan) after at least 1 h of stabilization. The samples were outgassed under vacuum (~10^{-5} mbar) at 423 K for 12 h before the adsorption measurements.

2.3. Physical Characterization Techniques. Standard powder X-ray diffraction (PXRD) measurements were carried out at room temperature using a Bruker D5005 diffractometer equipped with a secondary graphite monochromator (Cu Kα radiation, λ = 1.5418 Å) and a scintillation counter. The diffraction pattern was scanned in the range 2θ = 5−70° (for the sake of clarity, the range 5−50° is only represented) with a step length of 0.02° and a counting time of 756 s per step.

3. FORMULATION OF THERMODYNAMIC ISOTHERMS

In previous studies,[35,36] we have presented a methodology for inferring complex sorption patterns through the formulation of "thermodynamic isotherms". Briefly, this approach relies first on the transformation of the bare *q* vs *P* isotherm into a thermodynamic equivalent that can be fitted to a "universal" model including a reduced set of affinity and energy heterogeneity parameters. Subsequently, the fitted thermodynamic isotherm can be subjected to antitransformation, allowing the reconstruction of the *q* vs *P* isotherm matching the experimental trends.

dx.doi.org/10.1021/jp2117856 | J. Phys. Chem. C 2012, 116, 9507−9516

A thermodynamic isotherm equation describing properly gas adsorption in SPCs can be expressed by a "scaling law" equation linking the integral free energy of adsorption relative to saturation, $-\Psi/RT$, expressed as a Kiselev integral, with the inverse dimensionless chemical potential of the gas phase, $Z = 1/-\ln(\Pi)$.

$$-\frac{\Psi}{RT} = \int_{\theta}^{1} [-\ln(\Pi)]\delta\theta = \frac{G^{\circ}}{1 + \frac{\lambda_1\lambda_2}{\lambda_1+\lambda_2}\Big|_A + \frac{\lambda_3\lambda_4}{\lambda_3+\lambda_4}\Big|_B} \quad (1)$$

with $G^{\circ} = -\Phi(P^{\circ})/RT$ and $\lambda_i = k_i Z^{mi} = (Z/Z_i)^{mi}$ for $i = 1{:}4$, being $Z_i = (1/k_i)^{1/mi}$. The subscripts "A" and "B" refer to different sites in the solid, corresponding, for instance, to different phases.

Equation 1 includes eight parameters organized in four couples: (m_1, k_1) and (m_2, k_2) accounting for gas adsorption in the first site and couples (m_3, k_3) and (m_4, k_4) being related to the second site. On a physical basis, m parameters are ascribed to the different sources of energy heterogeneity of the sorbate/sorbent system (including a phase transition). Hence, m parameters could be regarded in principle as a characteristic number for flexible materials upon adsorption. On the other hand, k parameters describe the affinity of the sorbate for the sorbent as a function of the sorbate/sorbent and sorbate/sorbate interactions.

In order to obtain statistically significant fittings avoiding correlation effects, we have adapted the four-step parameter fitting strategy presented in a previous study for aromatic/MFI and C6-C8/MFI systems.[39] Each set of (m_i, k_i) parameters was fitted using a least-squares nonlinear optimization method based on the Levenberg–Marquardt algorithm by comparison of predicted and experimental integral free energies of adsorption. Parameter G° was kept constant in the fittings, its value being computed directly from the *raw* isotherms through eq 2.

$$G^{\circ} = \int_0^1 -\ln(\Pi)\delta\theta = \int_0^1 Z^{-1}\delta\theta \quad (2)$$

A q vs P equation for S-shaped isotherms can be subsequently obtained from the derivative of eq 1

$$\frac{\delta\theta}{\delta Z} = -Z\frac{\delta}{\delta Z}\left[\frac{G^{\circ}}{1 + \frac{\lambda_1\lambda_2}{\lambda_1+\lambda_2} + \frac{\lambda_3\lambda_4}{\lambda_3+\lambda_4}}\right] \quad (3)$$

Equation 3 allows the derivation of two analytical expressions describing gas adsorption in the limits $Z \to 0$ and $Z \to \infty$ (see ref 40 for calculation details)

- Primitive I ($\lambda_3 \ll \lambda_1 \ll \lambda_2$):

$$\theta \approx \frac{G^{\circ}k_1 Z^{m_1+1}}{(1 + k_1 Z^{m_1})} \quad (4)$$

- Primitive II ($\lambda_2 \ll \lambda_4 \ll \lambda_3$):

$$\theta = 1 - \frac{G^{\circ}}{k_3}\frac{m_3}{(m_3 - 1)}Z^{-(m_3-1)} - \frac{G^{\circ}}{k_2}\frac{m_4}{(m_4 - 1)} Z^{-(m_4-1)} \quad (5)$$

Equation 5 can be further simplified at low sorbate loadings to an expression accounting for the Henry's adsorption domain of the isotherm

$$H = \frac{\delta\theta}{\delta\Pi}\Big|_{\theta\to 0} = \frac{1}{\Pi \ln^2(\Pi)}\frac{\delta\theta}{\delta Z} = \frac{G^{\circ}m_1}{\Pi \ln^2(\Pi)}\frac{\lambda_1}{(1 + \lambda_1)^2} \quad (6)$$

4. RESULTS

4.1. Purity of the Samples. The near-room-temperature PXRD patterns measured for the six (amino)-MIL-53(Al) samples prepared in this study before outgassing reflect in all cases the genesis of pure crystalline phases with no indication of aluminate formation (see Figure SI2, Supporting Information). The different samples display the narrow pore (np) monoclinic structure under ambient conditions (i.e., in the presence of moisture). After heating at 713 K, all the samples except pure MIL-53(Al)-NH_2 evolve to the lp phase, as inferred from temperature dependent XRD patterns performed under ambient air atmosphere (see ref 32 for further details). The unit cell turns into orthorhombic with the space group *Imma*. Table 1 lists the values of unit cell parameters and unit cell volume of the lp phase measured for samples A–D by indexation of PXRD patterns. The unit cell volume of the MIL-53(Al) framework shows a positive increase with the degree of amine functionalization.

Table 1. Crystalline Data for A–D Samples (lp2 Phase) at 713 K

formula	MIL-53(Al) 0% (A)	MIL-53(Al) 11.1% (B)	MIL-53(Al) 20% (C)	MIL-53(Al) 50% (D)
a [Å]	6.593(2)	6.63(4)	6.63(4)	6.61(7)
b [Å]	16.617(8)	16.78(5)	16.81(9)	16.61(5)
c [Å]	12.860(4)	12.80(2)	12.77(1)	13.04(4)
V [Å^3]	1409.0	1425.5	1424.9	1434.1

The purity of the MIL-53(Al) samples was also inspected by ^{1}H NMR, ^{13}C NMR, and DRIFT spectroscopy (graphs not shown). The liquid ^{1}H NMR spectra display characteristic singlet and doublet peaks in the range 7.0–8.2 belonging to the aromatic rings. The ^{13}C NMR spectra of pure MIL-53(Al)-NH_2 (F) exhibit five broad signals in the range 149.5–115.4 ppm ascribed to aromatic carbon atoms and one signal at 174.9 ppm belonging to carboxylate groups. No signals attributed to DMF molecules are observed, and the whole spectrum is consistent with that reported by Stock and co-workers.[38] In the case of DRIFT spectra, three sharp bands centered at 3680, 3500, and 3390 cm^{-1} and a broad band centered between 3000 and 2500 cm^{-1} can be observed belonging to bridging OH and pending NH_2 groups.

4.2. Textural and Morphological Properties. Table 2 collects the most relevant textural properties of the synthesized (amino)-MIL-53(Al) materials, as inferred from N_2 adsorption/desorption isotherms at 77.4 K, while Figure 1 plots the corresponding isotherms. The measured micropore volumes (t-plot) lay in the range 0.43–0.51 cm^3/g with BET surface areas of 1000–1100 m^2/g. These data fall into the range of previous works on pure MIL-53(Al)[28] and MIL-53(Al)-NH_2.[38]

For samples A–D, typical type I and fully reversible adsorption isotherms (i.e., absence of detectable hysteresis loops) are observed, suggesting the absence of guest-induced structural transformations upon N_2 adsorption. In good keeping with the adsorption pattern of zeolites, these materials show a sharp adsorption trend at low N_2 pressures, the first adsorption points being measured for relative pressures $<10^{-5}$. Nevertheless, as formerly pointed out by Stock and co-

dx.doi.org/10.1021/jp2117856 | J. Phys. Chem. C 2012, 116, 9507–9516

Table 2. Composition and Adsorption Data of (Amino)-MIL-53(Al) Samples and List of Relevant Energies and Breathing Pressures for CO_2 Adsorption/Desorption

							first transition (lp1 → np)			second transition (np → lp2)		
sample	%abdc theoretical	%abdc measured[a]	V_{micro}[b] (cm^3/g)	S_{BET}[b] (m^2/g)	H[d] (mmol·g^{-1}·kPa^{-1})	$\Delta G°$ (J/g)	$\Delta G_{ads\text{-}des,G1}$[a] (kJ/mol)	ΔF_1 (lp1 → np)[b] (kJ/mol)	$P_{G,I}$[a] (kPa)	$\Delta G_{ads\text{-}des,G2}$[a] (kJ/mol)	ΔF_2 (np → lp2)[b] (kJ/mol)	$P_{G,II}$[a] (kPa)
A	0	0	0.51	1041	0.27	−0.9	−1.4	0.4	15.0	−2.3	3.3	665
B	11.1	10 ± 2	0.48	1048	0.36	−2.0	−1.2	1.2	10.4	−3.3	2.8	740
C	20	18 ± 2	0.51	1090	0.44	−1.9	−1.2	0.6	11.8	−3.9	3.6	960
D	50	49 ± 2	0.46	1100	0.93	−1.7	−0.3	0.8	7.4	−3.5	5.6	1110
E	66.7	62 ± 5	0.50	1017	1.39	−2.2	−0.4	1.2	8.1	−3.5	6.8	1260
F	100	100	0.37	940[c]	1.96	−1.7	−3.4	1.6	29.6	−2.7	8.6	1770

[a]Measured by NMR. Values estimated from the thermodynamic isotherm representation (data in J/g of solid for $\Delta G°$ and kJ/mol of sorbate for $\Delta G_{ads\text{-}des}$). [b]Measured by N_2 adsorption at 77.4 K. Values estimated by fitting Tóth curves for each phase according to ref 43 (data in kJ/mol of solid). Standard deviation about 10%. [c]Calculations made from the desorption branch. [d]Henry constant for CO_2.

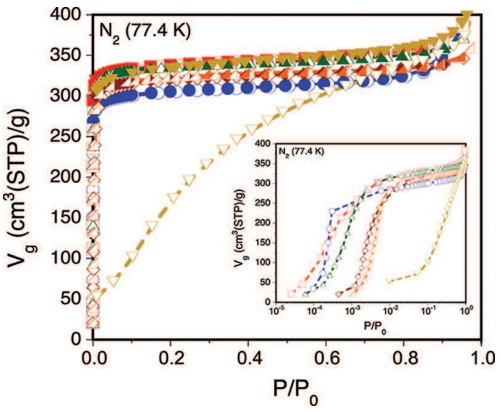

Figure 1. N_2 adsorption/desorption isotherms at 77.4 K of MIL-53(Al) (A), MIL-53(Al)-11.1%NH_2 (B), MIL-53(Al)-20%NH_2 (C), MIL-53(Al)-50%NH_2 (D), MIL-53(Al)-66.7%NH_2 (E), and MIL-53(Al)-NH_2 (F). Empty and filled symbols refer, respectively, to adsorption and desorption data. The curves are a guide to the eye.

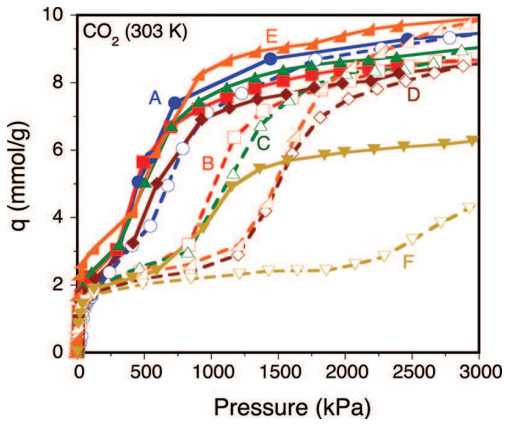

Figure 2. CO_2 adsorption/desorption isotherms at 303 K on MIL-53(Al) (A), MIL-53(Al)-11.1%NH_2 (B), MIL-53(Al)-20%NH_2 (C), MIL-53(Al)-50%NH_2 (D), MIL-53(Al)-66.7%NH_2 (E), and MIL-53(Al)-NH_2 (F). Empty and filled symbols refer, respectively, to adsorption and desorption data. The curves are a guide to the eye.

workers,[38] we can observe a broad hysteresis loop between the adsorption/desorption branches for pure MIL-53(Al)-NH_2. Sample MIL-53(Al)-66.7%NH_2 (E) also shows a hysteresis loop upon N_2 adsorption/desorption, though more moderate.

Figure SI3 (see Supporting Information) shows representative SEM micrographs of the MIL-53(Al) materials with different degrees of amine functionalization. Regardless of the amine loading, the materials show comparable particle sizes (about 0.5−1 μm).

4.3. CO_2 Adsorption/Desorption Behavior. Figure 2 plots the CO_2 isotherms at 303 K for the six (amino)-MIL-53(Al) materials considered in this study. As already reported for pure MIL-53(Al) (A) and MIL-53(Al)-NH_2 (F), the different samples display two distinct adsorption steps assigned, respectively, to lp1 → np and np → lp2 phase transitions at low and high CO_2 pressures.[31] Noteworthy, a plateau level of ca. 2 mmol/g is attained for the different samples, corresponding to ca. 0.5 mol of CO_2/mol of μOH.[41] This result suggests that all samples possess an equal number of adsorption sites for the np phase. The saturation loading shows a marked reduction from ca. 9 mmol/g for pure MIL-53(Al) (A) to 6 mmol/g for MIL-53(Al)-NH_2 (F), reflecting in the latter case a lower amount of sorption sites for the lp phase. At low pressures (<100 kPa), we can observe a linear correlation of Henry's constant with the abdc content (see Table 2).

Furthermore, the breathing pressure corresponding to the np → lp2 phase transition increases with the abdc content from a value of 590 kPa for pure MIL-53(Al) (A) to 1920 kPa for pure MIL-53(Al)-NH_2 (F). The higher stability of the np phase in the abcd rich samples is attributed to stronger hydrogen bonding involving NH_2 moieties and the $[AlO_6]_\infty$ groups, as recently reported by Kapteijn and co-workers,[31] but without formation of neither carbamates nor carbonates. As we advanced in our previous communication,[32] the higher breathing pressure range measured on the pure MIL-53(Al)-NH_2 (F) sample, 2200−3000 kPa, differs significantly from the value of 1300−2000 kPa reported by Couck et al.[27] An explanation for such a difference might arise from the different crystallite sizes originating from different synthesis recipes.

This increased interaction can also be argued to explain the different unit cell expansion behavior upon dehydration for pure MIL-53(Al) and MIL-53(Al)-NH_2 samples. As a matter of fact, pure MIL-53(Al) shows a sudden expansion of the unit cell upon dehydration due to the removal of hydrogen bonds inside the structure (see Figure 2), whereas pure MIL-53(Al)-NH_2 does not show a unit cell opening, since hydrogen bonding already occurs in the framework.

4.4. Thermodynamic Representations for N_2 Adsorption and CO_2 Adsorption/Desorption Isotherms. Figure 3 plots some representative thermodynamic isotherm representa-

dx.doi.org/10.1021/jp2117856 | J. Phys. Chem. C 2012, 116, 9507−9516

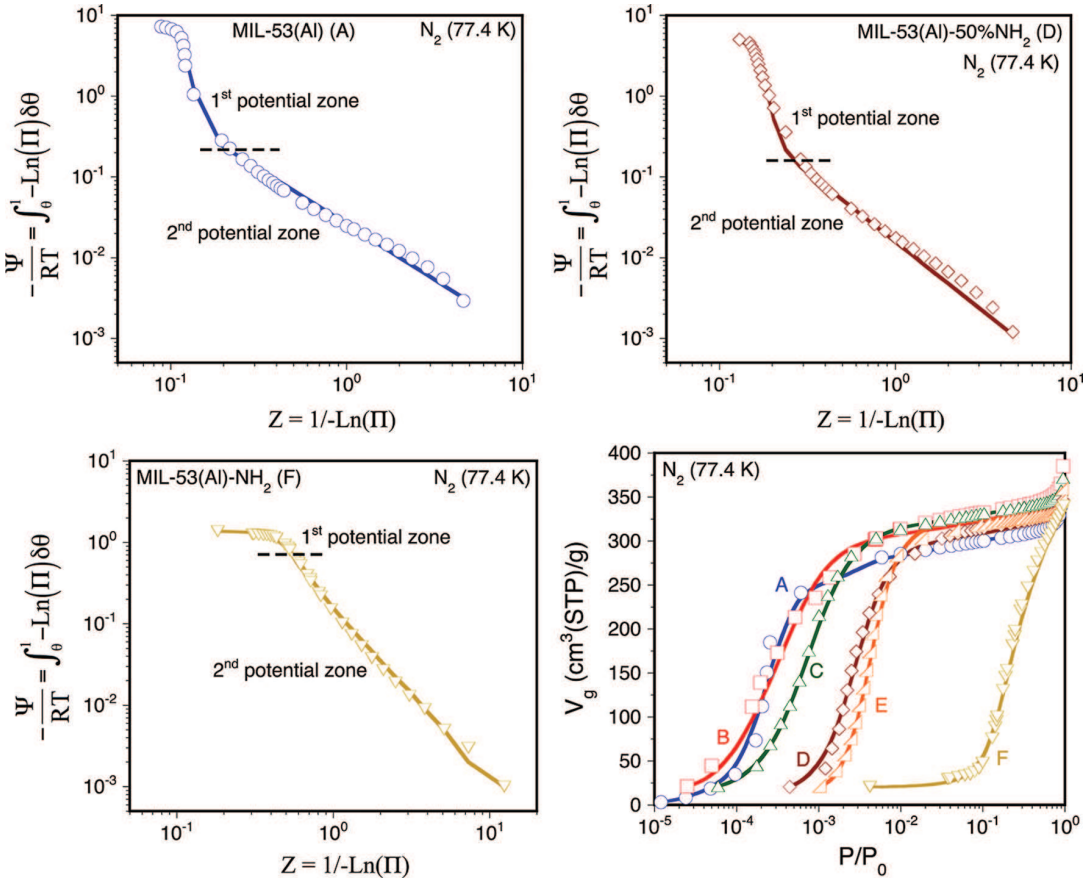

Figure 3. Thermodynamic isotherm representations of N_2 adsorption at 77.4 K on MIL-53(Al) (A), MIL-53(Al)-50%NH_2 (D), and MIL-53(Al)-NH_2 (F) and reconstructured isotherms (down, right) for samples A–F.

Table 3. Fitted Parameters of the Thermodynamic Isotherm for N_2 Adsorption/Desorption at 77.4 K on (Amino)-MIL-53(Al)

			first zone		second zone	
n	branch	$G°$	m_1	$Z_1 \times 10^2$	m_2	$Z_2 \times 10^2$
0	ads/des	7.26	13 ± 4	11.9 ± 0.1	1.38 ± 0.04	2 ± 1
11.1	ads/des	6.76	13.5 ± 0.4	12.0 ± 0.1	1.53 ± 0.04	2.1 ± 0.1
20	ads/des	6.25	13.5 ± 0.1	13.6 ± 0.1	1.71 ± 0.02	2.9 ± 0.4
50	ads/des	5.01	14.0 ± 0.2	16.8 ± 0.1	1.72 ± 0.05	3.6 ± 0.3
66.7	ads	4.79	17.6 ± 0.1	18.1 ± 1	1.49 ± 0.01	2.0 ± 0.1
100	ads	1.37	6.40 ± 0.2	52.0 ± 0.2	2.11 ± 0.05	36 ± 2

tions for N_2 adsorption at 77.4 K on samples MIL-53(Al) (A), MIL-53(Al)-50%NH_2 (D), and MIL-53(Al)-NH_2 (F), as well as the corresponding reconstructed isotherms by numerical integration of eq 3. Table 3 lists the set of fitted parameters to eq 1. The thermodynamic isotherm can be well described by eq 1 but with only one term in the denominator, as only one step in the isotherms is observed.

Figure 4 plots the evolution of the slope of the adsorption curves, $\delta V_g/\delta\Pi$, against the relative pressure for the different (amino)-MIL-53(Al) materials prepared in this study. The experimental slopes can be successfully reproduced and resolved using eq 6. Materials A–E show a defined Henry's linear region at low pressure (constant slope), while the simulated trend for the pure MIL-53-NH_2 sample (F) shows a nonlinear region at pressures $<10^{-4}$.

In a similar way, Figure 5 plots some representative thermodynamic isotherm representations for CO_2 adsorption/desorption at 303 K on samples MIL-53(Al) (A), MIL-53(Al)-50%NH_2 (D), and MIL-53(Al)-NH_2 (F), as well as the corresponding reconstructed isotherms by numerical integration of eq 3. Table 4 lists the set of fitted parameters to eq 1. Unlike N_2 adsorption, the thermodynamic isotherms for CO_2 adsorption/desorption can be well described by eq 1 including two terms in the denominator, as two steps in the isotherm are observed. Moreover, for the complete A–F series, the materials show a defined Henry's linear region at low pressures (see values listed in Table 2).

5. DISCUSSION

5.1. General Trends of Fitted Parameters as a Function of the Degree of Amine Functionalization. The data listed in Tables 2 and 3 suggest a correlation between the energy heterogeneity and affinity parameters for N_2 adsorption at 77.4 K as a function of the degree of amine

dx.doi.org/10.1021/jp2117856 | J. Phys. Chem. C 2012, 116, 9507–9516

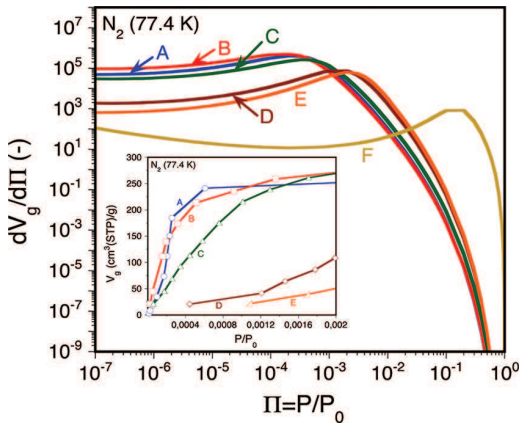

Figure 4. Evolution of the slope of the N_2 isotherms at 77.4 K plotted in Figure 5 for the different (amino)-MIL-53(Al) materials obtained by fitting of eq 3 as a function of the relative pressure.

functionalization in the MIL-53(Al) framework. This correlation is more remarkable for the first potential zone. Indeed, the m_1 parameter shows a marked reduction for the pure MIL-53(Al)-NH_2 sample compared to the bare and partially aminated counterparts, this result being accompanied by an increase of Z_1 (or k_1) parameter and a reduction of $G°$. This observation can be linked to a displacement of the adsorption curve to higher pressures as the degree of amine functionalization increases. A similar evolution pattern can be argued for the set of parameters m_2 and Z_2, the second potential zone being also displaced to higher pressures for the pure MIL-53(Al)-NH_2 sample.

CO_2 adsorption on the different amine-functionalized MIL-53(Al) samples shows, within the limits of the experimental error, invariable m_1 and Z_1 parameters corresponding to the first potential zone. The second potential zone becomes larger with the degree of amine functionalization, with m_2 and Z_2 parameters showing, respectively, a negative and positive increase. This combination of parameters makes the second potential zone evolve to larger pressures with the amount of amine groups in the MIL-53(Al) framework. Finally, the third and fourth potential zones accounting for the np → lp2 phase transition show a combined increase of the (m_3, Z_3) and (m_4, Z_4) couples. These trends suggest a more homogeneous CO_2 adsorption pattern in the MIL-53(Al) solid with a higher degree of amine functionalization, probably due to more energetically similar metastates between the two limiting phases. However, a possible effect of the amine loading on the particle size distribution, making them narrower at higher loadings, cannot be ruled out.

Similar trends are observed for the (m_3, Z_3) and (m_4, Z_4) couples of parameters in the case of CO_2 desorption. The first zone is characterized by m_1 parameters showing a marked decrease with the amine loading with a slight increase of Z_1 parameter. We link this latter trend to the presence of a higher level of energetically different metastates between the lp1 and np phases during CO_2 desorption. Finally, the fitted parameters for the second potential zone suggest a decrease of Z_2 parameter, especially for the pure MIL-53(Al)-NH_2 sample.

5.2. Absence of Henry's Region for N_2 Adsorption in Pure MIL-53(Al)-NH_2. The N_2 sorption pattern at 77.4 K for MIL-53(Al)-66.7%NH_2 (E) and pure MIL-53(Al)-NH_2 (F) shows the presence of hysteresis loops that spread to the low-pressure region, differing from the Langmuir-type trend found for A−D samples. This irreversibility can be attributed to a partial breathing of the samples upon guest accommodation. These hysteresis loops provide evidence of energy heterogeneity of sorption centers in these frameworks due to structural modification upon adsorption.

More insight about the energy heterogeneity of the different (amino)-MIL53(Al) materials can be gained by means of our thermodynamic isotherm formulation (see Figure 3 and Table 3). For all the materials, two different potential trends can be clearly distinguished, matching the general qualitative behavior observed for zeolites and "rigid" MOF-5 and CAU-1.[35] Both potential trends can be characterized by two m slope values (i.e., m_1 and m_2) in such a way that $m_1 > m_2$, suggesting a different pore filling pattern at the early stage of adsorption and at high loadings. The series of A−E samples show m_1 values slightly lower than those measured on NaY and HZSM-5 zeolites[37] but keeping consistent with what is expected for a material with relatively homogeneous adsorption strengths. In contrast, in the case of pure MIL-53(Al)-NH_2 (F), a much lower value for parameter m_1 has been measured ($m_1 < 7$). This observation can be attributed to a more flexible structure of the latter material in the presence of adsorbed N_2 at cryogenic temperatures.

As we advanced in a previous study,[36] one interesting characteristic of Figure 4 is the absence of a linear trend typical of Henry's region at low pressures for the pure MIL-53(Al)-NH_2 (F) sample. In this case, eq 6 predicts a monotonous quasi-linear increase of the slope for relative pressures $<10^{-6}$. Note that this pressure value is usually considered as a threshold value for the beginning of Henry's (linear) region in zeolites. We attribute this unexpected observation to the sorbate-induced structural deformation on these materials, providing higher energy heterogeneity than for A−E samples. We have already demonstrated in a previous publication[42] that linear trends in Henry's region (constant slope) are only possible as long as $m_1 > 12$ irrespective of the k_1 values, as is usually the case encountered in zeolites for N_2 and Ar adsorption at cryogenic temperatures.

5.3. Phase Transition Energies for the (Amino)-MIL-53(Al)/CO_2 System. The lp1 → np and np → lp2 phase transitions can be characterized by plotting the free energy difference between the adsorption and desorption branches as a function of pressure (i.e., $\Delta G_{ads\text{-}des} = \Delta G_{des} - \Delta G_{ads} < 0$), as computed directly from the thermodynamic isotherm representations (see Figure 5). A graph can then be obtained showing two characteristic peaks belonging to each phase transition (see Figure 6). The peak energies correspond to the integral free energy difference of the sorbate at the phase transition, $\Delta G_{ads\text{-}des,G}$. Table 2 lists the $\Delta G_{ads\text{-}des,G}$ values computed for the different solids. The second peak obtained at higher pressures shows a clear translation to higher values with the degree of the amine functionalization of the MIL-53(Al) framework, suggesting higher phase transition energies.

In addition to the $\Delta G_{ads\text{-}des,G}$ and $\Delta G°$ energies estimated directly from the thermodynamic isotherm representations, a free energy accounting for the sorbate-free phase transition of the bare solid, ΔF_S(np → lp), can be estimated using the methodology recently proposed by Boutin and co-workers.[41,43,44] The estimation of the free energy ascribed to the solid phase transition at zero sorbate loading, ΔF_S(np → lp), needs to establish isotherms describing the intrinsic adsorption behavior of the np and lp phases. Assuming that the two phases

dx.doi.org/10.1021/jp2117856 | J. Phys. Chem. C 2012, 116, 9507−9516

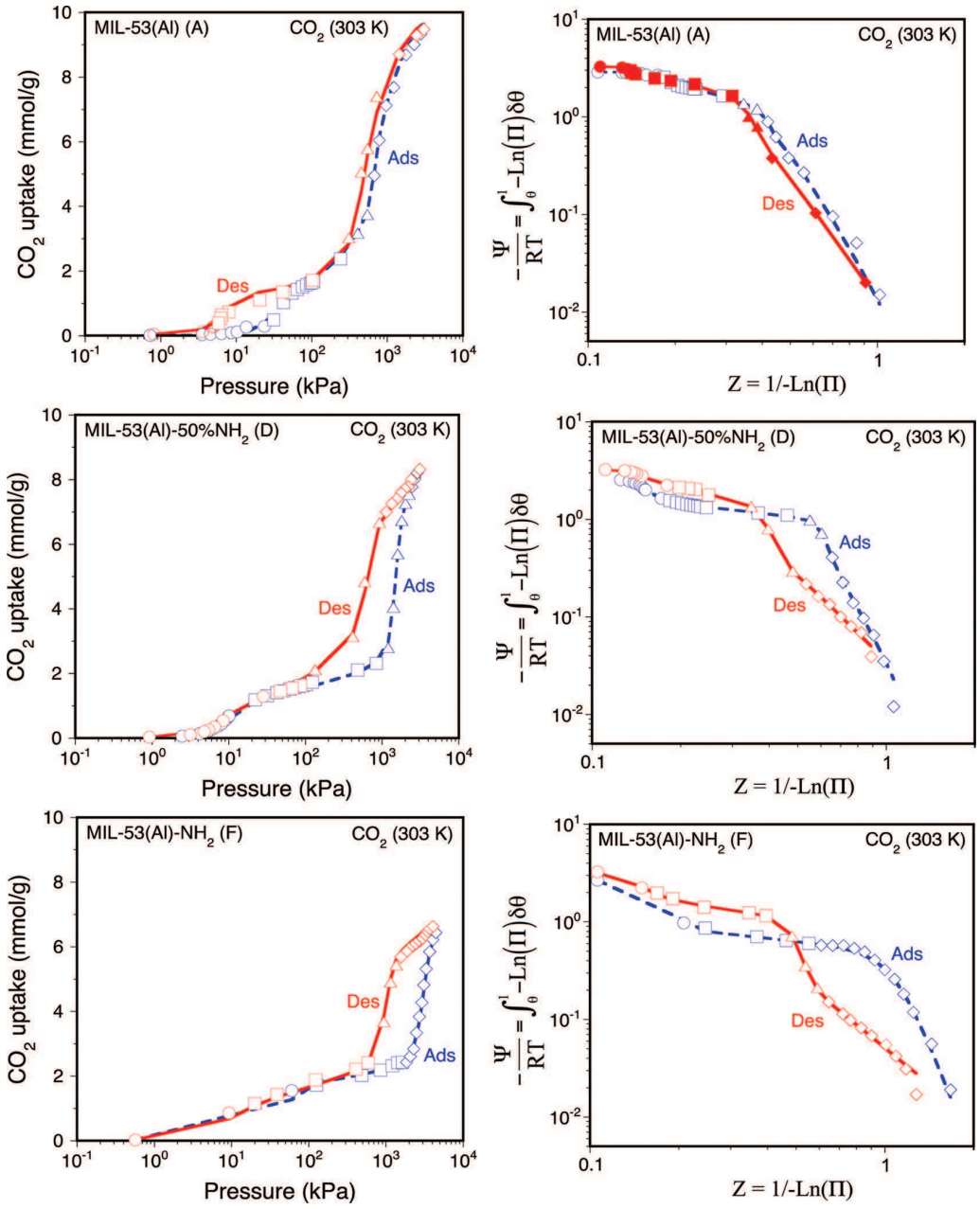

Figure 5. On the right, thermodynamic isotherm representations of CO_2 adsorption at 303 K on MIL-53(Al) (A), MIL-53(Al)-50%NH_2 (D), and MIL-53(Al)-NH_2 (F); on the left, experimental and reconstructured isotherms. The symbols ○, □, △, and ◇ refer, respectively, to the first, second, third, and fouth potential zones as defined by eq 1.

are at thermodynamic equilibrium at the breathing pressure (point G), this energy can be estimated as a difference of surface potentials for CO_2 adsorbed in each phase at this point[43]

$$\begin{aligned}\Delta F_S(\mathrm{np} \rightarrow \mathrm{lp2}) &\approx \Delta G_S(\mathrm{np} \rightarrow \mathrm{lp2}) \\ &= -[\Phi_{\mathrm{lp2}}(\Pi_G) - \Phi_{\mathrm{np}}(\Pi_G)] = \\ &= RT[(\int_0^{\Pi_G} q\delta[-\ln(\Pi)])_{\mathrm{lp2}} - (\int_0^{\Pi_G} q\delta[-\ln(\Pi)])_{\mathrm{np}}] \end{aligned} \quad (7)$$

The integrals in eq 7 require the fitting of an isotherm curve for each phase starting from the available experimental data. Here, we have chosen the Tóth and the Freundlich models for inferring the isotherms corresponding, respectively, to the lp and np phases, that is

Tóth(lp1+2):

$$q = q_M \frac{Kp}{[1 + (Kp)^n]^{1/n}} \quad (8)$$

Freundlich(np):

$$q = Kp^n \quad (9)$$

The relevant parameters in both isotherm models (K, n) have been fitted for the A−F samples using a least-squares

dx.doi.org/10.1021/jp2117856 | J. Phys. Chem. C 2012, 116, 9507−9516

Table 4. Fitted Parameters of the Thermodynamic Isotherm for CO_2 Adsorption/Desorption at 303 K on (Amino)-MIL-53(Al)

			first zone		second zone		third zone		fourth zone	
N	branch	G°	m_1	$Z_1 \times 10^2$	m_2	$Z_2 \times 10^2$	m_3	$Z_3 \times 10^2$	m_4	$Z_4 \times 10^2$
0	ads	2.87	19 ± 3	19.3 ± 0.1	2.05 ± 0.03	33.1 ± 0.1	44 ± 23	41.7 ± 0.4	5.7 ± 0.6	39 ± 1
	des	3.26	45 ± 6	14.4 ± 0.1	1.9 ± 0.1	32.1 ± 0.9	19 ± 3	35 ± 2	4.34 ± 0.03	28.6 ± 0.1
11.1	ads	2.77	19 ± 1	17.6 ± 0.1	1.46 ± 0.03	23 ± 7	65 ± 13	52 ± 3	5.8 ± 0.4	44 ± 1
	des	3.56	40 ± 8	14.6 ± 0.1	2.6 ± 0.2	25.5 ± 0.5	20 ± 6	34.7 ± 0.9	4.1 ± 0.1	30.6 ± 0.2
20	ads	2.69	19 ± 1	17.4 ± 0.1	0.86 ± 0.02	27 ± 9	24 ± 3	52.0 ± 0.4	4.3 ± 0.6	38 ± 3
	des	3.46	26 ± 4	15.2 ± 0.1	1.9 ± 0.2	27.9 ± 0.9	54 ± 5	37 ± 4	6.0 ± 0.1	30 ± 10
50	ads	2.54	16 ± 1	16.1 ± 0.1	0.65 ± 0.03	28.6 ± 0.5	28 ± 4	60.0 ± 0.4	6.2 ± 0.3	50 ± 1
	des	3.23	18 ± 3	15.4 ± 0.2	1.8 ± 0.1	28.9 ± 0.6	59 ± 6	39 ± 3	3.2 ± 0.1	25.8 ± 0.6
66.7	ads	2.44	19 ± 1	16.4 ± 0.1	0.69 ± 0.02	32.7 ± 0.4	39 ± 11	60.4 ± 0.4	8.2 ± 0.7	58 ± 1
	des	3.32	27 ± 14	15.1 ± 0.6	2.7 ± 0.3	27.1 ± 0.8	45 ± 9	40 ± 3	6.3 ± 0.2	42.9 ± 0.6
100	ads	2.67	19 ± 1	19.0 ± 0.1	0.44 ± 0.04	34 ± 0.8			7.9 ± 0.2	88.1 ± 0.6
	des	3.32	14 ± 1	15.2 ± 0.1	0.80 ± 0.08	17.1 ± 0.9	20 ± 1	47.4 ± 0.2	2.6 ± 0.1	21 ± 1

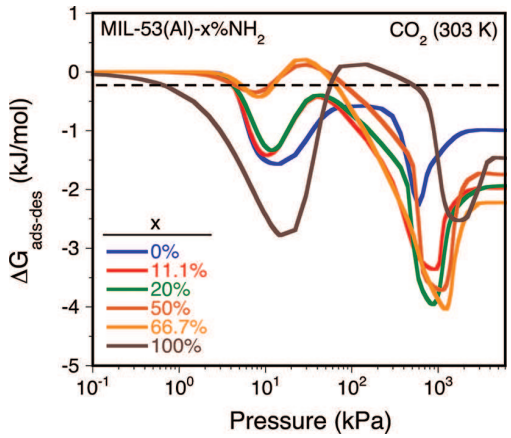

Figure 6. Evolution of the free energy difference between the CO_2 adsorption and desorption branches as a function of pressure for the different (amino)-MIL-53(Al) materials prepared in this study.

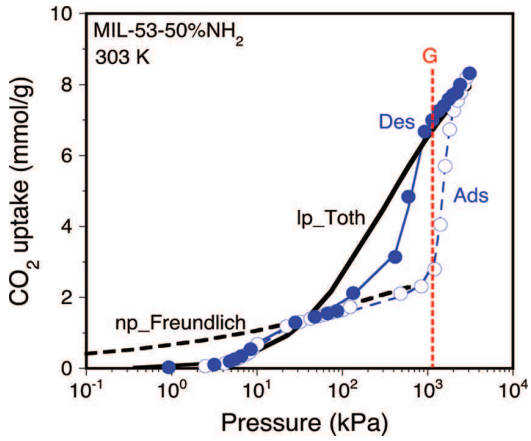

Figure 7. Example of fitting of Tóth (eq 9) and Freundlich (eq 10) isotherm models for the lp(1 + 2) and np phases for the MIL-53(Al)-50%NH_2 sample. The label "G" refers to the np → lp2 breathing pressure.

nonlinear optimization method based on the Levenberg–Marquardt algorithm by comparison of predicted and experimental CO_2 loadings belonging, respectively, to the (amino)-MIL-53(Al)_lp(1 + 2) and (amino)-MIL-53(Al)_np phases. Parameter q_M has been kept constant at the corresponding plateau indicated in Figure 2. As an example, Figure 7 shows the fitted isotherms for the MIL-53(Al)-50% NH_2 (D) sample. The adjusted parameters, as well as the corresponding fittings for the other samples, can be found in the Supporting Information (Table SI1).

Table 2 lists the maximum energy differences between the adsorption and desorption curves at point G (the minima in Figure 6), the estimated transition energies, and the total free energy dissipated in a complete adsorption/desorption cycle for the different (amino)-MIL-53(Al) samples. This latter energy can be computed using the expression

$$\Delta G^\circ = \oint [-\ln(\Pi)]\delta\theta = G^\circ_{ads} - G^\circ_{des} \quad (10)$$

As can be inferred from Table 2, the phase transition energy for the np → lp2 transition is dramatically promoted with the degree of amine substitution in the MIL-53(Al) framework, evolving for a value about 3.2 kJ/mol for the pure MIL-53(Al) (A) to 8.6 kJ/mol for pure MIL-53(Al)-NH_2 (F). This higher energy reflects the higher stability of the np phase compared to the lp2 phase by incorporating amine groups in the MIL-53(Al) framework, matching the trends provided by Kapteijn et al.[31] in a recent theoretical (DFT) study.

6. CONCLUSIONS

We have shown in this study that the complex breathing pattern of (amino)-MIL-53(Al) with different degrees of amine functionalization upon N_2 and CO_2 adsorption/desorption can be conveniently described and parametrized through the use of thermodynamic isotherm representations. The energy heterogeneity and affinity parameters for N_2 and CO_2 adsorption/desorption can be successfully correlated to the degree of amine substitution in the MIL-53(Al) framework. The (m_3, Z_3) and (m_4, Z_4) couples provide direct information about the np → lp2 phase transition zone.

Moreover, this approach provides an easy measure of the energy dissipated during a complete adsorption/desorption cycle, as well as peak minima for the integral free energy difference of the sorbate centered at the phase transition pressures. The np → lp2 phase transition energy is dramatically promoted with the degree of amine substitution (from 3.3 to 8.6 kJ/mol, respectively, for pure MIL-53(Al) and MIL-53(Al)-NH_2 samples), reflecting a higher stability of the np phase.

dx.doi.org/10.1021/jp2117856 | J. Phys. Chem. C 2012, 116, 9507–9516

■ ASSOCIATED CONTENT

Supporting Information

Figures showing the synthesis of MIL-53(Al), PXRD patterns and SEM images of MIL-53(Al)-NH_2 materials and a table showing fitted parameters for isotherms. This material is available free of charge via the Internet at http://pubs.acs.org.

■ AUTHOR INFORMATION

Corresponding Author

*Phone: +33 (0) 472445368. Fax: +33 (0) 472445399. E-mail: marc.pera-titus@ircelyon.univ-lyon1.fr.

Notes

The authors declare no competing financial interest.

■ ACKNOWLEDGMENTS

The authors would like to express their gratitude to the European Comission (FP7-NMP NANOMOF program) for funding.

■ GLOSSARY

G° Integral free energy of the sorbate at P° [-]
H Henry's constant, eq 6 [-]
k Parameter in eqs 1, 4, and 5 [-]
m Exponent in eqs 1, 4, and 5 [-]
P Pressure [Pa]
P° Saturation pressure [Pa]
q_M Saturation loading [mol/kg]
R Gas constant [8.314 $J \cdot mol^{-1} \cdot K^{-1}$]
T Temperature [K]
Z $1/-\ln(\Pi)$ [-]

Greek Symbols

Φ Surface potential of the sorbate [J/kg of solid]
λ kZ^m [-]
μ Chemical potential [J/mol]
Π P/P^o [-]
θ Surface coverage [-]
Ψ Integral free energy relative to saturation [J/kg]

Acronyms

DA Dubinin–Astakhov isotherm
lp Large-pore phase
np Narrow-pore phase

■ REFERENCES

(1) Kitagawa, S.; Uemura, K. *Chem. Soc. Rev.* **2005**, *34*, 109–119.
(2) Férey, G. *Chem. Soc. Rev.* **2008**, *37*, 191–214.
(3) Horike, S.; Shimomura, S.; Kitagawa, S. *Nat. Chem.* **2009**, *1*, 695–704.
(4) Finsy, V.; Ma, L.; Alaerts, L.; De Vos, D. E.; Baron, G. V.; Denayer, J. F. M. *Microporous Mesoporous Mater.* **2009**, *120*, 221–227.
(5) Finsy, V.; Kirschhock, C. E. A.; Vedts, G.; Maes, M.; Alaerts, L.; De Vos, D. E.; Baron, G. V.; Denayer, J. F. M. *Chem.—Eur. J.* **2009**, *15*, 7724–7731.
(6) Farrusseng, D.; Aguado, S.; Pinel, C. *Angew. Chem., Int Ed.* **2009**, *48*, 7502–7513.
(7) Allendorf, M.; Houk, R.; Andruszkiewicz, L.; Talin, A.; Pikarsky, J.; Choudhury, A.; Gall, K.; Hesketh, P. *J. Am. Chem. Soc.* **2008**, *130*, 14404–14405.
(8) Fairen-Jimenez, D.; Moggach, S. A.; Wharmby, M. T.; Wright, P. A.; Parsons, S.; Düren, T. *J. Am. Chem. Soc.* **2011**, *133*, 8900–8902.
(9) Bureekaew, S.; Shimomura, S.; Kitagawa, S. *Sci. Technol. Adv. Mater.* **2008**, *9*, 1–12.
(10) Férey, G.; Serre, C. *Chem. Soc. Rev.* **2009**, *38*, 1380–1399.
(11) Serre, C.; Millange, F.; Thouvenot, C.; Nogues, M.; Marsolier, G. R.; Louër, D.; Férey, G. *J. Am. Chem. Soc.* **2002**, *124*, 13519–13526.
(12) Millange, F.; Serre, C.; Férey, G. *Chem. Commun.* **2002**, 822–823.
(13) Walker, A. M.; Civalleri, B.; Slater, B.; Mellot-Draznieks, C.; Cora, F.; Zicovich-Wilson, C. M.; Roman-Perez, G.; Soler, J. M.; Gale, J. D. *Angew. Chem., Int. Ed.* **2010**, *49*, 7501–7503.
(14) Boutin, A.; Coudert, F. -X.; Springuel-Huet, M. -A.; Neimark, A. V.; Férey, G.; Fuchs, A. H. *J. Phys. Chem. C* **2010**, *114*, 22237–22244.
(15) Millange, F.; Guillou, N.; Medina, M. E.; Férey, G.; Carlin-Sinclair, A.; Golden, K. M.; Walton, R. I. *Chem. Mater.* **2010**, *22*, 4237–4245.
(16) Millange, F.; Guillou, N.; Walton, R. I.; Greneche, J.; Margiolaki, I.; Férey, G. *Chem. Commun.* **2008**, 4732–4734.
(17) Volkringer, C.; Loiseau, T.; Guillou, N.; Ferey, G.; Elkaim, E.; Vimont, A. *Dalton Trans.* **2009**, 2241–2249.
(18) Serre, C.; Bourrelly, S.; Vimont, A.; Ramsahye, N. A.; Maurin, G.; Llewellyn, P. L.; Daturi, M.; Filinchuk, Y.; Leynaud, O.; Barnes, P.; Férey, G. *Adv. Mater.* **2007**, *19*, 2246–2251.
(19) Llewellyn, P. L.; Bourrelly, S.; Serre, C.; Filinchuk, Y.; Férey, G. *Angew. Chem.* **2006**, *118*, 7915–7918.
(20) Bourrelly, S.; Llewellyn, P. L.; Serre, C.; Millange, F.; Loiseau, T.; Férey, G. *J. Am. Chem. Soc.* **2005**, *127*, 13519–13521.
(21) Ramsahye, N. A.; Maurin, G.; Bourrelly, S.; Llewellyn, P. L.; Serre, C.; Loiseau, T.; Devic, T.; Férey, G. *J. Phys. Chem. C* **2007**, *112*, 514–520.
(22) Trung, T. K.; Trens, P.; Tanchoux, N.; Bourrelly, S.; Llewellyn, P. L.; Loera-Serna, S.; Serre, C.; Loiseau, T.; Fajula, F.; Férey, G. *J. Am. Chem. Soc.* **2008**, *130*, 16926–16932.
(23) Llewellyn, P. L.; Horcajada, P.; Maurin, G.; Devic, T.; Rosenbach, N.; Bourrelly, S.; Serre, C.; Vincent, D.; Loera-Serna, S.; Filinchuk, Y.; Férey, G. *J. Am. Chem. Soc.* **2009**, *131*, 13002–13008.
(24) Férey, G.; Serre, C. *Chem. Soc. Rev.* **2009**, *38*, 1380–1399.
(25) Walton, K. S.; Millward, A. R.; Dubbeldam, D.; Frost, H.; Low, J. J.; Yaghi, O. M.; Snurr, R. Q. *J. Am. Chem. Soc.* **2008**, *130*, 406–407.
(26) Fukushima, T.; Horike, S.; Inubushi, Y.; Nakagawa, K.; Kubota, Y.; Takata, M.; Kitagawa, S. *Angew. Chem., Int. Ed.* **2010**, *49*, 4820–4824.
(27) Couck, S.; Denayer, J. F. M.; Baron, G. V.; Remy, T.; Gascon, J.; Kapteijn, F. *J. Am. Chem. Soc.* **2009**, *131*, 6326–6327.
(28) Loiseau, T.; Serre, C.; Huguenard, C.; Fink, G.; Taulelle, F.; Henry, M.; Bataille, T.; Férey, G. *Chem.—Eur. J.* **2004**, *10*, 1373–1382.
(29) Marx, S.; Kleist, W.; Huang, J.; Maciejewski, M.; Baiker, A. *Dalton Trans.* **2010**, *39*, 3795–3798.
(30) Torrisi, A.; Mellot-Draznieks, C.; Bell, R. G. *J. Chem. Phys.* **2010**, *132*, 044705–044717.
(31) Stavitski, E.; Pidko, E. A.; Couck, S.; Remy, T.; Hensen, E. J. M.; Weckhuysen, B. M.; Denayer, J. F. M.; Gascon, J.; Kapteijn, F. *Langmuir* **2011**, *27*, 3970–3976.
(32) Lescouet, T.; Kockrick, E.; Bergeret, G.; Pera-Titus, M.; Farrusseng, D. *Dalton Trans.* **2011**, *40*, 11359–11361.
(33) Walton, K. S.; Snurr, R. Q. *J. Am. Chem. Soc.* **2007**, *129*, 8552–8556.
(34) Bae, Y. -S.; Özgür Yazaydin, A.; Snurr, R. Q. *Langmuir* **2010**, *26*, 5475–5483.
(35) Pera-Titus, M.; Savonnet, M.; Farrusseng, D. *J. Phys. Chem. C* **2010**, *114*, 17665–17674.
(36) Aguado, S.; Bergeret, G.; Pera-Titus, M.; Bats, N.; Farrusseng, D. *New J. Chem.* **2011**, *35*, 546–550.
(37) Lescouet, T.; Kockrick, E.; Bergeret, G.; Pera-Titus, M.; Aguado, S.; Farrusseng, D. *J. Mater. Chem.* **2012**, in press.
(38) Ahnfeldt, T.; Gunzelmann, D.; Loiseau, T.; Hirsemann, D.; Senker, J.; Férey, G.; Stock, N. *Inorg. Chem.* **2009**, *48*, 3057–3064.
(39) Pera-Titus, M. *J. Phys. Chem. C* **2011**, *115*, 3346–3357.
(40) Pera-Titus, M. *J. Colloid Interface Sci.* **2010**, *345*, 410–416.
(41) Boutin, A.; Couck, S.; Coudert, F.-X.; Serra-Crespo, P.; Gascon, J.; Kapteijn, F.; Fuchs, A. H.; Denayer, J. F. M. *Microporous Mesoporous Mater.* **2010**, *140*, 108–113.

(42) Pera-Titus, M.; Llorens, J. *Appl. Surf. Sci.* **2010**, *256*, 5305−5310.
(43) Coudert, F. -X.; Jeffroy, M.; Fuchs, A. H.; Boutin, A.; Mellot-Draznieks, C. *J. Am. Chem. Soc.* **2008**, *130*, 14294−14302.
(44) Boutin, A.; Coudert, F. -X.; Springuel-Huet, M. -A.; Neimark, A. V.; Férey, G.; Fuchs, A. H. *J. Phys. Chem. C* **2010**, *114*, 22237−22244.

DOI: 10.1002/cctc.201200288

The Origin of the Activity of Amine-Functionalized Metal–Organic Frameworks in the Catalytic Synthesis of Cyclic Carbonates from Epoxide and CO_2

Tristan Lescouet,[a] Céline Chizallet,[b] and David Farrusseng*[a]

The conversion of carbon dioxide into bulk chemicals at lower energy cost is a scientific and technological challenge.[1,2]

Acid–base-pair catalysts are interesting for such applications because they can promote concerted reactions. The adsorption of CO_2 occurs on the basic sites to form activated species; then, the epoxide coordinates onto the neighboring acidic site and ring-opening occurs by nucleophilic attack of the activated species. One example of rationally designed acid–base catalysts is amine-functionalized mesoporous Ti(Al)-SBA-15.[3] Ratnasamy and co-workers reported a "volcanic plot" of the reaction rate as a function of amine basicity, in which secondary amines showed the optimum reactivity. They suggested that CO_2 is too-weakly activated on primary amines, whereas it is too-strongly adsorbed onto tertiary amines. Hence, moderate CO_2-adsorption onto amine-functionalized solid acids appears to provide good candidates as catalyst for this reaction.

It is generally acknowledged that metal–organic frameworks (MOFs) are appropriate materials for designing single-site acid–base catalysts.[4–6] In a spectroscopic study on MOFs, Gascon et al. showed the functionalization of MOF-5 by an amino substituent (2-amino-1,4-benzenedicarboxylate), also known as IRMOF-3. The amine group acted as an electron donor (Lewis base) on CO_2.[7] This "amino effect" on CO_2-adsorption has been experimentally observed on various MOFs and was later confirmed by ab initio calculations.[8–11] The concept of concerted reactions on acid–base MOFs has been reported by Baiker and co-workers in the synthesis of propylene carbonate with amine-containing mixed-linker MIL-53 (co-catalyzed by tetraalkylammonium halides).[12] A turnover frequency (TOF) of 400 h^{-1} was measured under solvent-free conditions. Another significant example is the activity of amine-functionalized UiO-66 in the cross-aldol reaction reported by De Vos and co-workers.[13]

Hence, we anticipated that the use of MOFs that contain acid–base pairs, such as a Brønsted acid MOF that is functionalized with NH_2, could lead to potential catalyst candidates for the synthesis of carbonate from CO_2.

Herein, we elucidate the role of the NH_2-functionalization of MIL-68(In)-NH_2[14] as a catalyst for the synthesis of styrene carbonate from styrene oxide and CO_2. Surprisingly, we show by using ab initio calculations and spectroscopic investigations that the modification of the electronic structure of the inorganic component by ligand-substitution has a much-larger impact on the activation of CO_2 than the amine substituents.

MIL-68(In) and MIL-68(In)-NH_2 were prepared by precipitation reactions of indium nitrate and terephthalic acid or aminoterephthalic acid in DMF.[15] X-ray diffraction, surface areas, DRIFT analysis, and the ^{1}H NMR spectra were in agreement with previous reports (see the Supporting Information). These results confirmed that the MOFs were empty of any organic solvent or occluded reactants.

MIL-68(In) and MIL-68(In)-NH_2 were tested in the synthesis of carbonate (Scheme 1). This evaluation was performed in a glass vial at 150 °C under CO_2 pressure (8 bar).

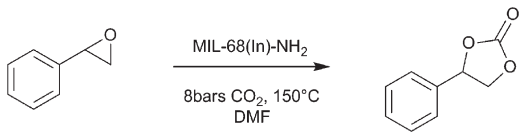

Scheme 1. Synthesis of styrene carbonate from styrene oxide.

The results are reported in Table 1 and compared with blank experiments that were conducted without the catalyst and tetramethylammonium bromide, which is a known active- and selective homogeneous catalyst.[16] The conversion of styrene oxide was clearly enhanced by NH_2-functionalisation: It in-

Table 1. Catalytic activity.

Catalyst	Conversion of styrene oxide[b] [%]	TOF[b] [h^{-1}]
blank	8	–
tetramethylammonium bromide	87	0.782
MIL-68 (In)[a]	42	0.544
MIL-68 (In)[a]	36	0.466
MIL-68(In)-NH_2[a]	74	1.059
MIL-68(In)-NH_2[a]	68	0.973
MIL-68(In)-NH_2[a]	70	1.002
MIL-68(In)-NH_2 (recycled)	53	0.758

[a] Independent catalytic tests; [b] conversion and TOF calculated after 8 h.

[a] *T. Lescouet, Dr. D. Farrusseng*
University of Lyon
Institut de Recherches sur la Catalyse et l'Environnement de Lyon (IRCELYON)
UMR 5256 CNRS, 2 Av. Albert Einstein
69626 Villeurbanne (France)
Fax: (+33) (0)4 72 33 53 99
E-mail: david.farrusseng@ircelyon.univ-lyon1.fr

[b] *Dr. C. Chizallet*
IFP Energies nouvelles
Rond-point de l'échangeur de Solaize, BP3
69360 Solaize (France)

Supporting information for this article is available on the WWW under http://dx.doi.org/10.1002/cctc.201200288.

creased from about 39(±3)% for MIL-68(In) to 71(±3)% for MIL-68(In)-NH_2.

MIL-68(In)-NH_2 was reused after Soxhlet extraction (CH_2Cl_2) in a second test; in this case, the conversion decreased from 74% to 53%. This slight decrease in activity could be explained by the reactant becoming stuck in the 1D channel of the MOF, even after the recycling process. Even though the XRD pattern of the material after the test was identical to that of the fresh material (see the Supporting Information, Figure S6), the BET surface area decreased significantly from 1100 to 720 $m^2 g^{-1}$. Analysis of the digested catalysts by ^1H NMR spectroscopy indicated a broad signal at $\delta = 7.3$ ppm, which corresponded to the aromatic protons of the reactant and product that remained in the pores (see the Supporting Information, Figure S7). From integration of the peaks, we estimated that one molecule was trapped by 10 linkers. We can assume that this entrapment blocks the access of the 1D channel to N_2, as reflected by the lower BET value.

Catalytic tests were performed in other high-boiling-point solvents (chlorobenzene and DMSO), which exhibited conversions below 5%. In addition, a slight conversion was obtained in DMF without a catalyst (blank test; Table 1). This result indicates that DMF plays a role in the reaction mechanism. We suspect that the products of DMF-degradation, such as dimethylamine, act as catalytic species.[17] However, no decomposition products were detected by NMR spectroscopy in the reaction mixture after the test.

Ab initio calculations were performed to evaluate the effect of amine-functionalization on the acid–base properties. Figure 1 shows the DFT-optimized structures of MIL-68(In)-NH_2, which were calculated by using a periodic plane-wave method, as implemented in VASP.[18] The exchange-correlation functional was treated within the generalized gradient approximation (GGA) that was parameterized by Perdew, Burke, and Ernzernhof.[19] Dispersion corrections were systematically included into the energies and forces, according to the DFT-D2 method reported by Grimme.[20] NH_2 groups were substituted on each linker, starting from MIL-68(In), and were arbitrarily placed so as to limit their interactions as much as possible. This class of MOFs is characterized by a 1D rod-shaped structure with channels of two sizes: large hexagonal channels (LC) and tight triangular channels (TC). The octahedral $InO_4(OH)_2$ units are connected together in a *trans* orientation of the hydroxy groups to form an infinite chain. DFT calculations suggest that the OH groups are tilted (out of the In–O–In plane).

The acidity of the octahedral $InO_4(OH)_2$ units was quantified by DFT calculations of the adsorption of basic probe molecules (CO, NH_3) on MIL-68(In) and MIL-68(In)-NH_2. With regards to CO, the traditional C adduct, –OH···CO, was modeled to account for the acidity of the proton, according to the usual assumption. Table 2 shows the corresponding adsorption energies. The sites that are located in the tight and large channels exhibit comparable adsorption energies for both probes, even if the adsorption is generally slightly more favorable in the tight channel, owing to enhanced van der Waals stabilization in the TCs. Moreover, following NH_2-functionalization of the framework, the adsorption is even slightly stronger; this result

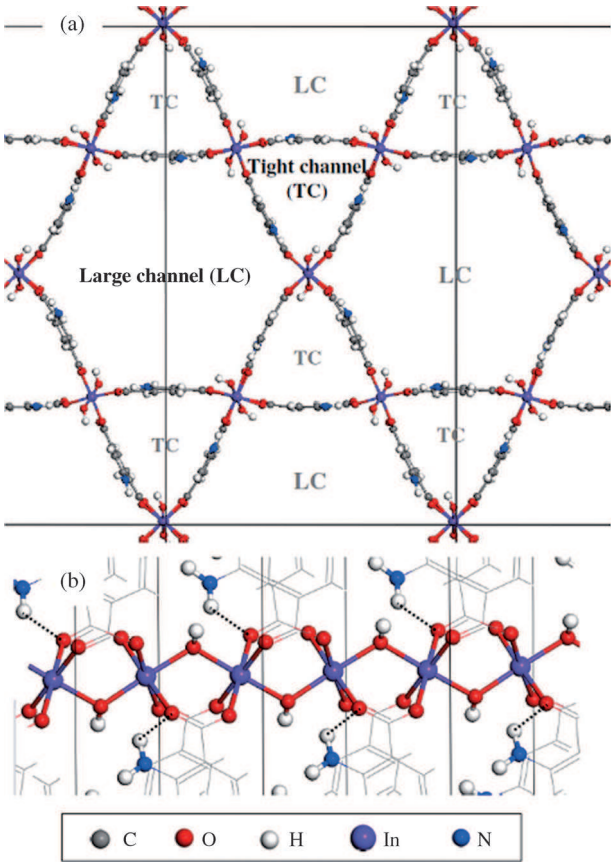

Figure 1. MIL-68(In)-NH_2: a) View of the lattice and the channels. b) View of the In chains; carbon atoms and the hydrogen atoms that are bonded to them are represented in grey line for the sake of clarity.

Table 2. Adsorption energies of CO and ammonia [kJ mol^{-1}] for MIL-68(In) and MIL-68(In)-NH_2, as evaluated by DFT calculations.

	MIL-68(In)	MIL-68(In)-NH_2
adsorbed molecule	large/tight channel	large/tight channel
CO	−22/−32	−28/−35
ammonia	−59/−67	−73/−78

can be tentatively assigned to the attractive effect of NH_2, which is likely to enhance the acidity of the proton. This enhancement is indicated by a slightly increased mean Bader charge on the protons of the OH groups after NH_2-functionalisation (+0.63e instead of +0.61e), even if the electrostatic charge of the proton is not the single parameter to rationalize its acidity.[21] Notably, for a given adsorption site (LC or TC), NH_2-functionalisation does not significantly affect the van der Waals contribution of the molecule/framework interactions.

Ammonia was not protonated in any case; however, the adsorption energies were significantly negative and were comparable to calculations that were performed on amorphous aluminosilicates (even after removal of the dispersion component, which was not included in previous reports).[22] The adsorption strength nevertheless remained more-favorable on zeolites.[23] These results confirm that MIL-68(In) shows mild Brønsted

acidity, which is slightly improved upon NH_2-functionalisation. This acidity is even higher than that on other carboxylate-based MOFs (MIL-53(Al) and IM-19).[24] In a later study, we showed that the bridging μ_2(OH) moieties in MIL-53 (Ga, Al) exhibit weak-to-moderate Brønsted acidity that can be correlated to the acidic mechanism of aromatic alkylation.[24]

It has already been reported that the substitution pattern on the linker can influence the electronic structure and/or -density of the inorganic backbone of the MOF and, thus, the catalytic properties that are associated with the acidic sites. For examples, Gascon et al. have reported the modification of the band-gap of various IRMOF solids by changing the substitution pattern on different linkers.[25] Garcia and co-workers have shown a similar effect on UiO-66, when substituted with NH_2, for the photocatalytic production of H_2.[26]

The interactions of CO_2 with MIL-68(In) and MIL-68(In)-NH_2 were investigated by CO_2-adsorption- and DRIFT measurements. CO_2-adsorption measurements were performed to identify the mode of CO_2-activation on MIL-68(In)-NH_2. MIL-68(In)-NH_2 had a higher affinity for CO_2-adsorption than its analogue with no amino groups (see the Supporting Information, Figure S5). Henry constants for CO_2 for MIL-68(In) and MIL-68(In)-NH_2 were 0.029 and 0.048 mmol g^{-1} kPa^{-1}, respectively, which gave a ratio of 1.69.

This enhancement in the Henry constant was in good agreement with molecular-modeling studies that were performed by other groups on MIL-53(Al)-NH_2.[9,11] In a similar fashion to MIL-68, MIL-53 possessed a rod-like structure with $AlO_4(\mu_2OH)_2$ units. DFT simulations showed that CO_2 were physisorbed on H bonds, mainly on the μOH bonds, and that carbamate species could not be formed whatever the pressure. On the other hand, the CO_2-adsorption enthalpies that were calculated by using the Grand Canonical Monte Carlo method at low coverage (at 0.01 bar) on MIL-53(Al) and MIL-53(Al)-NH_2 revealed a slightly higher heat of adsorption for the amine: −23.2 kJ mol^{-1} versus −27.5 kJ mol^{-1}.[11] Therefore, we conclude that CO_2 is weakly activated on MIL-68 without carbamate-formation for the amine-functionalized MIL-68(In)-NH_2. In addition, DRIFT analysis of the MIL-68(In)-NH_2 sample at 25 °C under a flow of CO_2 did not show any modification of the bands at 3500 and 3390 cm^{-1}, which corresponded to the symmetric and asymmetric stretching of the primary amine (Figure 2). This result confirms that no carbamate species were formed through the NH_2/CO_2 interactions.[9,27,28]

In addition, it has been reported that DMF may activate CO_2 and stabilize the carbonate intermediate by elongating the C–O bond, as observed by Yamada and co-workers.[29] This combined Brønsted acid/Lewis base co-catalyst has been shown to be highly efficient in the synthesis of carbonate.[12,30,31]

Herein, we have shown that the synthesis of cyclic carbonate from CO_2 and styrene oxide can be accomplished by using the intrinsic properties of MOFs in the presence of DMF. MIL-68 shows moderate Brønsted acidity, whereas CO_2 is not dissociated into carbamate on the NH_2 sites. This study shows that electronic effect prevails for substituted-MIL-68 catalysts. Surprisingly, amine-substitution increases the interactions between the MOF and the basic probe molecules, as calculated by using DFT. Hence, we have shown that the gain in catalytic activity arises from the enhanced Brønsted acidity, which originates from the substitution pattern of the linker. Simultaneously, DMF seems to act as a co-catalyst and activates the CO_2. We believe that this finding opens up new perspectives in the rational design of MOFs for catalysis by applying approaches that are used in the development of molecular catalysts.

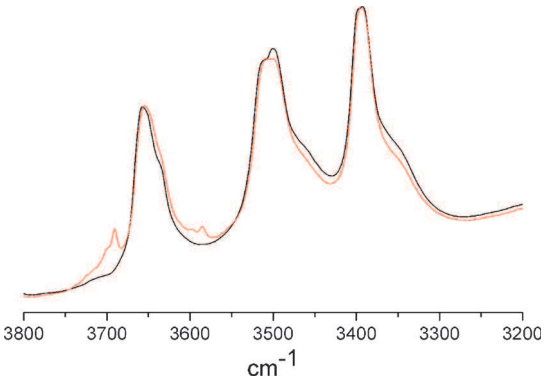

Figure 2. DRIFT spectra of MIL-68(In)-NH_2 at 25 °C under Ar (black line) and CO_2 steam (red line); peaks at 3585 and 3690 cm^{-1} are the remaining gas signals after removal of the CO_2 background signal.

Experimental Section

Indium nitrate hydrate, 2-aminoterephthalic acid (NH_2-bdc) or terephthalic acid (bdc), styrene oxide, anhydrous DMF, and CH_2Cl_2 were purchased from Sigma–Aldrich and used as received.

Synthesis

MIL-68(In)-NH_2 and MIL-68(In) were obtained by precipitation in a Pyrex beaker (capacity 100 mL) starting from a mixture of 0.86 M indium nitrate (4.82 mL, 4.14 mmol) in anhydrous DMF and 0.33 M 2-aminoterephthalic acid or terephthalic acid (10.06 mL, 3.32 mmol) in DMF. The reaction mixture was stirred for 5 min and 1.38 M 4-diazabicyclo[2.2.2] octane (DABCO, 4.83 mL, 6.67 mmol) in DMF was added. The reaction mixtures were stirred for 120 min at RT. The precipitates were washed with DMF at 160 °C followed by Soxhlet extraction (CH_2Cl_2) for 24 h to remove any remaining free acid. The resulting mass of dried MIL-68(In)-NH_2 and MIL-68(In) was 880 and 750 mg, respectively.

Recycling

MIL-68(In)-NH_2 was removed from the reaction mixture by centrifugation (4000 rpm) and washed overnight by Soxhlet extraction (CH_2Cl_2). The dried material was ready to reuse.

Catalysis

Styrene oxide (0.2 mL, 210.4 mg, 1.75 mmol) and anhydrous DMF (1.8 mL, 1699.2 mg, 23.25 mmol) were loaded in a glass vial (3 mL). The typical amount of catalyst was 50 mg. The system was heated at 150 °C under magnetic stirring (1000 rt min^{-1}) and the reaction was performed for 8 h by introducing CO_2 (8 bar) into the vial. The concentrations of styrene oxide and styrene carbonate were deter-

mined by GC analysis (Perkin–Elmer Autosystem that was equipped with a Supelcowax 10 column) of the samples with toluene as an external standard. In all of the experiments, no by-products were observed. The catalytic tests were repeated independently two- or three times to estimate the reproducibility and accuracy of the results.

DFT calculations

Density functional theory (DFT) calculations were performed by using a periodic plane-wave method, as implemented in VASP 5.2.[18] The exchange-correlation functional was treated within the generalized gradient approximation (GGA), which was parameterized by Perdew, Burke, and Ernzernhof,[19] and the electron-ion interaction was described by the projector-augmented wave (PAW) scheme[32] with an energy cutoff of 400 eV. Energies were calculated with the $1\times1\times3$ Kpoints mesh. Dispersion corrections were systematically included to energies and forces, within the DFT-D2 method reported by Grimme.[20] Full optimization of the structures was performed until the forces on each atom in each direction were inferior to 2.10–2 eV $Å^{-1}$. Atomic charges were calculated by Bader charge analysis[33,34] with an increased cutoff (500 eV) and fine FFT grid ($250\times420\times80$ points).

Acknowledgements

The authors gratefully acknowledge the European Commission and the NANOMOF program (FP7-NMP). Calculations were performed at the IFPEN HPC center and at the IDRIS/CINES HPC centers (Project numbers x2011086134 and x2012086134, funded by GENCI). We thank Frederic Meunier for the advice with the DRIFT analysis.

Keywords: ab initio calculations · amines · Brønsted sites · carbonates · metal–organic frameworks

[1] T. Sakakura, J.-C. Choi, H. Yasuda, *Chem. Rev.* **2007**, *107*, 2365 – 2387.
[2] T. Sakakura, K. Kohno, *Chem. Commun*. **2009**, 1312 – 1330.
[3] R. Srivastava, D. Srinivas, P. Ratnasamy, *Microporous Mesoporous Mater.* **2006**, *90*, 314 – 326.
[4] D. Farrusseng, S. Aguado, C. Pinel, *Angew. Chem.* **2009**, *121*, 7638 – 7649; *Angew. Chem. Int. Ed.* **2009**, *48*, 7502 – 7513.
[5] M. Savonnet, S. Aguado, U. Ravon, D. Bazer-Bachi, V. Lecocq, N. Bats, C. Pinel, D. Farrusseng, *Green Chem.* **2009**, *11*, 1729 – 1732.
[6] M. Savonnet, A. Camarata, J. Canivet, D. Bazer-Bachi, N. Bats, V. Lecocq, C. Pinel, D. Farrusseng, *Dalton Trans.* **2012**, *41*, 3945 – 3948.
[7] J. Gascon, U. Aktay, M. D. Hernandez-Alonso, G. P. M. van Klink, F. Kapteijn, *J. Catal.* **2009**, *261*, 75 – 87.
[8] B. Arstad, H. Fjellvåg, K. Kongshaug, O. Swang, R. Blom, *Adsorption* **2008**, *14*, 755 – 762.
[9] E. Stavitski, E. A. Pidko, S. Couck, T. Remy, E. J. M. Hensen, B. M. Weckhuysen, J. Denayer, J. Gascon, F. Kapteijn, *Langmuir* **2011**, *27*, 3970 – 3976.
[10] J. G. Vitillo, M. Savonnet, G. Ricchiardi, S. Bordiga, *ChemSusChem* **2011**, *4*, 1281 – 1290.
[11] A. Torrisi, R. G. Bell, C. Mellot-Draznieks, *Cryst. Growth Des.* **2010**, *10*, 2839 – 2841.
[12] W. Kleist, F. Jutz, M. Maciejewski, A. Baiker, *Eur. J. Inorg. Chem.* **2009**, 3552 – 3561.
[13] F. Vermoortele, R. Ameloot, A. Vimont, C. Serre, D. De Vos, *Chem. Commun.* **2011**, *47*, 1521 – 1523.
[14] M. Savonnet, D. Bazer-Bachi, C. Pinel, V. Lecocq, N. Bats, D. Farrusseng, FR Patent 09/05.107, **2009**.
[15] M. Savonnet, D. Bazer-Bachi, N. Bats, J. Perez-Pellitero, E. Jeanneau, V. Lecocq, C. Pinel, D. Farrusseng, *J. Am. Chem. Soc.* **2010**, *132*, 4518 – 4519.
[16] V. Caló, A. Nacci, A. Monopoli, A. Fanizzi, *Org. Lett.* **2002**, *4*, 2561 – 2563.
[17] J. Muzart, *Tetrahedron*, **2009**, *65*, 8313 – 8323.
[18] G. Kresse, J. Hafner, *Phys. Rev. B* **1994**, *49*, 14251 – 14269.
[19] J. P. Perdew, K. Burke, M. Ernzerhof, *Phys. Rev. Lett.* **1996**, *77*, 3865 – 3868.
[20] S. Grimme, *J. Comput. Chem.* **2006**, *27*, 1787 – 1799.
[21] F. Leydier, C. Chizallet, D. Costa, P. Raybaud, *Chem. Commun.* **2012**, *48*, 4076 – 4078.
[22] C. Chizallet, P. Raybaud, *ChemPhysChem* **2010**, *11*, 105 – 108.
[23] T. Bucko, J. Hafner, L. Benco, *J. Chem. Phys.* **2004**, *120*, 10263 – 10277.
[24] U. Ravon, G. Chaplais, C. Chizallet, B. Seyyedi, F. Bonino, S. Bordiga, N. Bats, D. Farrusseng, *ChemCatChem* **2010**, *2*, 1235 – 1238.
[25] J. Gascon, M. D. Hernandez-Alonso, A. R. Almeida, G. P. M. van Klink, F. Kapteijn, G. Mul, *ChemSusChem* **2008**, *1*, 981 – 983.
[26] C. G. Silva, I. Luz, F. X. Llabres i Xamena, A. Corma, H. Garcia, *Chem. Eur. J.* **2010**, *16*, 11133 – 11138.
[27] R. Srivastava, D. Srinivas, P. Ratnasamy, *J. Catal.* **2005**, *233*, 1 – 15.
[28] J. Zhang, S. Zhang, K. Dong, Y. Zhang, Y. Shen, X. Lv, *Chem. Eur. J.* **2006**, *12*, 4021 – 4026.
[29] Y. Sugawara, W. Yamada, S. Yoshida, T. Ikeno, T. Yamada, *J. Am. Chem. Soc.* **2007**, *129*, 12902 – 12903.
[30] X.-B. Lu, X.-J. Feng, R. He, *Appl. Catal. A* **2002**, *234*, 25 – 33.
[31] X.-B. Lu, Y.-J. Zhang, B. Liang, X. Li, H. Wang, *J. Mol. Catal. A* **2004**, *210*, 31 – 34.
[32] G. Kresse, D. Joubert, *Phys. Rev. B* **1999**, *59*, 1758 – 1775.
[33] G. Henkelman, A. Arnaldsson, H. Jonsson, *Comput. Mater. Sci.* **2006**, *36*, 354 – 360.
[34] E. Sanville, S. D. Kenny, R. Smith, G. Henkelman, *J. Comput. Chem.* **2007**, *28*, 899 – 908.
[35] C. Volkringer, M. Meddouri, T. Loiseau, N. Guillou, J. Marrot, G. Ferey, M. Haouas, F. Taulelle, N. Audebrand, M. Latroche, *Inorg. Chem.* **2008**, *47*, 11892 – 11901.
[36] T. Ahnfeldt, D. Gunzelmann, T. Loiseau, D. Hirsemann, J. r. Senker, G. Ferey, N. Stock, *Inorg. Chem.* **2009**, *48*, 3057 – 3064.

Received: May 4, 2012
Revised: June 8, 2012
Published online on ■■ ■■, 0000

What a pair! MOF MIL-68(In)-NH_2[14] was used to catalyze the synthesis of styrene carbonate from styrene oxide and CO_2. Amine substitution on the linker of MIL-68(In) promotes the synthesis of cyclic carbonate from styrene epoxide and CO_2. Ab initio calculations and in situ characterization indicate that ligand substitution has a larger impact through electronic effects on the Brønsted site than through CO_2 activation.

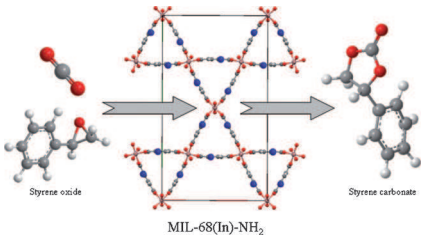

*T. Lescouet, C. Chizallet, D. Farrusseng**

■■ – ■■

The Origin of the Activity of Amine-Functionalized Metal–Organic Frameworks in the Catalytic Synthesis of Cyclic Carbonates from Epoxide and CO_2

CARBON 50 (2012) 1861–1870

Available at www.sciencedirect.com

SciVerse ScienceDirect

journal homepage: www.elsevier.com/locate/carbon

Transition metal loaded silicon carbide-derived carbons with enhanced catalytic properties

Lars Borchardt [a], *Frédéric Hasché* [c], *Martin R. Lohe* [a,d], *Martin Oschatz* [a], *Franz Schmidt* [a], *Emanuel Kockrick* [a,b], *Christoph Ziegler* [e], *Tristan Lescouet* [b], *Alicja Bachmatiuk* [d], *Bernd Büchner* [d], *David Farrusseng* [b], *Peter Strasser* [c], *Stefan Kaskel* [a,*]

[a] *Department of Inorganic Chemistry, Dresden University of Technology (TU-Dresden), Bergstrasse 66, 01062 Dresden, Germany*
[b] *Institut de Recherche sur la Catalyze et l'Environnement de Lyon (IRCELYON), University Lyon 1, CNRSC, 2, Av. Albert Einstein, 69626 Villeurbanne, France*
[c] *The Electrochemical Energy, Catalysis, and Materials Science Laboratory, Department of Chemistry, Chemical Engineering Division, Technical University Berlin, 10623 Berlin, Germany*
[d] *Leibniz Institute for Solid State and Materials Research Dresden (IFW Dresden), Institute for Solid State Research, Helmholtzstrasse 20, 01069 Dresden, Germany*
[e] *Department of Physical Chemistry, Dresden University of Technology (TU-Dresden), Bergstrasse 66b, 01062 Dresden, Germany*

ARTICLE INFO

Article history:
Received 19 October 2011
Accepted 17 December 2011
Available online 23 December 2011

ABSTRACT

Carbide-derived carbons (CDC) with incorporated transition metal nanoparticles (~2.5 nm) were prepared using a microemulsion approach. Time-consuming post synthesis functionalization of the carbon support material can thus be avoided and nanoparticle sizes can be controlled by changing the microemulsion composition. This synthesis strategy is a technique for the preparation of highly porous carbon materials with a catalytically active component. In particular we investigated the integration of ruthenium, palladium, and platinum in a concentration ranging from 4.45 to 12 wt.%. It was found that the transition metal has a considerable influence on sorption properties of resulting nanoparticle-CDC composite materials. Depending on the used metal salt additive the surface area and the pore volume ranges from 1480 m^2/g and 1.25 cm^3/g for Pt to 2480 m^2/g and 2.0 cm^3/g for Ru doped carbons. Moreover, members of this material class show impressive properties as heterogeneous catalysts. The liquid phase oxidation of tetralin and the partial oxidation of methane were studied, and electrochemical applications were also investigated. Primarily Pt doped CDCs are highly active in the oxygen reduction reaction, which is of great importance in present day fuel cell research.

1. Introduction

For many years micro- and mesoporous carbon materials have been in the special focus of scientific research. Particularly the outstanding adsorption properties combined with high chemical and hydrothermal stability [1–4] highlight the important role of this material class in the fields of hydrogen [5] and hydrocarbon energy storage, gas separation and purification, catalysis and electronics.

Nevertheless, most of the well known active carbon materials exhibit widely distributed irregularly curved pores with narrow bottle-necks [6] which turn out to be unsuitable for

* *Corresponding author:* Fax: +49 35146333632.
E-mail address: stefan.kaskel@chemie.tu-dresden.de (S. Kaskel).
0008-6223/$ - see front matter © 2012 Elsevier Ltd. All rights reserved.
doi:10.1016/j.carbon.2011.12.036

certain applications due to significant limitations in diffusion kinetics. Therefore the synthesis of mesoporous carbon materials have been studied extensively in the last decade [7–9]. Materials exhibiting narrowly distributed pore sizes are the ordered mesoporous carbons, synthesized from ordered mesoporous silica by exo-templating [10]. Depending on the template used, pore sizes can easily be adjusted. As one of the first Ryoo et al. have shown that such an ordered silica-templated carbon with a cubic pore geometry exhibits narrowly distributed pores of 3.1 nm diameter [9].

Another promising class of advanced carbon materials can be synthesized by the selective extraction of metal atoms out of metal carbides [11–15]. These carbide-derived carbons (CDC) also offer adjustable pore diameters as well as high specific surface areas (~2000 m^2/g) and pore volumes (~0.64 cm^3/g) [14–16]. Thus, CDCs are potential candidates as gas storage materials with outstanding hydrogen (~3 wt.%, 77 K, 1 bar) and hydrocarbon capacities (e.g. 16 wt.% methane, 298 K, 35 bar) [17]. Moreover these CDC materials are particularly discussed as electrode materials for super capacitor applications due to their large specific surface areas and high specific capacitances [16,18–20]. Especially hierarchically structured CDC materials containing micro- and mesopore systems have remarkable performances in supercap applications. They exhibit specific capacitances of up to 170 F/g in organic and 200 F/g in aqueous electrolytes [21–24]. While the structure of the carbon material plays an important role, several studies have demonstrated that transition metal additives such as iron or ruthenium influence the structure and adsorption properties of the resulting CDC materials dramatically [25–30]. Moreover the addition of transition metals to carbon materials can also serve as a supplementary source for catalytic functionality.

In the following we present a strategy for the synthesis of silicon carbide-derived carbon materials containing nanoscaled, catalytically active transition metal particles based on polymeric precursors. Since post synthetic functionalization of carbon materials with catalytically active species often leads to sintering and agglomeration processes an *in situ* functionalization approach is described [31]. Thus the inverse microemulsion technique was used to form porous matrices with incorporated, highly dispersed metal compounds [31–33].

A microemulsion in general describes a ternary thermodynamic stable system of a non-polar oil phase, a surfactant and a polar phase. The inverse microemulsion in particular contains aqueous nanodroplets dispersed in an organic phase [34–35]. These nanodroplets serve as size-restrictive reactors for the growth of the nanoparticles. Thus the particle size of growing catalytic particles can be precisely tuned within a few nanometers by the molar water to surfactant ratio (R_W value) [33,36]. Incorporation of these particles is achieved by adding a polycarbosilane precursor to the organic phase, which finally polymerizes. These nanoparticle containing polycarbosilane composite materials were pyrolyzed in order to obtain silicon carbide, followed by silicon extraction by high temperature chlorination (Fig. 1). At the end of this process a highly porous carbon material with immobilized catalytically active nanoparticles is generated.

The aim of this paper is to introduce this new synthesis strategy for metal containing carbide-derived carbons. CDCs containing ruthenium, palladium and platinum have been prepared and possible applications for these materials have been studied. In this context the oxidation reaction of tetralin as well as the partial oxidation of methane have been tested as examples for both heterogeneous liquid and gas phase catalysis. Furthermore platinum doped CDCs were tested in the oxygen reduction reaction as an example for an application in electrochemistry. Depending on the used transition metal impressive performances in relevant catalytic reactions were achieved.

2. Experimental section

A scheme showing the steps for the preparation of metal doped CDC composites, comprising the preparation of metal containing polymeric PCS (M = Ru, Pd, Pt), ceramic SiC and carbonaceous CDC composites is given in Fig. 1. Detailed experimental procedures as well as information on characterization techniques are provided with the Supporting information part.

3. Results and discussion

3.1. *Materials structure*

Although the motivation of adding metal chlorides into a CDC synthesis was to create catalytically active species, remarkable influences on carbon microstructures and physisorption properties have also been noticed. While all metal/SiC composite materials are non-porous ($S_G < 16\ m^2/g$), the corresponding CDC materials exhibit high surface areas between 1500 and 2500 m^2/g and pore volumes up to 2 cm^3/g (Table 1).

Especially CDC-Ru exhibits a very high specific surface area (up to 2480 m^2/g), and high micro- and total pore volume (up to 0.7 cm^3/g and 2.0 cm^3/g, respectively). The shape of this isotherm is type IV and the pore size distribution, calculated by QSDFT shows a hierarchical pore structure of micropores of approximately 0.9 nm and mesopores of 3.1 nm (inset Fig. 2). The hysteresis loop is seen at $0.4 < p/p_0 < 0.75$ caused by the capillary condensation in the mesopores.

CDC-Pd and CDC-Pt also have high, but comparably lower surface areas and pore volumes (Table 1) which are similar to those of metal free bulk CDCs obtained from the same polymer-precursor ($S_g = 1420\ m^2/g$; $V_{micro} = 0.56\ cm^3/g$) [41]. The materials exhibit a hierarchical pore structure with micro- and mesopores of comparable size. It is known that many transition metals can serve as graphitization catalysts. Especially Fe, Co, Ni, Mn are known to catalyze the transformation of amorphous carbon into more ordered structures, but there are also some reports about the use of palladium as a graphitization catalyst [29]. Furthermore it is known that transition metal chlorides, like ruthenium chloride influence the chlorination process by increasing the etching rate [27,30]. Detailed information and Raman investigations about this topic are provided with Supporting information.

Elemental composition of the materials was investigated by energy dispersive X-ray spectroscopy (Table 2). All CDC materials contain silicon below the detection limit, so an effective silicon etching during the chlorination process can

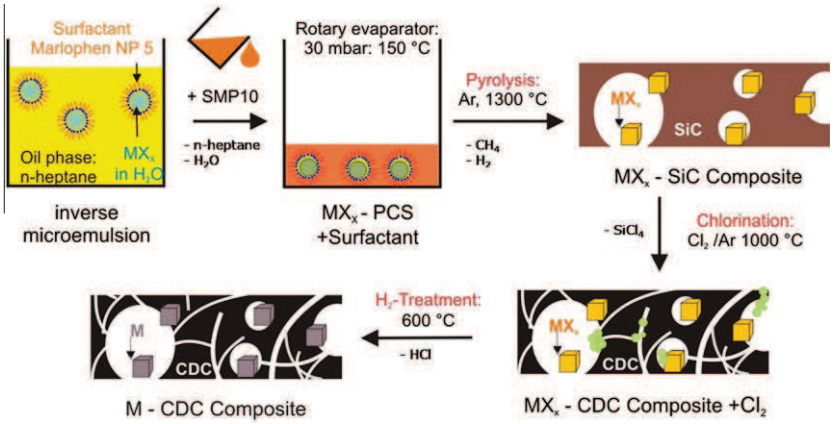

Fig. 1 – Synthesis strategy for the preparation of metal containing polymeric PCS (M = Ru, Pd, Pt), ceramic SiC and carbonaceous CDC composites synthesized by inverse microemulsion method, pyrolysis, chlorination and hydrogen treatment, respectively.

Table 1 – Nitrogen physisorption data of silicon carbide-derived carbons with different metal additives.

Sample code	S_g [a] [$m^2\ g^{-1}$]	$V_{p,\ total}$ [b] [$cm^3\ g^{-1}$]	$V_{p,\ micro}$ [c] [$cm^3\ g^{-1}$]	$V_{p,\ meso}$ [$cm^3\ g^{-1}$]	$d_{micropore}$ [d] [nm]	$d_{mesopore}$ [d] [nm]
CDC-Ru	2480	2.00	0.7	1.3	0.9	3.1
CDC-Pd	1540	1.35	0.5	0.85	0.9	3.1
CDC-Pt	1480	1.25	0.4	0.85	0.8	3.3
SiC-X (Ru, Pd, Pt)	<16	<0.01	–	–	–	

[a] S_g estimated at $p/p_0 = 0.05–0.3$.
[b] Total pore volume calculated at $p/p_0 = 0.95$.
[c] micro pore volume calculated for pores $d < 2$ nm.
[d] Pore diameter calculated by QSDFT methods for slit pores at 77 K using carbon kernel.

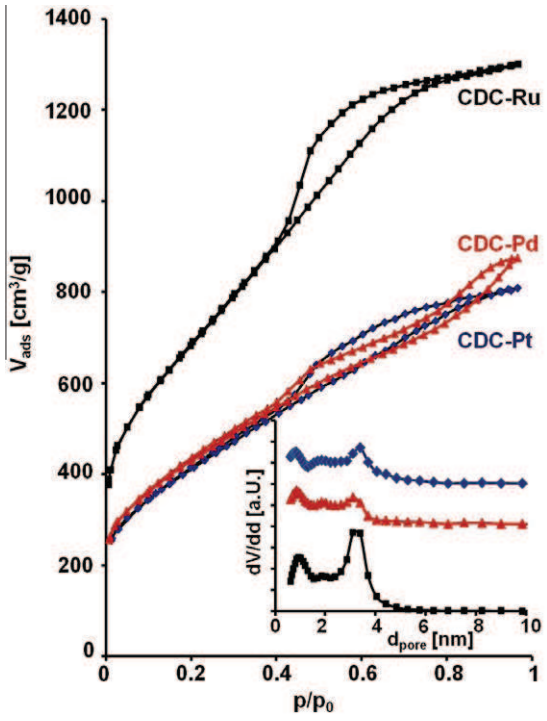

Fig. 2 – N_2-physisorption isotherms at 77 K and corresponding pore size distributions estimated by QSDFT model (inset) of carbide-derived carbons prepared with different metal salt additives.

be assumed. Furthermore oxygen content is lower than 0.5 wt.% for all composites. Compared to the theoretical value CDC materials contain the inserted metal in a decreased amount (metal content of 17 wt.% would be expected for theoretical yield of 22%). On the one hand this is contributed to the fact that the surfactant used in the microemulsion approach also combusts into carbon partially, thus lowering the metal to carbon ratio in the final composite. On the other hand and maybe more importantly a generation of gaseous $MCl_{x(g)}$ *species can explain the deficiency compared to the expected metal content.*

To further characterize these nanoparticles transmission electron microscopy was carried out.

The microemulsion technique has found to be a useful approach for the size selective incorporation of metallic nanoparticles as reported recently [32,33,35,37].

Fig. 3 shows TEM images of the well defined structured CDC-Pt (Fig. 3a and c), CDC-Pd (Fig. 3e) and CDC-Ru materials (Fig. 3f) compared with a commercial low-graphitized Pt/Vulcan XC 72R catalyst (Fig. 3b and d).

Fig. 3a and b clearly show significant differences in the carbon structure between a carbon black and the CDC supports. Carbon blacks display amorphous irregular conglomerates of carbon particles with diameters of about 50 nm. The network creates void spaces of 50 nm and more. The CDC support, in contrast, is characterized by a much denser and more regular structure with much smaller pore sizes. Surprisingly, the particle density in Fig. 3c appears to be higher compared to that in Fig. 3d, despite the much low-

Table 2 – Elemental compositions of CDC samples calculated from energy dispersive X-ray spectroscopy.

Sample code	m_{metal} [wt.%]	m_{metal} [wt.%] theoretical
CDC-Ru	7.0	17
CDC-Pd	6.5	17
CDC-Pt	12	17
CDC-Pt_b	4.45	10

erPtloadings.Excellentuniformdispersionofplatinumnanoparticles of 2.5 ± 0.6 nm size on the CDC support is shown in Fig. 3c. Electrochemical measurements and CO pulse chemisorptions have shown that these nanoparticles are catalytically accessible (further details are provided with Supporting information).

Furthermore Foley et al. have reported that the electron rich graphene sheets in the carbon support interact with and thus stabilize the platinum nanoparticles [38].

Due to the low overall metal content of the samples and the small particle size of only a few nanometers, further TEM investigations were carried out on the samples to characterize the nature and composition of the incorporated metal nanoparticles. The particles were investigated by comparing lattice spacings determined from the TEM images with literature data, and local EDX measurements. It is known

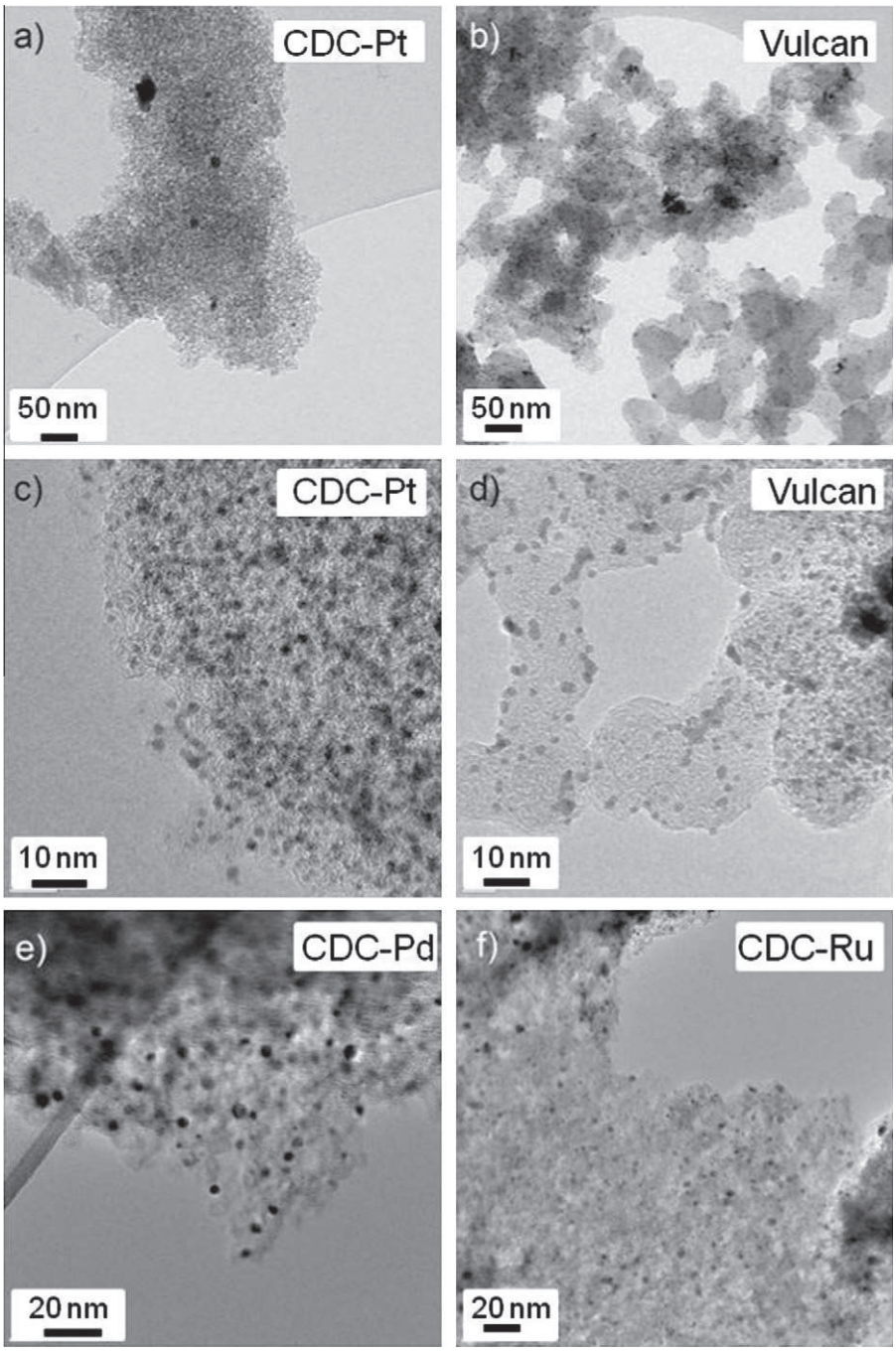

Fig. 3 – TEM image for CDC-Pt catalyst (a) 50 nm scale, (c) 10 nm scale, commercial Pt/Vulcan XC 72R catalyst (b) 50 nm scale, (d) 10 nm scale, CDC-Pd catalyst (e) 20 nm scale and CDC-Ru catalyst (f) 20 nm scale.

from literature, that palladium particles supported inside a ceramic SiC matrix will form palladium silicides at certain temperatures. Yoshimura et al. have shown that Pd/PdSi core–shell particles are formed due to the reaction of the metal particles and the surrounding SiC matrix at temperatures between 1173 K and 1373 K [39]. Additionally Lamber et al. reported on the formation of Pt_3Si by heating platinum with a silica substrate under reducing atmosphere [40]. As it would be expected, the heat treatment combined with a high temperature chlorination of the materials also leads to the formation of silicides in some cases, possibly due to the reaction of gaseous $SiCl_4$ with the metal nanoparticles. In the case of CDC-Pt materials Pt to Si ratios between 9:1 and 2:1 have been found using EDX analysis of single particles. For the CDC-Ru and CDC-Pd samples the silicon content is typically below 10%, and even Si-free particles can be found (for further details please see Supporting information).

3.2. Catalysis

3.2.1. Selective methane oxidation

The catalytic properties of ceramic and carbonaceous composites were tested in selective methane oxidation. In order to avoid oxidation of the porous carbon matrix, a low oxygen concentration was chosen. In the first step, methane is oxidized into carbon dioxide and water. In the following carbon monoxide and hydrogen can be formed using appropriate catalyst systems. In previous studies we have shown that the CeO_2/Pt-CDC system is a promising catalyst for the selective methane oxidation. Furthermore we have shown that no carbon combustion of the CDC matrix was obtained [38]. However, the catalytic performances were strongly related on the nature of the porous matrix. In the present studies the influence of the transition metals were studied on the catalyst performance of silicon carbide (SiC-X) and carbide-derived carbon composites (CDC-X).

According to the methane conversions of different SiC-X and CDC-X composites the catalytic activity is strongly dependant on the applied metal sites and is presented in Fig. 4. Ruthenium (SiC-Ru), palladium (SiC-Pd) and platinum SiC-composite materials (SiC-Pt) offer significant activities. Methane conversions were obtained below 375 °C for ruthenium, palladium and platinum ceramic composites. However in comparison to transition metal/CDC composites these ceramics show lower performances due to the low porosity and the resulting limited accessibility of active centers.

After chlorination, all CDC composites show considerable higher activities compared to the SiC intermediates (Fig. 4). The latter can be explained by significantly higher specific surface areas and pore volumes of CDC composites (Table 1). Ru-, Pd-, Pt-containing carbonaceous composites promote methane conversions up to 17% at 475 °C for CDC-Pt. Additionally, only these composites promote reforming reactions explaining the higher methane conversions. The syn-gas production is strongly dependant on the applied transition metals since for palladium (CDC-Pd) and platinum systems (CDC-Pt) carbon monoxide and hydrogen can be already identified at significantly lower temperatures (250 °C) compared to the ruthenium based system (CDC-Ru: 400 °C). In agreement to previous studies, the hydrogen yield and carbon monoxide selectivity increases with higher reaction temperatures up to 12% and 42% at 475 °C for the CDC-Pt catalyst, respectively [38]. Interestingly, the CO formation is shifted for the palladium based catalyst (CDC-Pd) to lower and hydrogen production to higher temperatures, respectively compared to the platinum system (CDC-Pt) (Fig. 4b). The latter suggests different reaction mechanisms for both catalyst systems. However, the corresponding ceramic SiC-Pd and SiC-Pt composites do not promote the syn-gas formation.

Additionally, no carbon oxidation of the CDC catalysts system were detected since the carbon balance as the molar ratio of all involved reactants and products remain constant in the studied temperature range. These results were confirmed by nitrogen physisorption measurements of fresh and used catalysts since similar specific surface areas, pore volumes and pore size distributions were obtained.

3.2.2. Catalytic tetralin oxidation

In comprehensive studies also the catalytic activity of carbonaceous CDC-X composites was tested in liquid phase tetralin oxidation. This reaction is widely used as a model reaction for industrial applications since the oxidation product 1-tetralone can be further used in diesel fuel additives and as a reactant for fine chemical applications. In contrast to literature reported procedures no additional aromatic or halogenated solvents were used. Additionally, pressurized molecular oxygen was used as oxidizing agent instead of more expensive peroxide species.

Similar as the methane oxidation discussed above, the tetralin oxidation is strongly dependant on the applied catalyst (Table 3). In contrast to the low activity for palladium systems (CDC-Pd), high tetralin conversions up to 28% and 44% were detected for the ruthenium (CDC-Ru) and platinum catalysts (CDC-Pt), respectively. This outstanding catalyst performance can be explained by the high activity of ruthenium and platinum species as oxidation catalyst in cyclohexene and tetraline oxidation. Furthermore the highly porous CDC matrix in combination with a hydrophobic surface leads to large hydrocarbon uptakes [24,41]. For all active composite materials similar selectivity of approximately 66% towards the formation of 1-tetralone was detected. Moreover, no additional by-products like naphthalene and 1-naphthalol were detected.

3.2.3. Oxygen reduction reaction (ORR)

The oxygen reduction reaction (ORR) is a sluggish, rate limiting reaction, which proceeds at the cathode side and therefore leads to significant cell potential and efficiency losses in hydrogen polymer electrolyte fuel cells (PEMFC).

A number of different catalyst concepts have emerged over the past years, which have shown promise to achieve the set Pt mass activity goals [42–49]; these include platinum monolayer catalysts, Pt skin catalysts, and dealloyed Pt nanoparticle catalysts. Conventional carbon black supports and their graphitized variations continue to be the most popular catalyst support materials. However, innovative concepts for novel carbonaceous supports, on which Pt nanoparticles exhibit the benchmark mass and specific ORR activities of the carbon-black supported Pt particles have remained scarse. Studies comparing conventional carbon and carbon nanotube

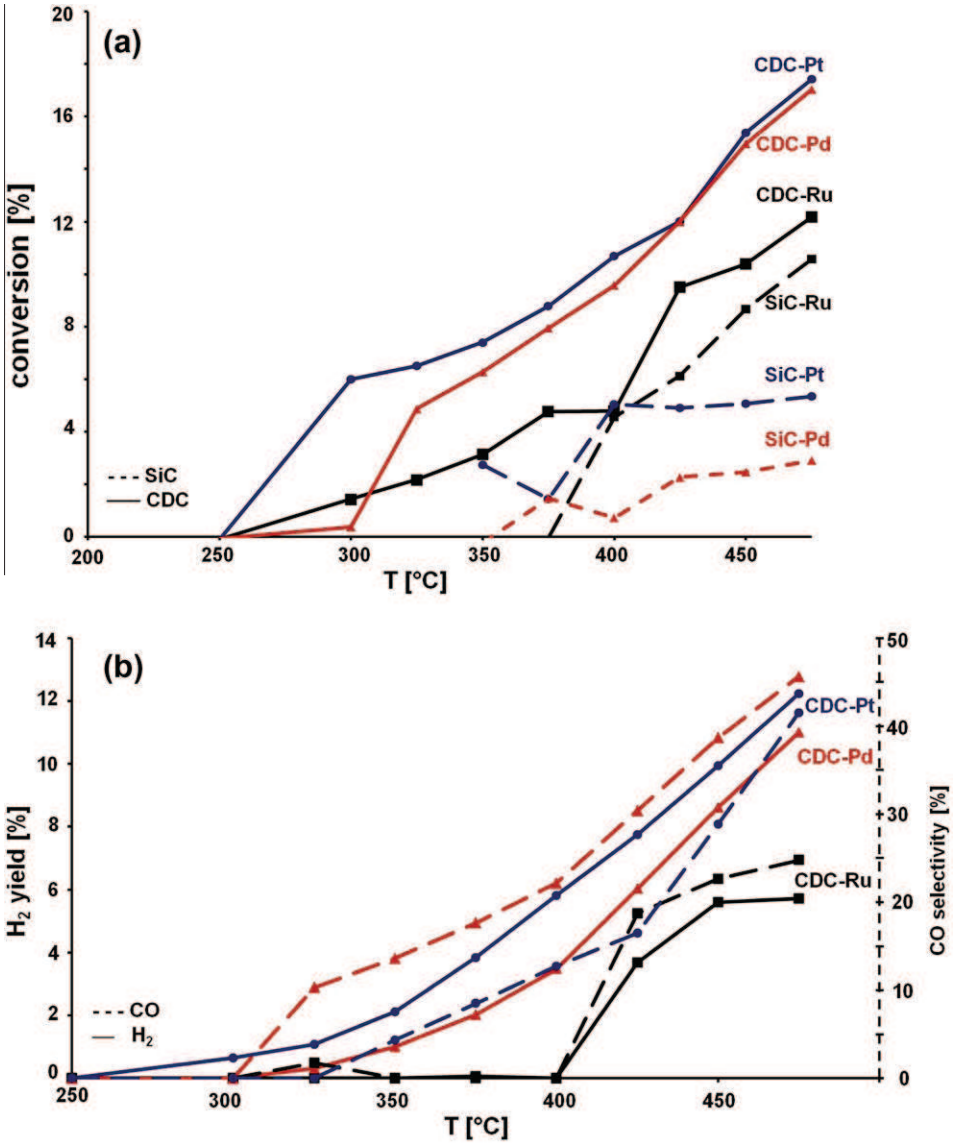

Fig. 4 – (a) Methane conversions, (b) CO-selectivities and hydrogen yields of ceramic SiC-X and carbonaceous CDC-X composites.

Table 3 – Tetralin conversion (X) into 1-tetralol and 1-tetralone and selectivity (S) into 1-tetralone of carbonaceous CDC-X composites at 90 °C and 8 bars of static oxygen for 6 h.

	CDC-Ru	CDC-Pd	CDC-Pt
X [%]	44	5	28
S [%]	66	67	67

supports [50] indicated that the support degradation plays a key role in the loss of the electrochemical active surface area of a cathode electrocatalyst at prolonged testing times [51–54]. Recently it was also shown that CDC materials exhibit superior performances as supports in direct methanol fuel cell applications (DMFC) [55].

The metal-doped CDCs described in this contribution offer high BET surface area, the possibility for controlled doping, high level of graphitization and structured frameworks. As such, it opens a promising prospect to achieve the long-term stability goals in fuel cell cathode catalyst research. Therefore platinum containing CDC-Pt_b has been studied according its electrocatalytic activity for the oxygen reduction reaction. We find catalytic ORR activities comparable and superior to state of the art Pt/carbon catalysts involving conventional carbon supports, making CDCs a viable alternative catalyst support.

CDC-Pt_b with a platinum loading of 4.45 wt.% were characterized with respect to their surface voltammetric behavior in supporting acid electrolyte as well as to their electrocatalytic reactivity for the oxygen reduction reaction (ORR) in acidic liquid electrolytes.

Fig. 5 (inset) shows the cyclic voltammetry (CV) profile for the CDC-Pt_b catalyst. The CDC-Pt_b catalyst exhibits a hydrogen absorption/desorption peak in the potential regime between 0.0 and 0.4 V vs. RHE, adjacent to a double layer capacitive current plateau starting at 0.4 V vs. RHE; anodically

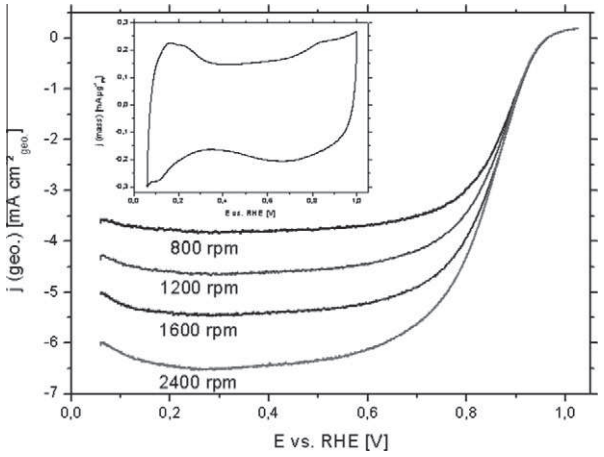

Fig. 5 – Electrochemical characterization for CDC-Pt_b catalyst, linear sweep voltammetry (LSV) with different rotating speeds performed anodically from 0.06 to 1.03 V vs. RHE with 5 mV s^{-1} in oxygen saturated 0.1 M $HClO_4$ at room temperature (inset) cyclic voltammetry (CV) conducted from 0.06 to 1.00 V vs. RHE with 100 mV s^{-1} in deaerated 0.1 M $HClO_4$ at room temperature.

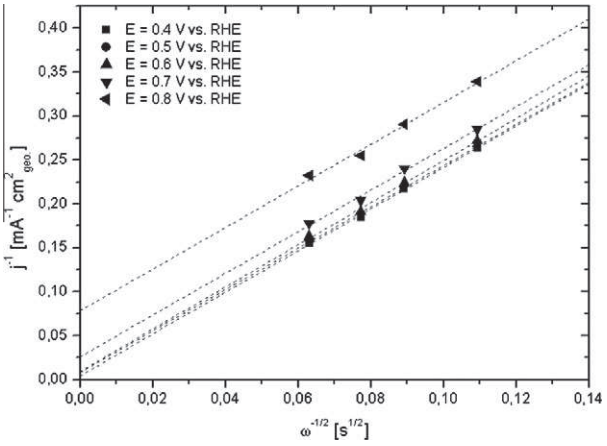

Fig. 6 – Koutecky–Levich plot for CDC-Pt_b at various potentials, data taken from Fig. 5.

thereof, the Pt hydroxide/oxide formation region is visible in the potential range of 0.7–1.0 V vs. RHE. The electrochemical active surface area (ECSA) of the supported Pt catalyst was estimated to 66 ± 4 m^2/g_{Pt} and is consistent with literature values [56]. For ideal spherical, not contacting particles of 2.5 nm the theoretical specific surface area is 112 m^2/g (Eq. (1)), thus this result highlights that the platinum nanoparticles on the mesoporous CDC support material are active and available for electrocatalysis.

$$S_g = A/m = 6/\rho \cdot d \quad (1)$$

S_g = specific surface area; A = surface area; m = mass; ρ = density of the material, d = diameter of the sphere.

Fig. 5 shows the oxygen reduction sweep voltammetry curves of CDC-Pt_b catalyst at several rotating speeds. All measured polarization curves exhibit a plateau behavior in the potential regime between 0.06 and 0.60 V vs. RHE, where oxygen diffusion to the catalyst surface becomes the rate limiting process [57,58] and hence is sensitively dependent on rotation rate. At an anodic potential of about 0.70 V vs. RHE, the polarization curves exhibit a reactive regime dominated by mixed kinetic and diffusion control. Past 0.9 V vs. RHE, the voltammetric profile appears largely kinetically controlled, that is the surface catalysis is the slowest component in the overall reaction process, while mass transport is comparatively fast. This is why the sweeps become independent of the rotating speed. At the open circuit potential of about 0.96 V vs. RHE electrocatalytic conversion of oxygen ceases.

To extract the intrinsic catalytic activity, $j_{kin,}$ of the CDC-Pt_b ORR catalyst, the measured ORR current density, j, in Fig. 5 was corrected for mass transport according to

$$1/j = 1/j_{kin} + 1/j_{dif} \quad (2)$$

where j_{dif} represents the diffusion limited ORR current density obtained from Fig. 5 at a given rotation rate. Table 4 reports the platinum mass and surface area based activity of the CDC-Pt_b catalyst and a commercial Pt/Vulcan XC 72R catalyst [54]. Platinum electrochemical active surface area and particle size are reported in Table 4.

The CDC-Pt_b catalyst exhibited a platinum based ORR mass activity, j_{mass}, of 0.19 ± 0.01 A mg_{Pt}^{-1} at 0.90 V vs. RHE and a platinum surface area based (specific) activity of j_{spec}, 283 ± 35 μA cm_{Pt}^{-1} at 0.90 V vs. RHE. Clearly, our CDC-Pt_b catalyst with its low platinum loading and high BET surface area shows favorable ORR performance and is in line with reported [56] Pt mass and specific activities of commercial platinum catalysts supported on conventional Vulcan XC 72R or multi walled carbon nanotubes. Thus, our study suggests that CDC supports are viable fuel cell catalyst supports that are capable to realize the full activity of Pt nanoparticles at superior corrosion stability. Furthermore this material was compared to a post synthetic functionalized CDC derived by commercial SiC (Supporting informations).

In order to determine the number of transferred electrons during the oxygen reduction, we used the Koutecky–Levich equation [57,58] (Eq. (3))

Table 4 – ORR catalyst performance.

Catalyst	$j_{(mass,0.9V[RHE])}$ [A mg_{Pt}^{-1}]	$j_{(spec,0.9V[RHE])}$ [μA cm_{Pt}^{-2}]	ECSA [m^2 g_{Pt}^{-1}]	Particle size [nm]
CDC-Pt_b	0.19 ± 0.01	283 ± 35	66 ± 4	2.5 ± 0.7
Pt/Vulcan XC 72R	0.15 ± 0.02	291 ± 40	53 ± 4	2.5 ± 0.6

$$1/j = 1/j_{kin} + 1/j_{dif} = 1/j_{kin} + 1/(B \cdot \omega^{1/2}) \quad (3)$$

$$B = 0.62 \cdot n \cdot F \cdot D(O_2)^{2/3} \cdot \upsilon^{-1/6} \cdot c(O_2) \quad (4)$$

Here, j is the current density, j_{kin} the kinetic current density, j_{dif} the diffusion limiting current density, ω the rotating speed, F the Faraday constant (F = 96,485 C mol^{-1}) and B is a parameter dependent on the experimental conditions. A theoretical value for B (Eq. (5)) of 0.467 mA cm$_{geo}^{-2}$ s$^{1/2}$ was predicted for the four electron oxygen reduction process using published data for oxygen solubility ($c(O_2) = 1.26 \times 10^{-3}$ mol l^{-1}), oxygen diffusivity ($D(O_2) = 1.93 \times 10^{-5}$ cm^2 s^{-1}) and kinematic viscosity of electrolyte ($\upsilon = 1.009 \times 10^{-2}$ cm^2 s^{-1}). We then extracted the value of B specific to our experiments using a Koutecky–Levich plot for the CDC-Pt$_b$ catalyst at various potentials (Fig. 6).

The plot of 1/j vs. $\omega^{-1/2}$ is linear and the fits run parallel, indicating a similar slope for various electrode potentials. The experimentally extracted mean B value for the various electrode potentials was 0.422 ± 0.003 mA cm$_{geo}^{-2}$ s$^{1/2}$.

The good agreement of the theoretical and experimental value of B corroborates the prevalence of the four electron over the two electron catalytic reduction pathway.

4. Conclusions

We have reported the synthesis of highly porous carbide-derived carbons with incorporated and highly dispersed nanoparticles. These materials were synthesized by using a microemulsion approach, followed by high temperature chlorination. Using this approach the nanoparticle species as well as their sizes can be controlled. Especially the incorporation of Pd, Pt and Ru salts was investigated here, showing that the chosen metal salts have eminent influence on the sorption properties of resulting carbide-derived carbons. In this context CDCs have been synthesized with specific surface areas of up to 2480 m^2 g^{-1} and specific pore volumes of up to 2.0 cm^3 g^{-1}. Furthermore these composite materials show impressive properties in different catalytic applications. We have shown that Ru doped CDCs for instance, are efficient catalysts in the liquid phase tetralin oxidation. These materials show a tetralin conversion of 44%, and a selectivity of 66% after 6 h and 20 h. In addition, all CDCs (doped with either Ru, Pd or Pt) also show very good performance in the partial oxidation of methane. The conversion of methane already starts at very low temperatures (250 °C). At these temperatures also carbon monoxide and hydrogen were identified, due to reforming reactions, making these materials highly interesting as catalysts for the production of syn gas.

With respect to possible use as fuel cell materials, also the electrocatalytic performance of platinum doped CDC was tested. We have shown that this material is a promising alternative support material for fuel cell cathode catalysts. The observed Pt mass and specific activities, as well as the electrochemical active surface area are higher or comparable to those of commercial state-of-art Pt/carbon catalysts with conventional carbon black materials. The *in situ* incorporation of Pt nanoparticles into the carbon framework offer significant advantages for the long-term stability and corrosion resistance.

Acknowledgements

The authors thank the Deutsche Forschungsgemeinschaft, especially the priority program 1181 Nanomat for funding this work as well as Annette Wittebrock for laboratory supporting, Dipl.-Chem. Mehtap Oezaslan for inspiring discussion and the Zentraleinrichtung Elektronenmikroskopie at Technische Universität Berlin for TEM supporting. The Electrochemical Energy, Catalysis, and Materials Science Laboratory are a part of the Cluster of Excellence "Unifying Concepts in Catalysis" (UniCat) within the framework of the Excellence Initiative launched by the German Federal and State Governments, managed by the Technische Universität Berlin, Germany.

Author contributions: L.B. designed and performed the experiments, synthesized the materials and analyzed the data. M.O. helped with the experiments and analyses. M.R.L., A.B., B.B. were responsible for the TEM analysis. F.H. and P.S. were responsible for the electrochemistry part. T.L., E.K. and D.F. were responsible for the tetralin oxidation and partial methane oxidation. FS was responsible for the CO chemisorptions, C.Z. was responsible for the Raman meassurment, S.K. supervised and coordinated the research. L.B., E.K. and M.R.L. co-wrote the paper. All authors discussed the results and commented on the manuscript.

Appendix A. Supplementary data

Supplementary data associated with this article can be found, in the online version, at doi:10.1016/j.carbon.2011.12.036.

REFERENCES

[1] Davis ME. Ordered porous materials for emerging applications. Nature 2002;417(6891):813–21.
[2] Joo SH, Choi SJ, Oh I, Kwak J, Liu Z, Terasaki O, et al. Ordered nanoporous arrays of carbon supporting high dispersions of platinum nanoparticles. Nature 2001;412(6843):169–72.
[3] Kruk M, Dufour B, Celer EB, Kowalewski T, Jaroniec M, Matyjaszewski K. Synthesis of mesoporous carbons using ordered and disordered mesoporous silica templates and polyacrylonitrile as carbon precursor. J Phys Chem B 2005;109(19):9216–25.
[4] Liang CD, Dai S. Synthesis of mesoporous carbon materials via enhanced hydrogen-bonding interaction. J Am Chem Soc 2006;128(16):5316–7.
[5] Yang ZX, Xia YD, Mokaya R. Enhanced hydrogen storage capacity of high surface area zeolite-like carbon materials. J Am Chem Soc 2007;129(6):1673–9.
[6] Kyotani T. Control of pore structure in carbon. Carbon 2000;38(2):269–86.
[7] Jun S, Joo SH, Ryoo R, Kruk M, Jaroniec M, Liu Z, et al. Synthesis of new, nanoporous carbon with hexagonally ordered mesostructure. J Am Chem Soc 2000;122(43):10712–3.
[8] Lee KT, Ji XL, Rault M, Nazar LF. Simple synthesis of graphitic ordered mesoporous carbon materials by a solid-state method using metal phthalocyanines. Angew Chem Int Ed 2009;48(31):5661–5.
[9] Ryoo R, Joo SH, Jun S. Synthesis of highly ordered carbon molecular sieves via template-mediated structural transformation. J Phys Chem B 1999;103(37):7743–6.

[10] Lu AH, Schueth F. Nanocasting: a versatile strategy for creating nanostructured porous materials. Adv Mater 2006;18(14):1793–805.
[11] Dash RK, Nikitin A, Gogotsi Y. Microporous carbon derived from boron carbide. Micropor Mesopor Mater 2004;72(1–3):203–8.
[12] Dash RK, Yushin G, Gogotsi Y. Synthesis, structure and porosity analysis of microporous mesoporous carbon derived from zirconium carbide. Micropor Mesopor Mater 2005;86(1-3):50–7.
[13] Gogotsi Y, Dash RK, Yushin G, Yildirim T, Laudisio G, Fischer JE. Tailoring of nanoscale porosity in carbide-derived carbons for hydrogen storage. J Am Chem Soc 2005;127(46):16006–7.
[14] Gogotsi Y, Nikitin A, Ye HH, Zhou W, Fischer JE, Bo Y, et al. Nanoporous carbide-derived carbon with tunable pore size. Nat Mater 2003;2(9):591–4.
[15] Presser V, Heon M, Gogotsi Y. Carbide-derived carbons–from porous networks to nanotubes and graphene. Adv Funct Mater 2011;21:810–33.
[16] Yushin G, Dash RK, Jagiello J, Fischer JE, Gogotsi Y. Carbide-derived carbons: effect of pore size on hydrogen uptake and heat of adsorption. Adv Funct Mater 2006;16(17):2288–93.
[17] Yeon SH, Osswald S, Gogotsi Y, Singer JP, Simmons JM, Fischer JE, et al. Enhanced methane storage of chemically and physically activated carbide-derived carbon. J Power Sources 2009;191(2):560–7.
[18] Chmiola J, Largeot C, Taberna PL, Simon P, Gogotsi Y. Desolvation of ions in subnanometer pores and its effect on capacitance and double-layer theory. Angew Chem-Int Ed 2008;47(18):3392–5.
[19] Chmiola J, Yushin G, Gogotsi Y, Portet C, Simon P, Taberna PL. Anomalous increase in carbon capacitance at pore sizes less than 1 nanometer. Science 2006;313(5794):1760–3.
[20] Korenblit Y, Rose M, Kockrick E, Borchardt L, Kvit A, Kaskel S, et al. High-rate electrochemical capacitors based on ordered mesoporous silicon carbide-derived carbon. ACS Nano 2010;4(3):1337–44.
[21] Krawiec P, Kockrick E, Borchardt L, Geiger D, Corma A, Kaskel S. Ordered mesoporous carbide derived carbons: novel materials for catalysis and adsorption. J Phys Chem C 2009;113(18):7755–61.
[22] Yeon SH, Reddington P, Gogotsi Y, Fischer JE, Vakifahmetoglu C, Colombo P. Carbide-derived-carbons with hierarchical porosity from a preceramic polymer. Carbon 2010;48(1):201–10.
[23] Oschatz M, Kockrick E, Rose M, Borchardt L, Klein N, Senkovska I, et al. A cubic ordered, mesoporous carbide-derived carbon for gas and energy storage applications. Carbon 2010;48(14):3987–92.
[24] Rose M, Korenblit Y, Kockrick E, Borchardt L, Oschatz M, Kaskel S, et al. Hierarchical micro- and mesoporous carbide-derived carbon as a high-performance electrode material in supercapacitors. Small 2011;7(8):1108–17.
[25] Ersoy DA, McNallan MJ, Gogotsi Y. Platinum reactions with carbon coatings produced by high temperature chlorination of silicon carbide. J Electrochem Soc 2001;148(12):774–9.
[26] Leis J, Perkson A, Arulepp M, Nigu P, Svensson G. Catalytic effects of metals of the iron subgroup on the chlorination of titanium carbide to form nanostructural carbon. Carbon 2002;40(9):1559–64.
[27] Kormann M, Gerhard H, Zollfrank C, Scheel H, Popovska N. Effect of transition metal catalysts on the microstructure of carbide-derived carbon. Carbon 2009;47(10):2344–51.
[28] Glenk F, Knorr T, Schirmer M, Gutlein S, Etzold BJM. Synthesis of microporous carbon foams as catalyst supports. Chem Eng Technol 2010;33(4):698–703.
[29] Lamber R, Jaeger N, Schulz-Ekloff G. Electron microscopy study of the interaction of Ni, Pd and Pt with carbon II. Interaction of palladium with amorphous carbon. Surf Science 1990;227:15–23.
[30] Käärik M, Arulepp M, Karelson M, Leis J. The effect of graphitization catalyst on the structure and porosity of SiC derived carbons. Carbon 2008;46:1579–87.
[31] Kockrick E, Schrage C, Grigas A, Geiger D, Kaskel S. Synthetic and catalytic properties of microemulsion-derived cerium oxide nanoparticles. J Solid State Chem 2008;181(7):1614–20.
[32] Kockrick E, Frind R, Rose M, Petasch U, Bohlmann W, Geiger D, et al. Platinum induced crosslinking of polycarbosilanes for the formation of highly porous CeO_2/silicon oxycarbide catalysts. J Mater Chem 2009;19(11):1543–53.
[33] Kockrick E, Krawiec P, Petasch U, Martin HP, Herrmann M, Kaskel S. Porous CeOX/SiC nanocomposites prepared from reverse polycarbosilane-based microemulsions. Chem Mater 2008;20(1):77–83.
[34] Uskokovic V, Drofenik M. Synthesis of materials within reverse micelles. Surf Rev Lett 2005;12(2):239–77.
[35] Althues H, Kaskel S. Sulfated zirconia nanoparticles synthesized in reverse microemulsions: preparation and catalytic properties. Langmuir 2002;18(20):7428–35.
[36] Henle J, Simon P, Frenzel A, Scholz S, Kaskel S. BiOX (X = Cl, Br, I) particles synthesized in reverse microemulsions. Chem Mater 2007;19(3):366–73.
[37] Kockrick E, Borchardt L, Schrage C, Gaudillere C, Ziegler C, Freudenberg T, et al. CeO2/Pt catalyst nanoparticle containing carbide-derived carbon composites by a new in situ functionalization strategy. Chem Mater 2010;23(1):57–66.
[38] Rajagopalan R, Ponnaiyan A, Mankidy PJ, Brooks AW, et al. Molecular sieving nanoparticle catalysts kinetically frozen in nanoporous carbon. Chem Commun 2004:2498–9.
[39] Yoshimura K, Teruyuki H, Sugimoto M, Yamamoto S, Yoshikawa M. Synthesis of palladium nanoparticles in a ceramic matrix using radiation grafting method. Rad Phys Chem 2011;80(4):587–90.
[40] Lamber R, Jaeger N. On the reaction of platinum with silica substrates: observation of the platinum silicide (Pt_3Si) phase with copper-gold (Cu_3Au) superstructure. J Appl Phys 1991;70:457–60.
[41] Kockrick E, Schrage C, Borchardt L, Klein N, Rose M, Senkovska I. Mesoporous carbide derived carbons for high pressure gas storage. Carbon 2010;48(6):1707–17.
[42] Strasser P. Dealloyed core shell fuel cell electrocatalysts. Rev Chem Eng 2009;25(4):255.
[43] Strasser P, Koh S, Anniyev T, Greeley J, More K, Yu C, et al. Lattice-strain control of the activity in dealloyed core-shell fuel cell catalysts. Nat Chem 2010;2(6):454–60.
[44] Gasteiger HA, Markovic NM. Chemistry: just a dream–or future reality? Science 2009;324(5923):48–9.
[45] Oezaslan M, Strasser P. Activity of dealloyed $PtCo_3$ and $PtCu_3$ nanoparticle electrocatalyst for oxygen reduction reaction in polymer electrolyte membrane fuel cell. J Power Sources 2011;196:5240–9.
[46] Srivastava R, Mani P, Hahn N, Strasser P. Efficient oxygen reduction fuel cell electrocatalysis on voltammetrically dealloyed Pt–Cu–Co nanoparticles. Angew Chem Int Ed 2007;46:8988–91.
[47] Yu C, Koh S, Leisch J, Toney M, Strasser P. Size and composition distribution dynamics of alloy nanoparticle electrocatalysts probed by anomalous small angle X-ray scattering (ASAXS). Faraday Discussions 2008;140:283–96.
[48] Oezaslan M, Hasché F, Strasser P. In-situ observation of bimetallic alloy nanoparticle formation and growth using high-temperature XRD. Chem Mater 2011;23(8):2159–65.
[49] Oezaslan M, Heggen M, Strasser P. Size-dependent morphology of dealloyed bimetallic catalysts: linking the nano to the macro scale. J Am Chem Soc doi:10.1021/ja2088162.

[50] Hasché F, Oezaslan M, Strasser P. Activity, stability and degradation of multi walled carbon nanotube (MWCNT) supported Pt fuel cell electrocatalysts. Phys Chem Chem Phys 2010;12(46):15251–8.
[51] Neyerlin KC, Srivasta R, Yu C, Strasser P. Electrochemical activity and stability of dealloyed Pt–Cu and Pt–Cu–Co electrocatalysts for the oxygen reduction reaction (ORR). J Power Sources 2009;186:261–7.
[52] Koh S, Strasser P. Dealloyed Pt nanoparticle fuel cell electrocatalysts: stability and aging study of catalyst powders, thin films, and inks. J Electrochem Soc 2010;157:585–91.
[53] Hasché F, Oezaslan M, Strasser P. Activity, stability, and degradation mechanisms of dealloyed $PtCu_3$ and $PtCo_3$ nanoparticle fuel cell catalysts. Chem Cat Chem 2011;3:1805–13.
[54] Hasché F, Oezaslan M, Strasser P. Activity, structure and degradation of dealloyed ptni3 nanoparticle electrocatalyst for the oxygen reduction reaction in PEMFC. J Electrochem Soc 2012;159:B25–34.
[55] Schlange A, dos Santos AR, Hasse B, Etzold BJM. Titanium carbide-derived carbon as a novel support for platinum catalysts in direct methanol fuel cell application. J Power Sources 2011;199:22–8.
[56] Gasteiger HA, Kocha SS, Sompalli B, Wagner FT. Activity benchmarks and requirements for Pt, Pt-alloy, and non-Pt oxygen reduction catalysts for PEMFCs. Appl Catal B 2005;56(1–2):9–35.
[57] Bard AJ, Stratmann M. Encyclopedia of Electrochemistry. Wiley-VCH; 2007.
[58] Hamann CH, Hamnett A, Vielstich W. Electrochemistry. Wiley-VCH; 2007.

Dalton Transactions c2dt31977b

1

Soft synthesis of isocyanate-functionalised metal–organic frameworks

Jenny G. Vitillo*, Tristan Lescouet, Marie Savonnet, David Farrusseng and Silvia Bordiga

A green route to isocyanate MOFs: a diphosgene-free method is here described to convert an amino-MOF into an isocyanate one.

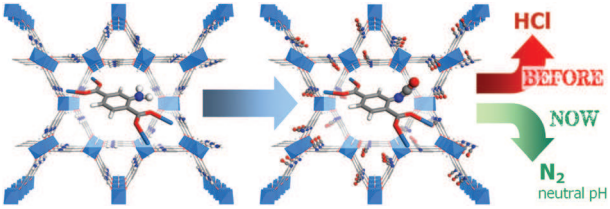

Please check this proof carefully. **Our staff will not read it in detail after you have returned it.**

Translation errors between word-processor files and typesetting systems can occur so the whole proof needs to be read. Please pay particular attention to: tabulated material; equations; numerical data; figures and graphics; and references. If you have not already indicated the corresponding author(s) please mark their name(s) with an asterisk. Please e-mail a list of corrections or the PDF with electronic notes attached – do not change the text within the PDF file or send a revised manuscript.

Please bear in mind that minor layout improvements, e.g. in line breaking, table widths and graphic placement, are routinely applied to the final version.

We will publish articles on the web as soon as possible after receiving your corrections; no late corrections will be made.

Please return your **final** corrections, where possible within **48 hours** of receipt, by e-mail to: dalton@rsc.org

Reprints—Electronic (PDF) reprints will be provided free of charge to the corresponding author. Enquiries about purchasing paper reprints should be addressed via: http://www.rsc.org/publishing/journals/guidelines/paperreprints/. Costs for reprints are below:

Reprint costs

	Cost (per 50 copies)	
No of pages	**First**	**Each additional**
2–4	£225	£125
5–8	£350	£240
9–20	£675	£550
21–40	£1250	£975
>40	£1850	£1550

Cost for including cover of journal issue:
£55 per 50 copies

The Royal Society of Chemistry

Proofs for Correction Dalton

Dear Author,

Paper No. c2dt31977b

Please check the proofs of your paper carefully, paying particular attention to the numerical data, tables, figures and references.

When answering the queries below please ensure that any changes required are clearly marked **on the proof**. There is no need to e-mail your answers to the queries separately from the rest of your proof corrections.

Editor's queries are marked like this [Q1, Q2, …], and for your convenience line numbers are indicated like this [5, 10, 15, …].

Many thanks for your assistance.

Query	Remarks
Q1 For your information: You can cite this article before you receive notification of the page numbers by using the following format: (authors), Dalton Trans., (year), DOI: 10.1039/c2dt31977b.	
Q2 Please carefully check the spelling of all author names. This is important for the correct indexing and future citation of your article. No late corrections can be made.	
Q3 Do you wish to add an e-mail address for the corresponding author?	
Q4 Ref. 9 and 40: Can these references be updated yet?	

Dalton Transactions

Dynamic Article Links

Cite this: DOI: 10.1039/c2dt31977b

www.rsc.org/dalton

COMMUNICATION

Soft synthesis of isocyanate-functionalised metal–organic frameworks†

Jenny G. Vitillo,*[a] Tristan Lescouet,[b] Marie Savonnet,[b,c] David Farrusseng[b] and Silvia Bordiga[a]

Received 29th August 2012, Accepted 9th October 2012
DOI: 10.1039/c2dt31977b

We have developed an original synthetic pathway for the conversion of a MIL-68(In)-NH_2 metal–organic framework into its corresponding isocyanate (–NCO) derivative. This two-step soft post-modification technique leads to highly porous isostructural materials.

Metal–Organic Frameworks (MOFs) are the latest generation of porous crystalline materials.[1–3] Their organic–inorganic hybrid nature allows their cavities to be modified by post-synthetic methods[4–7] in order to tune their hydrophilicity/hydrophobicity[8] or acidity/basicity.[9] Even if this characteristic is not a prerogative of MOFs, in this case the versatility and scope of the reactions are decidedly wider than for zeolites and mesoporous silicates. The functionalisation of MOFs by post-synthetic methods (PSM) is an emerging, efficient approach to tuning the properties of porous coordination polymers at the molecular scale.[9–13] Many post-functionalisation approaches have been developed for MOFs; they range from simple condensation reactions to more complex methods involving protection/deprotection steps.[14–18]

MOFs constructed from 2-aminoterephthalate are excellent starting precursors for post-synthetic functionalisation: this is due to the affordability of this linker and because one can employ the same synthesis conditions as for their unfunctionalised counterparts.[19–21] Unfortunately, the weak nucleophilicity of aromatic amines limits their application. In contrast, strongly electrophilic groups such as isocyanates have been shown to be highly versatile in this respect, allowing the introduction of various carbamate and urea functional groups.[22] The direct synthesis of MOFs possessing such functional groups is difficult, however, so in general these groups are introduced by post-synthetic means. Interestingly, it is possible to transform amino into isocyanate groups in MOFs, but the present method requires the use of diphosgene (route 1 in Scheme 1). In fact, the treatment of MIL-53(Al)-NH_2 (MIL: Materials from Institut Lavoisier, Al(OH) (2-amino-1,4-benzenedicarboxylate)) leads to the corresponding MIL-53(Al)-NCO.[22,23] This method cannot, however, be applied to most MOFs, because the diphosgene treatment involves HCl formation, which in turn leads to the solubilisation of the solid.

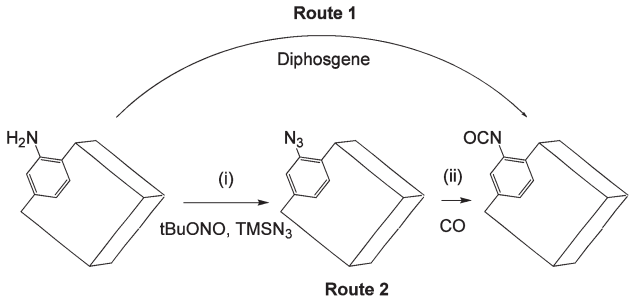

Scheme 1 Possible synthetic routes to MOFs with pendent isocyanate groups.

The protection–deprotection approach is a general concept that allows this limitation to be circumvented. Very recently, Kitagawa[24] and Cohen[25] reported the first light-driven deprotection of MOFs in order to reveal "dormant" reactive functionalities.[18] In particular, Sato *et al.*[24] have shown that azide groups in MOFs can be transformed into nitrene species upon photoactivation.[24–26] Nitrenes in the triplet spin state are very reactive species that can easily react with gas molecules, solvents and organic compounds.[27,28] In fact, in the presence of CO and upon UV irradiation, the transformation of MOF-N_3 to MOF-NCO has been reported,[24] in analogy to what was reported previously for matrix-isolated aryl azides under cryogenic conditions.[29–31] The possibility of converting azide into isocyanate has also been reported for the reaction of these species with metal carbonyls[32–37] or through the Curtius rearrangement of acyl azide groups. Unfortunately, the azide to isocyanate conversion was performed over a very long reaction time with a requirement for continuous cooling with liquid nitrogen in order to transform the inert singlet-state azide group into the reactive triplet species. Moreover, a very low amount of isocyanate was obtained after 12 h.[24]

The present study concerns an original procedure for synthesising MOF-NCO from a MOF based on 2-amino-1,4-BDC (BDC: 1,4-benzenedicarboxylate) by a two-step soft post-modification technique (route 2 in Scheme 1). This new method combines two reactions already reported in the literature that here are juxtaposed for the first time. This combination makes it possible to exploit the advantages of both the amino and isocyanate precursors in order to derive new MOFs. As a proof of concept, this

[a]*Dipartimento di Chimica and NIS Centre of Excellence, Università di Torino, Via Pietro Giuria 7, 10125 Torino and INSTM UdR Torino, Italia*
[b]*IRCELYON, Institut de recherches sur la catalyse et l'environnement de Lyon, Université Lyon 1 – CNRS, 2 avenue Albert Einstein, F-69626 Villeurbanne Cedex, France*
[c]*IFP Energies Nouvelles, BP n°3, 69360 Solaize, France*

†Electronic supplementary information (ESI) available: Experimental procedures, XRPD and nitrogen adsorption measurements, MIL-68(In) structure, thermal gravimetric analysis of MIXMOF-MIL-68(In)-N_3, IR spectra obtained for different reaction temperatures and times of CO/MIL-68(In)-N_3. See DOI: 10.1039/c2dt31977b

study deals with the post-modification of In(OH)(2-amino-1,4-BDC), hereafter denoted MIL-68(In)-NH_2.[38,39] This material has been chosen because, despite its good stability in air, it easily hydrolyses in water, making the diphosgene treatment unsuitable for MIL-68. This method can be applied to other MOF structures with varying degrees of functionalisation: these results and the properties of the MOFs that can be obtained by exploiting the rich reactivity of isocyanate groups will be described elsewhere.[40] The first step involves the conversion of MIL-68(In)-NH_2 into the corresponding azide compound MIL-68(In)-N_3 by following a post-synthetic method reported previously.[38,41] In the second step, MIL-68(In)-N_3 is thermally activated in the presence of CO to form MIL-68(In)-NCO. Due to the high reactivity of the aryl nitrenes, it is important that these groups are sufficiently widely spaced within the material for reactions between them to be prevented.[42] For this reason, an $–NH_2$ diluted structure was considered as a starting material. This material was synthesised using an 80 : 20 ratio of BDC and BDC-NH_2 (MIXMOF-MIL-68(In)-20%NH_2). The preservation of the ligand ratio in the synthesised material and its homogeneity were demonstrated previously.[43,44] The integration of the aromatic proton signals of BDC-NH_2 (7, 7.35 and 7.75 ppm) in ^{1}H-NMR (Fig. 2a) accordingly indicated that 18.22% of the total linkers of this material are BDC-NH_2.

MIL-68(In) materials are MOFs constituted of wires of $InO_4(OH)_2$ octahedra linked by BDC-based linkers, giving rise to a Kagomé structure characterised by two families of 1D pores of hexagonal (17.8 Å, nucleus–nucleus distances) and triangular shape (7.8 Å). MIXMOF-MIL-68(In)-20%NH_2 was (i) treated with *t*BuONO and $TMSN_3$ in THF overnight at room temperature to produce the corresponding azide intermediates; (ii) dried in air and activated under ultra-high vacuum at 90 °C overnight in order to remove all the solvent and water molecules; and (iii) reacted three times with an excess of CO (300 mbar) at 120 °C for 48 h (total reaction time).

The crystallinity and surface area of each sample were verified by X-ray powder diffraction (XRPD) and nitrogen adsorption and compared with theoretical values (Table S1 and Fig. S2†). The transformation of $–N_3$ into –NCO was followed by Fourier transform infrared (FTIR) and ^{1}H-NMR spectroscopies.

The IR spectra of MIXMOF-MIL-68(In)-N_3 samples before and after the reaction with CO are reported in Fig. 1a (black and red curve, respectively). The spectrum of activated MIXMOF-MIL-68(In)-N_3 was characterised by a sharp IR absorption at 3662 cm^{-1} associated with the structural isolated hydroxyls, an intense band at 2118 cm^{-1} due to the stretching of azide groups and a complex set of signals below 1790 cm^{-1} mainly associated with framework modes. The negligible intensity of signals at 3506 and 3393 cm^{-1} assigned to N–H stretching was an indication of the total amino-to-azide transformation that was also confirmed by ^{1}H-NMR (see below). After the reaction with CO, the only significant change in the IR spectrum (red curve) was the consumption of $–N_3$ and the growth of a strong band at 2285 cm^{-1} characteristic of the –NCO group.[24] The transformation of $–N_3$ species into –NCO is confirmed by the sequence of spectra in Fig. S6,† in which an isosbestic point is visible at about 2230 cm^{-1}. An estimation of the degree of conversion was difficult to be achieved by FTIR because of the high extinction coefficient of both azide and isocyanate groups.

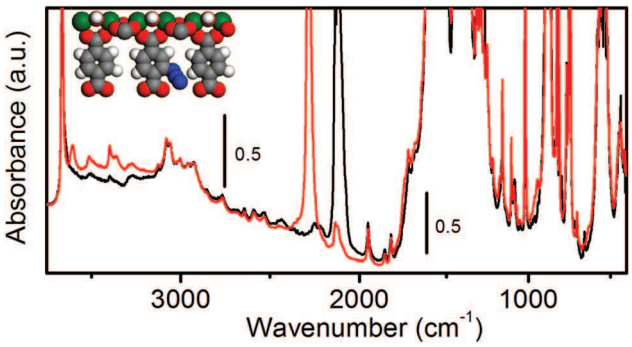

Fig. 1 FTIR spectra of MIXMOF-MIL-68(In)-N_3 degassed at 90 °C overnight (black curve) and after the reaction with 300 mbar of CO at 120 °C for 48 h (red curve). In the pictorial scheme of the MOF walls, the atoms are represented as spheres with the colour code: red (oxygen), grey (carbon), white (hydrogen), blue (nitrogen) and green (indium).

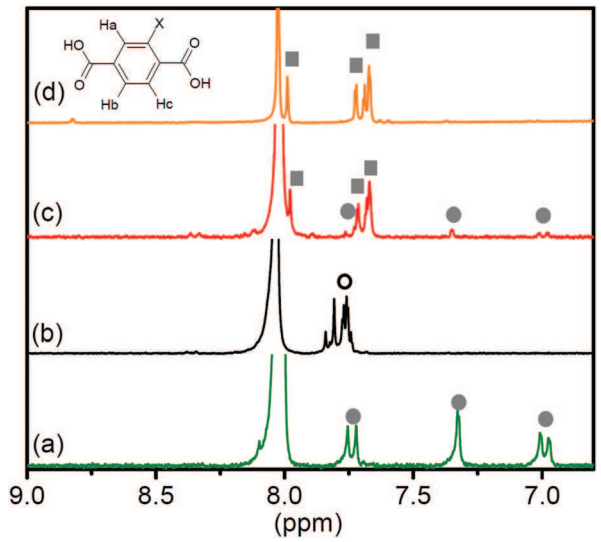

Fig. 2 ^{1}H-NMR spectra of MIXMOF-MIL-68(In)-NH_2 (a), MIXMOF-MIL-68(In)-N_3 (b) and MIXMOF-MIL-68(In)-NCO (c). The spectrum of MIXMOF-MIL-53(Al)-NCO obtained *via* diphosgene treatment is also reported for comparison (d). Before measurements all samples were digested in HF/DMSO-d_6.[22] Filled circles refer to amino signals, empty circles to azide species and filled squares to isocyanate groups.

The full conversion of azide into isocyanate groups was confirmed by ^{1}H-NMR.

^{1}H-NMR was used to follow the modification of the ligand substitution due to the strong shift of its aromatic protons and to quantify the degree of conversion of azide into isocyanate groups. The spectra are reported in Fig. 2.

A singlet at 8.02 ppm corresponds to the aromatic protons of pure terephthalic acid. The spectrum of MIXMOF-MIL-68(In)-NH_2 (green curve) exhibits two doublets (7 ppm, H_b, and 7.75 ppm, H_c) and a singlet (7.35 ppm, H_a, filled circles) that are not present after the transformation of amino into azide groups (black curve). The MIXMOF-MIL-68(In)-N_3 spectrum is characterised by a broad signal at around 7.75 ppm (empty circle). The spectrum of MIXMOF-MIL-68(In)-NCO (red curve) shows two doublets at 7.6 (H_b) and 8 ppm (H_c) and a singlet at 7.6 ppm

(H_a) (squares). These signals can be associated with the formation of isocyanates as seen for the spectrum obtained for MIXMOF-MIL-53(Al)-NCO (80 : 20 ratio between BDC and BDC-NH_2, orange curve) following the diphosgene route.[22] In the isocyanate-modified materials (red and orange curves) the signals related to amino groups (filled circles) are observed due to side reactions. Their weak intensity confirms the very low concentration of these species, in agreement with FTIR results.

XRPD measurements indicated that the reaction with CO did not affect the MIXMOF-MIL-68(In) pattern (Fig. S2†). These findings were further confirmed by nitrogen adsorption measurements that demonstrate that the MOF pore structure is not modified after the reaction with CO (Fig. S1 and Table S1†).

In conclusion, this new two-step synthesis extends the possibility of post-functionalisation with isocyanate groups to a higher number of MOFs than was achievable with the diphosgene route, with these MOFs representing intermediates for the design of diverse sophisticated and functional porous MOFs. Moreover, the thermal activation of $-N_3$ groups in MOF materials, by avoiding the use of solvents, offers the possibility of further extending the nitrene chemistry.[29–31]

Financial support from the European VII framework through STREP project NANOMOF Contract number: FP7-NMP-2008-LARGE-2 is gratefully acknowledged.

Notes and references

1 G. Férey, *Science*, 2001, **291**, 994–995.
2 M. Eddaoudi, J. Kim, N. Rosi, D. Vodak, J. Wachter, M. O'Keeffe and O. M. Yaghi, *Science*, 2002, **295**, 469–472.
3 S. Horike, S. Shimomura and S. Kitagawa, *Nat. Chem.*, 2009, **1**, 695–704.
4 S. J. Garibay, Z. Q. Wang, K. K. Tanabe and S. M. Cohen, *Inorg. Chem.*, 2009, **48**, 7341–7349.
5 J. Lee, O. K. Farha, J. Roberts, K. A. Scheidt, S. T. Nguyen and J. T. Hupp, *Chem. Soc. Rev.*, 2009, **38**, 1450–1459.
6 J. G. Vitillo, L. Regli, S. Chavan, G. Ricchiardi, G. Spoto, P. D. C. Dietzel, S. Bordiga and A. Zecchina, *J. Am. Chem. Soc.*, 2008, **130**, 8386–8396.
7 Z. Q. Wang and S. M. Cohen, *Chem. Soc. Rev.*, 2009, **38**, 1315–1329.
8 J. Canivet, S. Aguado, C. Daniel and D. Farrusseng, *ChemCatChem*, 2011, **3**, 675–678.
9 M. Savonnet, A. Camarata, J. Canivet, D. Bazer-Bachi, N. Bats, V. Lecocq, C. Pinel and D. Farrusseng, *Dalton Trans.*, 2012, DOI: 10.1039/c1032dt11994c.
10 S. Aguado, J. Canivet, Y. Schuurman and D. Farrusseng, *J. Catal.*, 2011, **284**, 207–214.
11 J. Gascon, U. Aktay, M. D. Hernandez-Alonso, G. P. M. van Klink and F. Kapteijn, *J. Catal.*, 2009, **261**, 75–87.
12 F. X. Llabrés i Xamena, A. Abad, A. Corma and H. Garcia, *J. Catal.*, 2007, **250**, 294–298.
13 C. D. Wu, A. Hu, L. Zhang and W. B. Lin, *J. Am. Chem. Soc.*, 2005, **127**, 8940–8941.
14 J. Canivet and D. Farrusseng, *ChemCatChem*, 2011, **3**, 823–826.
15 S. M. Cohen, *Chem. Rev.*, 2012, **112**, 970–1000.
16 R. K. Deshpande, J. L. Minnaar and S. Telfer, *Angew. Chem., Int. Ed.*, 2010, **49**, 4598–4602.
17 D. J. Lun, G. I. N. Waterhouse and S. G. Telfer, *J. Am. Chem. Soc.*, 2011, **133**, 5806–5809.
18 R. K. Deshpande, G. I. N. Waterhouse, G. B. Jameson and S. G. Telfer, *Chem. Commun.*, 2012, **48**, 1574–1576.
19 S. Couck, J. F. M. Denayer, G. V. Baron, T. Remy, J. Gascon and F. Kapteijn, *J. Am. Chem. Soc.*, 2009, **131**, 6326–6327.
20 T. Loiseau, C. Serre, C. Huguenard, G. Fink, F. Taulelle, M. Henry, T. Bataille and G. Férey, *Chem.–Eur. J.*, 2004, **10**, 1373–1382.
21 M. Kandiah, M. H. Nilsen, S. Usseglio, S. Jakobsen, U. Olsbye, M. Tilset, C. Larabi, E. A. Quadrelli, F. Bonino and K. P. Lillerud, *Chem. Mater.*, 2010, **22**, 6632–6640.
22 C. Volkringer and S. M. Cohen, *Angew. Chem., Int. Ed.*, 2010, **49**, 4644–4648.
23 E. Dugan, Z. Wang, M. Okamura, A. Medina and S. M. Cohen, *Chem. Commun.*, 2008, 3366–3368.
24 H. Sato, R. Matsuda, K. Sugimoto, M. Takata and S. Kitagawa, *Nat. Mater.*, 2010, **9**, 661–666.
25 K. K. Tanabe, C. A. Allen and S. M. Cohen, *Angew. Chem., Int. Ed.*, 2010, **49**, 9730–9733.
26 M. J. Rosseinsky, *Nat. Mater.*, 2010, **9**, 609–610.
27 L. Horner and A. Christmann, *Angew. Chem., Int. Ed.*, 1963, **2**, 599–608.
28 R. C. Larock, *Comprehensive Organic Transformations: A Guide to Functional Group Preparations*, Wiley-VCH, New York, 1999.
29 I. R. Dunkin and P. C. P. Thomson, *J. Chem. Soc., Chem. Commun.*, 1982, 1192–1193.
30 I. R. Dunkin, T. Donnelly and T. S. Lockhart, *Tetrahedron Lett.*, 1985, **26**, 359–362.
31 N. P. Gritsan, *Russ. Chem. Rev.*, 2007, **76**, 1139.
32 R. J. Angelici and G. C. Faber, *Inorg. Chem.*, 1971, **10**, 514–517.
33 D. E. Fjare, J. A. Jensen and W. L. Gladfelter, *Inorg. Chem.*, 1983, **22**, 1774–1780.
34 J. S. McIndoe and B. K. Nicholson, *J. Organomet. Chem.*, 1999, **573**, 232–236.
35 P. Leoni, M. Pasquali, D. Braga and P. Sabatino, *J. Chem. Soc., Dalton Trans.*, 1989, 959–963.
36 L. A. P. Kane-Maguire, M. Manthey and B. Robinson, *J. Chem. Soc., Dalton Trans.*, 1995, 905–908.
37 H. Werner, W. Beck, H. Engelmann and H. S. Smedal, *Chem. Ber.*, 1968, **101**, 2143.
38 M. Savonnet, D. Bazer-Bachi, N. Bats, J. Perez-Pellitero, E. Jeanneau, V. Lecocq, C. Pinel and D. Farrusseng, *J. Am. Chem. Soc.*, 2010, **132**, 4518–4519.
39 C. Volkringer, M. Meddouri, T. Loiseau, N. Guillou, J. Marrot, G. Ferey, M. Haouas, F. Taulelle, N. Audebrand and M. Latroche, *Inorg. Chem.*, 2008, **47**, 11892–11901.
40 T. Lescouet, J. G. Vitillo, D. Farrusseng and S. Bordiga, *J. Mater. Chem.*, 2012, manuscript in preparation.
41 M. Savonnet, E. Kockrick, A. Camarata, D. Bazer-Bachi, N. Bats, V. Lecocq, C. Pinel and D. Farrusseng, *New J. Chem.*, 2011, **35**, 1892–1897.
42 H. Deng, C. J. Doonan, H. Furukawa, R. B. Ferreira, J. Towne, C. B. Knobler, B. Wang and O. M. Yaghi, *Science*, 2010, **327**, 846–850.
43 T. Lescouet, E. Kockrick, G. Bergeret, M. Pera-Titus, S. Aguado and D. Farrusseng, *J. Mater. Chem.*, 2011, **22**, 10287–10293.
44 M. Pera-Titus, T. Lescouet, S. Aguado and D. Farrusseng, *J. Phys. Chem. C*, 2012, **116**, 9507–9516.

RESUME en français

Les Metal-Organic Frameworks résultent de l'organisation de clusters métalliques et de molécules organiques chélatantes qui forment un réseau cristallin poreux. Leur découverte a permis des avancées majeures dans le domaine du stockage et de la séparation des gaz. Malheureusement la faible stabilité et l'acidité modérée de ces matériaux ne les rendent que peu compétitifs par rapport aux zéolites dans le domaine du raffinage ou de la dépollution. Il s'agit d'explorer, avec ces matériaux, de nouvelles applications catalytiques en tirant partie de leur principale qualité : leur modularité. En effet le large choix de métaux, de ligands, ainsi que la post fonctionnalisation de ces derniers permet la synthèse contrôlée de matériaux possédant des propriétés de flexibilité, de confinement ainsi qu'un environnement chimique similaire à celui des sites actifs des enzymes. Ce travail s'inspire du procédé catalytique des enzymes pour obtenir des MOFs hautement sélectifs en conditions douces. Nous décrivons le développement de méthodes pour encapsuler des catalyseurs organométalliques dans des pores calibrés afin de modifier la sélectivité d'une réaction d'oxydation et stabiliser le catalyseur. Quatre MOFs supportant des groupes amino ont été synthétisés afin de permettre leur post fonctionnalisation. Les propriétés de flexibilité ainsi que la distribution des sites potentiellement actifs du MOF MIL-53 ont également été contrôlés grâce à la fonctionnalisation partielle de la structure. Enfin ces amino MOFs furent post fonctionnalisés en isocyanate en deux étapes afin d'améliorer la réactivité de la structure et de permettre le greffage de diverses amines. Ces outils pourraient permettre à court terme la conception de MOFs dont les pores ont un environnement semblable aux metalloenzymes.

Titre en anglais
Development of MOFs as supports or host for organometallic complexes

RESUME en anglais

MOFs are generated from the association of metallic clusters connected by organic linkers to form crystalline porous materials. Their discovery was a breakthrough in the domain of separation and gas storage. Unfortunately, MOFs have a low stability and moderate acidity and cannot compete with zeolites for use in industrial catalysis. To design a viable MOF catalyst, we can take advantage of its almost infinite possibility of customisation. Indeed, a large choice of metal, linkers or post synthetic modifications allow the creation of environments similar to the active sites of enzymes and can lead to the synthesis of solids with analogue flexibility or "molecular recognition" properties. This work takes inspiration from enzymes to mimic their ability to catalyse reactions with high chemio-, region- and enantio-selectivity in mild conditions. We developed a method for the encapsulation of organometallic complexes in the large pore of MOF MIL-101. The selectivity of an oxidation reaction was modified and the catalyst was stabilised within the MOF. In addition, four amino functionalized MOFs were synthesized as starting materials for post functionalization. Their flexibility and the active site distribution were controlled by the use of a "mixed linker" strategy: functionalized linkers were diluted with unfunctionalized ones during the synthesis. Lastly, these amino-MOFs were post-functionalized in two steps in isocyanate in order to ameliorate the structure reactivity and allow for the grafting of a large range of amines. This work brings the tools for the synthesis of potential "artificial enzymes".

DISCIPLINE
Catalyse et Chimie-Physique des matériaux

MOTS-CLES: metal organic frameworks • flexibility • post-synthesis • isocyanate • catalysis

IRCELYON, 2 avenue Albert Einstein, 69626, Villeurbanne cedex